UNIVERSITY OF CAMBRIDGE

Development of a hydrogel-based microfluidic model of the lymph node

Corrado Mazzaglia

Department of Engineering / MRC Cancer unit
Wolfson College, University of Cambridge

August 2022

This thesis is submitted for the degree of Doctor of Philosophy.

This thesis is the result of my own work and includes nothing which is the outcome of work done in collaboration except as specified in the text.

It is not substantially the same as any work that has already been submitted before for any degree or other qualification.

It does not exceed the prescribed word limit of 60000.

Corrado Mazzaglia

Acknowledgements

I would like to express my sincere gratitude to my supervisors Dr Jacqueline Shields and Dr Shery Huang for their invaluable advice, continuous support and trust throughout my PhD degree. I am deeply grateful to all Shields lab members for creating such a cheerful, inspirational and supportive atmosphere. Particularly Hafsa Munir, Luisa Pedro, Sarah Davidson, Jake Cridge, Will Moody, Leonor Nunes Rodrigues, Tik Shing Cheung, Anna Clay and Carlo Zimarino.

Also, I would like to thank the Biointerface group for broadening my view on new research areas and ideas and importantly, Ye Liu, Iek Man Lei, and Yaqi Sheng for the close scientific collaborations carried out during these years. I am also grateful to Andy Wang, Ruishan Liu, Edward Cozens, Adithya Vivek, Magali Ferro, Pooya Davoodi, Lizzie Gill, Duo Zhang, Saeed Fathi, Marzia Calcagno, Yang Cao, Harvey Shi, Yifei Pan.

I would like to acknowledge Dr Alessandro Esposito and his lab members for sharing crucial equipment and particularly Dr Andrew Trinh for his help with microscopy experiments.

Besides, I would like to extend my genuine thanks to the Hutch core staff, the CIMR flow team, Ares and the Cavendish Physics workshop for being so supportive, helpful and for their responsiveness. I would like to acknowledge the W D Armstrong Trust for funding my PhD study, and Wolfson College for supporting my attendance at conferences.

Finally, I would like to thank my family for the endless love and support in these last years for which I am grateful.

Abstract

Lymph nodes (LNs) are immunological hubs where antigen and naïve lymphocytes meet to mount antigen specific immune responses. In cancers, the tumour-draining lymph node (TDLN) is the site of initial anti-tumour immune response. The TDLN undergoes dramatic reprogramming in response to tumour drainage that is still partly unclear. *In vivo* models do not easily permit us to follow events longitudinally or to manipulate the environment, while currently there is a lack of *in vitro* platforms that recapitulate the LN complexity to study its role in response to antigens and in disease.

First, I have tried to adapt an existing PDMS-based device to model the LN. Having encountered some limitations, I have then developed a novel hydrogel-based LN-on-chip device. I have optimized a fluidic system, cell culture conditions and hydrogel composition to obtain long term culture of lymphoid primary cultures from spleen with a stromal cell line of fibroblastic reticular cells (FRCs). Different hydrogel formulations were tested and characterized with multiple techniques focusing on maintaining physiological cell morphology in the new 3D environment. In addition, a LN-like architecture was achieved where B cells are segregated from T cells, into B cell follicles.

After optimization of the 3D cellular system with built-in fluidics, I applied the model to different context. Initially, PMA/Ionomycin, a strong cell activator, was perfused to obtain a general activation response. Then, LPS was used to trigger a reaction to a bacteria-derived antigen. Finally, using the OT-I model, I have used the device to trigger an antigen specific immune response to an OVA peptide.

In the final part of the thesis, I modelled a TDLN *in vitro*. The LN device was incubated with tumour conditioned media (TCM) and IL-7 downregulation was observed, similarly to *in vivo* murine melanoma models. Then, to increase the complexity of the source of the tumour cues, a new tumour model was developed through 3D bioprinting, which also includes a shell of cancer associated fibroblasts (CAFs) and immune cells to form a complex engineered tumour microenvironment (TME). Incubation of the LN device with conditioned medium from the engineered TME also induced downregulation of IL-7.

Unlike current *in vivo* models that require node dissection at each discrete time point, this system allowed the monitoring of tissue remodelling in real-time via live imaging and measure molecular changes at a surface markers level as well as gene expression.
Overall, this platform can represent a valid tool to study in vitro the LN complexity in a more tractable way.

Table of Contents

Nomenclature

Abbreviations

ANOVA	Analysis Of Variance
APC	Antigen Presenting Cell
B220	Protein Tyrosine Phosphatase Receptor Type C
BAFF	B Cell Activating Factor
BECs	Blood Endothelial Cells
CAD	Computer-aided design
CAF	Cancer-Associated Fibroblasts
CCL19	C-C Motif Chemokine Ligand 19
CCL21	C-C Motif Chemokine Ligand 21
CCR7	C-C Motif Chemokine Receptor 7
CD11b	Cluster of Differentiation 11b
CD11c	Cluster of Differentiation 11c
CD169	Cluster of Differentiation 169
CD3	Cluster of Differentiation 3
CD34	Cluster of Differentiation 34
CD4	Cluster of Differentiation 4
CD44	Cluster of Differentiation 44
CD45	Cluster of Differentiation 45
CD62L	Cluster of Differentiation 62L or L-Selectin
CD69	Cluster of Differentiation 69
CD8	Cluster of Differentiation 8
CM	Central Memory
CTLA-4	Cytotoxic T Lymphocyte Antigen 4
CXCL10	C-X-C Motif Chemokine Ligand 10
CXCL13	C-X-C Motif Chemokine Ligand 13
CXCR5	C-X-C Motif Chemokine Receptor 5
DC	Dendritic Cell
DMEM	Dulbecco's Modified Eagle Medium
ECM	Extracellular matrix
EDTA	Ethylenediaminetetraacetic Acid
EM	Effector memory
eGFP	Enhanced Green Fluorescent Protein
EGFR	Epidermal Growth Factor Receptor
FBS	Foetal Bovine Serum
FDC	Follicular Dendritic Cell
FoxP3	Forkhead Box P3

FRC	Fibroblastic Reticular Cell
GC	Germinal Centre
GelMA	Gelatin methacryloyl
GFP	Green Fluorescent Protein
HA	Hyaluronic acid
HEPES	(4-(2-hydroxyethyl)-1-piperazineethanesulfonic acid)
HEV	High-Endothelial Venules
HLA	Human Leukocyte Antigen
HPV	Human Papillomavirus
HSV-1	Herpes Simplex Virus Type 1
ICAM-1	Intercellular Adhesion Molecule 1
ICI	Immune Checkpoint Inhibitors
IFNγ	Interferon γ
IFR	Interfollicular region
IL-10	Interleukin-10
IL-4	Interleukin-4
IL-6	Interleukin-6
IL-7	Interleukin-7
Itgα7	Integrin-A 7
LAP	Lithium phenyl-2,4,6-trimethylbenzoylphosphinate
LEC	Lymphatic Endothelial Cell
LFA-1	Lymphocyte Function-Associated Antigen-1
LN	Lymph Node
LNSC	Lymph Node Stromal Cells
LPA	Lysophosphatidic Acid
LPS	Lipopolysaccharide
LTBR	Lymphotoxin B Receptor
LYVE1	Lymphatic Vessel Endothelial Hyaluronan Receptor 1
MA	Methacrylated
mAB	Monoclonal Antibody
MACS	Magnetic-Activated Cell Sorting
MHC	Major Histocompatibility Complex
MRC	Marginal Reticular Cells
NDLN	Non-Draining Lymph Node
NK	Natural Killer Cells
NO	Nitric Oxide
OVA	Ovalbumin
PAA	Poly(acrylic acid)
PAAm	Polyacrylamide
PBMC	Peripheral Blood Mononuclear Cell
PBS	Phosphate buffered saline

PDGFRα	Platelet-Derived Growth Factor A
PDMS	Polydimethylsiloxane
PDPN	Podoplanin
PEGDA	Poly(ethylene glycol) diacrylate
PEO	Polyethylene oxide
PF127	Pluronic F127
PMA	Phorbol Myristate Acetate
PNAd	Peripheral Node Addressin
PTA	Peripheral Tissue Restricted Antigens
PVA	Poly(vinyl alcohol)
qPCR	Quantitative Polymerase Chain Reaction
RBC	Red Blood Cell
RGD	Tripeptide Arg-Gly-Asp
RPMI	Roswell Park Memorial Institute
RT	Room Temperature
S1P	Sphingosine-1-Phosphate
S1PR1	S1P Receptor 1
scRNA	Single Cell RNA Sequencing
SCS	Sub-Capsular Sinus
SEM	Scanning Electron Microscope
SHG	Second Harmonic Generation
SLA	Stereolithography
SLO	Secondary Lymphoid Organ
TCM	Tumour Conditioned Media
TCR:	T cell Receptor
TDLN:	Tumour-Draining Lymph Node
TGF-B:	Transforming Growth Factor β
TLR	Toll-Like Receptor
TME	Tumour Microenvironment
TMECM	Tumour Microenvironment Conditioned Medium
TNFα	Tumour Necrosis Factor A
TRC	T cell Zone Reticular Cells
Treg	T Regulatory Cell
VCAM-1	Vascular Cell Adhesion Protein 1
VEGF	Vascular Endothelial Growth Factor
WT	Wildtype
α-SMA	A-Smooth Muscle Actin

CHAPTER 1

INTRODUCTION

1.1 Lymph Node

The lymph nodes (LNs) are secondary lymphoid organ (SLO) - immune hubs – distributed throughout the body as part of the lymphatic system and primarily function to maintain tissue fluid balance and homeostasis. LNs are interconnected by a network of lymphatic vessels, which drain protein-rich extracellular fluid (or lymph) from tissues, carry it through the lymph nodes and back into the bloodstream via the thoracic duct. By doing this, LNs sample draining lymph surveying for pathogens or altered self-antigens, and as such, they are able to initiate adaptive immune responses. In the organ parenchyma, innate and adaptive cell populations co-exist in a highly dynamic environment in which cells constantly enter and exit to enable efficient communication and rapid responses to potential threats. Furthermore, LNs serve as a site where naïve lymphocytes, that have not encountered an antigen yet, interact with tissue-specific self-antigens leading to their deletion as a mechanism of protection from autoimmune responses [1].

1.1.1 LN architecture

LNs are small bean-shaped, opalescent structures, containing a large number of lymphocytes, macrophages and antigen presenting cells (APCs) as well as stromal populations, separated in functional units called lobules. Mice have 22 identifiable LNs while humans have about 450 [2]. The function of these organs is highly dependent on their spatial organization and on a directed migration and retention of their components to specific zones, regulated by chemical gradients (Figure 1.1). B cells and T cells reside in distinct areas within the organ where they interact with APCs and undergo clonal expansion once engaged [3]. A fibrous capsule of dense connective tissue and collagenous fibers wraps the organ sending trabeculae inside the LN that reach towards the center. The subcapsular sinus (SCS) is present as a cavity between the capsule and the cortex. It is lined by lymphatic endothelial cells (LECs), that are interspersed with $CD169^{+}$ macrophages, which capture and present antigen to B cells. The SCS is a space traversed by both reticular fibers and cells, which receives the afferent vessels, continues with the trabecular sinuses, and joins the medullary sinus in the medulla of the lymph node. Molecules below 70kDa, such as antigens, metabolites and chemokines, are rapidly able to exit the SCS, percolating through the T and B cell zones via a system of small channels called conduits [4,5]. The remaining lymphatic fluid passes from the SCS into the cortical and medullary sinuses before exiting the LN via the efferent lymphatics [6]. The cortex lies just underneath the SCS and constitutes the B cells zone. Here, the B cells are tightly assembled in

spherical follicles with follicular dendritic cells (FDCs) that are able to trigger the formation of germinal centers by presenting antigens to B cells captured from the SCS [7]. These are sites where mature B cells proliferate, differentiate, and mutate their antibody genes. Deeper within the organ lies the paracortex that constitutes the T cell zone, formed mostly of T cells with its associated stroma. Finally, the innermost layer of the LN is the medulla that contains large blood vessels, sinuses and medullary cords. The medullary sinus drains the lymph into the efferent lymphatic vessels while the medullary cords contain antibody-secreting plasma cells, B cells and macrophages.

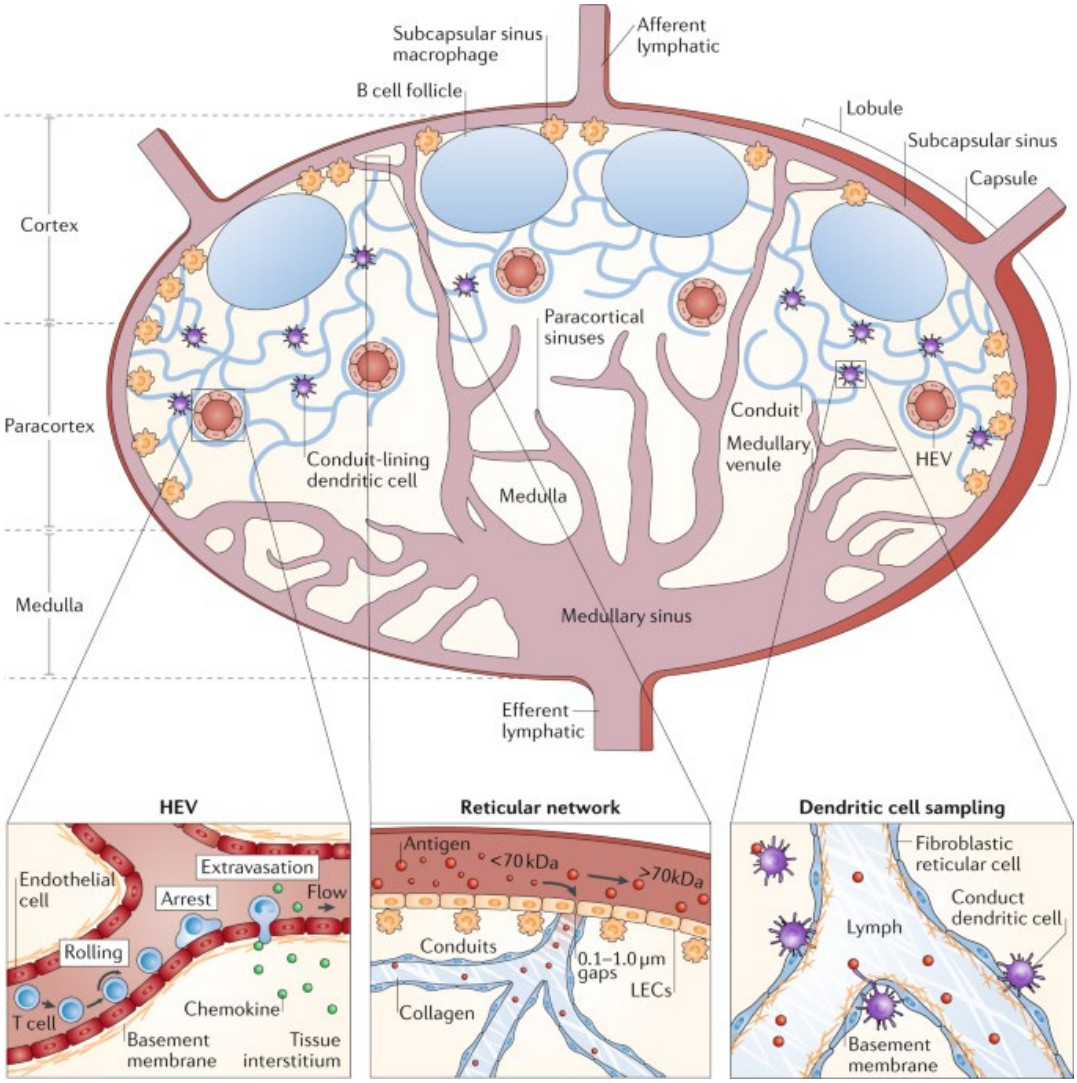

Figure 1.1 Lymph nodes architecture. Schematic showing the LN structure, its three main compartments (cortex, paracortex and medulla) and their main components. HEVs in the paracortex are the sites of extravasation of lymphocytes from the blood stream. FRCs create a reticular network of conduits for improved delivery of antigens to DCs and B cells. Reproduced from [8].

1.1.2 Immune cells trafficking

Entry into LN

In the late 1950s Sir James Gowans was the first to show in rats that lymphocytes constantly circulate between blood and peripheral SLOs, such as LNs [9,10] suggesting the existence of a rapid turnover of lymphocytes in the blood. Subsequently, it was found that immune cell trafficking is a finely regulated process and that the mechanism and trafficking pathway differs depending on the type and state of the immune cell. Travel to the LN is mediated by either the blood or lymphatic vasculature.

Non-activated naïve T cells preferentially enter the LN through specialized high endothelial venules (HEVs) located in the interfollicular (IFR) and paracortical regions of the node. Lymphocyte entry is a multi-step process beginning with cellular rolling [11]. This process occurs when T cells decelerate and start weak interactions with HEV ECs, tethering, and begin rolling along the endothelium via CD62L (L-selectin) – sialomucin interactions, expressed on T cells and ECs respectively. Subsequently, T cells undergo a firmer shear-resistant arrest primarily mediated by an interaction between the β2 integrin LFA-1 (CD11a/CD18) on lymphocytes and ICAM-1/ICAM-2 on HEV ECs. LFA-1 expression on T cells, unlike CD62L, is not constitutively active but is induced by ECs-associated chemokines: CCL19 and CCL21. LFA-1 engages ICAM-1 on endothelial cells to facilitate cellular adhesion. The T cells then start intraluminal crawling and transmigration through the basal lamina which helps immobilizing chemokines for cell guidance. This process is regulated by the lipid mediator lysophosphatidic acid (LPA). LPA accumulates at high concentrations surrounding HEVs, and induces changes in endothelial cell morphology, which facilitates transendothelial migration via a paracellular route[12]. B cells enter LNs in a comparable manner but attracted by different chemokines such as CXCL13.

While naive T cells enter LNs through HEVs, activated subsets preferentially enter via the afferent lymphatic vessels[13]. Activated, effector and memory T cells are collected by a plexus of blind-ended lymphatic capillaries which converge into afferent lymphatic vessels and drain into the SCS of the LN [14]. T cells subsequently cross the lymphatic endothelium in specific 'hotspots' in the basal lamina and enter the LN parenchyma. Existing research suggests that activated T cells become trapped in the molecular meshwork of the SCS and crawl in a random

fashion until they locate pores in the basal lamina [15]. Transmigration across the endothelium is subsequently an integrin- and chemokine-dependent process.

Like effector and memory T cells, Tregs and DCs also utilise the lymphatic vasculature to enter LNs. Tregs express elevated levels of the membrane-bound lymphotoxin, LTα2β1 [16]. When Tregs reach the SCS, LTα2β1 engages the lymphotoxin β receptor (LTBR) on LECs, activating the non-classical arm of the NFκB (NIK) pathway. NIK signalling upregulates VCAM-1 on Tregs and downregulates the intercellular tight junction protein VE-cadherin on LECs [17]. These changes allow Tregs to cross the SCS and enter the LN parenchyma. In contrast, DCs use the atypical chemokine receptor CCRL1 to enter LNs. CCRL1 scavenges CCL19 and CCL21 surrounding the ceiling of the SCS, creating a chemokine gradient which directs DCs through the floor lymphatics and into the LN parenchyma [18].

Migration and positioning

After the immune cells enter the LN parenchyma, a process of migration across the lymphoid tissue begins to obtain the right cellular compartmentalization. In this process the stromal components seem to play a major role in the creation of finely regulated chemical gradients.

Fibroblastic reticular cells (FRCs) form a 3D network of reticular fibres which acts as a scaffold for migrating immune populations. FRCs continually secrete the CCR7 ligands, CCL19 and CCL21, which remain bound to the reticular network. These chemokines guide naïve T cells and antigen-bearing DCs into the LN paracortex and are essential for proper LN function. Disruption of either CCR7 on immune cells, or ligands CCL19 or 21, as occurs in paucity of lymph node T cells (PLT mice), results in delayed immune responses [19,20]. Naïve T cells subsequently adopt a 'random-walk' pattern of motility[21], making rapid and non-directional movements across the FRC scaffold, contacting numerous DCs in the search for stimulating antigen[22]. Antigen-engagement triggers guided migration, as T cells are directed towards specialized inflammatory niches to facilitate differentiation into effector and central memory (CM) subsets [23]. Effector and CM T cells are subsequently positioned in critical locations in the LN, ready for an immune response [24]. In addition, it has been shown that autotaxin (ATX) produced by FRCs generates LPA, which through its enzymatic activity, locally enhances T cell contractility and motility in the lymph node reticular network [25].

B cells display similar patterns of migration but rely on CXCL13 produced by follicular dendritic cells (FDCs) to provide guidance cues to B cell follicles, rather than FRCs [26].

Exit from LN

Lymphocytes egressing from the LN parenchyma migrate into the cortical or medullary sinuses and exit the node via the efferent lymphatics. This extensively studied process is dominantly regulated by sphingosine-1-phosphate (S1P) activity and a few other molecules[27,28]. S1P is a sphingolipid that mediates diverse cellular processes, including cell survival, cytoskeletal rearrangements, and cellular chemotaxis[29]. Its concentration in the body is highly regulated to create gradients, and it is more abundant in the blood and lymph than in the lymphoid organs to allow egress. S1P receptor (S1PR) is expressed by T cells and can be downregulated when it binds S1P, therefore keeping it at low levels in circulating T cells. When entering the lymph node, T cells gradually start upregulating S1PR allowing them to follow the S1P gradient towards the efferent lymphatics. In addition to S1P-induced receptor internalization, the C-type lectin CD69 has also been reported to regulate S1PR surface expression in T cells. CD69, an early T cell activation marker can be upregulated in T cells by various inflammatory mediators, such as type I interferons and has been shown to induce S1PR internalization and degradation, therefore inhibiting egress of newly activated T cells[30].

Similarly, B cells also crawl on FRC networks to reach the B cell follicles, via the CXCL13–CXC-chemokine receptor 5 (CXCR5) axis. During their migration towards the centre of the follicle, B cells upregulate S1PR1 expression[31]. After some time, B and T cells start internalizing their chemokine receptors (namely, CXCR5 and CCR7), desensitising them to CXCL13 and CCL21 and allowing the S1P signal to dominate.

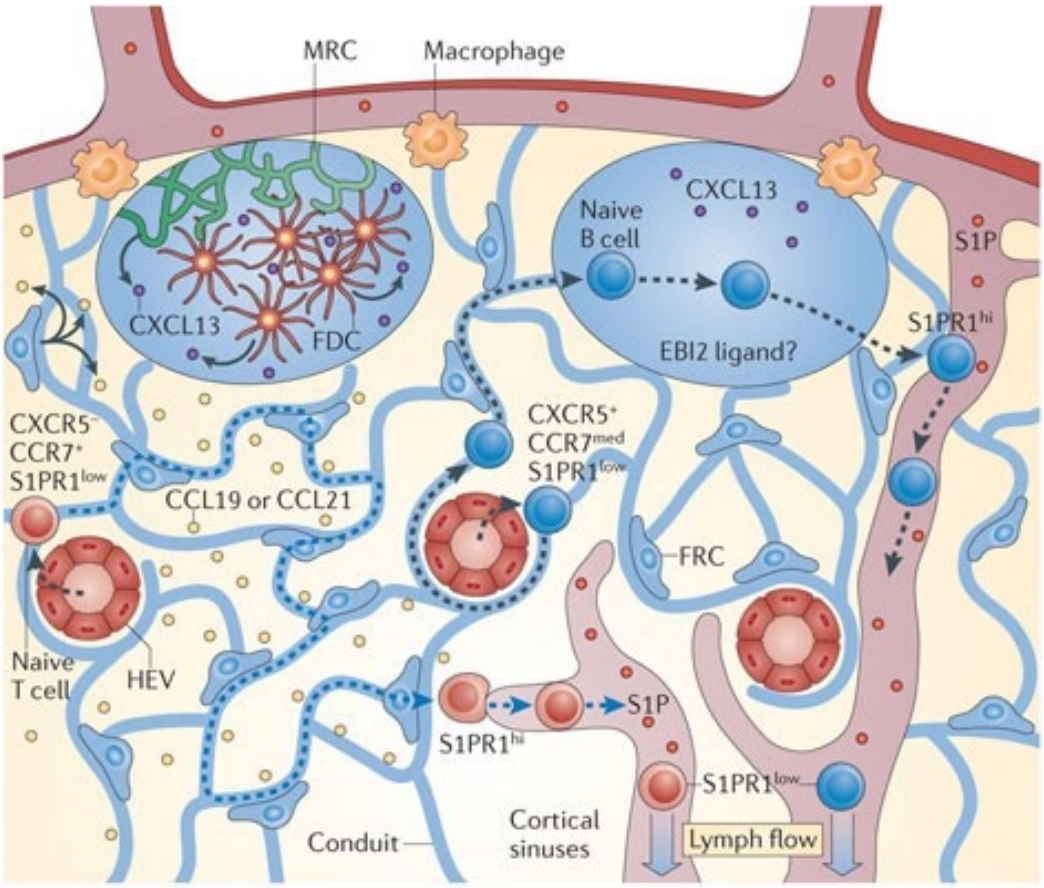

Figure 1.2 Immune cells trafficking. B cells (blue zones) and T cells (yellow zone) resides in distinct compartments. Supporting stromal components (lymphatics, pink; HEV, red; and FRC, blue) provide structural support and routes of trafficking. Naïve lymphocytes can traffic via two ways of entrance. Naïve lymphocytes can enter the parenchyma through HEVs or afferent lymphatic vessels, and once in the LN crawl along a network of conduits formed by the FRCs following chemokine gradients they produce. CCL19 and 21 guide migration into T cell zones, whereas CXCL13 drives chemotaxis of cells into B cell follicles, T cell exit relies on S1P present on endothelial cells of the LN. Reproduced from [32].

1.1.3 Stromal populations in the LN

The stromal populations in the LN were historically regarded as merely structural features of lymphoid tissues. However, these cells are now appreciated as essential regulators of immune cell trafficking, fluid flow, and LN homeostasis. It has been shown that stromal cells, in particular FRCs and LECs play a pivotal role as early as LN organogenesis, before lymphocytes populate the organ. Lymph node stromal cells (LNSCs) drive growth and maturation of LN anlagae to accommodate the influx of mature lymphocytes that only occurs after birth [33]. Their ability to maintain the organ architecture is then retained during the whole life through

secretion of key chemokines for lymphocytes retention. In disease, these pathways can be disrupted resulting in altered organ architecture [34].

LNSCs can be divided into main subclasses based on markers surface expression and are fibroblastic reticular cells (FRCs) ($gp38^{+}CD31^{-}$), follicular dendritic cells (FDCs) ($gp38^{+/-}CD31^{-}$), lymphatic endothelial cells (LECs) ($gp38^{+}CD31^{+}$), blood endothelial cells (BECs) ($gp38^{-}CD31^{+}$), integrin $\alpha7^{+}$ pericytes (IAPs) ($gp38^{-}CD31^{-}ITGA7^{+}$), and a small proportion (<5%) of otherwise undefined stroma ($gp38^{-}CD31^{-}ITGA7^{-}$) [35].

Fibroblastic Reticular Cells (FRCs)

FRCs represent a population of immunologically specialized fibroblasts found within the paracortex of the LN. They are highly contractile cells that support lymph node expansion [36]. Although once considered solely for their structural role, FRCs are now accepted as a key player, actively involved in many different processes crucial for the LN. Single cell RNA sequencing has recently shed light on the LNSCs heterogeneity and discovered nine LN non-endothelial stromal cells clusters: $Ccl19^{hi}$ T-zone reticular cells (TRCs), marginal reticular cells (MRC), FDCs, and perivascular cells. In addition, $Ccl19^{lo}$ TRCs, likely including cholesterol-25-hydroxylase^{+} cells located at the T-zone perimeter, $Cxcl9^{+}$ TRCs in the T-zone and interfollicular region, $CD34^{+}$ SCs in the capsule and medullary vessel adventitia, indolethylamine N-methyltransferase^{+} SCs in the medullary cords, and $Nr4a1^{+}$ SCs in several niches [37] .

FRCs form a 3D network of reticular fibres which extend from the HEVs into the B cell follicles, throughout the organ [38]. These fibres, with ECM-rich cores, act as a scaffold for migrating lymphocytes and dendritic cells, allowing the cells to reach their correct positions within the LN. Interestingly, it is this close collaboration between FRCs and the lymphocytes with whom they interact that supports the reticular network via TNF/lymphotoxin signalling [39,40]. FRCs can promote B cell follicle formation through activation of B cells expressing type 2 inflammatory cytokines, indirectly through IL-4Rα pathway [41]. Key to LN function and immune responsiveness, flowing lymph which enters the SCS then percolates through a system of small conduit structures formed by FRC networks. These conduits, which are formed of a collagen core and lined with perlecan and ERTR7 basement membrane amongst others ECM components, allow rapid transport of soluble factors below 70KDa deep into the LN. Factors transported include chemokines and soluble antigen for APCs to sample [6,42,43]. FRCs are implicated in many different key mechanisms such as immune cell survival, recruitment,

peripheral tolerance and inflammation[44]. They produce various pro-survival factors for lymphocytes such as IL-7, which helps maintain naïve T cell survival [45] , IL-6 and B cell specific survival factors BAFF, VEGF, and retinoic acid (RA). FRCs continually secrete the CCR7 ligands, CCL19 and CCL21, which acts as a guide to direct immune cells to their correct positions within the node. Interestingly, FRC-derived signals are required for trafficking and retention of resting but not activated lymphocytes [46]. Moreover, CCL21 secreted from FRCs promotes fluid flow in conduits, which enhances the organization of FRC networks. Conversely, blocking lymph flow in peripheral LNs downregulates CCL21 and CCL19 gene expression in FRCs [47].

FRCs also contribute towards peripheral tolerance. FRCs directly present peripheral tissue restricted antigens (PTAs) to self-reactive $CD8^+$ T cells, inducing cell death [48]. Contrary to thymic selection, this process is dependent on the Deaf1 transcription factor rather than AIRE[49]. Inversely, FRCs can acquire self-peptide MHCII complex directly from DCs to present and delete self-reactive $CD4^+$ T cells [50]. Finally, recent evidence shows that FRC can directly impact T cell responses via antigen presentation [48 50]. These data together suggest that changes in lymph flow and the factors they produce in inflammatory tissues promotes changes to FRC networks that perpetuate changes in immune cell trafficking, sampling of lymph, and antigen-specific immune responses [51].

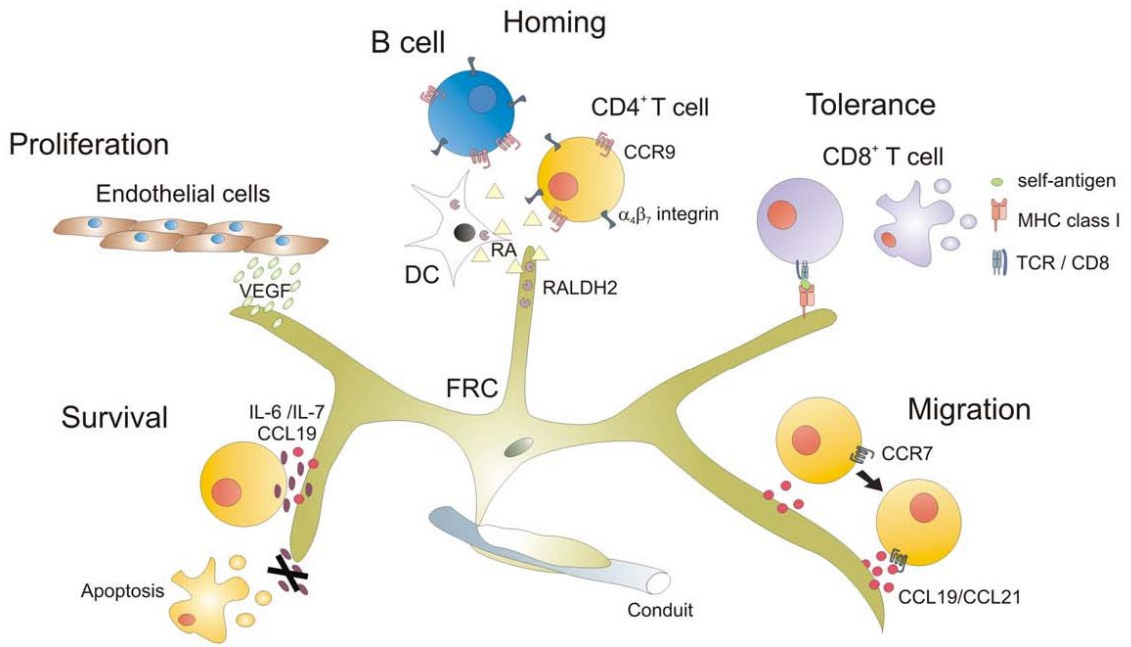

Figure 1.3 Role of fibroblastic reticular cells in the lymph node. Some of the major functions exerted in the LN by FRCs. Reproduced from [52].

Lymphatic endothelial cells (LECs)

The lymphatic vasculature provides a route for dendritic cell and lymphocyte migration into and out of LNs parenchyma [53]. The lymph transported within is rich in proteins, lipids, chemokines, antigens and exosomes [54,55]. It has been recently observed that post-surgery lymph exudate taken from human melanoma patients is enriched in melanoma-associated proteins such as LDH, S100B, and S100A8 compared to plasma where they were shown nearly undetectable [56,57]. Lymphatic endothelial cells (LEC) control these processes by expression and gradients of CCL21[58], IL-7[59], sphingosine-1-phosphate, and adhesion molecules [60]. Initially thought to be passive conduits, the last decade has seen a growing body of evidence to suggest an active role for LECs and the overall lymphatic vasculature in multiple processes. Recently, single-cell sequencing of human lymphatics in LNs has shown a new degree of heterogeneity and in particular six different LEC subtypes have been described and are associated with distinct locations in the LN where they can exert specific functions. For instance, SCS LECs and medullary sinus (MS) LECs differentially from the other types express neutrophils chemoattractant that facilitate quick response against pathogens through expression of CD209[61]. LECs express several identified markers such as podoplanin, prospero-related homeobox 1 (Prox-1), lymphatic endothelial-specific hyaluronic acid receptor-1 (LYVE-1), and common lymphatic endothelial and vascular endothelial receptor-1 (Clever-1)[53]. It has been shown that LECs play a variety of active roles in shaping immune responses and tolerance: they can modulate DC trafficking via LYVE-1 interactions with hyaluronan[62] and they can directly impact T cell behaviour through antigen presentation on MHC-I and II [63–65]. Moreover, LECs can scavenge material from lymph, and can then either 'archive' antigen or pass it on to other immune cells to be presented [66–68].

Blood Endothelial Cells (BECs) & Pericytes

BECs and pericytes represent the final stromal populations within LNs. BECs line specialized vessels called HEVs, which are responsible for lymphocyte entry via the extravasation cascade. Pericytes are a minor population, identified by the expression of α-smooth muscle actin (α-SMA), and integrin-α 7 (Itgα7) [33,69]. The cells function as a scaffold to maintain vascular integrity and secrete chemotactic factors to enhance lymphocyte recruitment. Podoplanin expression on FRCs in close contact with HEV has also reported to be essential for vascular integrity [70]. Herzog et al. showed that mice with deletion of podoplanin exhibited bleeding in lymph and identified a central role for PDPN-CLEC-2-mediated platelet activation and subsequent S1P release in HEV integrity. Besides lymphocyte recruitment, BECs perform

often underappreciated roles in immune regulation [69]. Like FRCs and LECs, BECs express PTAs [48,71]. While clonal deletion has not been directly demonstrated for BECs, it is likely that the cells also perform tolerogenic functions. In turn, recent single cell sequencing studies have shown that medullary veins lack the machinery to recruit naïve lymphocytes, but instead recruit myeloid populations upon inflammation [72]. This highlights the unexpected dynamism of BECs.

1.5 Extracellular matrix

In the human body, nearly all tissue cells reside in an extracellular matrix (ECM) consisting of a complex 3D fibrous intricate network composed of an array of multidomain macromolecules organized in a cell/tissue-specific manner. ECM is not a mere structural component but is bioactive, dynamic and regulates several cell functions such as proliferation, adhesion, migration, polarity, differentiation, and apoptosis [73]. The wide distribution of fibres and gaps found in the matrices provide complex biochemical and physical signals to cells and these are often found altered in disease. ECM is constantly deposited, modified and degraded by fibroblasts that play a key role in remodelling and are responsible both for depositing new matrix and for breaking down ECM fibres by secreting metalloproteinases (MMPs), a disintegrin and metalloproteinase (ADAMs), other proteases and elastases. In tissue repair, pro-inflammatory stimuli such as TGF-β can regulate this remodelling activity [74]. Increasing evidence indicates that the general matrisome and matrix stiffness in disease differ from the healthy tissue, due to active remodelling and deposition carried out by the tissues stromal compartment. This will be discussed in section 1.2.3.

The ECM comprises approximately 300 proteins. Major components include collagens, proteoglycans, elastin, and cell-binding glycoproteins, each with distinct physical and biochemical properties. Here, I will discuss the major macro groups found in the majority of tissues.

Collagen

Collagen is the most abundant component of the connective tissue and composed of 3 polypeptide α chains that form a triple helical structure. In vertebrates, 46 distinct collagen chains assemble to form 28 collagen types that are categorized into fibril-forming collagens (e.g., types I, II, III), network-forming collagens (e.g., the basement membrane collagen type

IV), fibril-associated collagens with interruptions in their triple helices, or FACITs (e.g., types IX, XII), and others (e.g., type VI). Collagen I forms the core of conduit structures.

Proteoglycans

Proteoglycans consist of a core protein to which glycosaminoglycan (GAG) side chains are attached. GAGs are linear, anionic polysaccharides made up of repeating disaccharide units. There are four groups of GAGs: hyaluronic acid, keratan sulphate; chondroitin/dermatan sulphate; and heparan sulphate, including heparin. Many chemokines and immunomodulatory factors such as VEGF, CCL21 and TGFb bind to ECM via proteoglycans, serving as a reservoir ready for release upon ECM degradation.

Laminin

The laminin family comprises about 20 glycoproteins that are assembled into a cross-linked web, interwoven with the type IV collagen network in basement membranes. They are heterotrimers (400–800 kDa) consisting of one α, one β, and one γ chain. Laminins are essential for early embryonic development and organogenesis [75]. Laminin surrounds the collagen core of conduit structures in LNs.

Fibronectin

Fibronectin is critical for the attachment and migration of cells, functioning as "biological glue". The fibronectin monomer (~250 kDa) is made of subunits which comprise three types of repeats: I, II, and III. Fibronectin is secreted as dimers linked by disulphide bonds and has binding sites to other fibronectin dimers, collagen, heparin, and cell surface receptors [76].

1.5.1 Extracellular matrix in the Lymph node

Studies have shown that the main molecules comprising LN ECM were types I, III, and IV collagens, laminin, elastin, tenascin, entactin, vitronectin, and fibronectin [77–79]. FRCs control this deposition [80]. The most abundant ECM molecule is by far fibrillar collagen which also composes the conduits structure. Collagen cores are surrounded by complex ECM envelope made of perlecan, fibrillin, laminin, fibronectin, nidogen and ERTR7 [81]. The conduits are small pathways, specific to the LN, wrapped by adjacent FRCs protrusion for delivery of antigens and cells through the parenchyma. Conventionally, it was thought that conduits could only deliver substances up to 70KDa, however, two recent works showed how IgM molecules,

considerably larger than 70KDa, were locally transported through the conduits system [82,83]. It is now known that also conduits are not a fixed structural network but are dynamic and respond to external stimuli. In infections it has been observed a reduced coverage of the conduits, leading to outflow of conduit contents into the lymph node parenchyma [84]. The ECM of secondary lymphoid organs has also been shown to regulate B cell fate, where specialized niches rich in laminins support long-term survival and antibody responses [85].

1.5.2 ECM in TME

Alteration in the density and composition of ECM occurs in many diseases such as tumours. The alterations toward both stiffness and degradation are contributed to tumour growth and progression. Cancer-associated fibroblasts (CAFs) are the main contributors to ECM stiffness and degradation together with cancer cells and tumour-associated macrophages [86]. The cells interact with almost all cells within the tumour microenvironment (TME) that could enable them to modulate ECM components for tumourigenic purposes. Cross-talks between CAFs with cancer cells and macrophage type 2 (M2) cells are pivotal for ECM stiffness and degradation [87]. It has been reported that such high deposition and degradation of ECM products in cancer patients, resulted into higher ECM products in their serum, making degradation by-products potential biomarkers [88]. There is growing evidence that suggest that ECM is not a passive bystander but has major roles in cell signalling and disease progression.

1.5.2 Synthetic extracellular matrix

For the creation of 3D hydrogel scaffold, a myriad of natural materials derived from different organisms is available. For instance, collagen is one of the most common and is extracted from bovine tendons or rat tails, gelatin from porcine or bovine skin, Matrigel® from murine sarcomas and alginate from brown seaweed. These offer the advantage of being inherently biocompatible. However, they can be also rapidly degraded by cells and can are not fully standardised e.g. Matrigel contains a range of factors including growth factors and cytokines with the potential to modulate cell behaviour and interfere with data interpretation. An alternative approach used either to eliminate dependence from living organisms or to give specific properties to existing natural polymers is the creation of synthetic or semi-synthetic polymers that mimic the ECM. In this process of biomimicry many hybrid combinations of different components have been created.

Water soluble polymers, such as poly(ethylene glycol) (PEG), poly(vinyl alcohol) (PVA), poly(2-hydroxyethyl methacrylate) (PHEMA), and polyacrylamide (PAM) can be crosslinked into simple viscoelastic hydrogel that are biocompatible and inert but lack of biological moieties [89]. In order to allow cell adhesion, these materials need therefore chemical modification by addition of functional groups, or to be mixed with natural polymers. Blends of synthetic and natural polymers have gained interest in biological and biomedical applications [90,91]. Another aspect to consider with synthetic materials is the crosslinking method which used which should be as mild as possible when cells are incorporated. PEG for instance can be chemically crosslinked with glutaraldehyde (GA) which can be toxic for cells or can be UV photocrosslinked in case of the modified PEGDA (PEG diacrylate).

A novel and particularly versatile type of material used in tissue engineering is the semi-synthetic polymer Gelatin methacryloyl (GelMA). GelMA is a modified gelatin which undergoes photocrosslinking when exposed to UV light in the presence of a photoinitiator molecule (Figure 1.4). The obtained hydrogels are biocompatible, cell adhesive and have tuneable mechanical properties [92]. Gelatin, as the denatured product of collagen, contains many arginine-glycine-aspartic acid (RGD) sequences that are important to promote cell attachment, as well as being target sequences for MMPs, making the hydrogels subject to matrix remodelling [93]. GelMA is also versatile from a processing perspective because require a few steps and reagents to be synthesized. Due to these features, GelMA has been extensively described for 3D cell culture applications and is emerging as a tissue engineering platform [94,95].

Thus, when modelling a tissue or disease state, the scaffold whether biological or synthetic, and its intrinsic properties can be an important consideration.

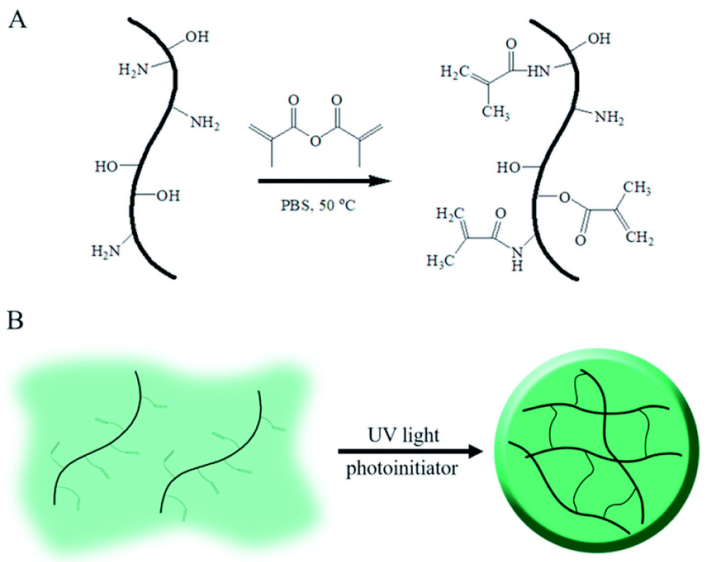

Figure 1.4 A) GelMA synthesis occurs at 50°C from gelatin and MA in PBS. **B)** formation of GelMA hydrogels with UV light and photoinitiator.

1.2 Lymph node in disease

The lymph node at steady-state, performs critical functions in maintaining peripheral tolerance and homeostasis. When the physiological equilibrium in the body is disrupted by an external stimulus, the LN usually responds with a series of changes to ensure an effective immune response. Lymphadenopathy, or swelling of the LN, is a very common consequence of such reaction and can occur in response to bacterial, viral, or fungal infections, autoimmune disease, and malignancy[96].

1.2.1 Antigen recognition and T cell activation

The LN is the site where adaptative immune reactions take place. In this process naive lymphocyte are instructed to specifically recognize and target an external antigen which has entered the body or an altered self-antigen. In order for this to occur, the antigen needs to be recognized at the body periphery and presented to the lymphocytes in the LN, resulting in their activation. Antigens are recognized and processed by APCs that conventionally include, macrophages, dendritic cells, B cells and Langherans cells. These cells are able to proteolytically process and present the antigen on the major histocompatibility complex class II molecules (MHCII) on their surface, only expressed by APCs, to T-cell receptors (TCRs) of $CD4^+$ T cells, effectively acting as bridges between innate and adaptive immunity. Interestingly, several recent works have shown MHCII expression by FRCs in the LN which

could act as unconventional APCs and have a crucial role at regulating self-tolerance [97–99]. Depending on the TCR co-receptor expressed by the T cells, CD4 of CD8, the activation process is mediated by different molecules. $CD4^+$ T cells, 'helper T cells', facilitate pathogens clearance by acting as strong activators of other immune cells, such as CD8+ T cells or 'cytotoxic T cells', and they are activated by MHCII molecules. $CD8^+$ T cells, on the other hand, are activated by another class of MHC molecules, MHC I which is expressed on most body cells and mediates clearance of pathogens that are able to infect any cell, such as viruses. Differently from T cells that require antigen digestion, B cells can recognize some bacterial antigens in their native form with their B cell receptor (BCR) [100]. Although this allows a fast immune response, to obtain a finely tuned and mature response that generates high-affinity antibodies, T-helper cells are required.

Upon engagement of their TCR, activated $CD4^+$ travel to the B cell follicles border by expressing CXCR5 and get in contact with MHCII on B cells. This first activation signal is accompanied by secreted cytokines and engagement of CD40 by CD40L on t cells. In response B cells proliferate, differentiate into antibody-secreting cells and into memory B cells, and form a structure called the germinal centre which leads to long-term plasma cells that generate antibody or of memory B cells.

Among the many molecular changes occurring in T cells activation, the earliest activation marker is CD69, which is an inducible cell surface glycoprotein expressed upon activation via the TCR or the IL-2 receptor (CD25) [101]. CD69 downregulates S1PR1 to promote retention in secondary lymphoid tissues and may play a role in regulating proliferation.

1.2.2 Lymph node in infections and inflammation

The observed increase in size of the LN in lymphadenopathies is closely related to the stromal compartment in the LN, although it is not understood to which degree it is required for maintaining an adequate immune response [102]. Lymph node remodelling in an immune response is a bidirectional relationship, with FRC upregulating CCL21 and CCL19 to recruit immune cells [99,103,104] and in turn, these may modulate FRCs; for example, DCs can regulate FRC microtubule networks and FRC contractility through PDPN–C-type lectin-like receptor 2 (CLEC-2) [80,105].

In a model of HSV infection, it was reported that LN enlargement is driven by lymphocyte retention in the node and via LNSCs expansion. Upon exposure, LNSCs increased their number significantly and displayed dramatically altered gene expression profiles up to 30 days after

infection. Interestingly, among the many altered genes, *gp38* (*Pdpn*) was upregulated in all LNSCs, indicating a more activated status. *Cxcl9*, a chemokine that together with CXCL10 supports T cell responses regulating their migration and activation status was also upregulated[106]. In LNs CXCL9 is required for the positioning $CD4^+$ T cells to the interfollicular and medullary zones, whereas CXCL10 affects $CD4^+$ T cells motility encouraging T cell-DC interactions[107]. CXCL9 and CXCL10, stromal derived pro-inflammatory chemokines that bind CXCR3 on T cells, seem to be ubiquitously present independently of the organ affected. For instance, they were found upregulated following SARS-CoV-2 infection and seemed link to hyperinflammation status[108]. Moreover, in chronic inflammation to the retina caused by *Toxoplasma gondii* it was found that T cells have a crucial role in controlling the parasite control and that CXCL9 and CXCL10 were upregulated to recruit Th1 cells. Interestingly blockade of CXCL10 was linked to higher parasite burden in the host[109]. These changes in the LN seem to be functional to ensure an optimal immune reaction. However, there are some cases in which the pathogen has developed mechanisms to impair the normal LN functioning. In HSV, while *Pdpn* was upregulated, *Ccl21* was downregulated. This implied that with HSV infection, while some effective immune activity was retained, cues guiding immune localization were disrupted to impair anti-viral immune responses. Similarly, CCL21 and CXCL13 were specifically downregulated by *Salmonella typhimurium* infection, through engagement of its LPS capsule with TLR4 [110]. This interaction increased its virulence and effectively drove immune suppression through interference of immune homing. In more severe infections, such as Ebola, FRCs are directly targeted, infected and destroyed during viral propagation and dissemination [111,112]. In chronic infections such as with HIV-1, regulatory T cells (Tregs) upregulate transforming growth factor-β1 (TGFβ1) production, which signals to FRCs to increase their ECM production. As a result, it seems that naive T cells no longer physically in contact with FRCs lose access to IL-7, causing T cell death and prolonged immunodeficiency[113]. In addition to the established positive roles in T cell responses in infection [114], it has also been reported that FRC and DC cooperate in a negative feedback loop, via iNOS production, to impair T cell expansion during acute inflammation.

The first line of defence when an antigen enters the LN via the afferent lymphatic is composed by SCS macrophages that prevent pathogen dissemination. In *Staphylococcus aureus* infection a disruption of SCS macrophage organization is observed compared to resting LN, probably due to the action of incoming migratory DCs through MYD88 receptor[115]. Also, within the SCS, LECs can respond to viral infection with influenza and vesicular stomatitis virus by

capturing and storing antigen [68]. This led to increased protective immunity from circulating memory $CD8^+$ T cells and enhanced protection upon rechallenge.

Finally, another population of immune cells quickly recruited to the LN after infection is neutrophils. It has been shown that 50% of immune cells in afferent lymphatics after intradermal injection of *pneumococci* is composed by these cells[116,117].

1.2.3 Lymph node in cancer

Many human cancers metastasize through the lymphatic system, with LN metastasis being a major site. It has been estimated that 80% of melanomas and carcinomas metastasize through the lymphatic system and 20% through blood vasculature and direct seeding [118], but we still do not understand how tumour cells are able to avoid immune-system-mediated clearance here.
LNs that lie immediately downstream of tumours, tumour draining lymph nodes (TDLNs), and drain lymph deriving from it undergo profound alterations due to the delivery of tumour-derived signals, which include antigen and metabolites [119,120]. Many of these changes happen before the arrival of tumour cells, to form the pre-metastatic niche. Communication from the tumour results in an enlargement of the LN, an increase in its cellularity, altered architecture, disruption of stromal constituents, and stiffness of the matrix. The FRC compartment within TDLNs expands and undergoes structural reorganization. FRCs display strikingly altered transcriptional profiles with expression of two FRC-derived factors key to LN function, CCL21 and IL-7, downregulated. Akin to infections, perturbation of these essential guidance cues can contribute to abnormal homing, localization and survival of immune cells [119]. In addition, it was observed that FRCs generate an altered conduit network that seems to be composed of wider conduits, resulting in increased flow into the parenchyma. This increase in lymph flow enhances the communication between the tumour and the sentinel TDLN. In addition to increasing the transport of tumour antigens and regulatory cytokines to the LN, increased lymph flow in the tumour margin causes mechanical stress-induced changes in stromal cells that stiffen the matrix and alter the immune microenvironment of the tumour [121]. Stiffness of the matrix, also due to an increased deposition of collagen by FRCs can affect the behaviour of different cell types. It has been reported that T cells cultured on substrates of increased stiffness exhibit lower proliferative responses as well as expression of lymphoid homing receptor L-selectin and inflammatory cytokine IFN-γ [122]. This stiff matrix of TDLNs may also serve to exclude immune cells from entering metastases once tumour cells have spread.

However, alteration of the stiffness by impairing collagen deposition with a drug called Losartan improved immune cell infiltration of metastatic lesions in mice [123]. Tumour derived factors driving the changes in FRC behaviour and function remain to be identified. However, it has been recently shown that lactate, a metabolite released by cancer cells, elicits upregulation of activation markers *Pdpn* and *Thy1* in FRCs of TDLNs, making them akin to activated fibroblasts found at the primary tumour site [124].

Concurrently, alterations are observed in the blood vasculature of TDLNs. A recent study in breast cancer reported an increase in the average density of HEVs and an increase in the overall size and branching of the venules[125]. Interestingly, HEVs also lost the expression of peripheral node addressin (PNAd), the ligand for L-selectin on incoming lymphocytes. In the absence of PNAd lymphocytes are unable to enter the LN. However, swelling is observed as in TDLN lymphocytes proliferation increases and egress from the organ is strongly reduced [126]. As a result, HEVs transition into becoming active blood-suppling vessels in TDLNs. As with blood vessels, lymphatics also dramatically change. In response to drained growth factors VEGF and VEGF-C, lymphatics undergo a dramatic expansion [127,128]. This facilitates the increased flow mentioned earlier, and also enhanced trafficking of immune and ultimately cancer cells. Unlike for inflammation [37], comprehensive single cell analyses of the LN stromal landscape in cancer have yet to be performed, and our understanding of the complex adaptions as tumours develop is still lacking.

Besides the lymphatics and vasculature, changes have also been reported in the immune composition of TDLNs. A gradual shift in immune infiltrates occurs as tumours establish [119,129]. In a B16-F10 footpad model of melanoma, an 8-fold increase in $B220^+$ B cells, and a 3-fold increase was observed in the levels of $CD3^+$ T cells of TDLNs [130]. Similar alterations have also been reported in other cancers, such as breast cancer [131]. Consequently, the levels of immune cells are increased within TDLNs. Despite these alterations T cells are largely dysfunctional in TDLNs; when tumour-specific T cells are adoptively transferred into tumour-bearing mice, T cells are rapidly killed or rendered non-functional [120]. As a result, T cells rapidly lose the capacity to mount an anti-tumour immune response in TDLNs. To date several theories have been suggested for the causes of this dysfunction, including an increase in the number of Tregs and a shift towards a more tolerogenic and suppressive LN stroma [120]. The precise mechanisms of action however still remain to be elucidated.

1.3 Studying the lymph node

1.3.1 Historical background

LNs have been recognized since ancient times by Hippocrates (*Corpus Hippocraticum*, V century BC) who described small spongy structures scattered throughout the body containing a fluid absorbed from the tissues named *ichor*. In spite of the ancient encounter, it took many centuries to fully understand the role of the LN as a part of a larger lymphatic system. A few factors were responsible for delaying the advent of breakthrough and discoveries compared to the development of medical practice in other fields. First, visualizing the lymphatic system in humans and animals had always been very challenging because lymphatics tend to collapse and mainly carry lymph which is a low-pressure clear fluid. However, it is not a lack of technical skills or tools to be blamed, neither the finesse of the skilful anatomists scattered throughout Europe. Most of the delay in fact is due to the ancients belief in erroneous theories on blood and lymph. For centuries Galen's theories on the liver[132] , which did not discern lymph vessels from veins were considered true and dominated the field of medicine for fifteen centuries. In the XVI century, together with discoveries on blood circulation by William Harvey, a new interest for the lymphatic system and LNs sparked, and during the Enlightenment period, it became clearer what was the exact role and architecture of the lymphatic system and LNs in particular. A widespread practice used by anatomists to learn about lymph and its relation to blood flow was mercury injections in the lymphatic system of different animals or human cadavers. Worth noting is the work by the anatomist Paolo Mascagni in the XVIII century, who determined that all the lymphatics pass through one or more LNs and by injecting mercury mixed with hardening wax he managed to study its structure and learn about LN vascularization[133]. LNs have been associated with infections for several years but interestingly only at the end of the XIX century doctors started including lymph node treatment in the context of cancer arriving in 1977 with Ramon Cabanas to coin the term 'sentinel lymph node', which describes the first lymph node draining directly from the tumour [134,135].

1.3.1 Studying the lymph node *in vivo*

Due to their association to infections and malignancies LNs have been studied in the clinic for years, mostly as a diagnostic indicator in lymphadenopathies. Currently, LNs are analyzed macroscopically to assess cancer staging and presence of metastasis with a series of tools

including ultrasounds, MRI imaging, CT scan. These approaches are very useful but are not very informative about cellular or molecular changes at a microscopical level.

For molecular research purposes, the only way of deeply studying LNs was *in vivo* either dissecting the organs from animals or humans. This approach indeed led to major discoveries although carrying a few limitations. For instance, the presence in the organism of too many confounding factors makes challenging extrapolating molecular changes caused by single agents. In addition, the experimental limit of dissecting the host at each experimental endpoint does not easily allow live cell tracking. In this regard, in more recent years technology advances in the field of microscopy allowed for live intravital microscopy mostly through the emergence of multiphoton microscopy. This novel technique proved to be a very powerful and valid tool for *in vivo* imaging thanks to its ability to penetrate deeper into the tissue up to 300µm for two-photon microscopy and 900µm for three-photon microscopy [136]. With these techniques it was possible to recognize single populations such as $CD8^+$ and $CD4^+$ T cells and also $cd11c^+$ cells in which a specific marker was conjugated to a fluorophore or specific structures by injecting conjugated antibodies directly in the mouse bloodstream[137]. This technique does have some limits; it requires specialized equipment, loss of sensitivity and resolution with increasing depth of tissue penetration, and the need to surgically exposed organs limits duration and longitudinal sampling, but nevertheless is an invaluable tool. Indeed, live intravital microscopy has been critical for revealing cell-cell interactions and migration dynamics in inflammation, such as DC-mediated activation of anti-tumour NK-cells, DC-$CD8^+$ T cells interaction for determining memory differentiation [138–141]. Other works that focused on cells homing into the LN showed how B cells enter the organ and position directly into the follicles while T cells remain in the paracortex. Interestingly, they do this crawling along the FRCs networks through an apparent 'random walk' [142]. Neutrophils on the other hand, during infections swarm towards the LN and two-photon microscopy revealed the essential role of LTB4 and other integrins for their right migration [143]. To sum up, the lack of ready to use reductionist 2D models makes studying the LN very challenging and *in vivo* models also carry their own limitations, particularly in live cell imaging.

1.3.2 Alternative methods for studying the lymph node - *ex vivo* models

An additional approach in the field of organ and disease modelling is the use of *ex vivo* models, short term cultures of whole organs or parts of them, where most of the operations are performed once the organ is taken out of the host animal. Specifically for the LN, some novel

models have been created for different purposes. For instance, explanted LNs have been used to identify novel drugs against *Leishmania major.* The authors extracted LNs from infected mice, and digested them to obtain a cell suspension which was then used to test different compounds, with the advantage of testing multiple molecules on one organ[144]. Although it could be argued that this model is very simplistic and does not maintain any cell interaction observed *in vivo,* other efforts have been made to strengthen this type of approach and overcome its limitations. In a recent work, it was demonstrated that explanted LNs from human patients could be maintained up to 24h. This was facilitated by a perfusion system, which could also be used to deliver therapies. An advantage of this model is that, as the organ remained intact, its overall architecture is preserved, making it a valid model for preclinical evaluation of personalised therapies[145]. However, access to intact human lymph nodes can be difficult due to ethical considerations and requirement of tissues for pathological review. With this in mind, researchers have used mouse lymph nodes instead, with an approach consisting of thick LN slices embedded into an agarose gel. Here, the organ architecture remains intact while also enabling convenient imaging of the exposed tissue slices. This model proved to be a valid tool to successfully study acute immunity and inflammation showing features comparable to *in vivo* behaviour. In particular, using OT-II model the LN slices secreted inflammatory molecules (TNFα, IFNγ and IL-4) and showed CD69 upregulation [146]. In addition, in a separate work it was also included into a two-way microfluidic system where tumour-lymph node interactions were investigated connecting *ex vivo* slices from both compartments[146,147]. Ongoing work carried out in the Shields lab, has made use of a similar technique, performing live staining of vessel and stromal features to allow tumour and immune cell tracking. We have shown that slices can be maintained for up to 72 hours, but in some cases, it was observed that lymphocytes readily left the tissue slices towards the surrounding gel without added stimuli. This could be due to the change in chemical cues to which the slices are exposed to from the *in vivo* to the culture system, affecting chemical gradients and the overall organ architecture.

1.4 *In vitro* models: from 2D to 3D

There is growing desire to reduce the use of *in vivo* models in favour of *in vitro* alternatives to model disease states because they are costly, carry ethical issues and often do not reproduce characteristics observed in human clinical data [148–150]. The advancement in technology has opened the way for more sophisticated *in vitro* systems that more accurately mimic the *in vivo*

scenario. Since the first cell cultures carried out by Ross Granville Harrison in 1907 during research into the origin of nerve fibres, the culture method has been improved and used to observe the growth and differentiation of cells outside the body [151]. Two-dimensional models have been extremely reliable and cheap tools used to investigate biological processes such as tissue morphology, mechanisms of diseases, drug action, protein production and the development of tissue engineering. Nevertheless, they also have limitations that in many cases make them inadequate candidates to recapitulate higher grades of biological complexity. Some of the key aspects of *in vivo* biological systems that cannot be covered in this kind of model are interaction between the cellular and extracellular environments, changes in cell morphology, cell polarity, and method of division [152].

Cells cultured in a 2D environment do not mimic the natural structures of tissues or tumours; cell-cell and cell-extracellular environment interactions are not represented as they would be in the tumour mass. These interactions are responsible for cell differentiation, proliferation, vitality, expression of genes and proteins, responsiveness to stimuli, drug metabolism and other cellular functions. After isolation from the tissue and transfer to the 2D conditions for instance, the morphology of the cells is altered, as is the mode of cell division. The changed morphology of cells may also affect their function [153,154], the organization of the structures inside the cell, secretion and cell signalling [155]. Another drawback of 2D culture is that the cells in the monolayer have unlimited access to the ingredients from the medium whereas cancer cells *in vivo*, receive variable quantities of nutrients and oxygen because of the natural architecture of the tumour mass. Furthermore, it has been observed 2D culture can alter the gene expression and splicing, topology and biochemistry of the cell [156]. In addition, adherent cultures are usually monocultures and allow for the study of only one cell type, which results in a lack of tumour microenvironment, or niches, which *in vivo* are required by cancer-initiating cells [157].

In light of these limitations, much interest has been recently brought towards 3D cell cultures, which have opened new ways to study cancer biology, promising advances in drug discovery and tissue engineering. As cells *in vivo* are surrounded by other cells and their ECM, using co-cultures in hydrogels that mimic the cells' physiological environment helps creating a more realistic situation. Indeed, simply by changing the 3D environment surrounding a cell is sufficient to induce morphological changes in epithelial cells and induce invasion[158]. Additionally, the body is a dynamic system which is subjected to various mechanical forces such as shear stress due to fluid flow, for example blood flow, interstitial fluid flow and urine flow, which is crucially important for the functioning of all tissues. This parameter is also integrable in 3D microfluidics systems. These systems allow co-cultures together with the

presence of microchannels that deliver signals and include physical forces. The field of mechanobiology has demonstrated that these forces have an effect on cell behaviour and intracellular signalling pathways and seems of crucial importance to create a system that takes them into account [159].

Depending on the method, 3D models can be divided into three main groups: scaffold free, scaffold-based and hybrid models (Figure 1.5B). Scaffold free models do not make use of any hydrogel for the creation of the 3D environment but are based on the ability of some cells to self-assemble into spherical structures (e.g. adult pluripotent epithelial cells). These include spheroids and organoids. Scaffold-based models rely on the use of biomaterials as matrices to mimic ECM-cell interactions and 3D bioprinting is a technique which can be used in this context. Hybrid models are created by a combination of physical scaffolds and hydrogel materials such as organ-on-a-chip technology.

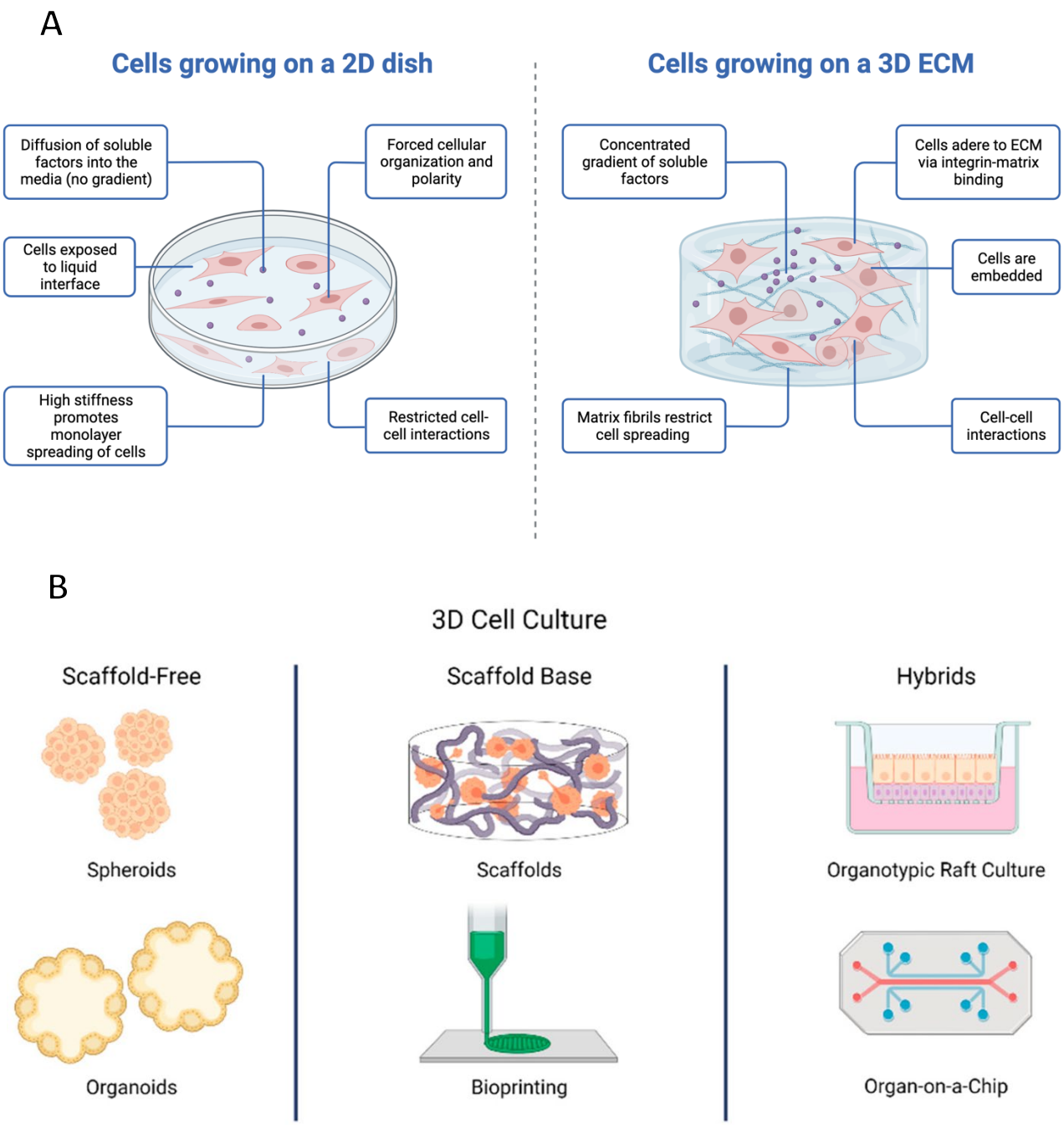

Figure 1.5 Overview of the different methods used for 3D cell culture. A) Comparison between 2D vs 3D cell culture systems **B)** Schematic showing the main techniques used in scaffold-free, scaffold base and hybrids 3D models.

1.6 3D models

The field of three-dimensional biology has seen a relentless expansion towards physiologically relevant platforms that brought to life a large number of organ-specific devices mostly with two general aims: 1) to create more biomimetic disease models to study specific aspects that

are difficult to study *in vivo* because of a lack of existing models, and 2) and in drug discovery, bridging the gap between findings in preclinical 2D cell culture models and *in vivo* systems [160]. Many drug candidates fail due to non-representative preclinical models that do not translate their outcomes into clinical models. It is estimated that only 1 out of 10,000 new drugs gains FDA approval and the overall failure rate in drug development is reported to be over 96% [161,162]. Not only this issue is not cost efficient but can also affect patient outcomes [163].

3D systems have the potential to bridge this gap because they provide an environment for multiple cell types that can interact with ECM components and be exposed to chemical gradients. However, they also carry some limitations that need to be considered. First, it is important to take into account the source of the cell type used to model the organ. For instance, immortalized cell lines are not thought to be ideal for *in vivo* correlation because they can lose their phenotype and accumulate somatic mutations [164,165], but offering virtually unlimited supply, they are considered valuable tool for initial drug discovery steps, and it is arguable that the same cells grown in 3D will be better predictors than in 2D cell culture. Several studies have identified differences between 2D and 3D cultures. For instance, in a lung cancer cell line NCI-H23, 24% of analyzed protein species were regulated in culture dependent manner and in colorectal SW480 cells, in a total of 4854 shared proteins between 2D- and 3D-cultured 383 proteins were differentially expressed [166,167]. Cytokine secretion is also altered in 2D compared to 3D cultures. For instance, secretion of CCL19 and 21 by tumour cell lines was found significantly higher in 3D compared to 2D cultures, in which CCL19 was not detected at all [168]. Moreover, RNA sequencing showed that tumour cell lines-derived extracellular vesicles (EVs) showed more *in vivo*-like features when extracted from 3D cultures. 2D EVs on the other hand correlated less with patient tumours [169]. Many works showed differences between 2D and 3D cell cultures at a genetic and protein level, but more complex is defining the *in vivo* correlation of these models. Data show that not all 3D cultures are the same and that increased complexity does not necessarily translate to more valid models. Conversely, other factors such as specific ECM-cell interactions and biophysical cues, including matrix stiffness, might have more predominant roles [170,171]. Two recent works have compared several breast tumour cell lines and an epithelial cell line grown in hyaluronic acid hydrogel, Matrigel and 2D cultures. Interestingly, several proteins such as EGFR, STAT3, STAT1 were affected by the composition of the chosen ECM suggesting high variability among different 3D culture systems [172,173].

Overall, patient-derived cells , adult stem cells or IPSCs are preferred alternatives for drug testing and toxicity studies because more physiologically relevant than cell lines. Moreover,

they are autologous, can offer personalized data and can help elucidate particular reactions in certain patient subpopulations [174]. Adult murine stem cells have been used to create a mini-gut perfusable model which exploited the self-organization and regeneration ability of these cells. Single cell sequencing revealed that intestinal stem cells, once forced into a villi-like disposition, differentiated in several cell types including rare populations found *in vivo* [175].

Another critical aspect is the ECM of choice. Nature-derived ECM such as collagen or Matrigel® are widely used but high batch-to-batch variability which affects composition and overall stiffness, can compromise and confound biological readouts [176]. Moreover, they are rapidly degraded in culture. Considering the inter- and intra-tumoural variabilities that are naturally found in cancer patients there is growing need for reliable and consistent ECM formulations. Matrigel® for instance, which is an ill-defined mixture of basal lamina ECM molecules and growth factors, is one of the most used materials in organ and cancer models. However, it is also one of the most batch to batch variable products and having a defined concentration lacks tunability [177]. Moreover, it is important to consider that commercially available hydrogels are not universal solutions for any cell type but different ECM formulation are required depending on the specific case [178]. In a recent study, a multi-organ chip was developed containing human heart, liver, bone and skin tissue niches in the presence of engineered vascular flow [179]. Importantly, this was enabled by singularly fine-tuning each specific environment to reach optimal physiological cell growth. For instance, collagen I gels were used for the skin compartment and fibrin gels for the heart. In addition, cell media were different for each compartment to ensure optimal growth as they require tissue-specific factors. A similar discussion needs to be developed regarding cell culture media which ideally also requires specific fine-tuning.

Organs-on-chip still require external hydrogel solutions but interestingly, 3D bioprinting has recently offered the opportunity to overcome ECM variability issues by printing scaffold-free tumouroid models. In this technique hydrogel were used to maintain the structures during and after printing but were then removed allowing the printed cells to self-assemble and produce their own native ECM [180]. Due to the countless models applied to different organs, to list them in their entirety would be beyond the scope of this introduction, but is extensively reviewed in Low et al. 2021 [181]. Therefore here, I will focus on highlighting the major advances for cancer and immunocompetent models.

1.6.1 3D cancer models

The interest towards creating 3D cancer models to recapitulate the tumour and its microenvironment (TME) has rapidly grown due to their potential applications. These include drug testing [179], cancer cell extravasation models to study metastases, disease modelling, and neoangiogenesis studies [182–184]. The complexity of these models gradually increased in order to obtain more physiologically relevant models. From the first tumour spheroids created by Sutherland et al. in 1971 [185], these platforms started including multiple cell types to simulate the TME complexity and also including vasculature. Tumour spheroids could be obtained with several techniques such as hanging-drop, bioreactors and non-adhesive plates.

Organ-on-chip represents a promising approach and the tumour devices developed in the last 20 years are innumerable. Their advantage is the inclusion of multiple cells in distinct areas in the presence of flow but these devices have been for years low-throughput. However, some of the platforms developed are also now commercially available such as microfluidics devices built by Emulate inc., Mimetas and many more, which will bring these to a larger audience [186]. The different components surrounding the tumour are known to act synergistically in the disease progression and there is need of techniques that include them with high spatial precision. 3D bioprinting was recognized as a promising tool for this purpose and in particular for the creation of patient-specific cancer models that would enable personalized drug screening [177,187]. Its main advantage is that by precisely depositing the injectable bioink in multiple cell layers, offers the opportunity to enhance the degree of complexity of these models by also incorporating stromal cells such as cancer associated fibroblasts (CAFs) and endothelial cells. In addition, being a partially automated process, it could be inserted into high-throughput screening pipelines [187].

The processes of cancer metastasis, and host tissue responses to metastatic colonization are still poorly understood. Models to study these steps *in vivo* typically involve injecting tumour cells into the circulatory system and exploring tumour extravasation and colonization in secondary tissues and microenvironments. These methods have high physiological relevance. However, they also have limitations in that they are time-consuming (experiments typically lasting 3-4 weeks), costly and are subject to data variability. Moreover, the methods cannot easily be used for real-time quantified monitoring at the single-cell level; they permit only end-point quantification, lacking real-time monitoring of dynamic phenomena and moving details. With this in mind, the development of novel systems *in vitro* is needed to investigate cancer

metastasis [184]. Good candidates to study this phenomenon may be represented by microfluidics models which build upon the 3D strategies described earlier.

Researchers have used microfluidic devices focusing on its vascular compartment and its role in disease. The channel obtained in the devices by soft lithography allows ECs to adhere on their walls. The obtained vessels have usually a rectangular cross section and seem like 'an extension' of a 2D culture plate to form a 3D object. Although not physiological *per se*, their main interest resides in their point of contact with an organ compartment in the middle of the device, which varies with the research interest. These "vessel-on-a-chip" devices have been used to investigate some critical steps in cancer metastasis, such as cancer cell intravasation and extravasation from the blood stream and to study haematological disease [188–190]. Microfluidic devices are most commonly made using polydimethylsiloxane (PDMS) because of the many advantages of this material. PDMS is a cheap, non-cytotoxic, autoclavable and gas permeable material. PDMS has also a low autofluorescence, making it suitable for fluorescence imaging. However, there are also some drawbacks associated with PDMS. For example, it is highly permeable to water vapour and organic solvents which may lead to evaporation and changes in osmolality of the solution contained inside the microchannels and it has been reported to be able to absorb drugs molecules, making it non-ideal for drug testing purposes [191]. In recent years, microfluidics models have been used to study cancer metastasis and because of their 'vessel and organ' conformation they were exploited to model tumour cells extravasation.

For instance, recently, an organ-specific 3D microfluidic model was created to study human breast cancer cell extravasation. The device was formed wither by a muscle- or bone mimicking (BMi) microenvironment generated with osteo-differentiated bone marrow mesenchymal stem cells with perfusable human microvascular networks composed of endothelial and mural-like cells. This device revealed that extravasation of breast cancer cells was considerably higher in presence of a BMi microenvironment compared to the unconditioned or muscle-like device [192]. Among several other models, a noteworthy device was created to study organ-specific cancer extravasation which included together brain, bone and liver compartments. In this multi-organ platform were found molecular changes observed also *in vivo*. For instance, after culture in the device, lung cancer cells showed epithelial-mesenchymal transition and invasive characteristics such as alterations in E-cadherin, N-cadherin, Snail1, and Snail2. Overall, this type of platforms can represent promising biomimetic tools to study metastasis to secondary organs and they have potential in the future for inclusion in drug testing pipelines [184].

1.6.2 Lymphatic vasculature microfluidics devices

Curiously, compared to the multitude of attempts to recreate blood vasculature *in vitro*, not many models that focus on lymphatic vasculature are available, despite their known role in cancer progression. It is estimated that 80% of carcinomas and melanomas metastasise via lymphatics [193] since are considered more advantageous routes than blood vessels given their leakier endothelium, lower shear stress and natural fluid draining function [194].

A PDMS-based microfluidic device was created to allow the investigation of both angiogenesis and lymphangiogenesis induced by tumour-stromal interactions [195]. Specifically, in this device human umbilical vein endothelial cells (HUVECs) and lymphatic endothelial cells (LECs) compartments were able to sprout simultaneously into a fibrin/collagen matrix laden with SW620 cells (human colon cancer cell line) and primary fibroblasts. This was observed only in case of the coculture presence and was due to the release of factors from the stroma that influenced both endothelial compartments. How this actually occurred was not furtherly investigated but the presence of primary fibroblasts in culture seemed to affect both the tumour cell lines and the endothelial compartments.

Another approach for the creation of *in vitro* vessels is EC lining-based method, which has advantages and differences from the previously shown one. This approach, which consists of seeding ECs directly into a hollow tubular structure of the desired size, enables immediate media perfusion, flow application with well-controlled biomechanical factors but is mostly suitable for vessels larger than 50µm in diameter [196]. A novel system that uses this method, called µLYMPH, made possible the creation of human lymphatic vessels in a collagen I gel matrix. This system allowed co-culture of lymphatic vessels with breast CAFs and demonstrated how a pro-inflammatory environment and especially IL-6, secreted from CAFs, have an effect on LECs resulting in a leakier endothelium [197]. Interestingly, a follow-up study showed it was also possible to analyse the differential gene expression of the LECs vessel exposed to different types of breast cancer cells suggesting this model as a potential tool to find critical pathways for new therapeutic targets [198].

1.6.3 Sacrificial materials – based microfluidics devices

Superseding PDMS microfluidics devices, other methods have been developed to create hydrogel based, vascularized and perfusable devices. To create 3D channels without the need of PDMS devices subtractive fabrication methods have been developed which use sacrificial materials in hydrogels. Several methods were developed that utilized different sacrificial inks

such as alginate fibers[199] , gelatin[200,201] , waxes [202,203] , Pluronic F127[204,205] and others. A work from the Chen lab exploited 3D printing of a sacrificial material composed of a mix of carbohydrates (carbohydrate glass), at temperatures above 100°C, to create a network of filaments, subsequently casted with cell-laden ECMs. These filaments, once removed, were successfully lined with endothelial cells and perfused [206]. In spite of their biocompatibility and water solubility, a limitation of these carbohydrates-based inks is the need of high temperatures for printing or removal of the materials which limits its use to cell-free hydrogels. A more recent work used a similar technique to create vascularized tissue constructs but utilized an aqueous fugitive ink composed of Pluronic f127 as sacrificial material. This could be easily printed and removed under mild conditions [207,208]. Pluronic F127 is composed of a hydrophobic poly(propylene oxide) (PPO) segment and two hydrophilic poly(ethylene oxide) (PEO) segments arranged in a PEO-PPO-PEO configuration. Pf127 is viscous at room temperature but below the gelation temperature, the hydrophobic PPO units are hydrated, such that individual PEO-PPO-PEO species become soluble in water giving rise to a gel-to-fluid transition that make it easily removable from printed constructs (Figure 1.6). GelMA was cast after printing of the sacrificial ink, and a vascularized structure was obtained. Within each construct, the diameter of printed filaments could be altered on demand by modifying the printing pressure, speed, or nozzle height and the material properties allow for complex structures [209]. An application of this method has been recently shown in the creation of a renal absorption model in which two channels representing the proximal tubule and the glomerulus capillary were created with pf127 and casted with an ECM. It was possible here to study hyperglycaemia conditions and measure changes in the endothelium [208]. More recently, to avoid the two-step process of creating a void in the hydrogel and then seeding endothelial cells, a one-step method was developed and resulted in complete endothelized vessels by seeding endothelial cells directly into gelatin, which was then removed at 37° C [200].

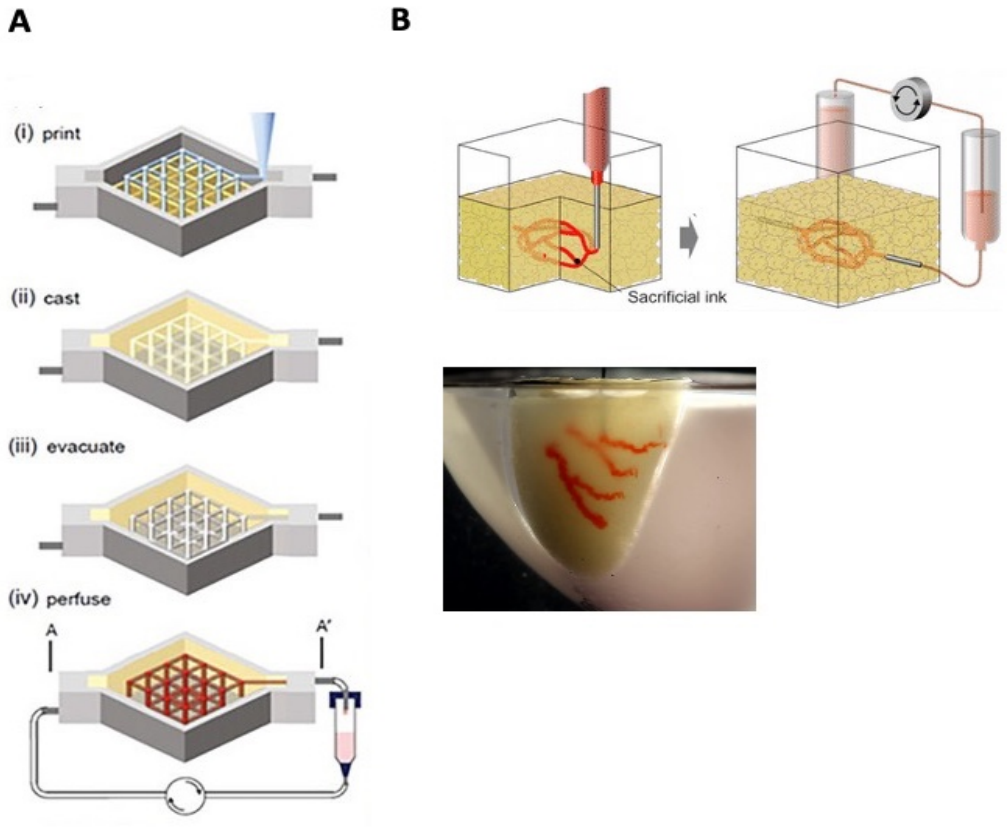

Figure 1.6 Overview of sacrificial printing methods for producing vascular channel structures. A) In-air printing, followed by casting with a matrix material. **B)** Embedded printing of a sacrificial ink. Reproduced from [207,210].

1.7 State of the art of Lymph node-on-chip models

Despite over 20 years of advances in the field that brought to valid models applied in pharmacological and toxicological contexts, to date a lymph node-on-a-chip that recapitulates all aspects of the organ is missing. Reasons for this delay are multiple and will be discussed here more in depth. The cell source is critical to obtain reaction which are comparable to *in vivo* pathophysiology; first, primary cell cultures are preferable in terms of function and phenotype, but are more fragile compared to immortalized cell lines and might necessitate of external growth and survival factors [211]; normal lymphocyte cell lines to constitute the organ parenchyma do not currently exist, instead cell lines tend to derive from leukaemia's or lymphomas which do not accurately represent a healthy LN. Indeed, completely relying on phenotypically altered and transformed cells would be counterproductive, confusing data interpretation and could threaten the *in vivo* translation potential of the model. These cells have

an altered surface marker profile and are more closely related to disease. This is due to the immortalization process which involves lymphocytes infection such as Epstein-Barr virus (EBV) [212]. Overexpression of lymphocyte activation markers may represent a major issue when studying activation reactions *in vitro* changing their sensitivity to external stimuli. An additional limitation is that, unlike most of the other organs in the body, LNs do not contain stem cells niches that provide undifferentiated cells that can be used in clinic and in tissue engineering because lymphocyte progenitors develop elsewhere from hematopoietic stem cells in the bone marrow [213]. However, the creation of IPSCs that can differentiate into functional lymphocytes is a very promising approach, but low differentiation efficiency and poor scalability of current methods may compromise their utilities [214–217].

The parameters needed for an ideal lymph node-on-chip must include a biocompatible scaffold that allows a 3D environment formation, a representative hydrogel which houses different cell types (T cells, B cells, macrophages, stroma), cell compartmentalization and flow application (lymph perfusion). So far, several independent devices have been created model the LN on-a-chip and here I will sum up the major attempts (Table 1.1). Some models have made use of conventional PDMS-based devices [147,218] while others created fluidic systems in hydrogels such as agarose [219]. An initial attempt is represented by a commercial perfusion bioreactor system named the Human Artificial Lymph Node reactor (HuALN®), built in polysulfone (PS) with two separate culture chambers and two perfusion systems. This model allowed long-term growth of cells embedded in agarose, genetic profiling and media retrieval for cytokine analysis. This model has been used to test glycoprotein vaccines, to study protein aggregates and immunogenicity of two antibodies, bevacizumab and adalimumab [220,221]. Interestingly in this model, lymphocytes were isolated from human peripheral blood mononuclear cells (PBMCs) to which matured dendritic cells (mDC) were added. For the stromal compartments lymph node stromal-like cells were generated in culture from mesenchymal stromal cells isolated from adipose tissue. Although an interesting attempt that combined many crucial LN factors, these models lack data showing physiological cell morphology and compartmentalization. Two recent works have shown the feasibility of perfusable multi-compartment devices for toxicology studies. They were both created with PDMS scaffolds and cells suspended in collagen hydrogels, but the main limitation is represented by the cellular components included. A stromal compartment was missing, and the representative T and B cells were derived by tumoural cell lines: Jurkat T cells isolated from leukemia patient and Raji B cells, lymphoblast-like cells from Burkitt's lymphoma [222,223].

A group of other models was developed that focused on studying chemotaxis and chemical gradients. By including DCs into hydrogel while chemotactic stimuli (CCL19 and CCL21) were perfused in the devices, it was possible to study cell motility dynamics and preferential migration towards specific cues [219,224,225]. With similar aims, T cell motility could also be investigated with such devices [226,227]. In other attempts, specific aspects or multiple cells interactions have been studied. For instance, a SCS-on-chip model was created to study cancer metastasis to the LN showing how biophysical effects of organ remodelling drive metastasis and how monocytes increase cancer cell adhesion in a lymph node flow-dependent manner [228]. Noteworthy is also a microfluidic system created in PDMS, elegantly designed to trap single cells and study cell-cell interactions [229]. Here, OT-I CD8 T cell interactions with B cells were investigated in early activation stages. In a different attempt, a microfluidic platform was developed to study the dynamic interactions between flowing lymphocytes and adherent DCs [230]. Finally, a LN model created by the Ingber group was shown to support the formation of lymph node follicles and germinal centers, related to vaccine responses. Introduction of a quadrivalent split virion influenza vaccine into the lymph node platform resulted in plasma cell formation, viral strain-specific anti-hemagglutinin immunoglobulin G (IgG) production, and cytokine secretion similar to that seen in serum of vaccinated humans [231].

LN-on-chip devices can be powerful reductionist platforms to study the immune system complexity with potential inclusion in drugs and vaccines development processes. So far, their application was confined to study specific functions of the native LN, with a restricted choice of cell types. To push the LN-on-chip field boundary, novel devices need to allow easy fabrication, include more cell types in a physiological 3D environment and importantly, obtain multiple readouts with different techniques from the same device.

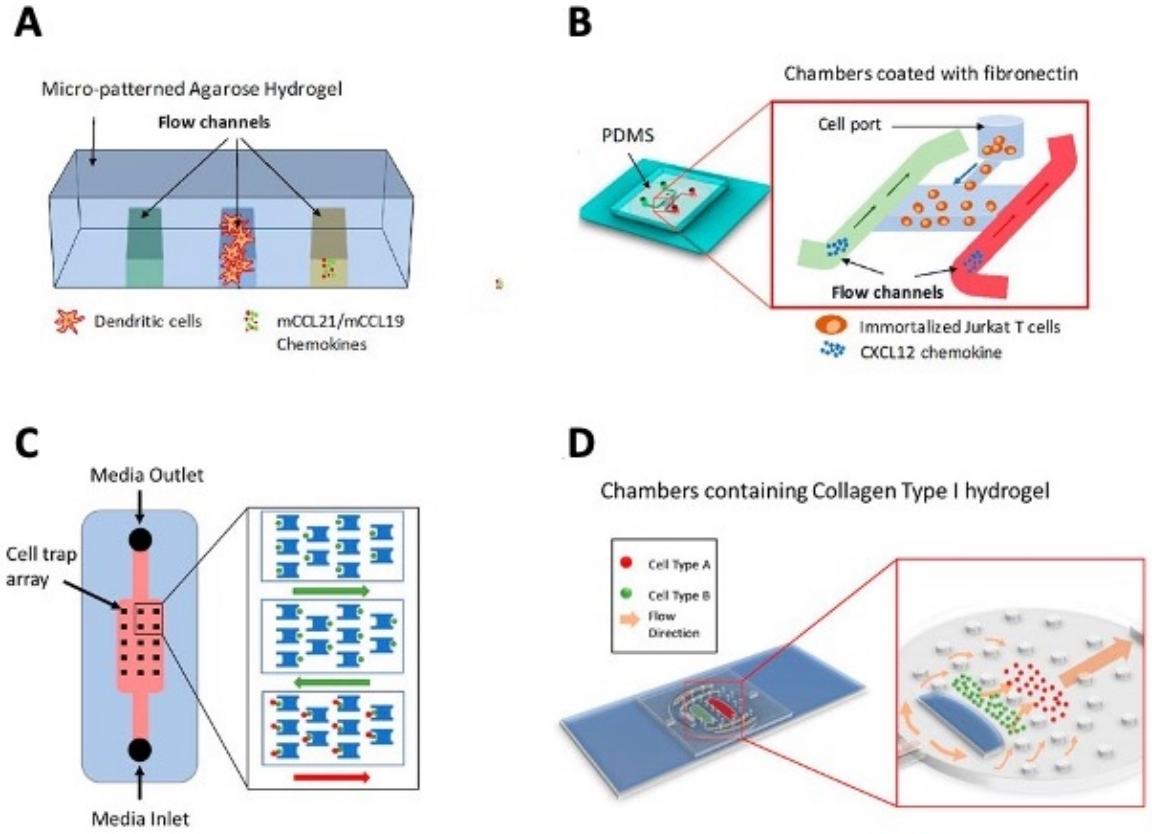

Figure 1.7 Some lymph node-on-chip models. Reproduced from [232]. **A)** Model with three channels in agarose designed for DCs chemotaxis and motility studies [219]. **B)** Model for T cell migration assays [226]. **C)** PDMS device designed with an array of cell traps for lymphocytes single cell-cell interaction imaging [229]. **D)** Compartmentalized device designed for cell interaction and drug response studies [222,233].

Replicated feature of lymph node	Lymph node Scaffolding material	ECM material	Microfluidics	Cellular component	Application	References
Chemotaxis and Chemokine Diffusion	Agarose	-Collagen hydrogel -Matrigel -Heparan Sulfate Proteoglycans	Yes, active pumping	Mouse bone-marrow derived dendritic cells	Dendritic cell chemotaxis Recreation of chemokine gradients (CCL21 and CCL19)	Haessler et al. (2009), Haessler et al. (2011)
	Photolithography-patterned PDMS	No hydrogel Fibronectin coating of surface	Yes, active pumping	Mouse bone-marrow derived dendritic cells	Dendritic cell chemotaxis. Recreation of single and competing chemokine gradients (CCL21, CCL19 CXCL12)	Ricart et al. (2011)
	Photolithography-patterned PDMS	No hydrogel Fibronectin coating of surface	Yes, active pumping	Human T cells from blood	-Blood derived T cells migration towards controlled gradients of CCL19 and CXCL12	Lin and Butcher, (2006)
	Photolithography-patterned PDMS	No hydrogel	Yes, active pumping	Mouse lymph node slices	Effective diffusion of cytokines in live mouse lymph node slices (TNFα, IL2 and IFNγ)	Ross and Pompano, (2018)
Subcapsular Sinus Dynamics	Adhesive microchannel affixed to a PDMS block previously cured in a polystyrene tissue culture plate	No hydrogel Portion of channel was functionalized by Fc specific anti-IgG Plates were blocked with BSA	Yes, active pumping	Thp1 human monocytic cell line LS174T human colon cancer cell line PANC-1 human pancreatic cell line	Effect of subcapsular sinus biophysical (flow and structure) and biochemical (adhesion molecule expression) remodeling on cellular adhesion	Birmingham et al. (2020)
Immune cellular interactions	Photolithography-patterned PDMS	No hydrogel Surface blocking using bovine serum albumin or pluronic F127	Yes, active pumping	Mouse primary T and B cells	Assay molecular events during lymphocyte activation Interaction between OT-I CD8 T cells and SIINFEKL-loaded MHCII-eGFP B cells Activation dynamics of CD8 OT-1 T cells and TRP1 transnuclear T cells	Dura et al. (2015)
	Photolithography-patterned PDMS	Collagen and fibronectin	Yes, active pumping	-MutuDC: Mouse dendritic cell line -MF2.2D, OVAII: Mouse CD4 T cell line -RF33.70/OVAI: Mouse CD8 T cell line	Dynamic interaction of flowing lymphocytes with adherent dendritic cells Effects of low and high shear stress variations on adhesion	Moura Rosa et al. (2016)
Response to Drugs and vaccines	Photolithography-patterned PDMS	Collagen	Yes, active pumping	-Jurkat human T cell line -Raji human B cell line -Thp1 human monocytic cell line	Model that replicates lymph node architecture, ECM components and flow Analysis of cell interactions and drug effects on cell dynamics	Shanti et al. (2020); Hallfors et al. (2021)
	-Polysulfone	Agarose	Yes active pumping (medium and gas)	-Human T and B cells purified from blood	HIRIS™III bioreactor that mimics long term interactions (14 days) between suspended lymphocytes and adherent dendritic cells	Giese et al. (2006), Giese et al. (2010); Sardi et al. (2016); Radke et al. (2017); Kraus et al. (2019)
	-Polycarbonate base plate			-Human dendritic cells derived from blood monocytes -Mesenchymal stromal cells (MSCs)	Used to test glycoprotein vaccines and the immunogenicity of protein aggregates	

Table 1.1 Summary of major existing *in vitro* lymph nodes on-chip and their characteristics. Reproduced from [232].

Thesis Aims

To date, attempts to create a lymph node-on-chip have been made using a variety of techniques, materials and cell sources. However, despite these efforts it has been possible to recapitulate only partial functions and specific aspects of the organ complexity.

Here, starting from a PDMS-based device used to investigate cancer cells extravasation, I have designed and created a new hydrogel-based model to study the LN, and compare the observed changes with *in vivo* data.

In this thesis, I will address the following specific aims:

1. **Manufacture and utilize an existing microfluidic model, applying it to the lymph node**

- Fabricating devices based on the original design from the Huang lab through soft lithography.
- Generate central compartment and 3D quasi-cylindrical vessels.
- Apply flow to the system.
- Identify limitations of current setup.

2. **Develop a new device to recapitulate the lymph node microenvironment**

- Design a new device built in hydrogel materials.
- Optimise the use of biophysical flow in the newly designed model for delivery of external cues, such as drugs and antigens.
- Development of optimal culture conditions – hydrogel composition, crosslinking time, cell number, cell behaviour.
- Recreate organ ultrastructure observed *in vivo* with presence of B cell follicles and T cell zone.

3. **Applying/Manipulating the system to measure responses**

- Identify changes in the immune populations (surface phenotype and functional changes) after conditioning by activation cues and tumour factors. Compare with lymph nodes isolated from tumour bearing mice and observe whether the *in vitro* model system accurately recapitulates the *in vivo* system
- Quantify lymph node response to treatment.

- Perturb system with tumour conditioned medium from 2D tumour cell cultured and tumouroids.

4. Create a new 3D bioprinted model of a pancreatic tumour

- Optimise a technique to 3D bioprint core-shell tumouroids structures.
- Investigate the tumouroids viability, phenotype and core-shell formation.
- Isolate tumour factors from the model to treat the LN device.
- Create a biomimetic tumour microenvironment (TME) that incorporate infiltrating immune cells.
- Treat the engineered TME with anti-CTLA4.

CHAPTER 2

MATERIALS AND METHODS

2.1 Cell Culture

2.1.1 Cell Lines and Cell Maintenance

The B16-F10 murine melanoma cell line was purchased from the American Type Culture Collection (ATCC; Cat: CRL-6475) and maintained in Dulbecco's Modified Eagle Medium (DMEM) (Gibco, Cat: 11995065) supplemented with 10% v/v fetal bovine serum (FBS; ThermoFisher) and 100 U/ml penicillin-streptomycin (ThermoFisher) (Full DMEM medium).

Fibroblastic reticular cells (FRCs) were isolated from the lymph nodes of $p53^{-/-}$ C57BL/6 mice as previously described [234235]. The cells were maintained in Roswell Park Memorial Institute formulation 1640 (RPMI-1640) (Gibco, Cat: 21875-034), supplemented with 10% v/v FBS, 1% v/v HEPES buffer (Gibco, Cat: 15630080), 100 U/ml penicillin-streptomycin and 15µM β-mercaptoethanol (Sigma) (Full RPMI medium).

C57BL/6 murine primary dermal lymphatic endothelial cells (LECs) were purchased from CellBiologics® (Cat No: C57-6064L) and cultured in endothelial cell medium purchased from CellBiologics® (Cat No. M1168) supplemented with 10% Foetal Calf Serum (FCS), 1% L-Glutamine, 0.1% Heparin, 0.1% Endothelial Growth Factor (EGF), 0.1% Vascular Endothelial Growth Factor (VEGF), 0.1% Endothelial Cell Growth Supplement (ECGS) and 1% Antibiotic-Antimycotic Solution, purchased as a kit from CellBiologics® (Cat No. M1168-Kit).

T zone fibroblastic reticular cells (TRC) were isolated from lymph nodes of $p53^{-/-}$ C57BL/6 mice as described previously [236]. The isolated fibroblasts were transfected with a lentivirus containing a plasmid carrying the Tomato protein and were used for easy detection during live-cell and confocal microscopy as well as in flow cytometry. The cells were maintained in full RPMI medium.

mM1 murine pancreatic ductal adenocarcinoma cell line (kind gift of Dave Tuveson, CSHL) was maintained in DMEM culture medium supplemented with FBS 10% and 5% penecillin-streptomycin.

Pancreatic Cancer associated fibroblasts previously isolated from KPC tumour-bearing mice were maintained in full RPMI medium [237].

2.1.2 Cell Passage

All cells were cultured in T75 or T175 cm^2 flasks (ThermoFisher) and incubated at 37°C in a 5% CO_2 environment. LECs were cultured in collagen-coated 25cm^3 tissue culture flasks (Thermo Scientific). A collagen coating solution was prepared using sterile nuclease-free water (Ambion), 50µg/ml Rat-Tail Collagen Type 1 (Corning, Cat No. 354236) and 0.1% acetic acid (VWR International). At 70-80% confluency the growth medium was removed, and the flasks were washed with cell grade PBS to remove excess serum. The cells were incubated with 0.25% trypsin (Gibco), at 37°C, to stimulate cell detachment. Once detached, the trypsin was neutralised by adding the appropriate culture medium. The cells were then counted by trypan blue exclusion and split into separate T75 or T175 cm^2 flasks. As a rule all cells were used until passage 35 (P35), at which point earlier passage stocks of the cell lines were thawed while LECs were not used above P12.

2.1.3 Generation of Conditioned Medium

B16-F10 cells were seeded at a density of $1.5x10^6$ cells in T175 cm^2 flasks. The following day the medium was replaced with low serum medium (RPMI-1640 supplemented with 2% FBS, 2% p/s, 10mM HEPES and 15µM β-ME). After 24 hours, the medium was harvested, centrifuged at 500g for 10 min, to remove cellular debris, and filter-sterilised using SteriFlip® vacuum filters (Merck). The medium collected from B16-F10 cells represents tumour-conditioned medium (TCM). TCM was then aliquoted and stored at -80°C until use.

For tumour microenvironment (TME) conditioned medium (TMECM) generation, tumouroids were singularly grown in 3D collagen gels laden with CAG.egfp splenocytes, and medium was collected after 24h of culture. Inclusion in the hydrogel laden with 30 x 10^6 splenocytes/ml was performed just after the alginate lyase treatment. The medium was supplemented with IL-7 and IL-4 as described previously and was composed of full RPMI and full DMEM in a 1:1 ratio. Finally, the medium was harvested through the same processed used for TCM generation.

2.1.4 Cryopreservation

1.5 x 10^6 cells were re-suspended in freezing medium (90% FBS, 10% DMSO) and placed in a single Nunc cryovial. The cryovials were transferred to a CoolCell® Freezing Container (Biocision) and stored at -80°C overnight, before long-term storage in liquid nitrogen. To recover cell lines the cryovials were thawed at 37°C and the toxic freezing medium was removed. The cells were resuspended in the appropriate cell culture medium and placed in a T75 flask for growth under standard conditions (37°C, 5% CO_2).

2.2 *Ex vivo* cultures

2.2.1 Murine LNs and spleens isolation

Spleens and LNs were isolated from mice (MRC ARES, Cambridge) and broken apart using a 25-gauge needle (0.5mm x 25mm). Broken tissues were filtered through a 70µm strainer (Thermo), using a 1mL syringe plunger (Soft-Ject), to create a single-cell suspension. Remnant tissues were flushed through with PBS. For splenic tissues, the single cell suspension was lysed in Red Blood Cell Lysis Buffer (RBC Buffer; 155 mM NH4Cl, 12 mM NaHCO3 and 0.1 mM EDTA in ddH2O) for 5 min, at room temperature (RT), before neutralisation with medium. RBC lysis was not conducted on LN samples. Immune cells were maintained in full RPMI medium containing IL-4 (20ng/ml, Peprotech 214-14) and IL-7 (10ng/ml, Peprotech 217-17) for the duration of the experiments.

2.2.2 MACS Isolation of B220$^+$ B cell populations

For B220$^+$ B cell enrichment, spleens were processed into a single-cell suspension as described in Section 2.2.1. B220$^+$ B cells were isolated using the Pan B cell Isolation Kit II (Miltenyi Biotec, 130-104-443). Isolated cells were counted with a haemocytometer and re-suspended at a density of 1 x 10^8 cells in 400µL of MACS Buffer (0.5% v/v BSA and 2mM EDTA in PBS). 50µL of Pan B cell Biotin-Antibody Cocktail (Miltenyi Biotec Cat: 130-095-130) was added to the suspension and incubated for 5 min at 4°C. The cells were re-suspended in 100µL of anti-biotin MicroBeads and 300µL of MACS buffer and left for 10 min at 4°C. Magnetic separations was then conducted. The cells were loaded onto a primed LS Column (Miltenyi Biotec, Cat: 130-042-401) attached to a QuadroMACS™ Separator (Miltenyi Biotec, Cat: 130-091-051). The column was washed with 3mL of MACS buffer to collect the unlabeled B220$^+$ B cells. Flow cytometry was performed to confirm purity. Viable cells were counted using a haemocytometer and re-suspended at the desired concentration for *in vitro* assays or for *in vivo* injections.

2.2.3 Mouse Strains

All mouse tissued were originated at the MRC Ares Animal Facility (Cambridge, UK) under the Project Licenses P88378375.

WT C57BL/6 mice were obtained from the in-house breeding facility and used for experimentation.

CAG-EGFP mice were purchased from the Jackson Laboratory (Stock No: 003291) – the mice

ubiquitously express enhanced GFP (EGFP) permitting its use in labelling studies.

OT-I mice (C57BL/6-Tg(TcraTcrb)1100Mjb/Crl) were purchased from Charles River company. These homozygous mice contain transgenic inserts for mouse Tcra-V2 and Tcrb-V5 genes. The transgenic T cell receptor was designed to recognize ovalbumin residues 257-264 (SIINFEKL) in the context of MHC class I and used to study the role of peptides in positive selection and the response of $CD8^+$ T cells to antigen.

2.3 Flow cytometry

2.3.1 Samples processing

In order to analyse the samples by flow cytometry or to achieve a single cell suspension for cell sorting and qPCR analysis the cells were retrieved from the hydrogels by enzymatic digestion. Samples were briefly disrupted with a pipette tip and incubated in 2mg/mL collagenase A (Roche; COLLA-RO), 2mg/mL collagenase D (Roche; COLLD-RO) for 20 min, pipetting occasionally to break apart the collagen fibres. Once the hydrogel completely liquified and no particles were visible, the digestion was deactivated using 10mM Ethylenediaminetetraacetic acid (EDTA). Finally, the samples were centrifuged at 300g for 5 min, resuspended in sterile PBS, and transferred to round-bottomed 96-well plates (Corning) ready for staining.

2.3.2 Staining samples for flow cytometry

The samples were resuspended in an appropriate volume of PBS and then seeded in 96-well round bottom, polypropylene coated plates (Corning). The cells were then pelleted at 300g for 5min and resuspended in 100µl of Live/Dead viability dye, diluted at a ratio of 1:1000 in PBS. For this flow cytometry panel, Live/Dead Violet (ThermoFisher, Cat: L34963) was used. After 10min at 4ºC the samples were pelleted, at 300g, for 5min and washed once in sterile PBS. An unstained control was also setup.

To detect external epitopes for the lymph node gels, the samples were stained with appropriate primary antibodies for 30min at 4°C. The primary antibodies were diluted 1:300 in FACS buffer (0.5% v/v BSA in PBS). The samples were then washed three times in FACS buffer and transferred into polystyrene tubes (Corning), ready for flow cytometry (Table 2.1). After surface staining, if intracellular epitope detection was required, samples were fixed and stained

in accordance with the FoxP3/ Transcription Factor Staining Kit (eBioscience, Cat: 00-5523).

Table 2.1 Flow Cytometry Antibodies. Table detailing the clone, species, company, dilution and conjugates for each of the primary antibodies used for flow cytometric studies.

Antibody	Clone	Species	Dilution	Conjugate	Company (Cat. No.)
B220	RA3-6B2	Rat	1:200	Biotin, APC-Cy7	Biolegend (103203), (103224)
CD11b	M1/70	Rat	1:200	PE	Biolegend (101208)
CD11c	N418	Armenian Hamster	1:200	PE-Cy7	Biolegend (117318)
CD34	RAM34	Rat	1:200	FITC, eFluor®660	Invitrogen (11-0341-82) Invitrogen (50-0341-82)
CD3ε	17A2, 1452C11	Armenian Hamster	1:200	AF488, PE	Biolegend (100210), (100308)
CD4	GK1.5	Rat	1:200	BV-785, AF488, PE, PE-Cy7	Biolegend (100453), (100423), (100408) Invitrogen (25-0041-82)
CD44	IM7	Rat	1:200	APC-eFluor 780	eBiosciences (47-0441)
CD62L	MEL-14	Rat	1:200	APC, PE-Cy7	Biolegend (104412), (103318)
CD69	H1.2F3	Hamster	1:200	APC	BD Pharmingen (560689)
CD86	GL-1	Rat	1:200	PE CY7	Biolegend (105030)
CD8a	53-6.7	Rat	1:200	BV-785, PE, APC eFluro780	Biolegend (100750), (100758) Invitrogen (47-0081-80)
NK-1.1	PK136	Mouse	1:200	PE	Biolegend (108708)
PDGFRα (CD140α)	APA5	Rat	1:300	Biotin, PE-Cy7	Biolegend (135910), (135911)
Podoplanin	8.1.1		1:200	Biotin, FITC	Biolegend (127405)
Thy-1	30-H12	Rat	1:300	Biotin, APC-Cy7	Biolegend (105328)
αSMA	1A4	Mouse	1:200	eFluor 570	Invitrogen (41-9760-82)

2.3.3 Data acquisition and analysis for flow cytometry

Following cellular staining, the samples were run on a LSR FortessaTM (BD Biosciences) supported by the FACSDIVATM program (BD Biosciences). As multiparametric staining was conducted, unstained cells and single-stained anti-rat/anti-hamster compensation beads (BD Biosciences; Cat: 552845) were run on the Fortessa to determine the extent of spectral overlap between fluorophores. Compensation was calculated during data acquisition on the

FACSDIVA™ software and modified to ensure a spectral overlap of no more than 20% between fluorophores. The acquired data was subsequently analysed using FlowJo® (FlowJo LLC).

2.4 Cell sorting followed by RNA analysis

For RNA processing, cell sorting was performed on a high-speed Influx Cell Sorter or a FACSAria (100 mmol/L nozzle, both BD Biosciences) into RLT lysis buffer (QIAGEN, # 79216). TRCs were sorted based on signal positivity for TdTomato while B and T cells were separated from the TdTomato negative portion by B220 and CD3 expression. RNA was then isolated with the RNeasy plus micro Kit (QIAGEN, #74034) and RNA quality and quantity was analyzed with a Bioanalyzer (Agilent Technologies). qRT-PCR using 20ng cDNA input material was performed using TaqMan assays with different primers/probes (all Applied Biosystems) (Table 2.2). qRT-PCR was performed on a StepOne Real Time PCR System instrument in a relative quantification setting (Life Technologies). Gene expression level are shown as 2–ddCt.

Table 2.2 List of Taqman primers used for real-time PCR showing Gene and Assay ID.

Gene	Assay ID
Acta2	Mm00725412_s1
Col1a2	Mm00483888_m1
IL-7	Mm01295803_g1
Rns18s	Mm03928990_g1
Ccl21A	-

2.5 Fabrication of the PDMS microfluidic device

The PDMS-based microfluidic device used in this project has been designed by the Huang lab using autoCAD. A shadowmask containing eight identical copies of the device design was used to create 'Master moulds' to be used for soft lithography in the Nanoscience center (West Cambridge site) clean rooms.

2.5.1 Soft lithography

The negative photoresist SU8 2100 (MicroChem) was spin-coated on a 4'' silicon wafer and the mask was then patterned by UV exposure. The wafer was washed with acetone and isopropyl alcohol (IPA) and dried over night at 150ºC before spinning the photoresist resin. The SU8 resin was spun onto the wafer at 500rpm for 15s at 500rad/s^2 and then 2900rpm for 30s at 500rad/s^2 to achieve the desired height of ~100µm. After spinning, the wafer was gradually brought to 80ºC to pre-bake for 30min. Then a shadow mask with the desired pattern was aligned to the photoresist resin and the wafer was exposed to UV light through the Contact Mask Aligner MJB-4 (Karl Suss). The photoresist was finally developed with Propylene glycol monomethyl ether acetate (PGMEA) to eliminate the non-illuminated parts and the final 'master' was obtained. Before casting it with polydimethylsiloxane (PDMS), the mask was silanized with a silane compound in order to make it hydrophilic and facilitate the PDMS peeling. Thus, it was treated with a plasma cleaner and put together with the molecule in a desiccator over night to let the reaction occur.

As shown in figure 2.1, channels 1, 3 and 5 have a width of 120µm and channels 2 and 4 have a width of 400µm. The height of all channels is 100µm. The central compartment of the device is connected to channels 1 and 5 via the gaps between the pillars (width = 200µm, length = 150µm, height = 100µm). The microfluidic devices were fabricated from PDMS by mixing the Sylgard ® 184 silicone elastomer curing agent with Sylgard ® 84 Silicone elastomer base (Dow Corning; Barry, UK) at a ratio of 1:10. After mixing, the PDMS mixture was poured onto the mask and air bubbles were removed by leaving the PDMS in a vacuum desiccator for 30min. The PDMS was subsequently cured for 5h at 60°C. The PDMS devices were cut out of the mask using a scalpel and cylindrical holes were punched into the inlets and outlets using a 0.50mm tissue- punch (Electron Microscopy Sciences; Hatfield, Pennsylvania, USA). Dust was removed from the devices using adhesive tape. The PDMS and round glass coverslips (diameter = 22mm) were then sterilised in ethanol overnight. The PDMS and coverslips were placed in the oven for 1 hour at 60°C to dry and remove the excess of ethanol.

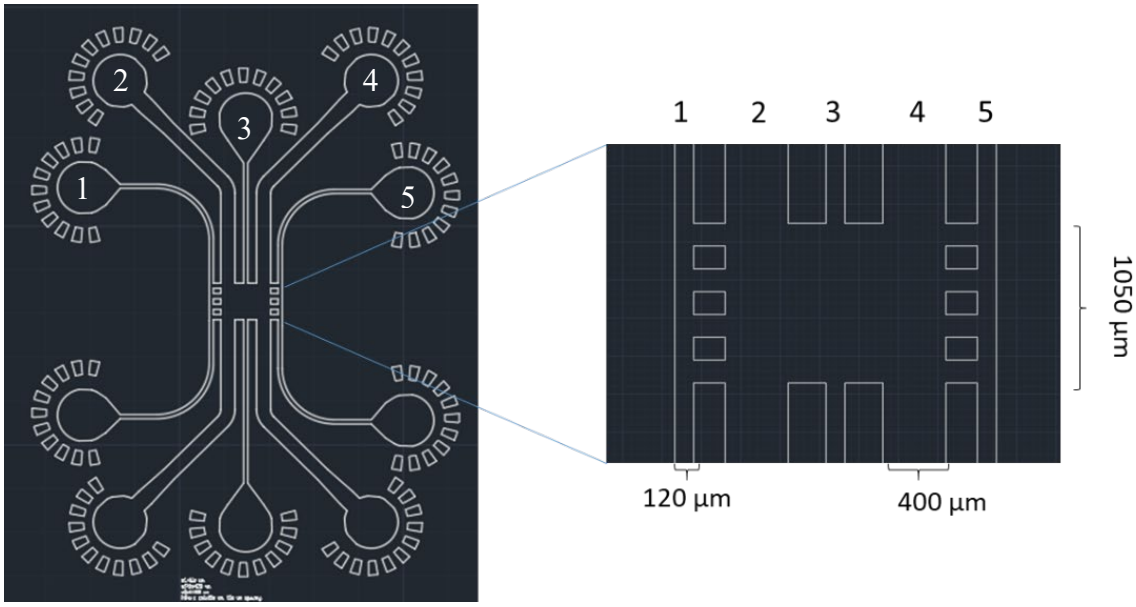

Fig 2.1. CAD design of the microfluidics device and close-up of the central compartment, showing the five channels and rectangular micropillars

Next, the surfaces of the PDMS and coverslips were plasma treated using a plasma cleaner and then the devices were adhered to the glass coverslips (Harrick plasma; Warrington, UK). During plasma treatment hydrocarbon groups are removed resulting in free silanol groups exposed on the surface. When in contact with the treated glass, Si-O-Si covalent bonds are formed and therefore create an irreversible seal of the microfluidic device. The bonded devices were transferred into sterile 35mm petri dishes (Greiner Bio-One; Gloucestershire, UK). Directly after plasma treatment, all channels within the devices were coated with poly-D-lysine (PDL, 1 mg/ml; Sigma; Haverhill, UK) by injecting approximately 10µl of PDL into the centre inlet. All inlets and outlets were covered with a drop of PDL. The devices were then incubated for 5h at 37°C and 5% CO_2. In order to prevent evaporation of PDL, deionised water (DIW) was added in each petri dish around the device. After 5h, the residual PDL and DIW was aspirated, and the individual channels of each device were washed with DIW. The devices were washed by adding 200µl of DIW on top of the inlets and drawing it through for three times in each channel using microcapillary gel loading tips (0.5mm diameter; Web Scientific; Cheshire, UK) as the inlets and outlets are too narrow for conventional tips. The washing of the channels with DIW was repeated another three times by drawing DIW through each channel on the opposite side. After washing, residual DIW was removed, and the devices were dried at 60°C for 18–24h to restore the surface hydrophobicity of the bonded surfaces.

2.5.2 Collagen I gel preparation

The gel used in the microfluidics devices obtained with soft lithography is made from collagen I from rat tail (Gibco™; Warrington, UK). Collagen I gel (per 100µl with a final concentration of 2mg/ml) was made by mixing 66.7µl collagen I (3mg/ml, sourced from rat tail; with a solution of 10µl 10x PBS (supplemented with 5µg/ml phenol red, pH 7.2), 1.5µl 1M NaOH (Sigma; Haverhill, UK), 10µl RPMI and 11.8µl DIW, while kept on ice. Immediately after mixing, the collagen I solution was slowly injected into the inlet of channel 2 (Figure 1) until a collagen I edge was observed between the pillars in the central compartment. After the fabrication process, collagen I gel was injected into the central compartment of the device, held in place by the surface tension between the pillars shown in Figure 1. Collagen I gel was used to mimic the lymph node ECM that mainly consists of collagen I. To allow the gel to set, it was left at room temperature for 10 min. Drops of 10µL of RPMI were added on top of all inlets and outlets in order to prevent shrinkage of the collagen I gel. The collagen I gel was then cross-linked for 1h at 37°C and 5% CO_2 to reach full crosslinking.

To create a LN 3D environment, FRCs or TRCs and LN isolates were grown in 3D collagen I hydrogels and injected in the central compartment of the device. The cell pellet was resuspended within the collagen I gel, to a final concentration of 10^5 FRC/ml and 5×10^6 LN cells/ml. Both cell types were also stained with CellTracker™ Green CMFDA (5-chloromethylflourescein; ThermoFisher; Hertfordshire, UK) by incubating the cells for 10min at 37°C and 5% CO_2 in RPMI basal medium containing CellTracker™ at a 1:5000 dilution. After crosslinking of the collagen I gel the outer channels of the devices were then coated with a collagen IV solution.

2.5.3 Creation of a collagen I – IV interface

After gel crosslinking, residual medium was removed from the device and 20µl of collagen IV (Sigma; Haverhill, UK) was added on top of the inlets of channel 1 and 5 (Figure 1) to mimic lymphatic vessels basal membrane. The collagen IV was slowly drawn through the outlets of these channels using microcapillary gel loading tips (0.5mm diameter; Web Scientific; Cheshire, UK). This was repeated by drawing collagen IV through from the opposite side. Devices with intact collagen I – IV interfaces were then incubated for 3h to allow sufficient time for collagen IV coating of channel 1 and 5 to provide a sufficient coated surface for cell

attachment. After incubation, the collagen IV-coated channels of the devices were washed with basal RPMI in a similar manner as washing the devices with DIW after PDL coating. The devices were washed with medium to remove residual collagen present in the device. After washing, the devices were submerged in RPMI and kept at 37°C and 5% CO_2 until further use.

2.5.4 Creating a cellular monolayer

In order to achieve a monolayer of cells in channels 1 and 5, the microfluidic devices were seeded with B16s (30×10^6 cells/ml). Excess medium was removed from the submerged devices. Prior to seeding, the cells were fluorescently stained with CellTracker™ Green CMFDA dye by incubating the B16s for 10min at room temperature. The B16s cell suspension was gently injected into the device by placing the pipette tip into the inlet and manually reducing the volume in the pipet from 10µl to 7µl. This was done to ensure a homogenous distribution of cells throughout the channel. The devices were then incubated for 2h at 37°C and 5% CO_2 to allow the cells to adhere to the collagen IV-coated channels. 1ml of RPMI was added in the petri dish around the device to maintain humidity. Subsequently, channels 1 and 5 were seeded with B16s (30×10^6 cells/ml) for a second time and directly after seeding the devices were turned upside down. Once again, 1ml of RPMI was added around the device and then incubated at 37°C and 5% CO_2 for 1h to let the cells adhere to the top of the channels. Subsequently, the device was turned back to its original position and submerged in RPMI, ready for imaging or further experiments.

2.6 GelMA

2.6.1 GelMA synthesis

Gelatin methacryloyl (GelMA) is a modified gelatin that undergoes substitution when it reacts in direct contact with methacrylic anhydride (MA). This reaction introduces methacryloyl substitution groups on the reactive amine and hydroxyl groups of the amino acid residues giving it the ability of photocrosslinking with the presence of a photoinitiator and short UV light exposure. In order to synthetize it, direct reaction of gelatin and MA is needed at 50ºC. Therefore, 5g of porcine gelatin (gel strength 300) were dissolved in DPBS at 50ºC on a magnetic stirrer. Then, 4ml of MA were added to achieve 60% degree of substitution. The

solution was then covered with aluminium foil and left to react for 3h. After the reaction was complete, the solution was purified by dialysis for 7d in DIW that was replaced daily. The solution then was freeze-dried for 48h and kept in -20ºC.

2.6.2 GelMA hydrogel

The GelMA dry powder was dissolved in PBS at 60ºC at the desired concentration with the addition of the water soluble photoinitiator Lithium phenyl-2,4,6-trimethylbenzoylphosphinate (LAP) at 0.5% w/v. The obtained solution was then aliquoted and stored at -20ºC until use. In order to crosslink the GelMA solution into a hydrogel, exposure to 405nm UV light for 10 seconds was sufficient.

2.7 Hydrogel-based device with central compartment

2.7.1 PDMS case creation

The mould for the PDMS case was designed using AutoCAD and built in aluminium at the University of Cambridge Department of physics workshop in West Cambridge (Figure 2.2) with the purpose of being reused. The cases were created by pouring PDMS (1:10 with the curing agent) in the moulds and curing at 60ºC for 4h. Subsequently, the cases were attached to a coverslip by surfaces plasma cleaning or with silicon glue. 30G sterile stainless steel needles were coated with peanut oil (Sigma cat:P2144) before the insertion in the designed side holes. The holes were designed to facilitate the application of flow within the channel by creating some cavities in the PDMS that were subsequently both used to insert needles for gel casting and to host tubing inlets and outlets.

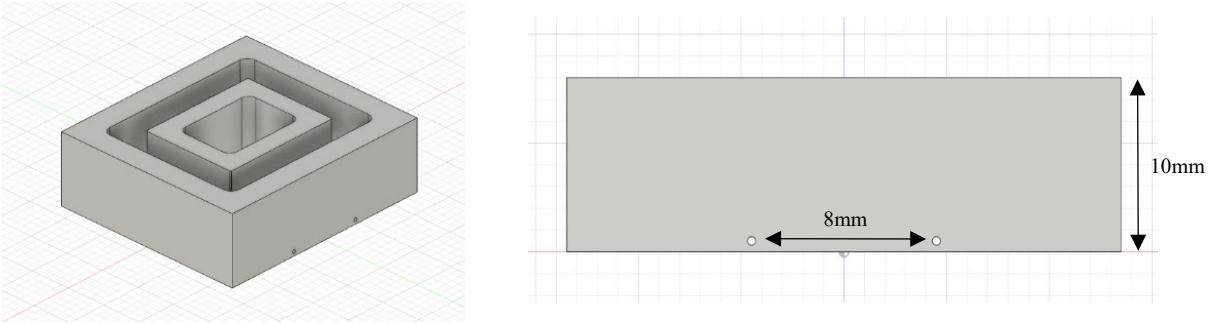

Fig 2.2. AutoCAD design of the mould for the device's case. The outer size of the obtained PDMS case is 18mm x 21mm x 8mm with a wall thickness of 3mm. The mould has on the longer side 2 holes (0.6mm) around 200µm from the base that pass through the entire mould designed for needle casting.

2.7.2 Moulding of channels and central compartment

After needles insertion, the device chamber was filled with liquid GelMA and quickly cross-linked with a handheld 405nm UV lamp for 10s. The needles were then slowly removed to create two hollow structures that were utilized as vessels while a central compartment between the two channels was initially cut out manually with a scalp. Subsequently, to optimise the shape and the reproducibility of the central compartment, a magnetic PTFE cube (8mm x 8mm x 8mm) with a steel core was built at the University of Cambridge Department of physics workshop in West Cambridge. PTFE was chosen to avoid the cube to stick to the hydrogel and ruin it while also facilitate the withdraw. In addition, the steel core made the cube magnetically removable after casting and cross-linking of the gel. The device was then washed twice with PBS and kept in medium at 37ºC overnight until LECs seeding. The concentration of LECs seeded in the channels was $25x10^6$ cells/ml. 5µl were perfused on both sides of the channels with a pipette (P10) and the device incubated for at least 2h to make the cells adhere to the bottom of the channel. The same seeding process was then repeated, and the device flipped 180º to make cells adhere to the opposite side. After 3h the device was then covered up with medium and kept until confluence for 2d at 37ºC with daily change of medium. After one day of LECs culture in the channels the central compartment was filled with collagen I gel laden with LN isolates and FRCs. Once reached LECs confluence in the channels, the devices are ready to be attached to the peristaltic pump and perfused.

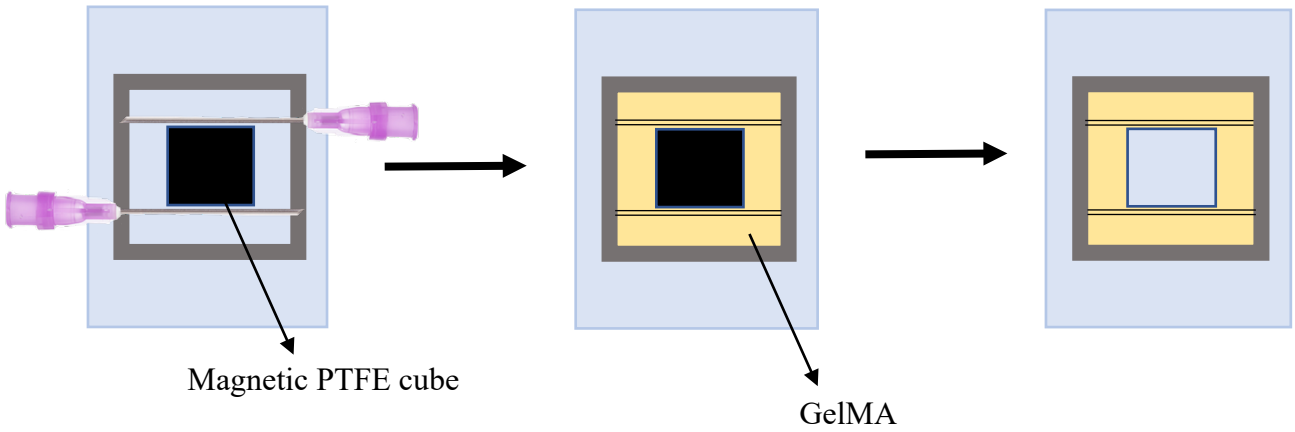

Figure 2.3 Moulding procedure for hydrogel-based device fabrication.

2.7.3 Cell viability assay in GelMA

In order to assess cell viability in GelMA over time, a cell viability test was performed by seeding 5 x 10^5 FRCs in 200µl of GelMA. FRCs were stained with 2µM calcein AM (Thermo Fisher) which stains exclusively live cells and Hoescht 33343 (Invitrogen) at a 1:5000 which stains nuclei. Cells were seeded in triplicate into two different 48 well plates and exposed to UV light for either 10s or 20s. Finally, the viability of the cells was tracked over 48h by live-cell imaging with a 10x objective. Quantification of green stained live cells was performed using ZEN software across five different fields of view for each condition. Live cells were individually counted.

2.8 Single hydrogel device

To create a single material device a hydrogel composed of both collagen I and GelMA was employed. Commercial GelMA dry powder (Sigma cat:900622) was dissolved in PBS to achieve a solution at the desired concentration of 10% w/v, while collagen solution was prepared according to the procedure described in 2.5.2 to a concentration of 2mg/ml. A successfully mixed solution was only achievable at a temperature range between 20 and 25ºC because of the contrasting crosslinking properties of the two materials. The collagen I solution

was prepared on ice where it maintains its liquid form with gelation process occurring at 37ºC after Ph neutralization. On the other hand, GelMA naturally undergoes thermal crosslinking below 22.5ºC and was kept in the incubator. The liquid GelMA was then mixed with the cell pellet. To keep both hydrogel solutions liquid and also avoid immediate crosslinking upon contact due to temperature difference, both were kept at room temperature for 2 min before pipetting the collagen I into the cell laden GelMA. This ensured achieving an evenly mixed product that was subsequently casted and UV crosslinked into the devices where needles were already put in place.

2.8.1 B cell follicles formation

The same hydrogel solution was used to form B cell follicles-like structures and mimic the lymph node architecture. For this purpose, the Collagen I/ GelMA hydrogel was laden with MACS isolated $B220^+$ cells (described in paragraph 2.2.2) and FRCs at the desired concentrations, loaded into a 1ml luer lock syringe, and kept at 4ºC for 15mins. As well as the GelMA solution, also the mixed solution with collagen I could solidify with temperature and this property was utilized to deposit spherical shapes in the device by syringe extrusion before filling the rest of the device chamber with a T cells and TRCs-laden solution. After keeping the device at 37ºC for 2 min UV light was applied for total crosslinking. The follicles were not UV crosslinked in order not to create a neat interface with the surrounding gel that would block intercompartmental cell interactions and solutes movement.

2.8.2 B cell spheroids

An attempt to create B cells spheroids was made to bypass the interface between hydrogel issues encountered when trying to recreate the LN architecture. With this method, multiple B cells spheroids were included in a hydrogel laden with T cells. The technique used was the hanging drop technique. In this technique, the desired number of cells is mixed into a 5mM methylcellulose solution, obtained by mixing a 0.02M methylcellulose stock solution with full RPMI supplemented with IL-7 and IL-4 for optimal lymphocyte growth. The obtained solution was then used to form 20µl drops that are hanged from the top part of a Petri dish and cultured overnight, after which they were collected by flushing fresh PBS. Here, the cells mixed with the methylcellulose solution were primary B cells and FRCs, at a concentration that allowed each single drop to contain 2.5×10^5 B cells and 5000 FRCs. Once collected they were ready to be included in 3D hydrogels and live imaged.

2.8.3 Mould optimization for flow – 3D printing

Due to the need for speedy changes to the mould design to improve its compatibility with pump-driven flow, 3D printing was chosen as suitable fabrication technique. A negative mould for the final PDMS case was designed with Onshape, a cloud-based CAD design platform (Figure 2.4). Therefore, a Ultimaker 3 printer was used to produce multiple copies of the design in Thermoplastic Polyurethane (TPU). The dimensions of the mould were reduced to 18mm x 18mm x 8mm which gave a 3mm thick PDMS case with an internal chamber measuring 10mm x 10mm x 8mm (Figure 2.4). The new mould still contained two holes to help the alignment with flow inlets and outlets after needle casting, but they were here enlarged to host some small tubing adapters. These adapters were used to facilitate the connection between the flow tubing and the channel and most importantly also to avoid leaking of liquid at the interface between the PDMS wall and the hydrogel. Deploying these adapters obtained by cutting small pieces of tubing (OD = 2.38mm), the pressure at that delicate interface was reduced and helped obtaining a leak-free system.

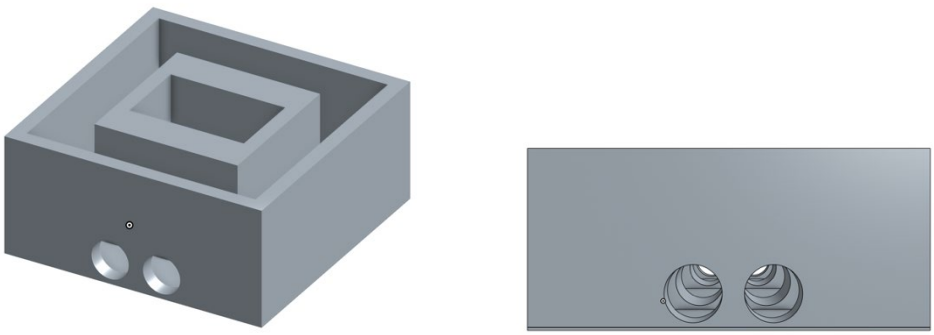

Fig 2.4. CAD model of the PDMS case mould.

2.9 Confocal microscopy

Imaging of the lymph node devices was performed without antibody staining. TRC and splenocytes from CAG.egfp were easily detectable while cells collected from OT-I or C57BL/6 were labelled before seeding with Hoechst 33342 (cat: C10337) or CellTrace Far Red Cell stain (cat: C34564). The devices were imaged using either the EVOS Cell Imaging System or Leica Sp5 confocal microscope.

Tumouroids were harvested and embedded in OCT for cutting into 10µm sections. Tissue sections were then air dried and fixed in a 1:1 mix of acetone and methanol, for 2 min at -20°C. Sections were then washed in PBS, for 10 min before incubation in blocking solution containing 10% chicken serum for 1 hour, at RT. Samples were then incubated with primary antibodies against PDGFRα (Goat IgG, R&D systems AF1062), Collagen I (Rabbit IgG, Biorad 2150-1410), Perlecan (Rat IgG, Invitrogen MA1-06821) and Osteopontin (Goat IgG, R&D systems AF808) diluted in blocking buffer, at 4°C, overnight. Following 3 x 5 min washes in PBST (PBS with 0.1% Tween), sections were incubated with 1:300 Chicken anti-Rat Conjugated AF488 (A21471), Donkey anti-Rabbit conjugated AF594 (A21207) and Chicken anti-Goat conjugated AF647 (A21469) for 1 hour, at RT. Sections were then counterstained with 1µg/ml of 4',6-diamidino-2-phenylindole (DAPI, Thermo, D1306), for 10 min, and mounted with 22 x 50 mm glass coverslips and SlowFade Gold Antifade Mountant (Life Technologies; Cat: S36936). Sections were imaged on a Leica SP5 laser scanning confocal microscope using a 10x and 40x oil objective.

2.10 Live-cell microscopy

The live-cell imaging experiments were performed with a Zeiss Z1 AxioObserver. Images of the cell-laden hydrogels were taken every 10 min to capture lymphocytes movement for a total duration of 24h. Depending on the experiment, different channels were used to capture stained cells: Brightfield, Td tomato, 488. When needed Z-stacks of three different positions of the well were taken to capture cells throughout the thickness of the gel.

To study immune cell migration in 3D collagen gels in the presence of the tumouroid, live-cell imaging experiments were performed with a Zeiss Z1 AxioObserver equipped with an incubator module that allowed cell growth at 37°C and 5% CO2 humidified atmosphere. The tumouroids were imaged with 20x objective, both in control wells and with α-CTLA4 treatment, in at least 3 fields of view at the edge of the printed structure every 8 mins for a total duration of 48h. Single cells from the obtained videos were detected together with their movement tracks using Trackmate, an open-source plugin for ImageJ. Quantification of tumouroids area and shape was performed in ImageJ. The ratio of minimum:maximum axis length was used as an approximation of sphericity and centre coordinates.

To monitor the cell migration relative to the tumouroid, a home-written python code was used to analyze the distance between cells and the center of tumouroid during their tracking

durations. In general, the center coordinates of the tumouroid (x_0, y_0) were first checked using ImageJ. Afterward, columns containing cell ID, x coordinate, y coordinate, and frame number were extracted from the csv file generated by Trackmate. For every cell at each given tracking frame, the cell-to-center distance (D) was calculated using the following equation, where (x_{nm}, y_{nm}) defines the x,y coordinates of cell n at the mth frame.

$$D = \sqrt{(x_{nm} - x_0)^2 + (y_{nm} - y_0)^2}$$

Intensity plots were then generated using cell-to-center distances versus corresponding time points in the total tracking duration.

2.11 Scanning electron microscopy

Scanning electron microscopy (SEM) was performed on polymerized GelMA (5% and 8%) and GelMA/collagen hydrogels (1mg/ml collagen and GelMA 7.5%, 5% and 4%). Following polymerization, the hydrogels were fixed with 4% PFA in PBS for 30 min at room temperature. Then, after three 10min washes in PBS and two 10min washes in ddH_2O, the hydrogels were transferred into disposable cryosectioning base moulds (ThermoFisher) and put at -80°C overnight. The samples were then lyophilized under vacuum with a freeze-drying system (Thermo Savant Modulyo) for 24h. The specimens were then gold-coated and imaged at 10 kV, magnifications of 500x, 1000x, and 4000x.

SEM images were analyzed using NIH ImageJ software. Average pore size was calculated in 500x images, following a diagonal line for each field of view and hand-measuring with a software option. Each SEM image had similar contrast and brightness, as well as the same electron beam voltage.

Fiber width was also measured in an analogous manner. Fiber widths were estimated using a line-drawing feature of ImageJ that reports line length in micron. Fiber were measured roughly at the midpoint of each fiber; Pixels were converted to micron measurements using SEM image scale bars.

2.12 Collagen fibers visualization through second harmonic generation (SHG)

To visualize the collagen fiber morphology and distribution, second harmonic generation acquisition of different hydrogel formulations laden with fluorescent TRCs was performed using a Leica SP5 at the MRC cancer unit with Dr Andrew Trinh. GelMA-only hydrogels were imaged as a negative control and GelMA/Collagen blends, both at t=0 and after 48h of TRC 3D culture. The hydrogel samples after culture were collected and transferred onto a glass-bottom Petri dish for optimal imaging. A Ti:Sapphire laser (Chameleon Vision 2, Coherent) was used for two-photon fluorescence excitation, with a wavelength of 880nm. The signal was collected using long working distance objectives (20x/0.40 and 40x/0.80 oil immersion objective (Olympus, Tokyo, Japan)) with a field of view of 110um. The SHG signal was obtained using a bandpass filter 435–445nm.

2.13 Microchannels fabrication - laser carving

To maximise the diffusion of factors and delivery of antigens to the cells embedded in the hydrogel, PALM MicroBeam laser microdissection system (Zeiss) was used to carve perfusable microchannels that stemmed from the main moulded channel. These experiments were performed at the MRC cancer unit. Generation of the microchannels within the hydrogel was performed using a nanosecond laser system (1-ns pulses, 100-Hz frequency, 355 nm) equipped with a 20×/0.4 NA objective, at a constant stage speed and a laser power. The devices were put into 35mm petri dishes without the bottom. The desired design of the microchannels was drawn via the laser system interface with a line drawing tool. Once optimized speed and power of the laser it was possible to achieve channels with the diameter of about 10 microns. To assess whether the microchannels were perfusable a solution of green fluorescent microbeads mixed in PBS was perfused with a syringe in the main channel.

2.14 Dextran diffusion assays

In the hydrogel-based device solute transport from out of the vessels into the collagen I compartment was visualized by dextran diffusion. Texas Red labelled 70kDa (cat: D1818), 10kDa (Blue Cascade) and 3kDa (FITC) solutions were prepared to final concentrations of 1mM. For the permeability assays, the dextrans solution was perfused into the acellular channel of the device at a fixed flow rate of 80µl/min. Solute transport was recorded by live-cell

imaging with time points taken every 5min over 1.30h per vessel. After this, the perfusion was kept for 2h after which the dextrans were fixed with 4% PFA and analysed by confocal microscopy.

2.15 PMA/Ionomycin activation assay

To assess whether lymphocytes in the hydrogel scaffold reacted to a general activation stimulus they were incubated with 20ng/mL phorbol myristate acetate (PMA) (Sigma, Cat No: P1585) and 1µg/mL Ionomycin (Sigma, Cat No: I0634). The activation solution was provided either through flow in the channel over night or as a 3h static incubation where the solution covered the cell-laden hydrogels. After the incubation, the cells were retrieved and analyzed by flow cytometry for surface markers expression. Specifically, expression of activation marker CD69 and cell phenotype shifts, CD44 and CD62L, were investigated.

2.16 OT-I $CD8^+$ T cells activation assay

Mechanistically, PMA/ionomycin provides a potent stimulation allowing us to bypass the T cell receptor activation. Therefore, to examine whether it was possible to trigger a specific response to an antigen, lymphocytes from OT-I mice were isolated and used in the device fabrication mixed in a 1:1 ratio with lymphocytes from wild-type CAG.egfp mice. The hydrogels were incubated and perfused with 10nM SIINFEKL ($OVA_{257-264}$) over night. After the incubation, the samples were digested for cells retrieval and analyzed by flow cytometry for activation markers. Green wild-type lymphocytes were in this assay utilized as an internal negative control in which upregulation of activation markers did not occur.

2.17 Cytokine array

Cytokine arrays were performed according to the R&D System Proteome Profiler Mouse XL Cytokine Array Kit (R&D Systems, #ARY028) product manual. Two milliliters of culture medium from lymph node 3D cultures laden with OT-I and CAGs in a 1:1 ratio were collected. The gels were differentially treated either with PMA, with SIINFEKL or just culture with medium supplemented with IL-7 and IL-4. The medium was centrifuged at 300g to remove cell debris and filtered through a 0.2µm syringe filter. After the different incubations the gels were digested enzymatically as described in 2.3.1. 1 mL of conditioned medium was used per

membrane of the cytokine array. Analysis was done by use of ImageJ with the "Protein Array Analyser" Macro.

2.18 Pumping systems

The microfluidic devices were designed to be perfused to deliver factors in the hydrogel. Two different pumping systems were used: an ultraslow peristaltic pump (Ismatec™ IPC-N 8 Peristaltic Pump) and a syringe pump (Harvard PHD 2000). As a circular loop system was possible to achieve only with the peristaltic pump, this was preferred over the syringe pump that having an 'infusion only' mode would have required large volumes of samples for each single device used in experimentations. Peristaltic tubing used was EZkem's 2-stop 6″ collar x 36″ length (0.25mm ID). It was adapted into a 0.38mm ID tygon tubing which was initially inserted into the device PDMS case with hand-cut metal needles tips. Subsequently, when tubing adapters were included in the PDMS case, the tubing was inserted in the adapters without need of metal needles.

2.19 Bioprinter Set-up

2.19.1 The deployable 3D bioprinter

The custom-made 3D bioprinter used in these studies was built by Huang lab and designed to be deployable and portable to allow easy transfer between labs and use in biosafety cabinets (Figure 5.8A). The portable bioprinter consists of a stepper motor (RS PRO Hybrid Stepper Motor 1.8°) driven printhead controlled by Arduino (Arduino Mega 2560), a robotic arm (uArm Swift Pro, UFactory, accuracy 0.2 mm) controlled by Python programme, and necessary supporting metal frames. The 3D bioprinter is composed by an in-house built printhead that was designed to be fixed on a foldable supporting metal scaffold and by a robotic arm that holds the stage and performs all the printing motions, easily programmable by the user. The programmable robotic arm provides flexibility for printing with versatile geometry inputs and performing customised functions based on Python codes. Driven by a stepper motor, the extrusion-based printhead provides 0.8µm per step dispensing accuracy. By tuning the extrusion rate and robotic arm moving speed, this printer can reach a printing resolution of around 150µm, which was adequate for retaining as-printed cell viability and creating the tumouroid core-shell features.

A home-written function composed by Huang lab was used here for tumouroid printing and allowed the user to calibrate the position, offering the opportunity to check and fine tune the core printing position in real time. This function was very useful for ensuring that the the cancer core was deposited at the desired location, ensuring repeatability. In addition, the custom nature of the platform allows creation of interchangeable 3D-printed stages that can be attached to the robotic arm depending on the support needed, including stages for glass slides and petri dishes.

To conduct 3D bioprinting experiments, a PLA-based stage designed using Autodesk Inventor was printed using Ultimaker 3. The stage was attached to the robotic arm to hold the Petri dish, which then moved along defined printing path once the home-written Python code was actuated on a computer. During the robotic arm movement, bio-ink, which is in this case a cell-laden hydrogel, was extruded from the printhead to form desired constructs on the petri dish.

2.19.2 Cell-laden gel preparation

For tumouroid printing, the hydrogel was prepared by dissolving 6%(w/v) gelatin powder (G1890, Sigma-Aldrich) and 1% sodium alginate powder (W201502, Sigma-Aldrich) in PBS, and was stirred at 60°C until transparent. The hydrogel was then sterilized using 0.22µm filter (1181465, Camlab) and kept at 37°C in an incubator before mixing with cells. MM1 cells and PanCAFs in a 3:1 ratio was used for the cancer compartment, and PanCAFs only were used for the stromal compartment. After being harvested, the cells for each compartment were combined according to the above ratio, centrifuged at 300g, and resuspended in hydrogel at 37°C to a final concentration of around $1.7*10^8$ cells/ml. The cell-laden gels for each compartment were then transferred into 1ml luer-lock syringes at 37°C and fitted with 25 Gauge needles. The syringes were kept at 4°C for 20 min to enable thermo-gelation before printing.

2.19.3 Tumouroid printing and post-printing treatments

Before printing, syringes containing the cell-laden gels were wiped using 70% ethanol to avoid contamination. To generate the core-shell structure, the syringe filled with the stromal compartment (CAFs) was first fitted in the printhead to print up to 6 structures (dimension around: 2mm x 2mm x 1.8mm) directly on a 35mm petri-dish The syringe was then changed to print the tumour cell compartment (dimension around: 1mm x 1mm x 1mm) inside each

stromal structure sequentially. The above printing process was repeated until enough tumouroids were printed. To crosslink alginate in the printed tumouroids, 104 mM $CaCl_2$ (C5670, Sigma-Aldrich) in sterile PBS solution was prepared and passed through a 0.22µm filter. For each 35mm petri-dish with up to 6 printed tumouroids, 3 ml of 104mM $CaCl_2$ solution was added and was then replaced with culture medium after 2 min of incubation at room temperature. After crosslinking, the tumouroids were manually transferred into 12-well culture plates coated with a layer of 2% (w/v) agarose (A9539, Sigma-Aldrich) gel. 48 hours after printing, alginate was removed by treating structures with Alginate Lyase (A1603, Sigma-Aldrich) which was added to the culture medium (DMEM and RPMI-1640 1:1 ratio). The enzyme solution was removed after 24 hours, and the medium exchanged daily until testing.

2.19.4 Optimization of tumouroids with a core-shell structure

To obtain tumouroids with a core-shell structure, stromal cells were first laden in a bioink containing gelatin and alginate printed in a block shape of a total size of ca. 2mm x 2mm x 2mm. Subsequently, after repositioning the needle at the center of the stromal block a cancer compartment of 1mm x 1mm x 1mm was extruded (Figure 5.8B). Due to its thermo-crosslinkable nature, the role of gelatin was to provide the bio-ink with enough mechanical strength to hold its own weight during printing, while Ca^{2+} ions crosslinking within alginate helped to maintain the shape of the structure after printing and when in culture. During culture, tumouroids were grown in agarose-coated 12-well plates to avoid cell adhesion (Figure 5.8B). The average printing time per tumouroid was approximately 90 s.

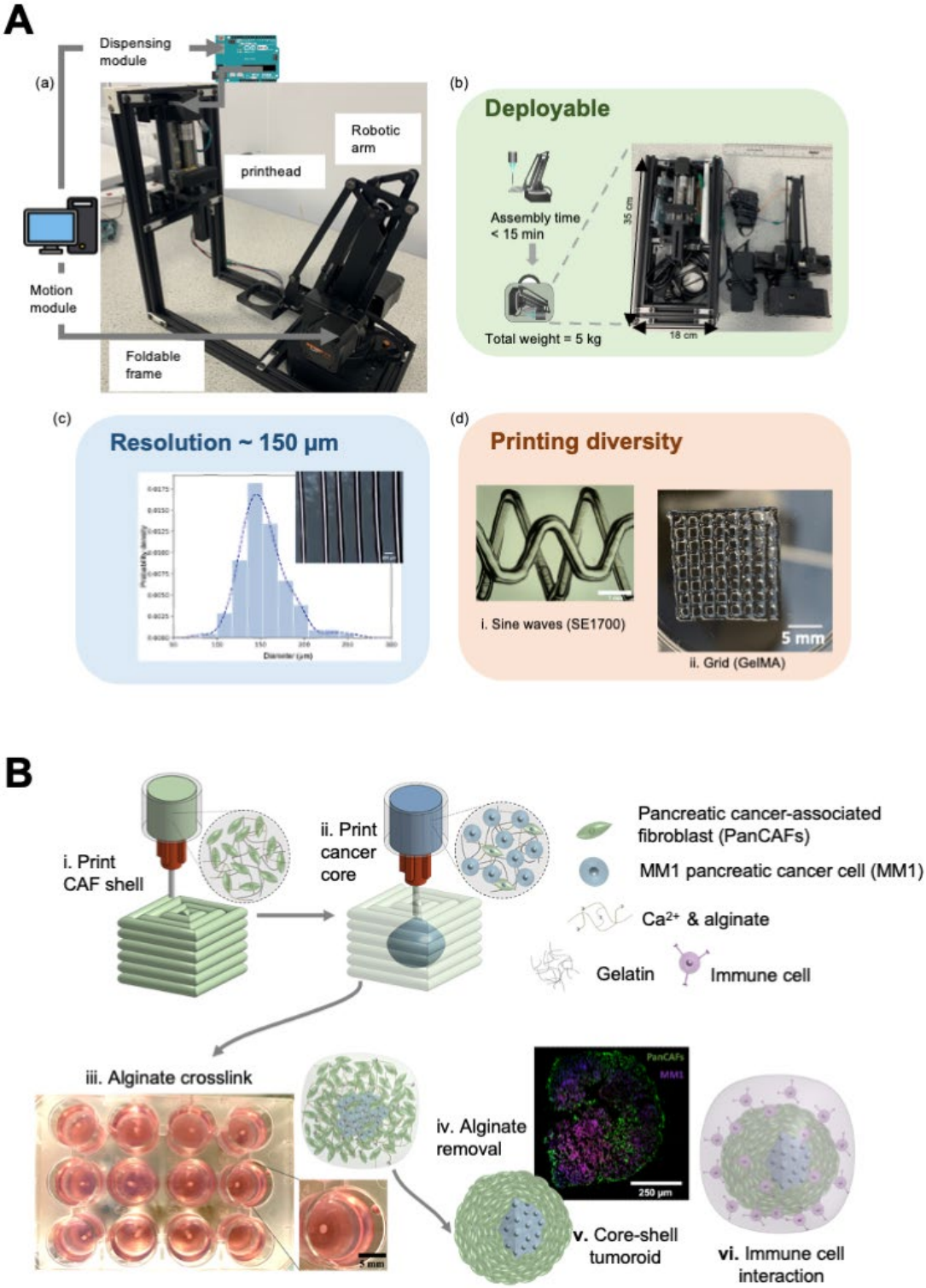

Figure 2.5 Deployable extrusion bioprinting to create a core-shell tumouroid. A) The deployable bioprinter can be folded, transported, and rapidly re-assembled for printing inside a biosafety cabinet. **B)** Schematic of the printing working flow from tumouroid printing (i, ii, iii), enzymatic treatment (iv, v) through to immune interaction (vi). Data from Yaqi Sheng.

In order to obtain scaffold-free structures, alginate had to be removed enzymatically while gelatin naturally dissolved at 37°C. The tumouroids were then treated with alginate lyase after 48h of culture and we observed that the concentration of alginate lyase was a key factor that affected the final shape and consistency of the tumouroids. First, with increasing alginate lyase concentration a slight reduction in tumouroid volume was observed (Figure 5.9A-D). In spite of the slight shrinkage however, more uniform, spherical structures were obtained with the higher concentration of 340µg/ml, compared with irregular morphologies generated with lower lyase concentrations (Figure 2.6E&F). In addition, when the tumouroids were not treated with lyase treatment a dramatic reduction in cell viability occurred, potentially due to alginate toxicity (Figure 2.6G&H). Additional factors influencing the final shape of the tumouroids were the cell concentration (>$1.7x10^8$cells/ml) and optimal mixing of cells in the bioinks to obtain homogeneous solutions. Formation of cell clusters that occurred when working with very high cell density negatively affected the overall shape of the structures.

After this initial optimization steps, optimal conditions were found to be cell concentration of $1.7x10^8$cells/ml followed by 340µg/ml alginate lyase treatment for 24h on day 2. These conditions enabled robust and reproducible tumouroids generation and were used from here for further experiments.

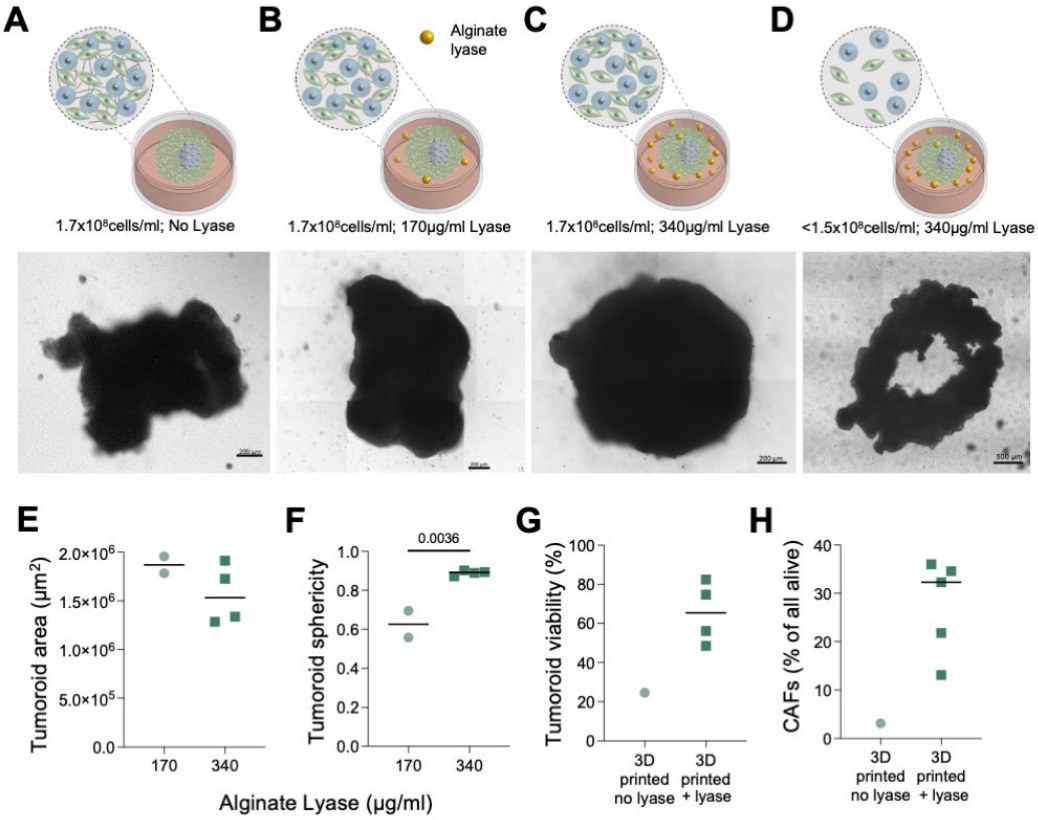

Figure 2.6 Alginate lyase treatment optimization for pancreatic cancer core-shell tumouroids. Representative brightfield tile scan images of tumouroids receiving **A)** no lyase, **B)** 170 µg/ml alginate lyase, **C)** 340 µg/ml and **D)** 340 µg/ml with low cell concentration <1.5 x 10^8cells/ml. Quantification of **E)** tumouroid area and **F)** sphericity following treatment with different concentrations of alginate lyase. **G)** Flow cytometry quantification of tumouroid viability with or without alginate lyase. **H)** Flow cytometry quantification of CAF frequency within tumouroids with and without alginate lyase treatment. Scale bars, 200 µm.

2.20 Statistical analysis

Statistical analysis was performed in GraphPad Prism. When comparing 2 conditions, T tests were used, and when comparing 3 or more groups a one-way ANOVA and Tukey post hoc test was performed. Data was deemed statistically significant with a P value of <0.05.

CHAPTER 3

PDMS-BASED DEVICE OPTIMIZATION

3.1 Introduction

The lymph node is an important immune hub that, draining extracellular fluid, helps maintaining the homeostasis and mounts adaptive immune reactions against pathogens and tumour antigens. Creating a 3-dimensional *in vitro* model of this organ, not only might help understanding cell interactions and reactions in a more tractable and physiological manner compared to 2D cultures, but also could represent an additional tool to test drugs that specifically target the lymph node and the immune system. Several efforts have been directed to the creation of novel 3D models using different approaches. An interesting methodology is the development of PDMS-based microfluidic devices obtained through soft lithography. In this widespread method these silicon chips have the advantage to combine the presence of an organ-specific hydrogel with its vasculature. Many are the examples in literature that show the potential of these devices in the context of organ-on-chips (Reviewed in [238], [239]). However, lymph node specific models that aim to include lymphatic vasculature are not numerous and often they are overly simplified in terms of cell types included in the system and do not consider important stromal compartments [232].

Here, I have tried to create a lymph node model adapting a PDMS-based device previously designed by Huang lab. These devices were used to study cancer cells transendothelial migration and to create a model of glioblastoma multiforme[240,241], however they contain all aspects needed to model the lymph node: afferent and efferent channels at the periphery (subcapsular sinus), a central 3D compartment (LN bulk), a vessel-LN interface and the capacity to apply flow (lymph flow, tumour derived factors and percolation through the central compartment).

3.2 Fabrication of the microfluidic devices

The PDMS device was built by casting the silicon compound on a master mould that contained the desired design. The master mould was manufactured through soft lithography in clean rooms (Figure 3.1A). After fabrication, the height of “hills” and “valleys” of the mould was checked with a Profilometer that confirmed the desired height of 100µm, which would define the height of the resulting channel. To make the silicon mould more hydrophilic and hence less sticky to silicon polymers, a silanization process was necessary. This ensured a repeated use of the mould through many cycles for the fabrication of the PDMS top parts of the device (Figure

3.1B). The treatment of these PDMS top parts with plasma, together with plasma treated glass slides, ensured a tight and irreversible bond between the two parts while also conferring them hydrophilic properties through the addition of silanol functional groups (SiOH) to the naturally hydrophobic material.

Importantly, temporary hydrophilic characteristics of the surfaces was essential both for cell adhesion and hydrogel anchoring. Thus, quickly after the plasma treatment a solution of poly-D-lysine (PDL) was injected to form a durable coating throughout the chip. Devices could then be used experimentally to create an interface between the vasculature and the hydrogel compartment. First, the central compartment was filled with collagen I mixed with cells that was thermally crosslinked. To initially develop the techniques needed to work on such a small scale, the matrix was initially acellular (3.1C). Before seeding cells in the outer channels to cover their surface a collagen IV coating was required to provide a substrate for even and stable endothelial cells adhesion. As a result, it was possible to create an intact Collagen I–IV interface between the central compartment and the outer channels of the device even after washing steps. A complete and intact collagen I-IV interface is required for the generation of a barrier between the cellular monolayer and the collagen I gel in the central compartment and is essential for applying flow to the channel successfully. The integrity of the interface was further confirmed when cells were seeded in the channel. In Figure 3.1D, one of the outer channels is shown just after B16 cells were seeded (*in lieu* of primary endothelial cells for optimization purposes) and started adhering to the walls without disrupting the interface. Without an interface, laminar flow could not be achieved, and perfusion critically disrupted the central compartment integrity.

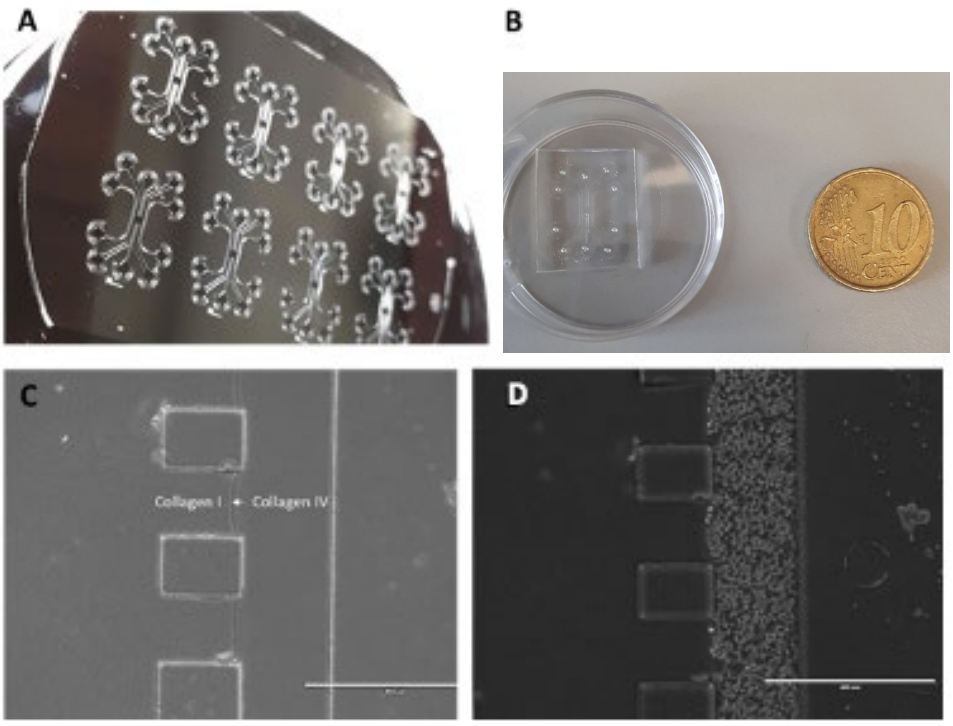

Figure3.1 Fabrication of the microfluidic device. A) A master mould is fabricated through soft lithography and used to create the top parts of the device. **(B)** Photograph showing PDMS device next to a 10 cents euro coin. **C)** A collagen I gel is inserted in the central compartment and after the creation of an interface with collagen IV, cells can be seeded in the outer channels **(D)**.

3.2 Optimising culturing a cellular monolayer

In order to examine the feasibility of seeding cells into the obtained microchannels and optimize cell density and working volumes, tumour cells (B16s) were injected and cultured in the two outer channels. After successfully establishing a confluent B16 monolayer in the channels, the same protocol could be applied to achieve a monolayer with LECs.

3.2.1 Culturing a B16 monolayer

Initially, the channels were seeded in the outer channels with a concentration of $5x10^6$ cells/ml. The cells adhered to the collagen IV-coated channel within two hours after seeding but this cell concentration was too low to achieve a confluent monolayer leaving many large gaps within the channel. This indicated the need for higher seeding densities, therefore the cell concentration for seeding B16s was increased. The optimal cellular density was found to be to $15x10^6$ cells/ml. Only about 5 microliters of this concentrated cell solution were actually injected into the channel inlet and were enough to come out of the outlet port. Figure 3.1D

shows the channel just after the seeding process by phase contrast. To facilitate cell detection B16 cells were stained with a green cell tracker prior to seeding allowing easy imaging with a confocal microscope (Figure 3.2A). In order to obtain a complete and lumenised microvessel, both the top and bottom layers of the channel were seeded with cells. With such concentration, a confluent monolayer of B16s was achieved after two days of culture and could be maintained up to at least 3 days. Confocal z-stack of the channel confirmed the obtainment of a cell-lined lumen as illustrated in Figure 3.2B.

Importantly, lumenization was possible but a large variety in morphology of the vessels was observed, especially at the interface between the pillars it was not possible to achieve identical positioning of the collagen interface among devices. It should be noted that although feasible, in general using the microfluidic device, achieving a Collagen I-IV interface and the seeding protocol were delicate processes and prone to error and user-dependant variability. A lumenised microvessel with a confluent monolayer on all four sides of the channel was not always reliably achieved as the cell confluency was not consistent over the whole surface. Crucially, because of the many delicate steps before the achievement of a full device with both functional outer channels, many devices were lost in the process.

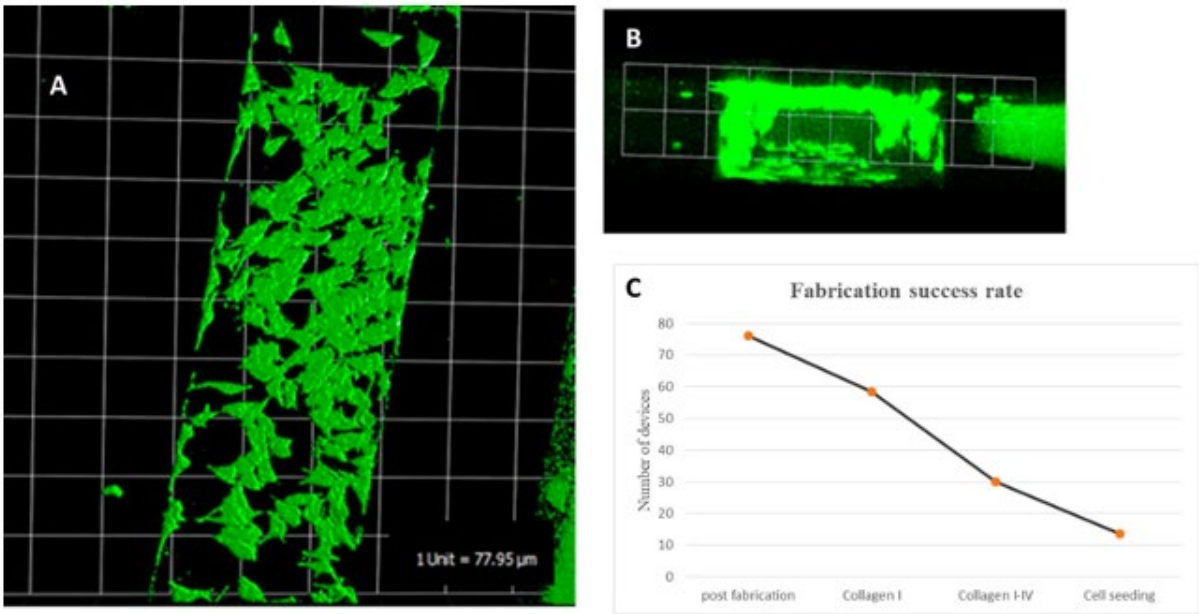

Figure 3.2 Creation of a cellular monolayer. A) Top view of a channel seeded with B16 cells stained with a green cell tracker after washing step. **B)** Confocal z-stack rendering of the vessel cross-section. **C)** Number of devices decreases during the different steps of the fabrication process.

A major point for failure in the manufacture process was reliable generation of the collagen I-IV interface. This device relies on square pillars (Figure 3.1C) to anchor collagen I gel to the central compartment; however, the viscosity of non-polymerised collagen may make it difficult to completely fill the intra-column spaces and inherently render the interaction with collagen IV weak compromising the interface integrity. To bypass this, a device with trapezoid columns was manufactured with the aim to make use of the surface tension property and make the vessels shape more consistent (Figure 3.3). Although a more regular interface could be obtained with this design, this did not present a significant improvement in the overall fabrication process tackling only one issue.

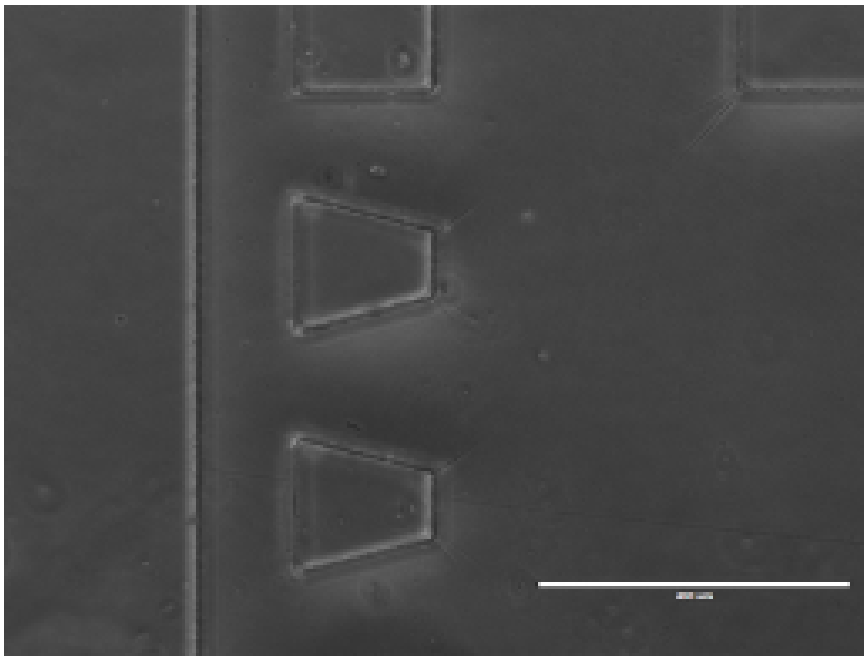

Figure 3.3 Modified design. The device was designed with 3 trapezium-shaped pillars, 100µm in height with the longer base of 200µm.

CHAPTER 4

GENERATION AND OPTIMIZATION OF THE HYDROGEL-BASED MODEL

4.1 Introduction

The PDMS device proved to be a very versatile tool with potentiality of applications in different contexts. Having identified some practical limitations of current devices in Chapter 3, we considered further limitation of these devices that needed to be overcome with the creation of a new hydrogel-based device. A major limitation encountered with the pillar-based set-up resulted from the enclosed nature and small size of the central compartment. This presented with difficulties filling the compartment, supplying sufficient nutrients and oxygenation to the central compartment and restricted its application mostly to imaging-based experiments, making in-depth investigation at a molecular level more challenging. In fact, cell retrieval from such devices is not simple and the yield of cells from each one is low, usually forcing the user to pool samples from different devices together in order to obtain detectable signal from RNA or proteins. Therefore, we tried to address the need to create a more reliable and accessible model of a lymph node. The ideal lymph node-on-a-chip would allow easy cell retrieval at the experimental end point to study surface markers and gene expression changes, while allowing manipulation of cellular compartments without losing physiological cell characteristics. To achieve this, both the organ-like compartment and the vessels were designed to be fully generated within a hydrogel, unlike the previous silicon model. In the optimization process the focus was directed, on one hand on finding a scaffold that structurally allowed channel formation and stable pump-driven flow application, on the other hand to tune the hydrogel composition to allow appropriate cell behaviour. The obtainment of embedded channels was here performed both with needle casting and sacrificial material printing technique.

In more recent years, many hydrogel-based models have been developed for various applications such as organ-on-chip, vascular models and personalized medicine[242,243] and some also included formation of lymphatic vessels to model the lymphatic system and lymphangiogenesis process *in vitro*[244,245]. These were fabricated either open or enclosed in PDMS devices with natural or synthetic polymers depending on the application. Here, the device was designed to be open for better manipulation, cells and media retrieval.

4.2 Generation of a bioprinted device

4.2.1 Sacrificial ink bioprinting generates perfusable channels

To circumvent previously described fabrication issues relying on fewer manual steps initially, for the creation of hydrogel-based devices a bioprinting approach was chosen. With this approach we aimed to generate, similarly to the previous PDMS-based device, two vessels lined with LECs that simulate the SCS within a PDMS case (Figure 4.1A) but with a greater degree of design flexibility and implementation. The vessels in this case were printed directly into a cell-laden compartment that contained immune and stromal cells with a custom-made extrusion bioprinter (Figure 4.1B). We chose as a scaffold material GelMA, a semi-synthetic polymer that crosslinks quickly under UV light exposure. The advantages of this material compared to collagen I are that the solution and the resulting hydrogel are easily tuneable to reach the desired concentration and its photocrosslinkable nature makes the device fabrication process very quick and user-friendly. To achieve the formation of the two channels within the gel laden mould then, a fugitive ink, Pluronic F127 (Pf127), was 3D printed in the shape of rods of the desired diameter directly within a GelMA hydrogel solution. Pf127 undergoes gel-to-fluid transition at ca. 4°C and this property was exploited to print solid rods at room temperature, then removed when the hydrogel was crosslinked around them by washing the channel with PBS at 4°C. Once washed, the remaining hollow channel, embedded in hydrogel, could be used to culture, and perfuse endothelial cells. Different formulations of fugitive ink were then tested to achieve consistent printing of 250µm wide tubular rods. Initially, sacrificial ink rods were achieved both with pf127 30% w/v and 40% w/v. However, they showed a noticeable variability in shape consistency and diameter among different prints, ranging between 1600µm and 300µm (Figure 4.1C-E). In this process, pf127 was printed first directly on a glass substrate, then the hydrogel solution was casted on top, and UV crosslinked. Noticeably, the width of the rods seemed to increase after casting, squeezed by the solution. Thus, embedded printing in the solution was preferred over the casting method, and in order to increase the resolution and the reproducibility among different prints, the ink was modified and mixed with high-molecular weight (8MDa) Polyethylene oxide (PEO). Figure 4.2A shows a channel of 250µm diameter printed with a formulation of pf127 30% w/v and PEO 0.8%. This ink showed a considerable improvement compared to the previous formulation in terms of consistency of rod diameter among prints. Removal of the sacrificial ink was successfully carried out by flushing it at 4°C with PBS. This left a hollow 250µm wide channel embedded

in GelMA. To test whether the channels were perfusable a red dye was injected through it with a syringe. Figure 4.2B shows the red dye flowing in the freshly printed channel.

In regular 2D culture, LECs require an ECM layer on top of the plastic to mimic the natural basal lamina on which they grow *in vivo*. This is achieved with gelatin, laminin or collagen IV and is also required in PDMS devices. Thus, during the channel optimization process, the ability of LECs to adhere directly to GelMA substrate was tested. Indeed, LECs cultured on top of a GelMA layer readily adhered and by 24 hours had formed a continuous monolayer, hence proving GelMA as a suitable substrate to fabricate a hydrogel-based device. (Figure 4.2D&E).

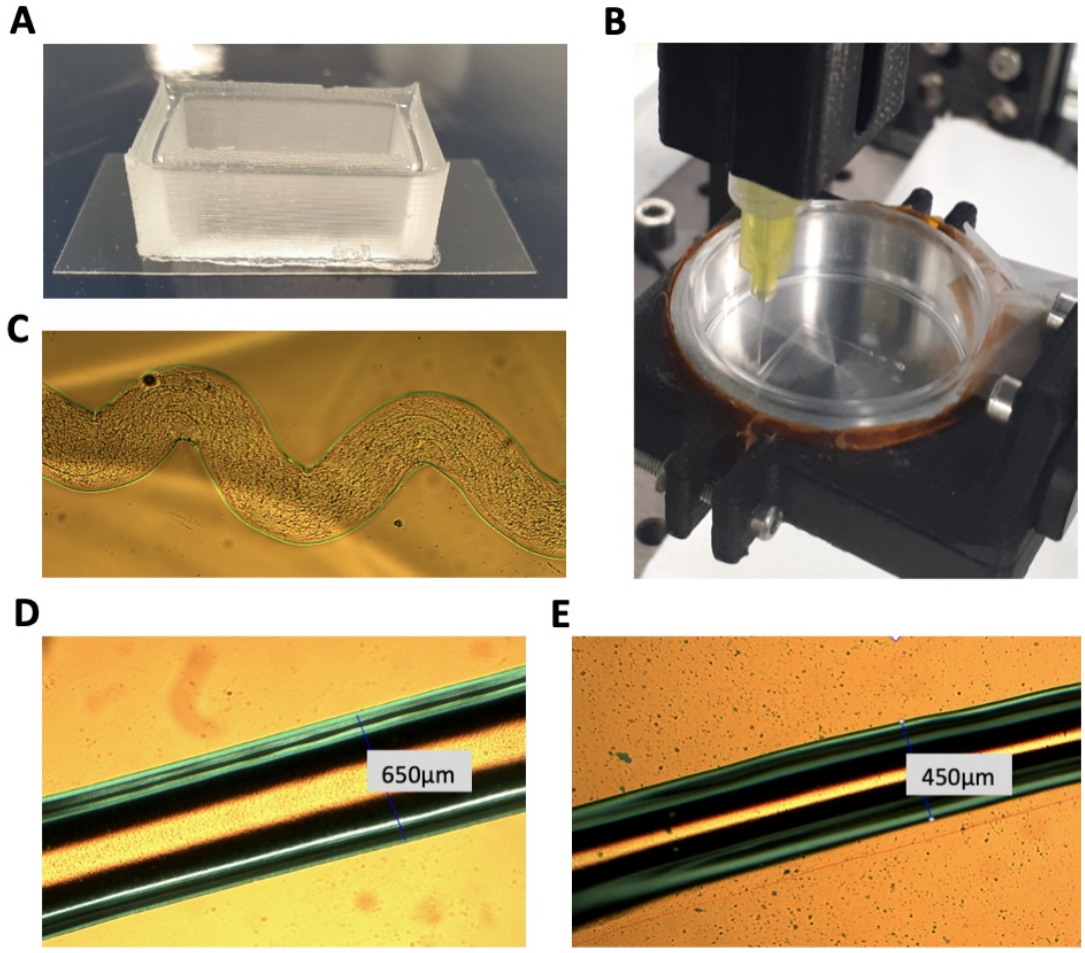

Figure 4.1 Pf127 successfully created embedded rods in GelMA. A) Photograph of the PDMS case attached to a glass coverslip used for embedded 3D printing. **B)** Extrusion bioprinting setup during printing process in GelMA. Sacrificial ink is extruded through a syringe pushed by a stepper motor on a petri dish inserted in the robotic arm. **(C)(D)(E)** Sacrificial ink rods variability examples. Brightfield images showing shape variability and diameter shown with labels. Diameters were measured with the microscope interface just after printing.

4.2.2 Bioprinted channels could not be reliably perfused – transition to needles

Sacrificial ink 3D printing seemed a promising tool for the creation of vessels with programmable shape however some issues were encountered that forced us to abandon this fabrication technique. We managed to create consistent perfusable vessels but notably we never succeeded in perfusing the vessels by connecting them to an external pump and tubing setup. In order to obtain stable perfusion, the channel in the hydrogel had to be physically connected to the tubing through a needle connector that was used to pierce the PDMS case and this operation often resulted in heavily compromised final device. An additional issue was represented by the vessel fabrication process: printing solid rods into a liquid GelMA solution often resulted into unexpected final rod shapes due to a floating movement in the liquid solution. Also, when the 3D printed vessels were characterized by flowing green fluorescent beads and confocal imaging they seemed collapsed, probably squeezed by the surrounding matrix during fabrication (Figure 4.2E). Therefore, we chose to utilize a needle casting technique instead. Despite the apparent limitation of a forced straight line channel, a few advantages were a defined diameter, consistently defined location on the xy plane and a clear circular lumen (Figure 4.2F). Here we used a 30G stainless steel needle for vessel casting and to make the setup adaptable to flow, the PDMS case was modified to host two holes that served as inlet and outlet both for casting and flow tubing use (described in Methods 2.7.1 and 2.7.2).

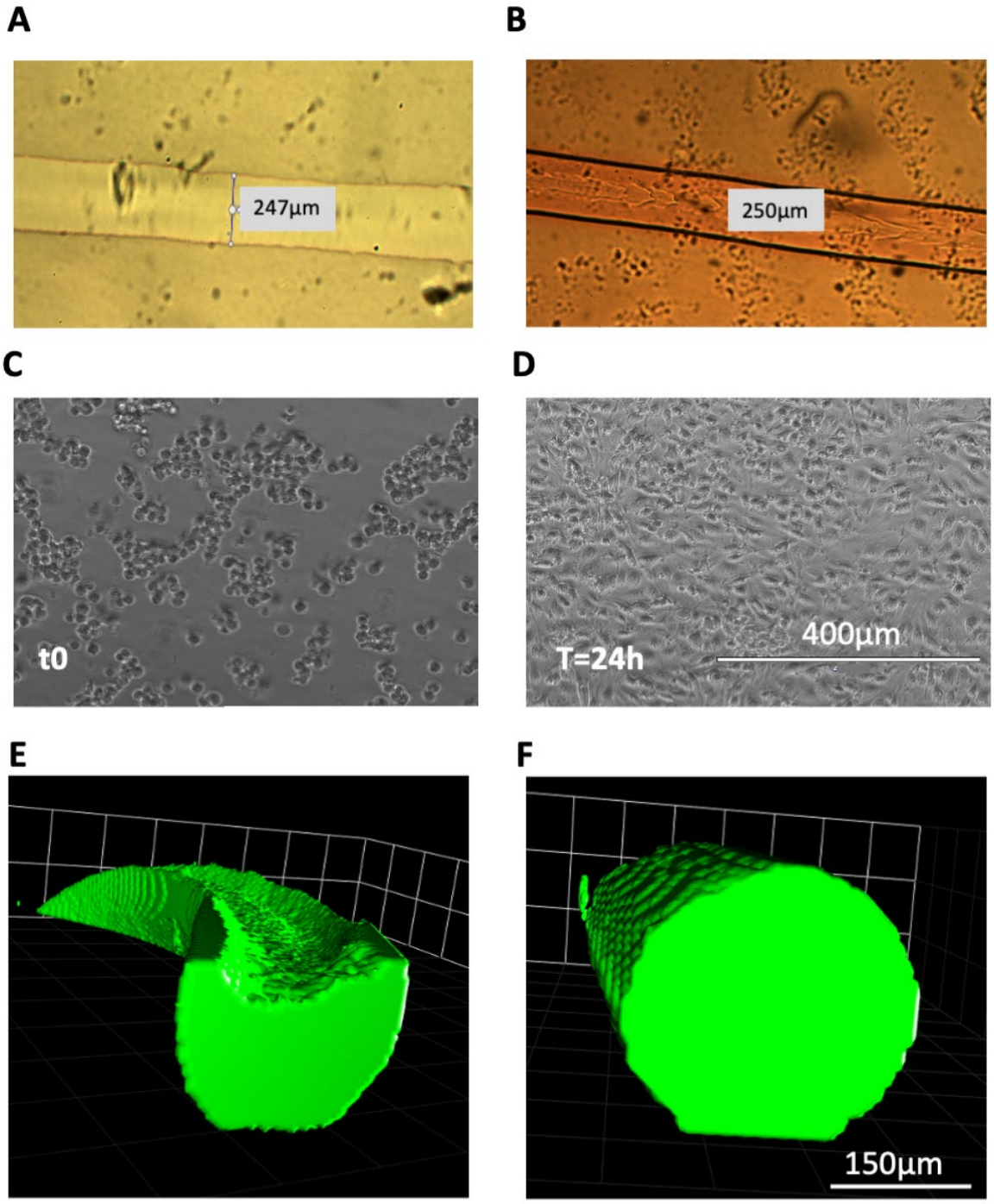

Figure 4.2 A) Representative Image of a channel obtained with Pf127 (30%) and PEO (0.8%) ink. **B)** Representative Image of a hollow channel after perfusion with a red dye. Labels show channels diameters. **(C)(D)** Brightfield images from a cell adhesion test where LECs were seeded onto GelMA layer. T0 and a cell monolayer after 24h of culture. Scale bar = 400µm. **E)** Confocal microscopy 3D rendering obtained with Volocity software after green fluorescent beads perfusion in 3D printed channel and needle casted channel **(F)**. Scale bar **(E)(F)** = 150µm

4.2.3 FRCs remain viable in GelMA but do not behave physiologically

While suitable conditions for vessels printing was achieved, the suitability of this GelMA scaffold for the cell-laden also had to be tested; both in terms of cell viability and cell behaviour. GelMA was chosen as cell substrate because of its biocompatibility, quick crosslinking time and tunability. To test whether it would also be suitable for cell culture, a viability assay was performed with Calcein AM staining, a fluorescent dye with excitation and emission wavelengths of 495/515 nm, used in cell-viability assays as it only permeates membranes of metabolically active cells. Lymph node FRCs ($5x10^5$/ml), which form a central part were then mixed with GelMA 10% w/v and exposed to UV light (405nm) either for 10s or 20s to tune the degree of crosslinking. The plate which was exposed for 20s was then live-imaged. Figure 4.3A shows representative images in a single plane of the gel at T0 and 24 hours. Manual quantification of captured images with ImageJ software confirmed that ca. 90% of cells were alive immediately after UV exposure (T0) and that after 24h, their viability remained high at 80% (Figure 4.3B) showing, in accordance with the literature, that short exposure to UV light does not seem to affect cell viability and that over time the percentage of live cells tends to remain consistently high. Even 4 days after UV exposure, which is a time that outstrips the length of any planned experiment on the final device, it is still possible to detect most cells as green and alive (Figure 4.3C).

While cells remained viable, the impact of growth in a synthetic environment on cell behaviour and morphology was also determined. *In vivo*, FRCs are found in a stretched conformation, forming a network for lymphocytes to travel along; in a 3D environment such as collagen I gel, they also tend to stretch in a few hours after seeding and form networks with neighbouring cells (Figure 4.3D). However here, despite their live state they did not come out of rounded shape even after 4 days in 5% or 10% GelMA (Figure 4.3D). This showed that although endothelial cells could stretch and proliferate when seeded on a GelMA surface, FRCs seeded within the hydrogel were not able to behave normally implying that some features of this matrix do not make it suitable for this application.

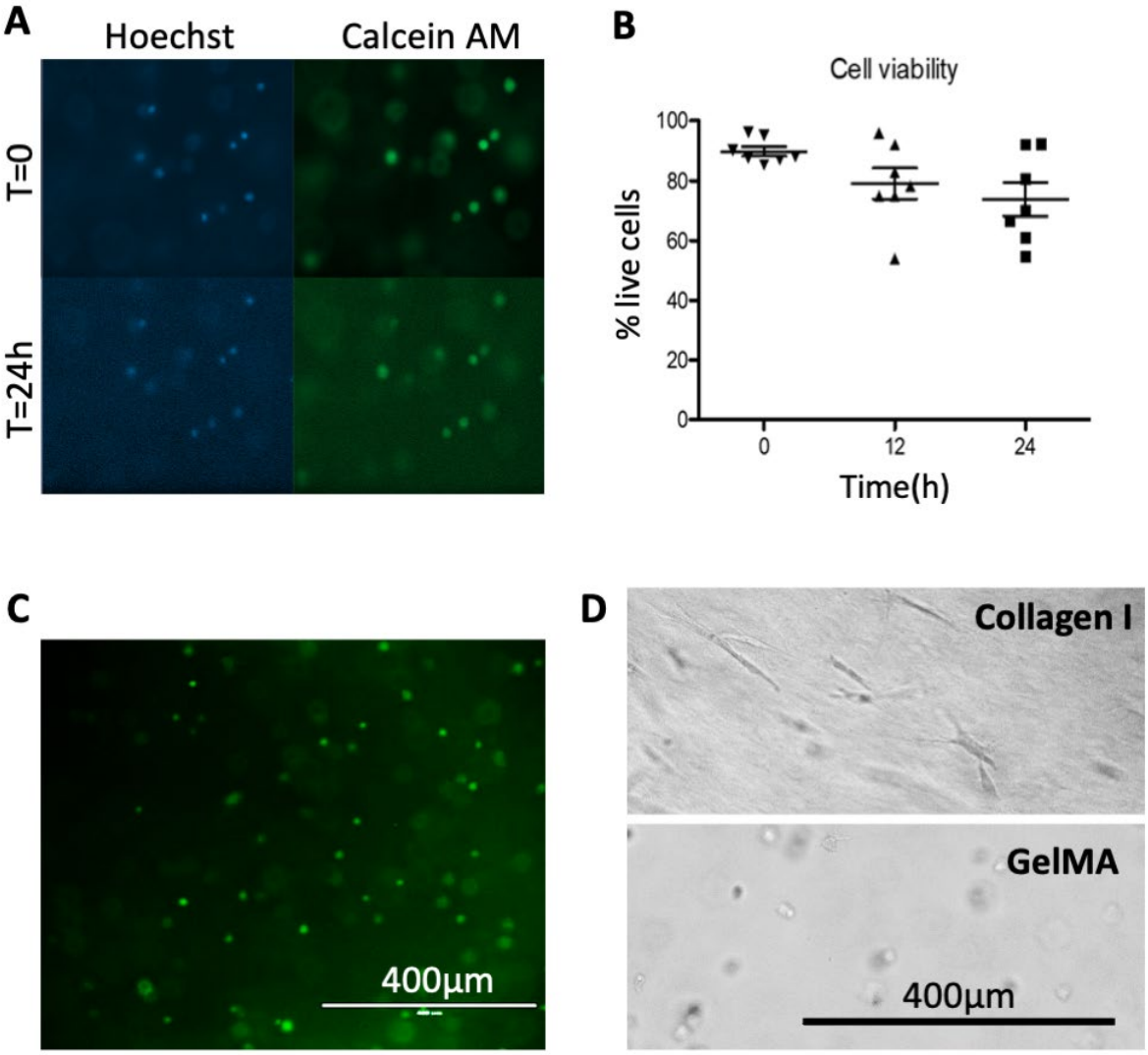

Figure 4.3 Cells remain viable in GelMA. A) Labelling of viable FRCs. Nuclei were stained with Hoechst (in blue) and Calcein AM (in green) which only marks cells that are metabolically active. Viability of cells was followed for 48h; t=0 (A) and t=24 (B). Live cells are blue and green. Dead or dying cells only blue. **B)** Quantification of live cells over time. Each dot representing the percentage of live cells in a field of view imaged with a 10X objective (n=7). **C)** FRCs appear still alive after 4d in static conditions. Scale bar = 400µm. **D)** Closeup brightfield images of FRCs cultured in 2mg/ml 3D collagen gel and 10% GelMA after 24h of culture.

4.3 Hydrogel-based devices with a central compartment

The FRCs ability to stretch is a crucial indicator for their function and behaviour in a hydrogel. As GelMA alone proved to be insufficient but FRCs, compared to 3D collagen I gels in which FRC behaviour and compatibility are very well described [246], the device was modified to include this material. As GelMA hydrogels provided enough structure for the channels

formation, and collagen is suited for cell behaviour but not compatible with formation of channels unless at high concentrations (>5mg/ml), the complementary characteristics of the two materials were combined; creating a GelMA scaffold for the vessels with a collagen I central compartment for the LN bulk (Figure 4.4A&B). In order to obtain this, two channels were casted with needles in 10% GelMA, LECs were seeded and allowed to adhere and stretch before lymph node cells and FRCs laden collagen I gel was poured into a cavity to form the central compartment; in this system LECs formed a full vessel while FRCs looked stretched and surrounded by lymphocytes (Figure 4.4F). In this way, it was possible to perfuse the vessel in the hydrogel, aligned with the two holes in which tubing adapters were inserted.

Initially, the central compartment was manually carved out of the GelMA layer with a scalpel, a very prone-to-error procedure as many devices were lost trying to cut the matrix as close as possible to the channel (Figure 4.4C). Subsequently, the process was made more reproducible and less prone to user-dependant variability, by utilizing a PTFE magnetic cube as a casting shape between the two channels (Figure 4.4D). This now provided a clean interface, with consistently sized and positioned central compartment. The cube size was optimized to leave ca. 500μm distance of the collagen I gel from the channel, and its hydrophobic and magnetic properties made it very easy to extract with a magnet from above. As shown in figure 4.4E, with this composition not only it was possible to create peripheral lymphatic vessels (the SCS), but also a central compartment with healthy and stretched FRCs surrounded by lymphocytes.

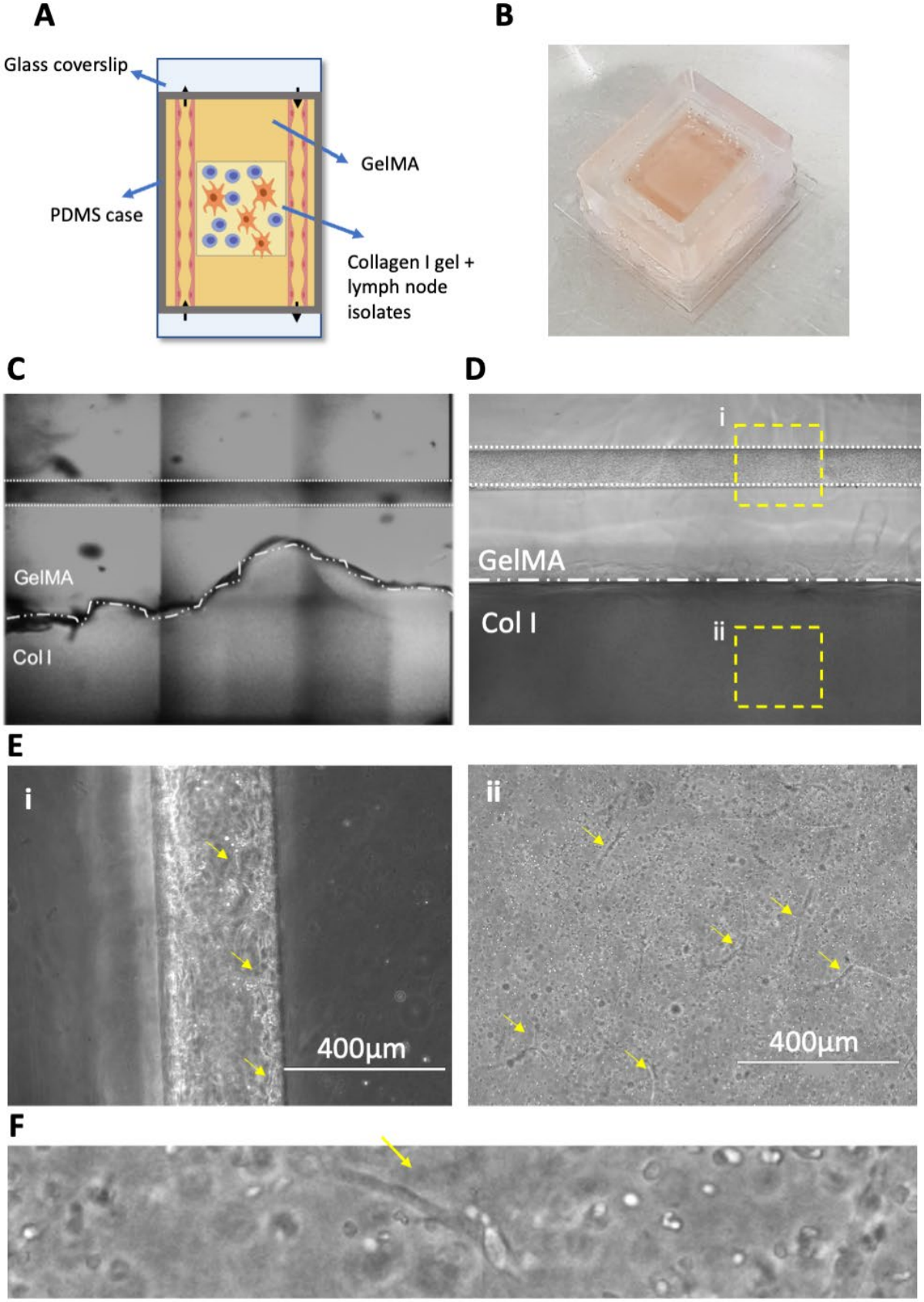
A
Glass coverslip
GelMA
PDMS case
Collagen I gel +
lymph node
isolates
B
C
GelMA
Col I
D
i
GelMA
Col I
ii
E
i
400µm
ii
400µm
F

Figure 4.4 A hydrogel-based device with central compartment was optimized. A) Top view representation of compartmentalized design within PDMS case. A central collagen I compartment containing the LN bulk lies between 2 lymphatic vessels embedded in GelMA **B)** Photograph of the device structure, showing the PDMS case on a glass coverslip, fabricated with built-inlets and outlets. **C)** Representative tile scan of the central compartment-GelMA interface when hand carved **D)** Tilescan image of a clean interface between the central compartment and GelMA after optimization with the magnetic PTFE cube. **E)** Representative micrograph of a full needle casted lymphatic vessel in GelMA and stretched FRCs with lymphocytes in the collagen central compartment. FRCs in collagen after 24h of culture show stretching into the matrix and protrusions (yellow arrows). inset i) high power field showing stretched LECs (yellow arrows). inset ii) high power field showing central compartment laden with FRCs and lymphocytes. Scale bar = 400µm **F)** Close-up image from inset Eii showing a stretched FRC (yellow arrow).

4.3.1 LECs react in engineered lymphatic vessels

Hollow channels of the desired diameter of ca. 300µm were successfully obtained by casting 30G needles in 10% GelMA and were tested for endothelial cell adhesion. It was found that the optimal seeding cell density was $25x10^6$ cells/ml to achieve an even monolayer. LECs were then cultured in the channels and a complete endothelium was only obtained after 48h (Figure 4.5A). Unlike devices described in chapter 3 lumen of needle cast channels were round and without protrusions that could disrupt laminar flow. Confocal microscopy subsequently confirmed the presence of a clear lumen (Figure 4.5B) and expression of endothelial surface markers such as CD31 (Figure 4.5C). Subsequently, LECs were tested for lymphatic specific markers such as Lyve-1 with or without the presence of flow as shown in Figure 4.6A&B.

Flow was then applied to the channel with a peristaltic pump to assess changes in the LECs in reaction to biophysical forces. Cell medium was perfused for 24h and under the microscope LECs appeared larger and consistent with previous studies, LECs began to display a more elongated phenotype than the static counterpart, aligning with the flow direction (Figure 4.6C&D). This alignment of LECs on the flow axis was due to active stretching and movement against the direction of flow.

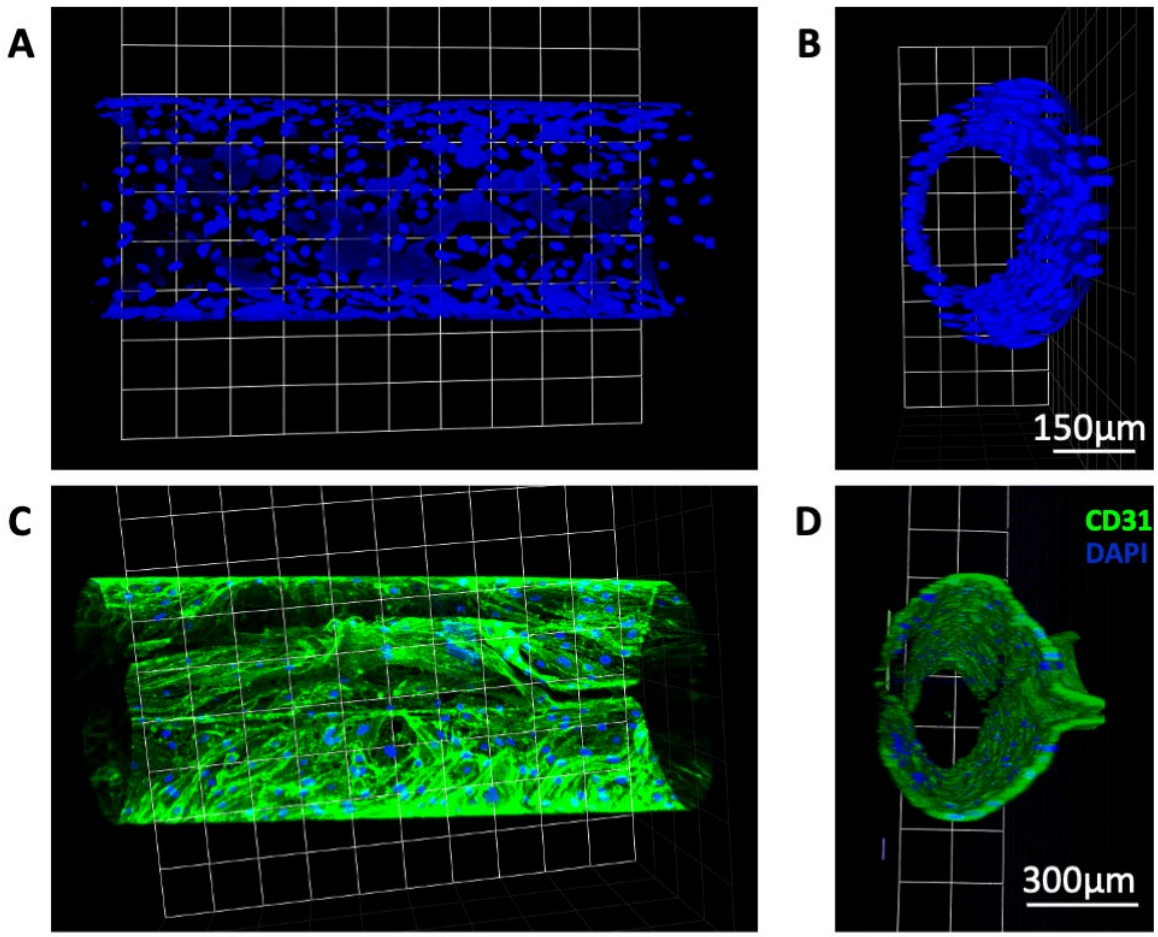

Figure 4.5 Engineered lymphatic vessel sinus A) Confocal microscopy image of a channel lined with LECs stained for nuclei (DAPI; in blue). **B)** Cross-section of open lumen obtained with z-stack 3D rendering. Scale bar = 150µm. **C)** Top view and **D)** cross section of a lymphatic vessel stained for CD31 (in green). Scale bar = 300µm. Images taken with 10x objective. Analysis and 3D rendering of open lumen obtained with Volocity software

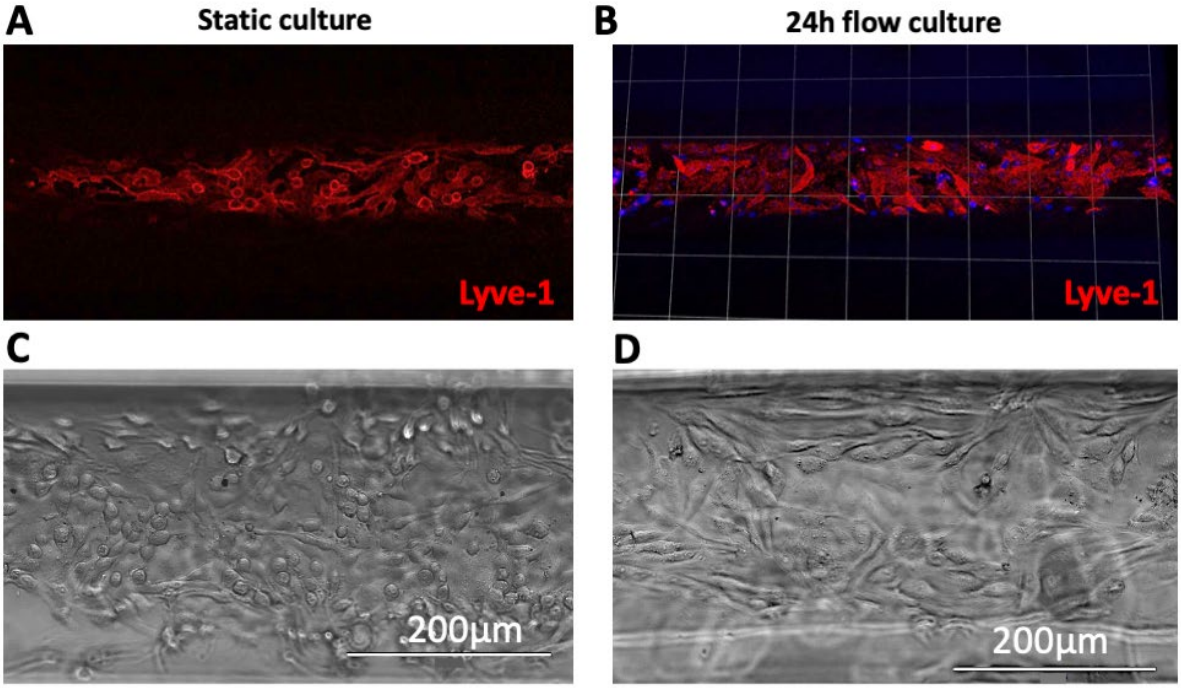

Figure 4.6 Lymphatic vessel was optimized for flow in GelMA A) Lyve-1 staining of LECs after static culture and **(B)** 24h of flow (Lyve-1 in red and DAPI in blue). **C)** Brightfield image of LECs in static culture and **(D)** elongated after 24h flow culture**.** Scale bar = 200µm.

4.3.2 Central compartment viability optimization

Initially, the central compartment was chosen to be composed of collagen I laden with FRCs and primary LNs extracts. After making the outer chamber fabrication reliable, the collagen I compartment laden with FRCs and primary LNs extracts was optimized. As lymph nodes are densely compacted cell masses, an FRC:Lymphocyte ratio was selected in order to obtain the maximum possible lymphocyte density. This needed to resemble the high cell density observed *in vivo,* but also consider the experimental need of clear live imaging for single cell tracking. The optimal lymphocyte concentration was determined to be $4x10^7$/ml in which FRCs were added at a ratio of 1:100. FRCs and the cues they produce are essential in lymph node maintenance *in vivo*. Thus, viability tests on the co-culture were then performed on cells within this 3D environment. Here, without FRCs present, fewer than 10% of total lymphocytes were viable after 48 hours. Their inclusion double cell viability, but this was still only 20% (Figure 4.7B). To boost viability, we therefore included addition exogenous cytokines typically produced by FRCs *in vivo*. Addition of IL-7 and IL-4 in the culture medium increased viability

drastically, and the presence of FRC further supported viability, which was now 70% at 48 hours.

We then focused on T and B cells, which are the dominant immune populations of the lymph node. For B cells, FRC alone had little impact on survival, nor did addition of IL-7. BAFF and April, known cytokines that stimulate B cells survival, were then tested but also did not seem to positively change B cells viability in this system. IL4 alone had little impact, however, when IL4, -7 and FRC were included, B cells viability dramatically increased (Figure 4.7C).

T cell viability remained relatively consistent across conditions, but addition of IL-7 to the culture medium seemed to be essential for $CD4^+$ and $CD8^+$ T cells survival, and as for B cells, the highest level of overall survival was observed when in the FRCs-lymphocyte co-culture were added both IL-7 and IL-4 (Figure 4.7D&E). Therefore, in future experiments, cytokines were included in the lymph node milieu.

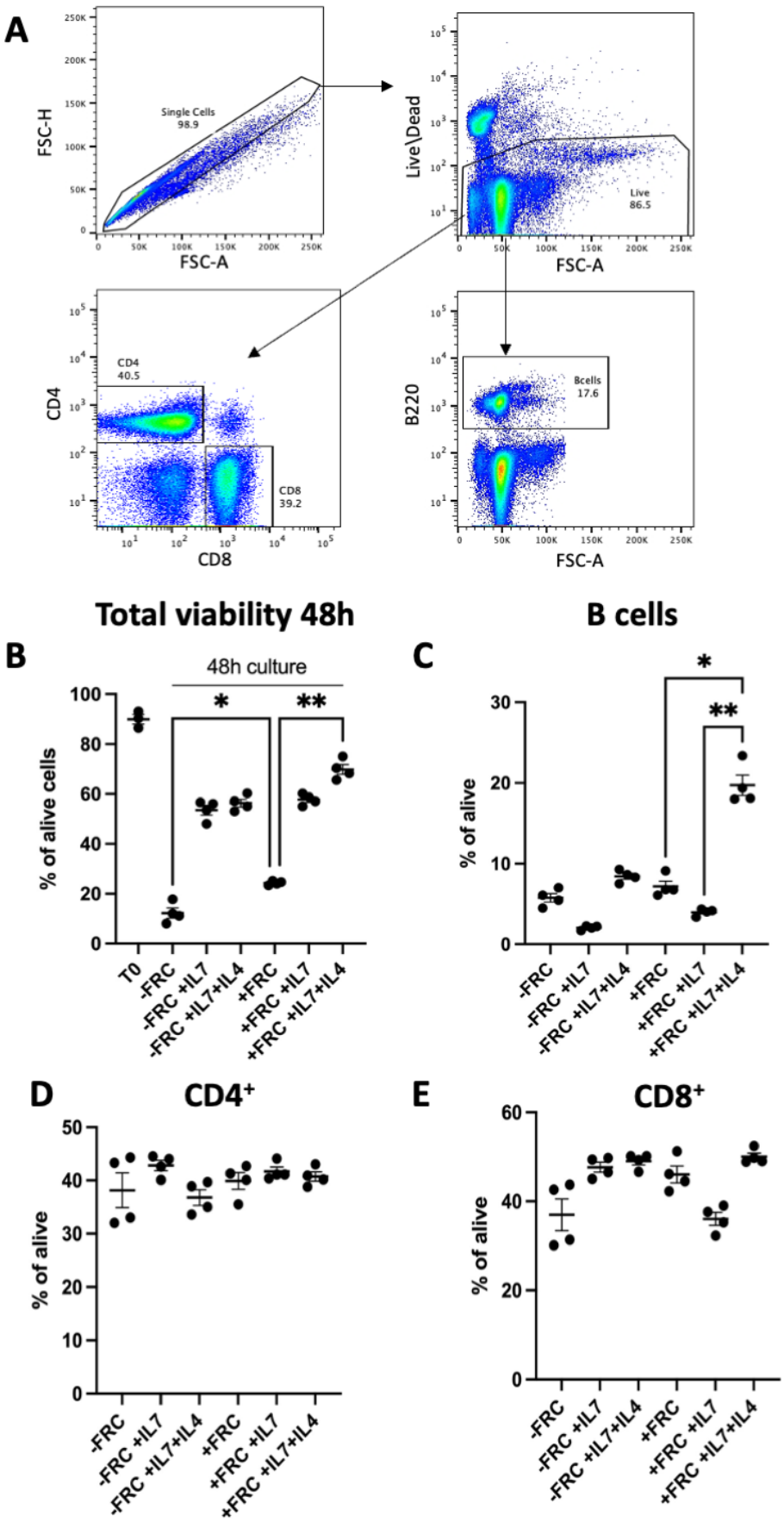
A
FSC-H
FSC-A
Single Cells
98.9
Live\Dead
Live
86.5
CD4
CD8
CD4
40.5
CD8
39.2
B220
Bcells
17.6
Total viability 48h
B cells
B
48h culture
% of alive cells
T0
-FRC
-FRC +IL7
-FRC +IL7+IL4
+FRC
+FRC +IL7
+FRC +IL7+IL4
C
% of alive
D
CD4+
E
CD8+

Figure 4.7 Lymphocytes viability optimization. A) Representative FACS plots showing the gating to identify the myeloid populations: $CD4^+$, $CD8^+$, $B220^+$. **B)** Flow cytometry quantification of total lymphocyte viability after 48h of 3D culture, in comparison to viability at T0, just after extraction from a lymph node. The test was performed with or without FRCs in the hydrogel, and with or without addition of IL-7 or IL-7 and IL-4 combined to the media. Quantification of individual populations shown as percentage of total live cells; $B220^+$ B cells **(C)**, $CD4^+$ T cells **(D)** and $CD8^+$ T cells **(E)**. Each dot (n=4) representing an independent experiment. Data are mean ± SEM. One-way ANOVA and Tukey's multiple comparisons tests were conducted. Ns = not significant ($p > 0.05$), * = $p \leq 0.05$, ** = $p \leq 0.01$, *** = $p \leq 0.001$, **** = $p \leq 0.0001$.

4.3.3 Factors do not diffuse in the central compartment

After optimizing viability of cells within the central compartment, it was essential to test whether factors that would be perfused through the channel reached the central compartment and with which speed. This is important also to evaluate which type of molecules are suited for the device and how long to perfuse to expect a cell reaction. To test this, a 70Kda fluorescent dextran solution was perfused through the channel while capturing images every 30 min for a total duration of 2h, then fixed with PFA for confocal imaging. Over this period, while a progressive fluorescent front was apparent in the GelMA compartment, no signal was detected in the central collagen compartment (Figure 4.8A). A neat front of fluorescence corresponding to the interface between GelMA and the collagen central compartment suggested that while factor within the perfusate could exit the vessel with convection through the hydrogel, they were not able to penetrate the collagen I gel organ-like central compartment after 2h of perfusion (Figure 4.8B).

This issue was further confirmed pharmacologically, using inflammatory cues. Static devices bathed in PMA received a strong activation stimulus to lymphocytes within the central compartment (Figure 4.8C). This was determined by CD69 expression which is one of the earliest markers to be upregulated in the lymphocyte activation process. In contrast, perfusion of PMA through the device vessel, failed to induce any upregulation of CD69 on immune cells which was consistent with the dextran assay (Figure 4.8C). Failure to deliver 'lymphatic' derived cues to the immune compartment identified this modification as unsuitable for further applications.

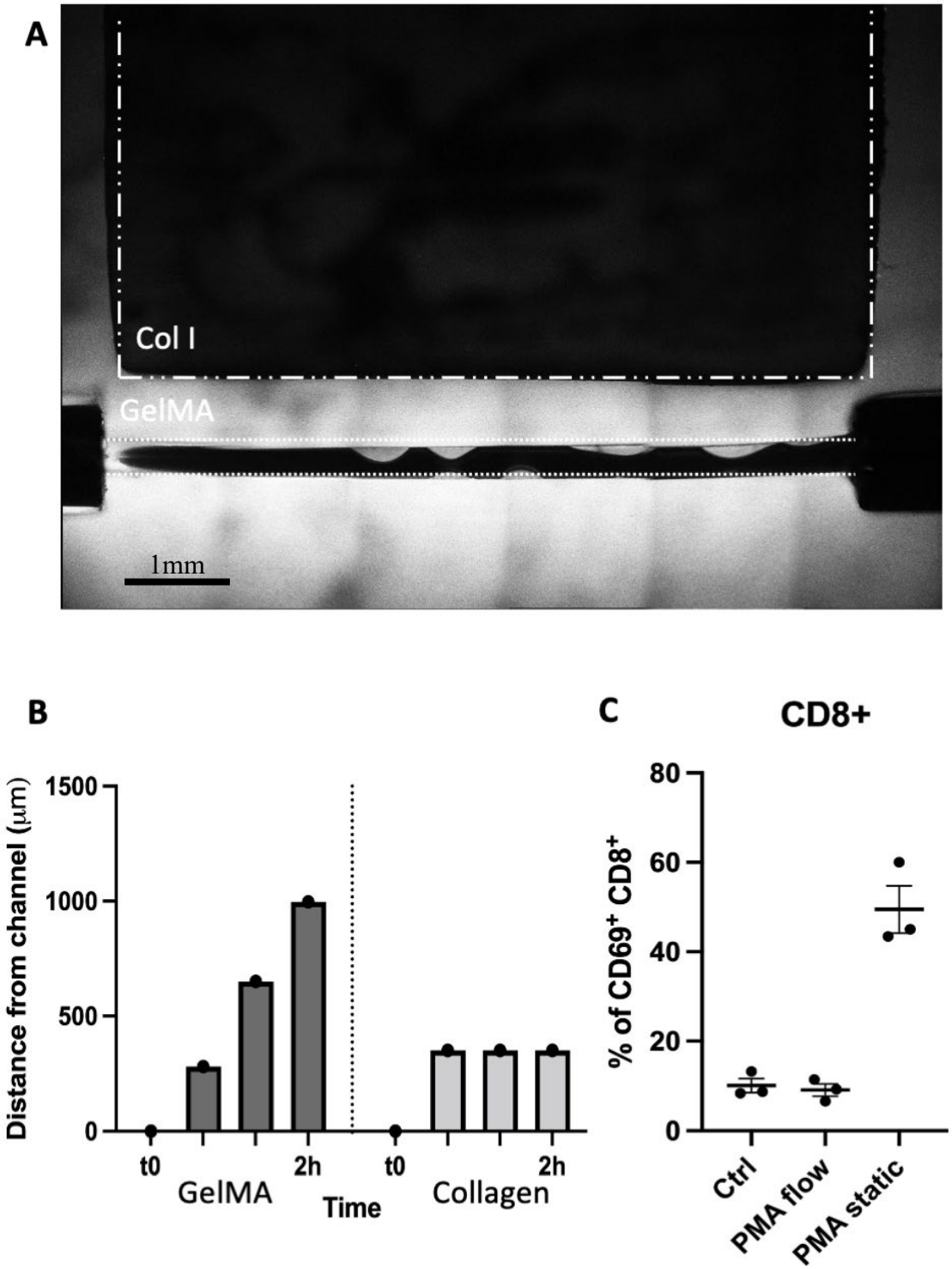

Figure 4.8 Perfused factors do not penetrate the central compartment. (A) Representative tile-scan image obtained with a confocal microscope shows the egress of 70kDa dextran from an acellular channel into GelMA but not Collagen I central compartment after 2h. Dextran shown in greyscale. Black represents no dextran within matrix. **B)** Quantification of fluorescent dextran front speed, calculated in the GelMA and at the device midpoint for 2h. **C)** Flow cytometry quantification of activated $CD69^+$ $CD8^+$ T cells after perfusion of PMA through the channel (PMA flow), or in static conditions bathing the gel (PMA static) vs. static control (ctrl). Each dot (n=3) representing an independent experiment. Data are mean ± SEM.

4.4 Single-hydrogel device

Learning that the set-ups to date exhibited significant limitations for a perfusable LN model, we further modified the device composition, which aimed to combine the previously observed effective characteristics into one single hydrogel: the ability of GelMA to make perfusable channels and the collagen I property to retain cell physiology. The same glass and PDMS base structure were used, but two vessels were here cast in a single hydrogel pour, which eliminated the central compartment and ECM interface (Figure 4.9A). Instead, the vessels were surrounded by and in intimate contact with lymph node cells. Initially, collagen I was mixed with large polysaccharides such as chitosan and Polyethylene glycol diacrylate (PEGDA) to improve its structural properties while enriching the hydrogel. However, for this application chitosan and collagen I were not found to be suited for successful and even mixing, while addition of PEGDA that had good mixability and convenient photocrosslinking like GelMA, allowed channels formation, but FRCs stretching was not observed after 48h and even at concentration as low as 1% v/v (Figure 4.9B).

Finally, a protocol to mix GelMA with collagen I was developed and commercial GelMA was used to minimize batch to batch variability and cell toxicity. With this last formulation, different concentrations were tested and a 5% GelMA, 1 mg/ml Collagen I hydrogel was found to be ideal for channel formation, physiological cell growth and flow application. Importantly, FRCs growing in 5% GelMA, 1 mg/ml Collagen for 48h, came out of rounded state, stretching and forming an extensive cell network (Figure 4.9C). We determined 7.5% GelMA to be the maximum limit to form reliable channels while also allowing stretching of FRCs in the matrix. On the other hand, a concentration of GelMA below 4% achieved good FRCs stretching but the ability to form channels and sustained flow were compromised (Figure 4.9D&E). Critically with GelMA 4% it was possible to form channels that were observable under the microscope but overall, when flow was applied, the devices were more prone to leakage of medium between the PDMS case and the hydrogel interface or blockage by hydrogel particles (Figure 4.9F). Cell viability in the different formulations did not present differences when tested with FRCs proving their live state although not able to move and stretch properly.

Therefore, from these preliminary studies the selected formulation used for further applications was 5% GelMA + 1 mg/ml Collagen I, due to its multiple favourable features (Table 4.1).

Following optimization of the hydrogel composition, we then set to enhance the reliability of flow in the device which still was subject to leakage of fluid at the interface between the inner wall of the PDMS case and the hydrogel, making the system not sealed. From the first PDMS device shown in figure 4.10, switching to a hydrogel-based device allowed easier and more extensive modifications to the custom-designed PDMS case for flow optimization. A first step was taken when a mould for the PDMS case was fabricated with holes on the sides for tubing housing (Figure 4.10B), however this was not enough to overcome the interface fragility. Then, another mould was designed but instead of making a mould to produce PDMS cases, it was directly 3D printed in series and mounted on glass slides (Figure 4.10C). This mould was designed with larger holes on the sides to host small tubing pieces protruding inwards too, with the idea of lowering the fluid pressure at the interface between hydrogel and PDMS. This approach turned out successful for sealed flow application, but the thermoplastic material used for the mould did not allow optimal sealing to the glass. Finally, a mould was designed with precasted tubing adapters on the side but in PDMS and indeed allowed consistent perfusion without leakage (Figure 4.10D).

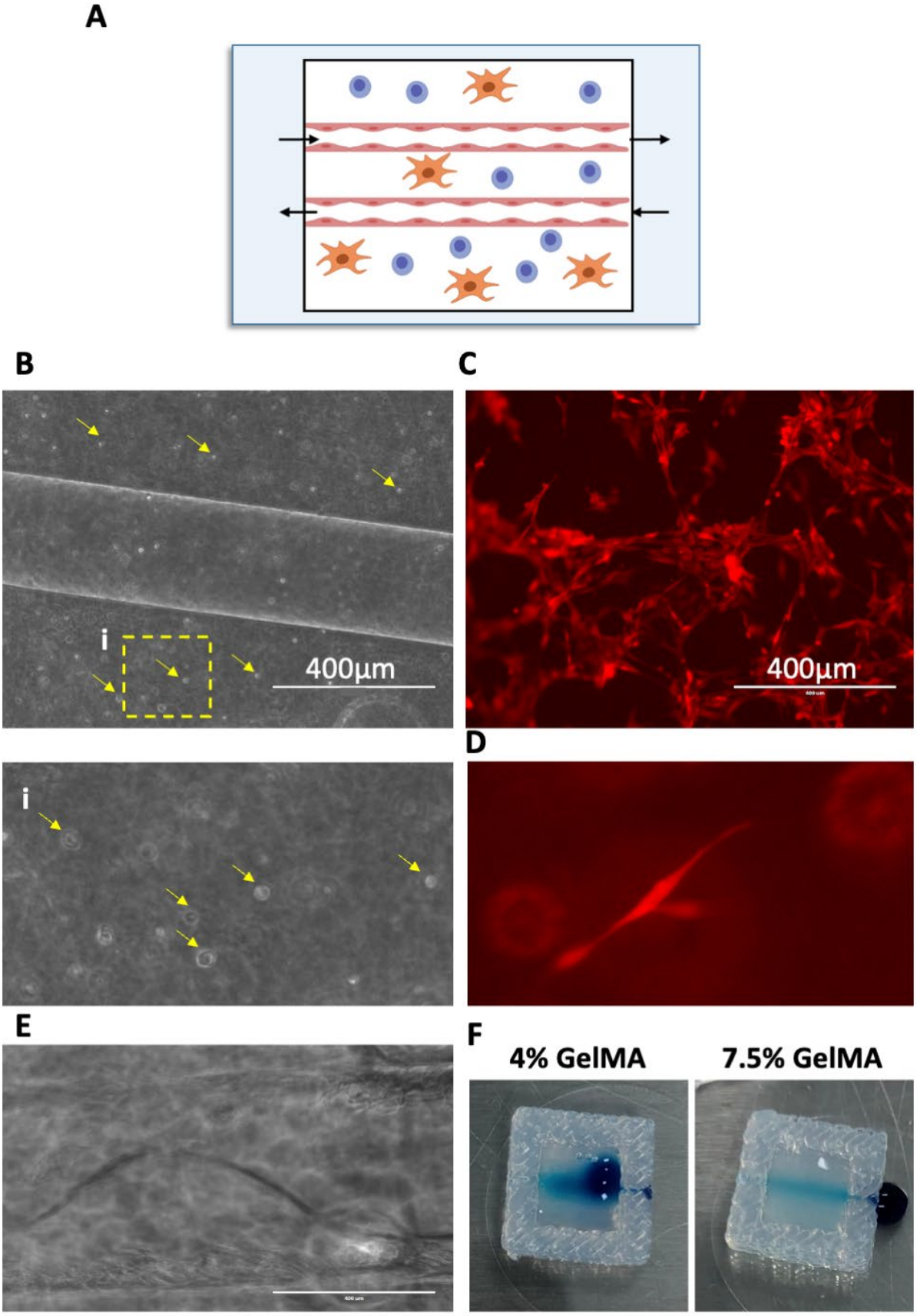
A
B
C
i
400µm
400µm
D
i
E
F
4% GelMA
7.5% GelMA

Figure 4.9 Single-hydrogel device. A) Top view representation of the new single-hydrogel device. Two needle cast lymphatic vessels are embedded in a matrix laden with FRCs and lymphocytes. **B)** Brightfield image of the vessel hydrogel interface in a device fabricated with 2 mg/ml collagen + 1% PEGDA, channel and FRCs that after 48h did not come out of their round shape (FRCs indicated by yellow arrows). Scale bar = 400µm. Inset i) closeup of non-stretched FRCs in the matrix **C)** representative confocal image of a 1mg/ml collagen gel + 5% GelMA hydrogel laden with stretched red TRCs after culture for 48h. Scale bar = 400µm. **D)** Fluorescent image of a stretched TRC in 1mg/ml collagen gel + 4% GelMA and **E)** in the same device a failed collapsed needle casted channel. **F)** Images showing devices fabricated with either 4% or 7.5% GelMA in which flow of a blue dye was perfused with the peristaltic pump. In 4% GelMA is observable the blue dye accumulating on top of the device.

Table 4.1 Table summarizing main hydrogel compositions explored and their main features.

GelMA	Collagen I	PEGDA	Flow application	FRCs stretching	Channel formation
	2.5mg/ml		no	yes	not good
5%			not good	no	not good
8%			good	no	good
10%			very good	no	good
4%	1mg/ml		not good	yes	good
5%	1mg/ml		good	yes	good
7.5%	1mg/ml		very good	yes	very good
	2mg/ml	1%	n/a	no	good
	2mg/ml	2%	n/a	no	good

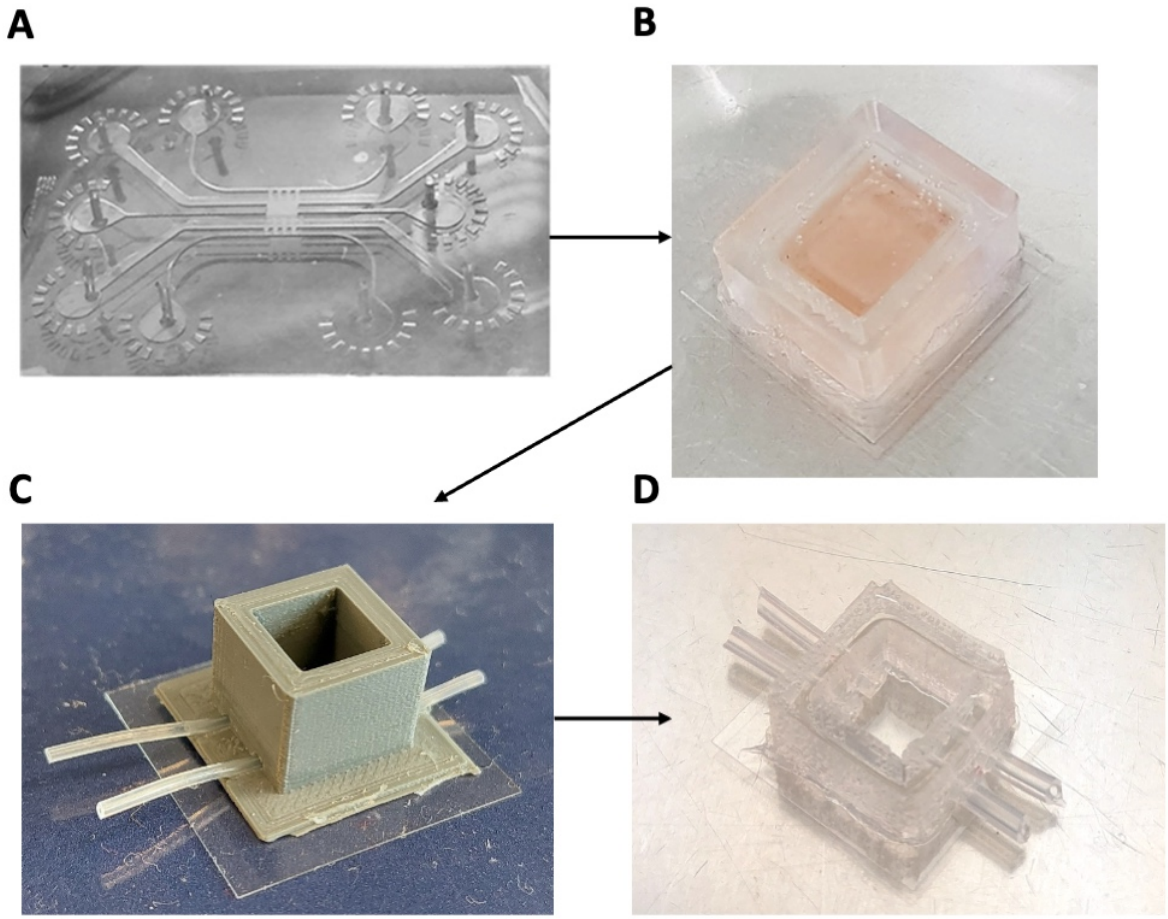

Figure 4.10 The device structure was optimized for flow application. A) PDMS-based microfluidic chip. **B)** Hydrogel-based device with a central compartment. Dimensions: 1cm x 0.8cm x 1cm. **C)** 3D printed case in PLA, with holes on the sides to house tubing adapters to facilitate flow application. Dimensions: 0.8cm x 0.8cm x 1cm **(D)** Final version of the PDMS case built with tubing adapters. Dimensions: 0.8cm x 0.8cm x 1cm.

4.4.1 Matrix characterization

To further characterise the blended hydrogel formulations, GelMA/collagen blends and GelMA only hydrogels were imaged with SEM for comparison (Figures 4.11 A-D). Blends containing GelMA concentrations of 4%, 5% and 7.5% were tested. GelMA-only gels were tested at 5% or 8%. SEM images analysis revealed a porous conformation in all samples, but GelMA-only formulas (Figures 4.11 A&B) displayed considerable structural differences compared with blends (Figures 4.11 C&D) that were furtherly analyzed. Quantification of hydrogel structures confirmed that indeed, GelMA-only gels contained significantly smaller pores than blends (Figure 4.11E), suggesting that pore size could be a crucial characteristic to allow immune movement through the matrix, and fibroblast stretching in 3D, together with the

presence of a fibres network. It was determined that in GelMA/collagen blends with 4% or 5% GelMA concentrations, the fibres network between pores presented with much thinner and longer fibres than pure GelMA, potentially serving as optimal anchoring points for FRCs that would then pull and remodel more easily the matrix (Figure 4.11F).

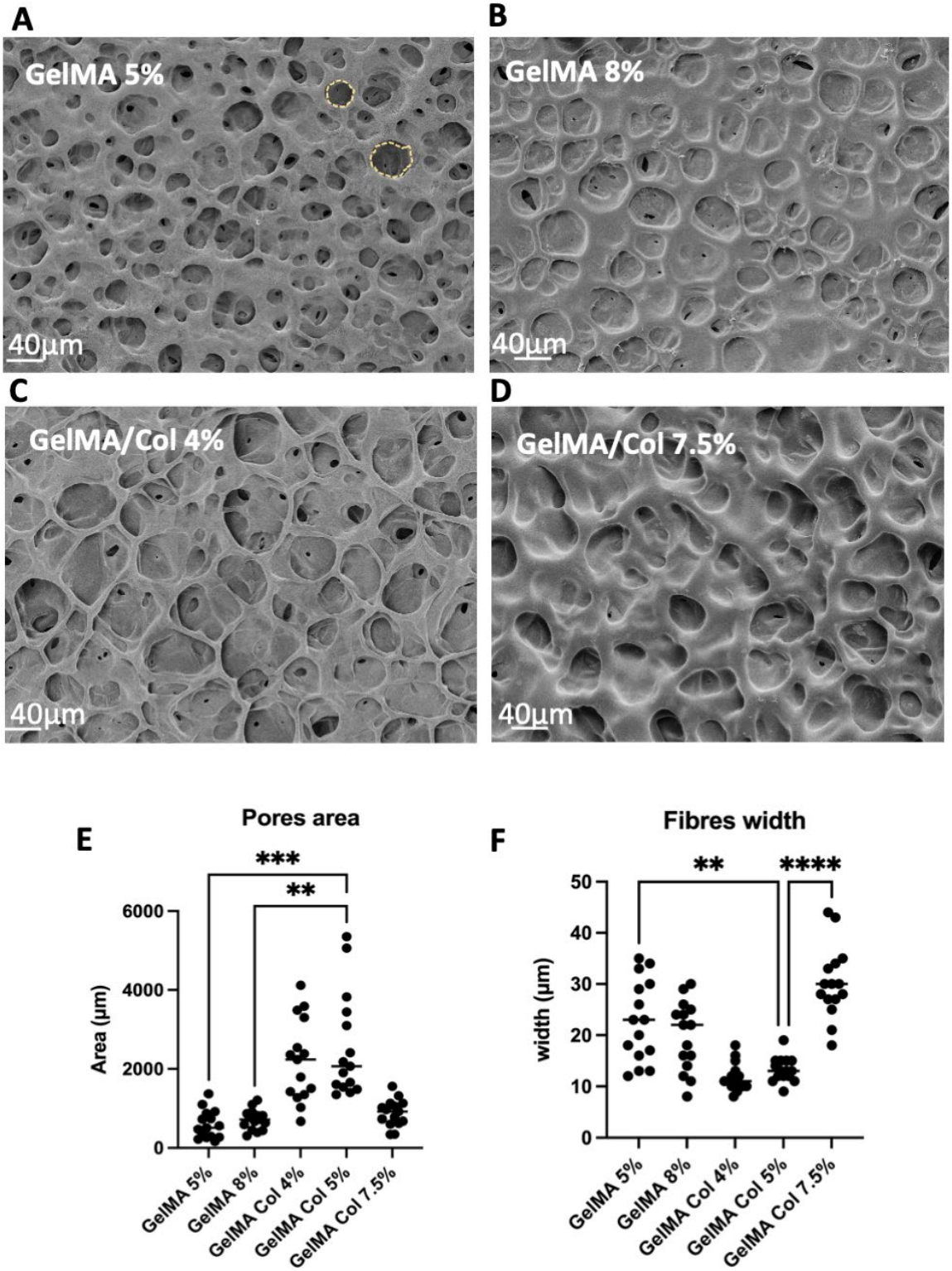

Figure 4.11 Scanning electron microscope analysis. SEM images of GelMA 5% **(A)**, GelMA 8% **(B)**, GelMA/Col 4% **(C)** and GelMA/Col 7.5% **(D)** prepared by freeze-drying and gold coating. Scale bar = 40μm. **E) F)** Quantification of pore area and fibers width within the gels using ImageJ. Pore area measured the large opening visible, as observed by the dotted yellow line in **(A)**. Fiber width was measured approximately at the midpoint of each fiber. Each dot (n= > 15) representing a single measurement taken from at least 3 fields of view. Images taken in the department of Engineering Cambridge by Alex Casabuena. Data are mean ± SEM. One-way ANOVA and Tukey's multiple comparisons tests were conducted. ns = not significant ($p > 0.05$), * = $p \leq 0.05$, ** = $p \leq 0.01$, *** = $p \leq 0.001$, **** = $p \leq 0.0001$.

In line with this, additional characterisation of the collagen component of gels was performed using second harmonic generation (SHG), a technique that allows label-free collagen fibres imaging in a 3D hydrogel. Immediately after crosslinking, neither GelMA-only hydrogels nor GelMA/collagen I blends, formed detectable collagen fibers. However, in FRC-laden hydrogel blends cultured for 48h it was possible to observe collagen fibrils, as shown in Figure 4.12A. Higher magnification of single cells revealed individual fibres distant from cells, and denser bundles of collagen fibres wrapped around FRCs at the anchoring points. This may be due to cells actively remodelling their surrounding environment to form collagen lined conduits or moving within the matrix (Figure 4.12B&C). Collagen lined conduits serve as an efficient route for antigen delivery and as a scaffold for cell trafficking. Indeed, formation of FRC directed conduit-like networks in our 3D culture could explain lymphocytes behaviour observed in live-cell imaging, where cells preferentially travel along FRC structures (Figure 4.12D).

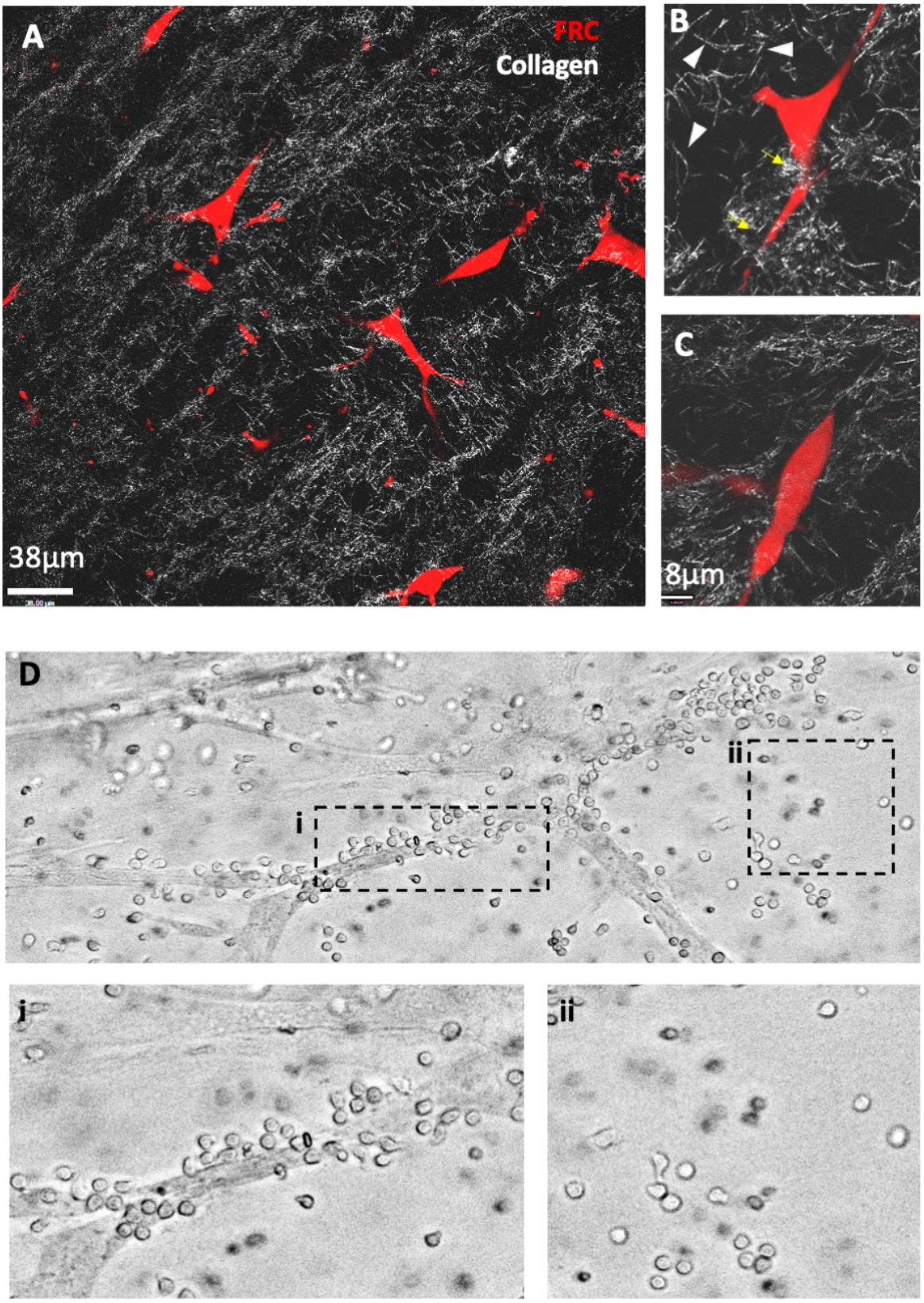
A
FRC
Collagen
38µm
B
C
8µm
D
i
ii
i
ii

Figure 4.12 Second harmonic generation analysis. (A) SHG image of a TRC-laden GelMA/collagen blend cultured for 48h showing collagen fibers (in white) and TRCs (in red), 20x magnification. Scale bar = 38µm. **B) C)** High power micropgraphs (40x magnification) showing single TRCs with collagen fiber clustering. Indicdial fibres (arrowhead), clusters (yellow arrow) Scale bar = 8µm. **D)** Brightfield image showing stretched FRCs in 3D culture and preferential clustering of lymphocytes along their protrusions (highlighted by yellow arrows). Inset i) close up of large number of lymphocytes in contact with FRC, ii) fewer lymphocytes distant from FRC. SHG images taken with Dr Andrew Trinh.

4.4.2 GelMA/Collagen blends maintain their shape during fibroblasts culture

Collagen *in vivo* and in hydrogels has inelastic properties therefore shrinks when cultured with fibroblasts that actively pull their fibres, losing the original shape, and potentially detaching from its substrate in the process. This property makes collagen particularly unsuited for longer-term tissue engineering applications, especially those containing fibroblasts as in this hydrogel-based device. We noted that in some cases with the central compartment device, in addition to not receiving perfused cues (Figure 4.8C), the collagen gels would also detach from GelMA following contraction.

Therefore, we tested gel behaviour of the blends, in terms of contraction. Gels were laden with $4x10^5$ FRCs/ml and cultured either in 2mg/ml collagen I gels or in GelMA/collagen blends at 2% and 5% GelMA, and contraction relative to T0 was quantified after 48 hours (Figure 4.13A). Collagen I gel laden with FRCs contracted as expected, and here maintained only 25% of the initial area. The formulation of 2% GelMA in collagen gel, also significantly contracted However, when 5% GelMA was incorporated no contraction was observed (Figure 4.13B). Hence, 5% GelMA/collagen I hydrogel was selected to conduct further experiments being suitable for long-term cultures and allowing both formation of channels and FRCs stretching.

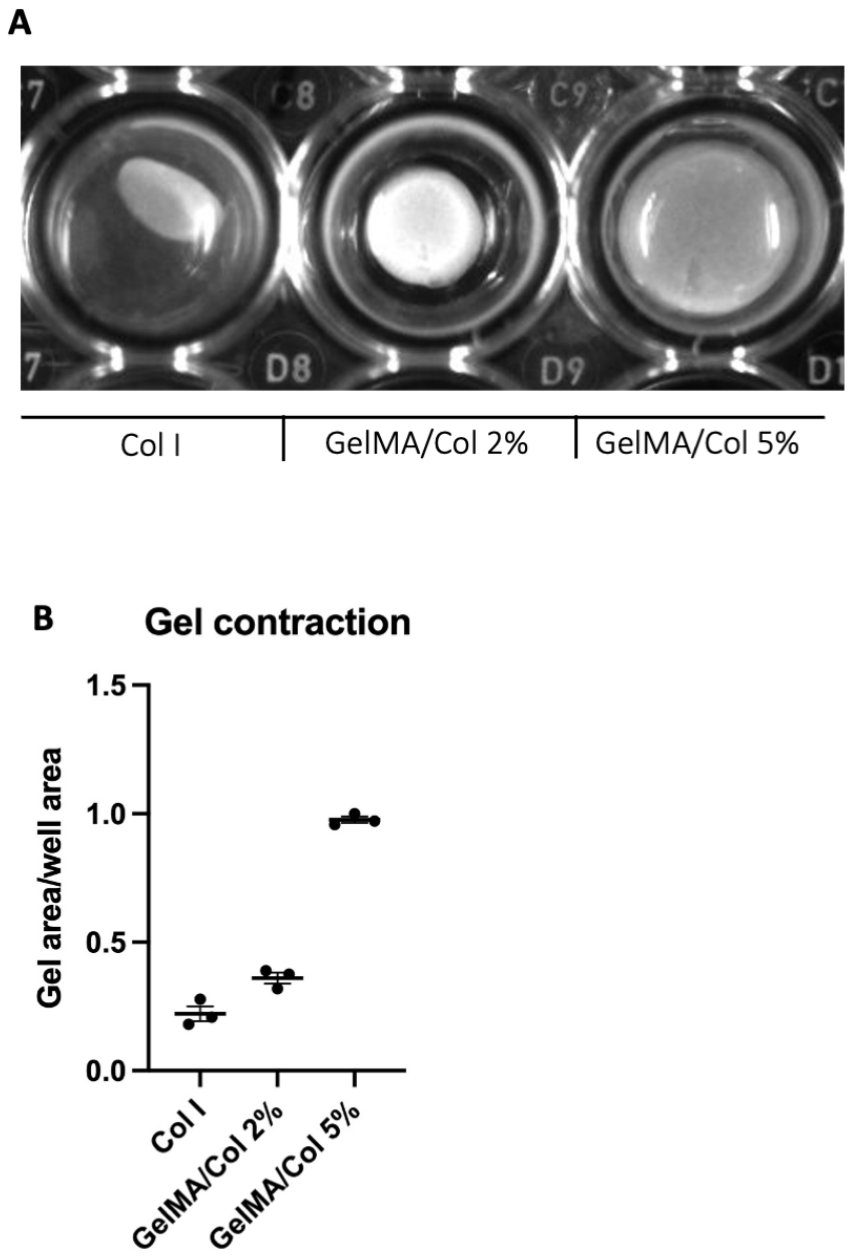

Figure 4.13 GelMA/collagen blends do not contract following FRCs culture. (A) Representative image of different hydrogel formulations (Collagen I, GelMA/collagen 2% and GelMA/collagen 5%) depicting contraction, after 48h of culture **B)** Quantification of Gel contraction showing gel area/well area ratio, calculated manually with ImageJ. Each dot (n=3) representing an independent experiment. Data are mean ± SEM.

4.4.3 Factors diffuse from the channel into GelMA/collagen

With an optimized matrix, we next investigated whether unlike previous versions, factors would actively egress from the channels into the cell laden hydrogel. A repeat of the flow set-

up in which 70KDa dextran solution was perfused through one of the channels showed fluorescent signal coming out of the channel immediately after perfusion and, without the presence of an interface, a fluorescent front progressed evenly to penetrate deep into the hydrogel Figure 4.14A. The fluorescence front was imaged with a live cell microscope and the speed of diffusion was calculated as the images showed that after one hour of perfusion the dextran travelled 550µm from the channel edge (Figure 4.14B). Thus, the updated, single pour approach supported a channel, appropriate cell behaviour and flowed factors would be able to bathe LN constituents as *in vivo*.

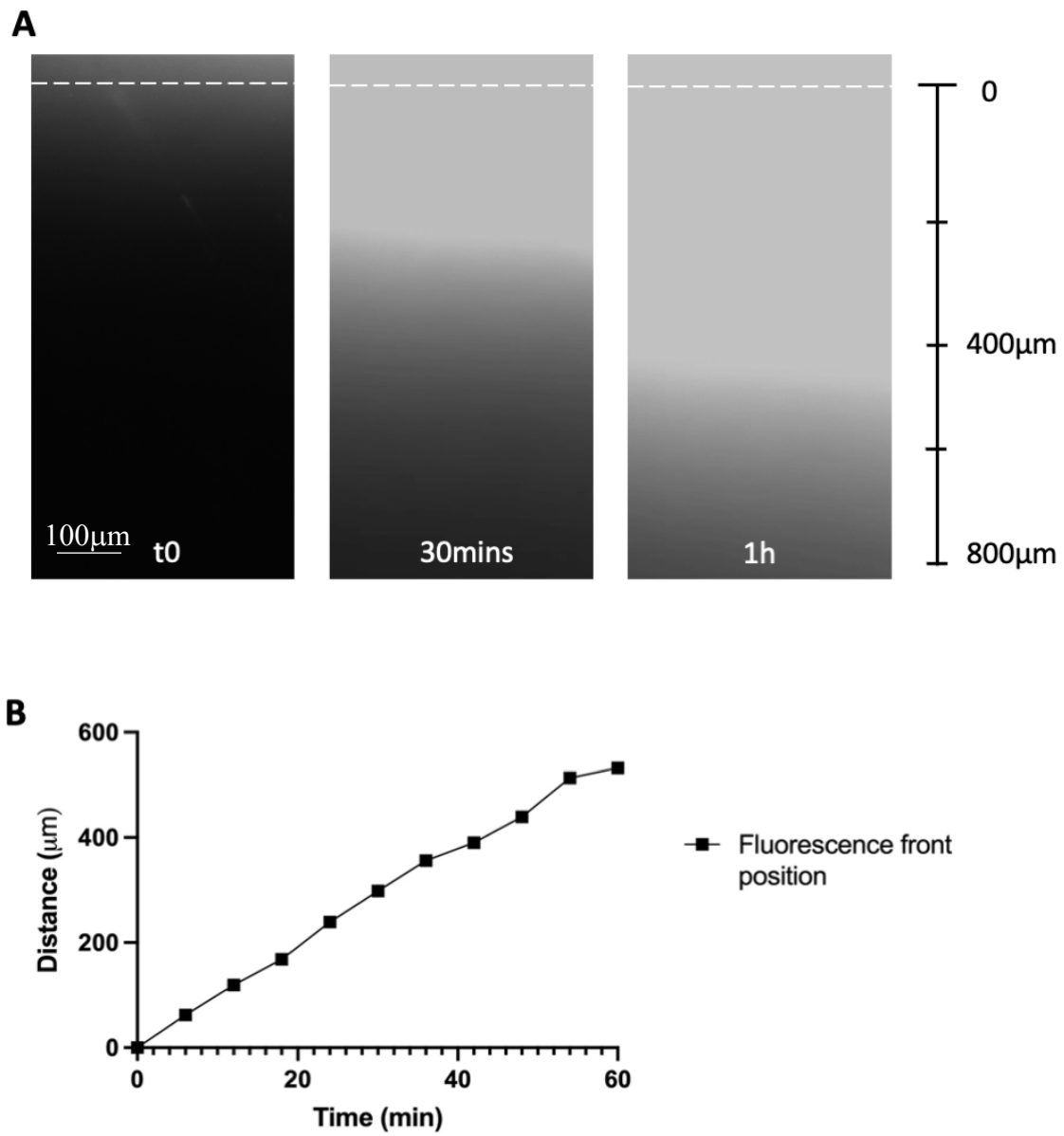

Figure 4.14 Factors are transported in the single-material hydrogel device. A) Images obtained with a confocal microscope shows the advancing front of 70kDa dextran (white) from an acellular channel through the GelMA/collagen blend at t=0, after 30min and 1h of dextran perfusion. White dotted line represents the channel edge and on the right the ruler to show the fluorescence front. **B)** Graph showing fluorescence front distance from the channel over time (on x axis).

4.4.4 Compartmentalization and LN architecture

Although we found good culture conditions for primary lymphocytes and FRCs in a 3D environment, a limit of the model was the overall architecture. *In vivo* organs are never homogeneous cell mixtures but maintain sophisticated ultrastructures where different types of cells are specifically positioned to perform a function. In the case of lymph nodes, compartmentalization is central to their function, where B cells follicles and T cells zone reside in spatially distinct areas and where most of the cellular crosstalk during activation and antigen presentation occurs at the interface between these two regions.

With this in mind, we set to impose the macro architecture of the LN within the device and form B cell follicle-like structures. To achieve this, spleens from CAG.egfp mice were used and B cells were purified by magnetic labelling. This gentle purification method was quick to perform and gave high purity population of B cells (ca. 90%) (Figure 4.15A). The B cell-enriched population was then used to create follicle structures while the rest of the splenocytes was used to compose the T cell zone. To make the 'follicle' B cells were suspended with collagen I/GelMA hydrogel and, while still in liquid state, blobs were deposited in the device and quickly photo crosslinked. The remaining B cell depleted immune cells (Figure 4.15B) were then mixed with TRCs, deposited on top of the blobs and the whole device was photocrosslinked for a second time. Figure 4.15C depicts dense green B cell follicle architecture formation amongst T cells and FRC. These structures were then analyzed by live imaging. B cell movement was absent inside the follicles, and lymphocytes and FRCs of the T cells zone were motile, but wrapped around the follicles, without being able to penetrate follicles (Figure 4.15D). This suggested that by crosslinking, the formation of a hard interface between hydrogels occurred to prevent cross-compartment interactions (Figure 4.15E).

A

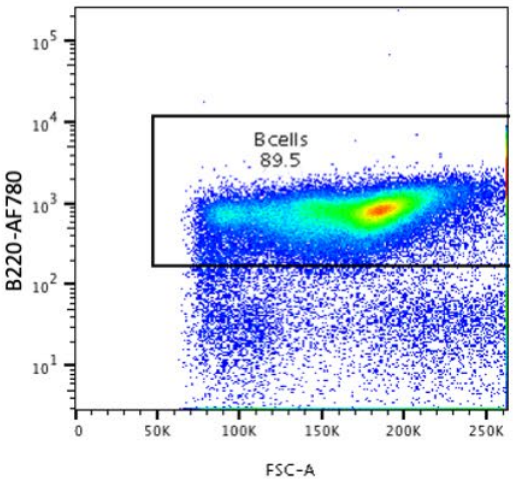
B cells
89.5
B220-AF780
FSC-A

B

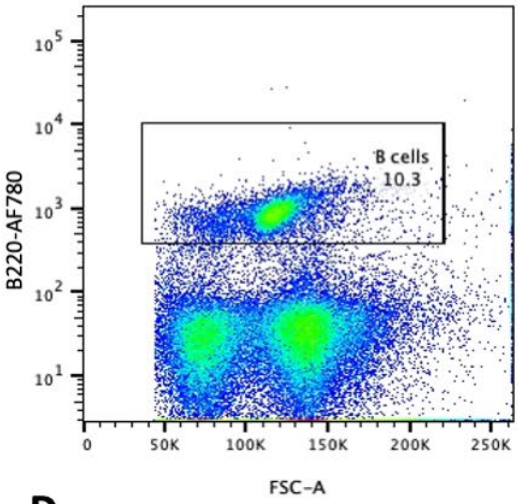
B cells
10.3
B220-AF780
FSC-A

C

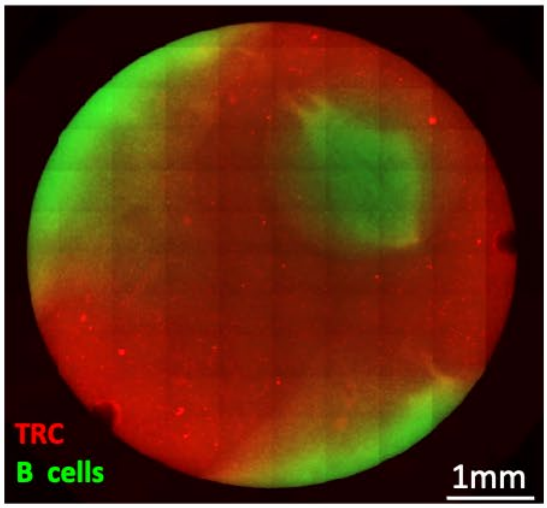
TRC
B cells
1mm

D

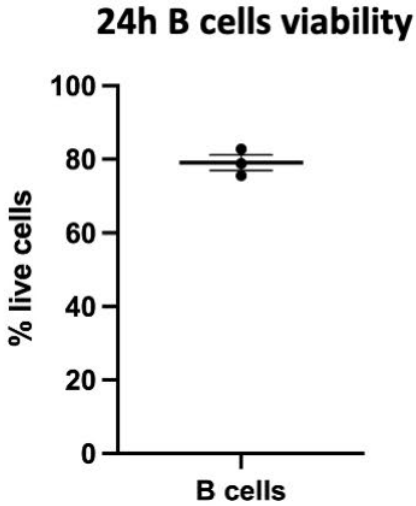
24h B cells viability
% live cells
B cells

E

Figure 4.15 LN architecture optimization. A) Enrichment of B220$^+$ B cells after magnetic purification, showing the B cell fraction in the purified portion and **B)** in the leftover portion containing mostly T cells. **C)** Tilescan of a whole well with immune compartmentalization after first crosslinking the B cell zones then the whole gel; B cell follicles in green and TRCs in red mixed with unlabeled lymphocytes from the negative fraction. Scale bar = 1mm **D)** Flow cytometry measurement of live B cells after follicles deposition and 24h culture. **E)** Merged brightfield image showing a defined interface between the B cell follicle (green) and the T cell zone laden with TRC (orange) after 24h of culture. Cells of the T cell zone were unable to penetrate the follicle to interact. Data are mean ± SEM.

To overcome this solid interface and obtain an interface-free system, we generated B cells spheroids. As lymphocytes that grow in suspension are not able to form spheroids spontaneously (Figure 4.16A), FRCs and B cells were mixed to form spheroids using the hanging drop method thereby simulating the B cell-supporting cell environment. To do this, B cells from CAG.egfp spleens were isolated and mixed with non-labelled FRCs at 1:10 and 1:50 FRCs to B cells ratio. While as expected B cells alone did not form a stable spheroid structure and crumbled during the harvest step, co-cultures formed spheroid structures (Figure 4.16B). These were then picked and cultured inside collagen I/GelMA hydrogel laden with TRCs, and T cells as described previously (Figure 4.16C), which was then crosslinked in one step. CAG.egfp labelling of B cells enabled easy identification of the spherical follicles structures, and it was possible to arrange multiple spheroids in each gel. Live-imaging data from these cultures showed FRCs in the spheroids stretching outwards getting in contact with TRCs, but no B cells movement was observed suggesting that, during the spheroids production process, most of the B cells were lost leaving a layer on cells associated with the FRCs hence making them positive for fluorescent signal. As this method did not turn out to be useful to our aims, it was eventually abandoned.

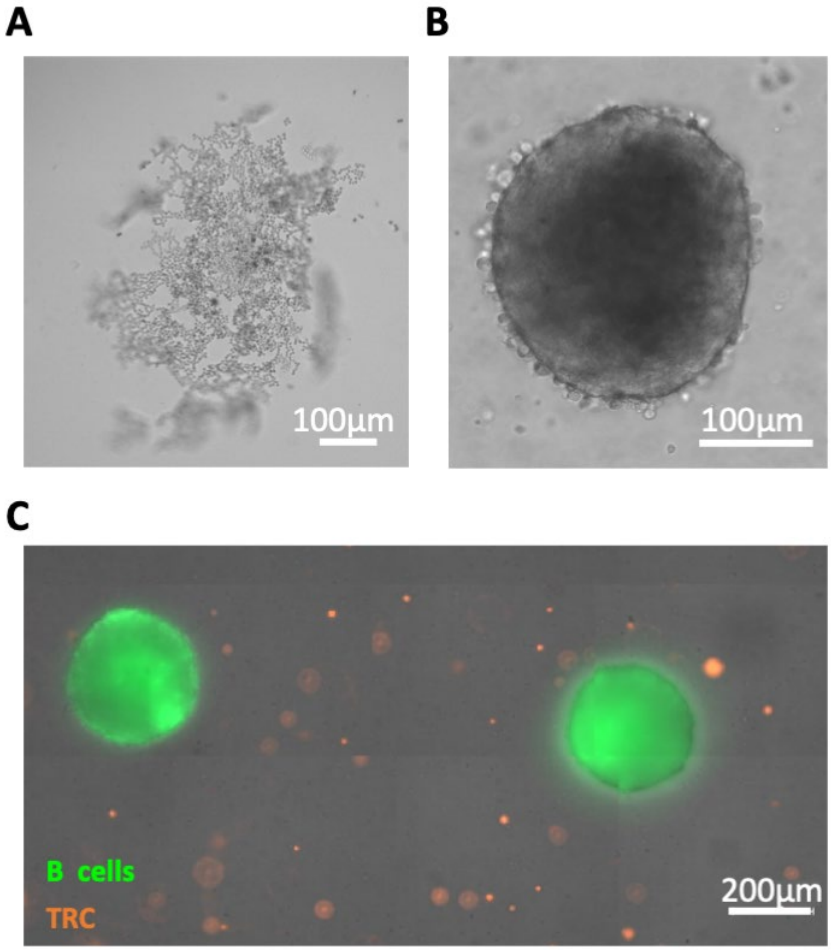

Figure 4.16 FRC/B cells co-culture does not form representative spheroids. (A) Brightfield image of an FRC/B cell (1:50 ratio) spheroid obtained after 24 hours with hanging-drop technique. Scale bar = 100µm **B)** Tilescan showing B cell/FRC spheroid follicles (in green) deposited in a hydrogel laden with lymphocytes and TRC (in orange). Scale bar = 200µm.

Finally, a new attempt was made to compartmentalize B cells into follicles with a similar approach to the first method described. Analogously to the previous method, B cell follicles were deposited first and then covered with the T cell zone components, however, instead of immediate photocrosslinking of the follicles resulting in the formation of a hard interface, thermal gelation property of collagen I/GelMA was instead exploited. The B cell/unlabelled FRC-laden hydrogel was loaded into a syringe and chilled at 4°C for 10 minutes after which, cool deposits were extruded into an empty device before surrounding them with the liquid T/labelled FRC cell-laden hydrogel solution. The device was then carefully put in an incubator to let the solid deposits start melting and merging with the surrounding solution, after 5 minutes

at 37°C the hydrogels were immediately photocrosslinked for 10 seconds. Figure 4.17A shows that this method resulted in the successful formation of two distinct cellular compartments with clear cell separation, similarly to a lymph node (Figure 4.17B), but without a hard interface (Figure 4.17Ai). Having confirmed this, we then went on to label T cells with a blue cell tracker dye, to further distinguish between cell compartments (Figure 4.17C), and devices were live-imaged for 24h. Movies showed overall increased motility of cells in the follicles compared to previous attempt, TRC stretching and B cell-T cell interaction at the follicle border.

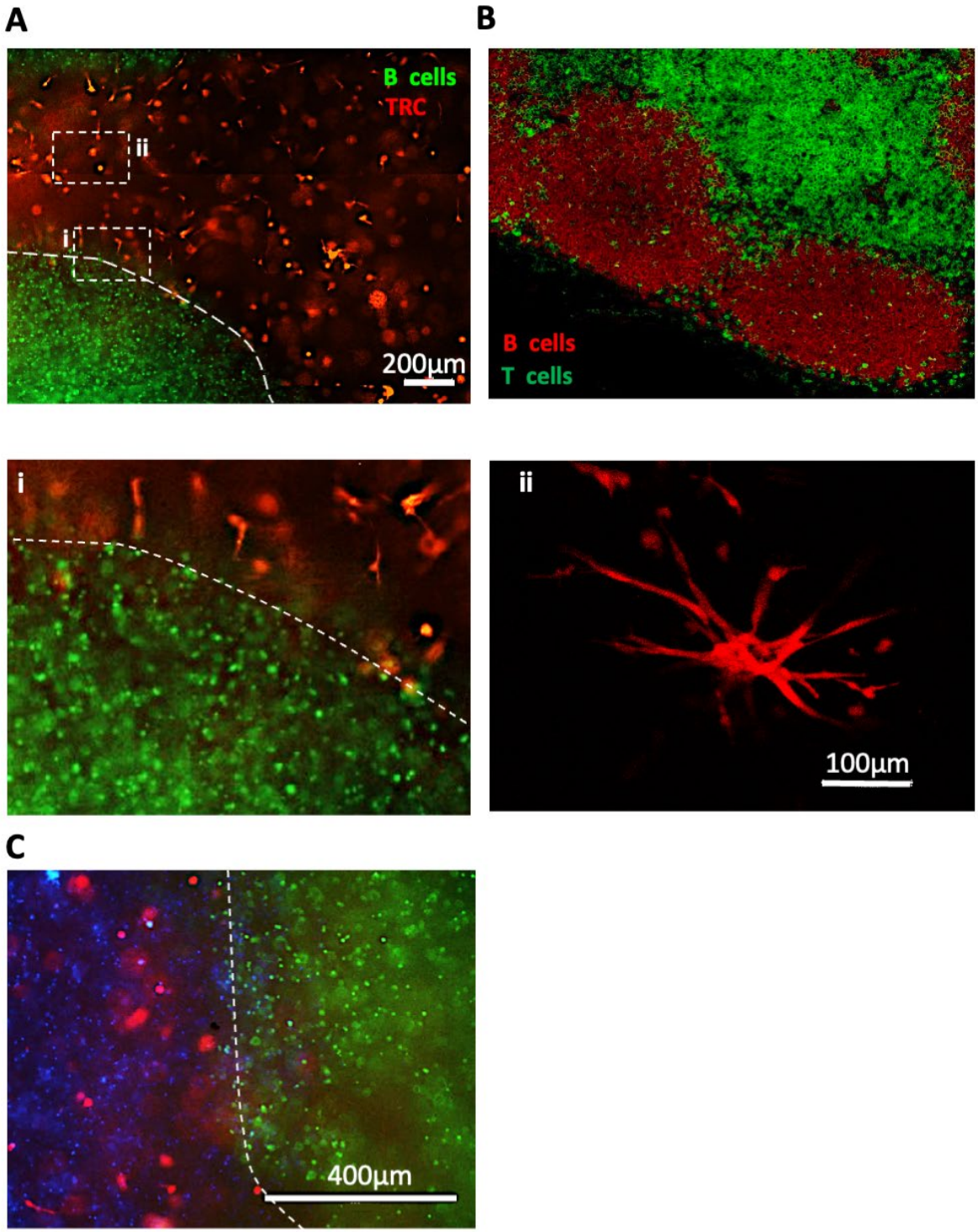

Figure 4.17 B cell follicle-like structure formation. (A) Representative confocal image showing formation of B-cell-like structure (in green, with unlabelled FRC) surrounded by a T cell zone laden with TRCs (in red). Dotted line denotes the T-B boundary. Scale bar = 200µm. **B)** Confocal image of a murine lymph node showing B cell follicles and clear T-B cell interface. B cells (B220, in red) and T cells (CD, in green)**.** Inset i; Closeup of the T-B boundary and inset ii; confocal image (40x magnification) showing single TRCs stretched and reaching into the hydrogel. Scale bar = 100µm.
C) Closeup of the interface between the extruded B cell-like structure (in green), surrounded by T cell zone laden with TRCs (in red) and T cells (live labelled in blue, stained with Hoechst). Scale bar = 400µm.

4.4.5 Conduits can be carved in the hydrogel via laser ablation

In vivo, the subcapsular sinus is connected to the T cell cortex via conduit structures (Figure 4.18A). This facilitates rapid delivery of small soluble cues such antigen or cytokines and growth factors into the deeper node where they can be received by dendritic cells and T cells. Therefore, a further step in the optimization of the device was taken to mimic these structures and assist deep perfusate percolation into the cell laden gel. To do this, a laser ablation technique was used. The laser capture microdissector is equipped with a regular microscopy optical system which, in parallel, has a laser to allow specific and controlled ablation in the area of interest. Here, the two main channels were needle-casted as previously described but additional carved microchannels were ablated by drawing them first through the microscope interface (Figure 4.18B). The system was calibrated changing laser power and beam speed of travel on the xy plane to obtain the most consistent channels. In figure 4.18B&C carved microchannel networks of carrying complexity and connectivity which stem from the main channel can be achieved. These were orientated in the direction of flow to maximise fluid flux into the microchannel conduits. To then probe whether the channels that were visible through brightfield microscopy were connected to the main channel's lumen and could receive perfusate derived material, green fluorescent microbeads were perfused through the main channel. Green fluorescent beads were rapidly detectable coming out into the carved microchannel after short perfusion (Figure 4.18D) confirming the presence of a functional connection to the 'sinus' channel.

Finally, we combined laser ablation with the previous steps the create a sinus channel linked to a T cell laden cortex and B cell follicle-like structures. Therefore, after deposition of the follicles the laser was used to precisely carve microvessels around them. This did not impact cells within the gel, and microbeads were used to show infiltration in the lymph node structure (Figure 4.18E).

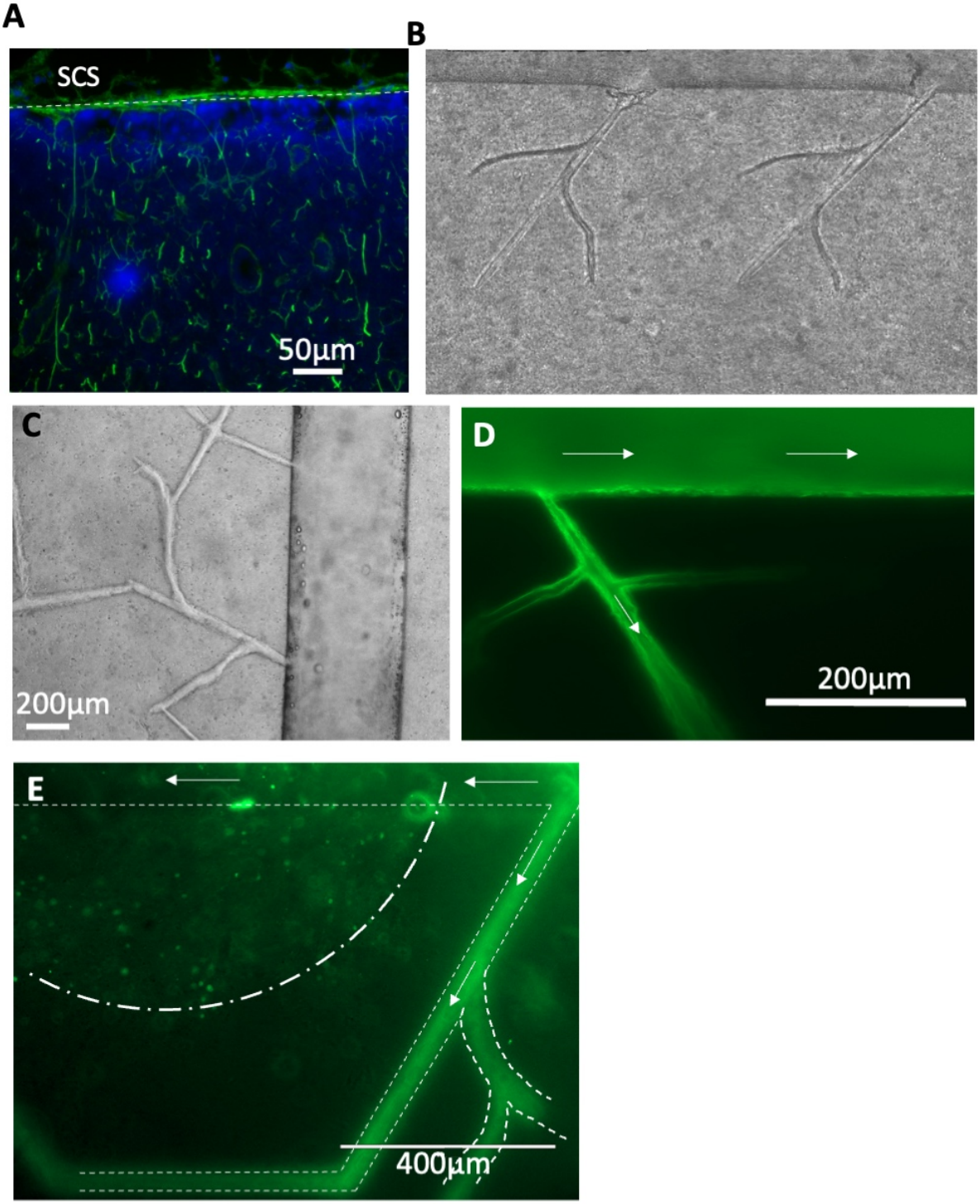

Figure 4.18 Conduits were successfully laser-carved via photoablation. A) Confocal image of an *ex-vivo* murine LN section showing the SCS and conduits (in green, staining Collagen I. **B)** Brightfield image showing repeated microchannels pattern along the main casted channel. **C)** Laser-carved vessels network into the cell-laden hydrogel connected to the main casted channel. Microchannel width obtained ca. 10µm. Scale bar 100µm. **D)** Vessel with laser-carved conduit after perfusion of 1µm fluorescent microbeads. Scale bar 200µm **E)** Fluorescent microscopy image showing laser-carved ramifications from a casted channel perfused with 1µm microbeads, next to an extruded B-cell follicle-like structure. Scale bar 400µm.

4.5 Summary

Here, I have shown the process for the creation of a murine hydrogel-based device of a lymph node containing lymphocytes and a stromal compartment represented by FRCs. Starting from a PDMS-based device, different limitations encountered have been tackled and optimized to obtain a device containing viable lymphocytes, cell compartmentalization and high level of complexity (Figure 4.19). First, I focused on cell viability of the different cell types included in the device to enable long-term culture. The majority of LN-on-a-chip model are produced by incorporating lymphoid tumour cell lines because of cell growth ease that however compromise phenotypical characteristics. In this model, external cytokines and a stromal population were essential elements for long-term cell growth. Then I focused on creating cell compartmentalization in the hydrogel gel to recreate the presence of B cell follicles, segregated from the T cell zone, as observed in *in vivo* LN. Finally, to increase structural complexity and maximise delivery of antigen deeply into the device I have created conduit structures by photoablation. Following these optimization steps, I then focused on applying the model to different applications, focusing on cells reactions to external stimuli and attempting to model the LN in the presence of cancer.

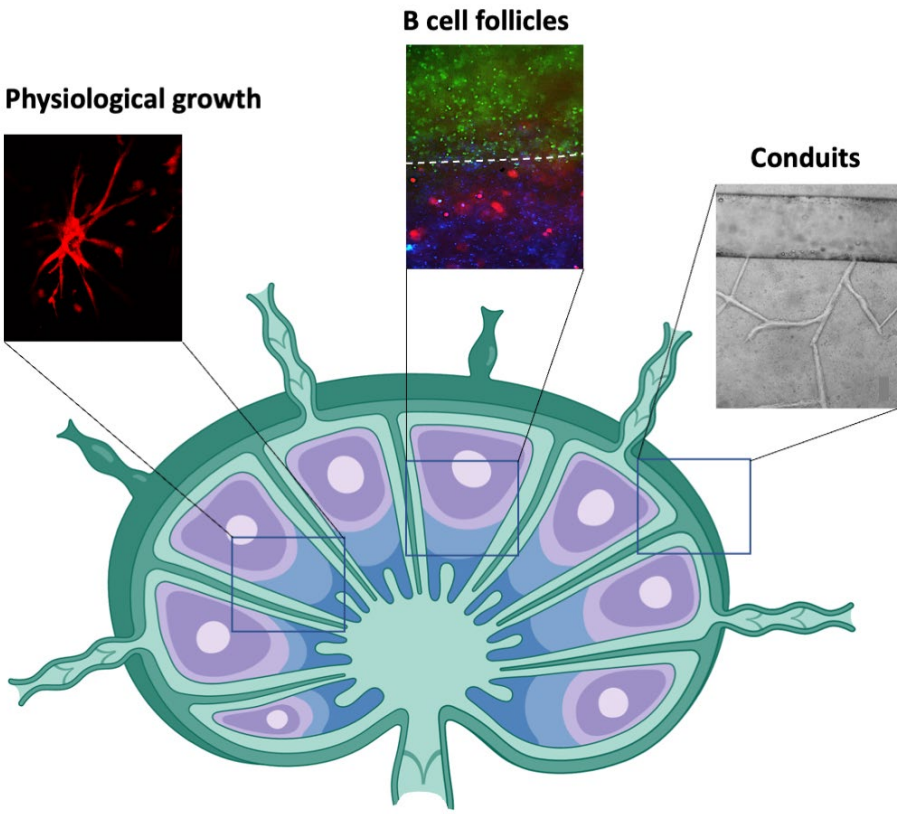

Figure 4.19 The LN-on-a-chip device recapitulates key architectural characteristics observed *in vivo*.

CHAPTER 5

APPLICATIONS OF THE MODEL

5.1 Introduction

Many attempts have been made in recent years to model the lymph node on-chip but none of the existing models so far succeeded in representing a complete tool, suited for multiple applications, either because of the fabrication technique or the cell types included. Most of the models so far have seen a limited number of cell types from the lymph node, restricting its applications, or have been created with immortalized cell lines that fail to fully reproduce morphological and functional characteristics of primary cells [232]. In this device we have used primary cell cultures from murine spleens, however, the model could be adapted to primary human cultures obtained either from either human blood or leftover tissues from a tonsillectomy. In this chapter, data from application of the latest derivative of the device are presented. The reductionist nature of the device allowed us both to measure molecular changes and to track cells interactions through live imaging, making this model open to multiple type of applications.

To validate functionality of this LN-on-a-chip device, we focused on a several aspects of the *in vivo* LN complexity such as lymphocytes reaction in response to different external inflammatory stimuli. LNs *in vivo* have the potentiality to quickly react to inflammatory cues and to mount adaptative immune response against specific antigens. Here, previously described molecular mechanisms in *in vivo* murine models were used as means of comparison to validate the device, first considering lymphocyte activation and then attempting to model reaction to tumour antigens, simulating a TDLN. In conclusion, this type of device allowed us to perfuse through selected factors, and at the experimental end point, easily retrieve cells to perform flow cytometry or qPCR for gene expression changes quantification. In addition, because of the open nature of the device, it was possible to analyze media collected both from the top and from the perfusate to measure the secreted molecules.

5.2 Cell yield increases with collagenase concentration but does not affect cell phenotype

A main advantage of an open device which is completely built in hydrogel is the easy access to the sample for analyses, compared to a traditional PDMS device. However, a crucial operation to exploit this is the release of the cells trapped in the hydrogel to generate a single cell suspension for analysis, while avoiding alterations in the phenotype in the process. Hence, extensive optimization work has been carried to determine optimal cell density and hydrogel

digestion conditions. Initially a protocol for murine tumoural tissues digestion was utilized. This involved use of Collagenase A and D, both at a concentration of 1mg/ml for 30 min to obtain a single cells suspension from the LN device. This protocol did allow digestion of the hydrogel; however, digestion was often partial, showing some small intact gel fragments, and resulting in a small cell yield when analyzed with flow cytometry. The number of cells obtained also was highly variable and ranging between 1×10^5 and even 3000 cells from a single gel (Figure 5.1A).

Collagenase/dispase, a frequently used enzyme mix was also tested as it is often used in literature for hydrogel digestions [247]. However, whilst yielding a larger number of cells from the device, it showed artefacts with surface markers expression such as cleavage of key immune markers such as CD4 and CD8 in T cells, which rendered them misinterpretable by conjugated antibodies, and was therefore abandoned (Figure 5.1B). This finding about collagenase/dispase was also confirmed with the literature where other group faced similar issues using the commercially available enzyme, especially with immune markers[248,249]. Finally, an increase in collagenase A and D concentrations from 1 to 6mg/ml, without increasing incubation time, resulted in consistent cell yield larger than 2×10^5 from only from half of each digested gel, without protein expression artifacts (Figure 5.1C) and allowing to use the remaining half for further downstream analysis.

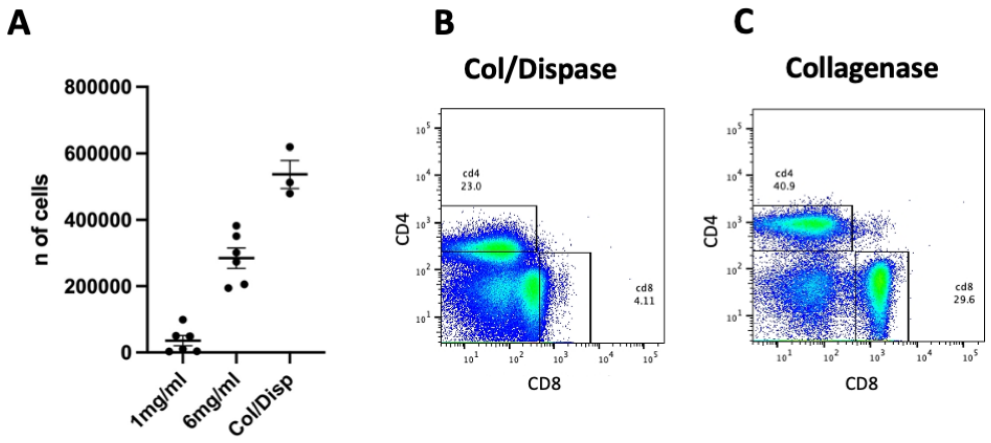

Figure 5.1 Collagenase does not affect cell phenotype. A) Graph indicating number of cells obtained by each digested hydrogel in different collagenase concentrations (1 and 6 mg/ml) and collagenase/dispase. **(B)(C)** FACS plots showing $CD4^+$ and $CD8^+$ populations with collagenase/dispase and collagenase.

5.3 Measuring immune responses in the LN-on-a-chip

5.3.1 Immune cells in the device react to activation stimuli

Once a reliable cell extraction protocol was established, a sufficient number of cells could be obtained from each device to analyse up to 16 markers by flow cytometry and also extract enough RNA for gene expression quantification.

We first used the device to test its capacity to respond to inflammatory stimuli, as may occur in the situation of an infection. We did this using PMA/ionomycin which are routinely used molecules to simulate an immune challenge and activate immune cells [250,251]. Initially, we treated the single-pour device by either bathing the device in PMA/Ionomycin in static culture for 4h, or with active flow through the channel only for 12h. A prolonged incubation with active flow was here chosen to ensure molecules transport throughout the device and obtain a similar reaction to what was previously observed in static incubation for 4h. This approach aimed to test that factors entering the device via the channel would successfully transit from the "lymph node sinus" into the cell-laden gel and reach target cells within the hydrogel. PMA/Ionomycin activates protein kinase C, while ionomycin is a calcium ionophore, therefore stimulation with these compounds bypasses the T cell membrane receptor complex. This will lead to activation of several intracellular signalling pathways, resulting in T cell activation and production of a variety of cytokines[252].

PMA/Ionomycin stimulation indeed generated drastic phenotypical changes both in $CD4^+$ and $CD8^+$ T cells (Figure 5.2). To characterize T cell phenotypes, we used CD44 and CD62L, markers expressed on the surface of lymphocytes. Specifically, with these markers it was possible to recognize naïve, effector memory and central memory T cells. Naïve T cells that have not encountered any antigen express high levels of CD62L and low levels of CD44. Effector memory express higher levels of CD44 but low levels of CD62L. Central memory T cells express both at higher levels. Due to PMA/Ionomycin stimulation, it was possible to observe a shift towards the effector memory phenotype from an initially naïve state. A decrease in the percentage of naïve (Figure 5.2B-E) and an increase of effector memory T cells occurred both in $CD4^+$ and $CD8^+$ T cells (Figure 5.2C-F), while the central memory population did not undergo a significant shift (Figure 5.2D-G). Importantly, in the presence of PMA/ionomycin, there was no difference in T cell phenotype between static and flow conditions. This indicated that when PMA was exclusively delivered through the channel, it was successfully able to transit into the hydrogel and stimulate T cells.

The switch in T cell phenotype with stimulation indicated that cells may indeed become more activated. To test this, CD69 expression was measured to determine lymphocyte activation status. CD69 is upregulated in early activation stages, and, following 4- or 12-hours stimulation, upregulation of CD69 levels was observed in $CD4^+$, $CD8^+$ and also $B220^+$ cells (Figure 5.2H-I-J).

Together these data proved that in this environment, lymphocytes were functional and ready to respond to external stimuli that could successfully be delivered through the channel and transported through the matrix.

A

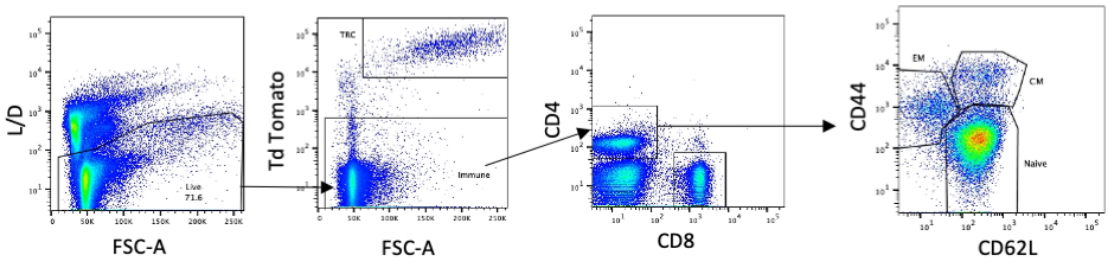
L/D
FSC-A
Td Tomato
FSC-A
CD4
CD8
CD44
CD62L
EM
CM
Naive

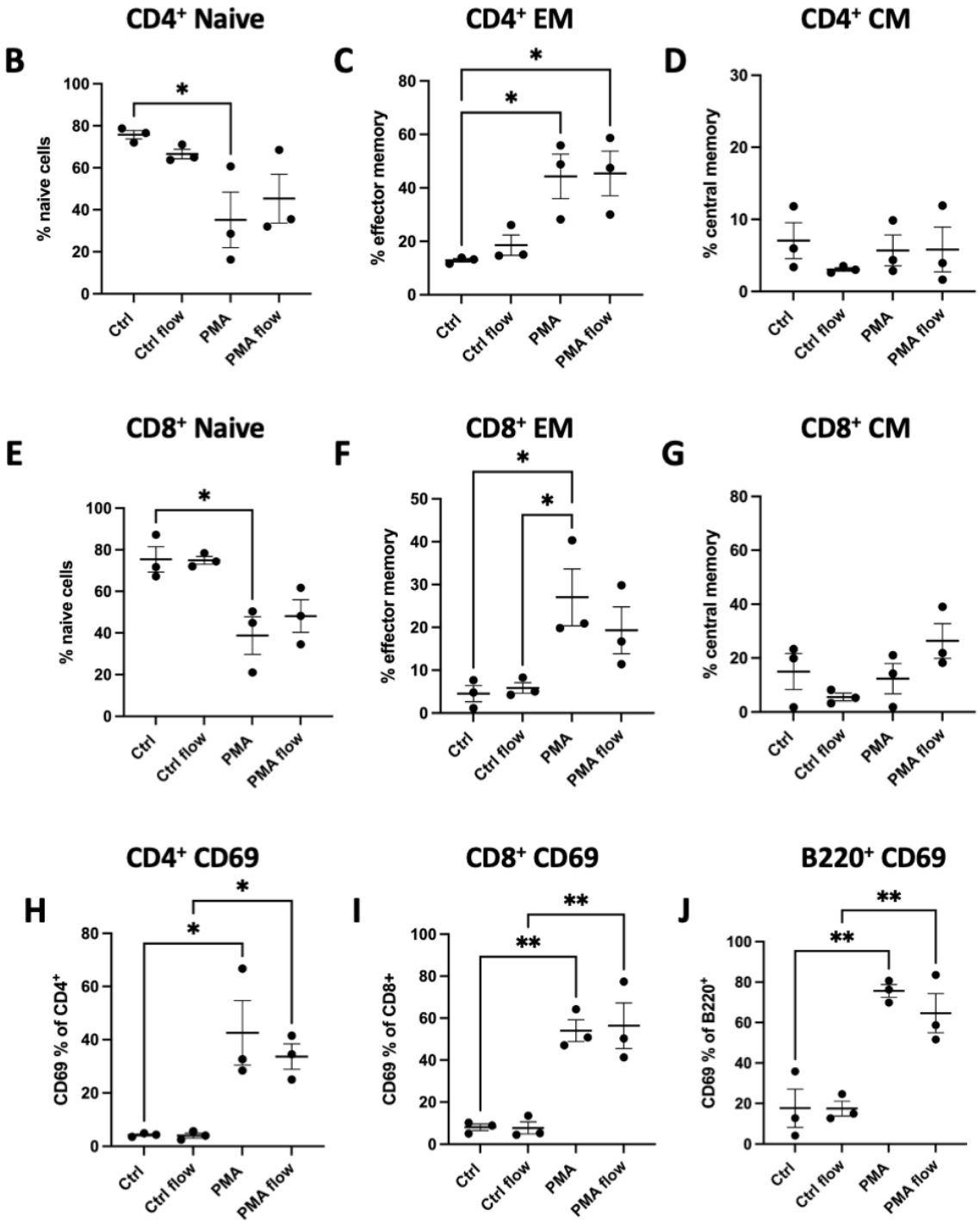
CD4+ Naive
B
% naive cells
CD4+ EM
C
% effector memory
CD4+ CM
D
% central memory
CD8+ Naive
E
% naive cells
CD8+ EM
F
% effector memory
CD8+ CM
G
% central memory
CD4+ CD69
H
CD69 % of CD4+
CD8+ CD69
I
CD69 % of CD8+
B220+ CD69
J
CD69 % of B220+
Ctrl
Ctrl flow
PMA
PMA flow

Figure 5.2 The LN device reacts to PMA/Ionomycin stimulation. A) Cell count obtained with flow cytometry representing number of cells after different enzymatic digestion conditions of the hydrogel, 1mg/ml and 6mg/ml Collagenase A and D. Each dot represents independent experiment (n=6). Flow cytometry quantification showing percentages of naïve, EM and CM among the $CD4^+$ T cells, **(B)(C)(D)** $CD8^+$ T cells **(E)(F)(G)** and $B220^+$ B cells **(H)(I)(J)**. Samples were incubated with PMA/Ionomycin or normal medium in static or flow culture conditions. Each dot represents independent experiment (n=3). One-way ANOVA and Tukey's multiple comparisons tests were conducted. ns = not significant ($p > 0.05$), * = $p \leq 0.05$, ** = $p \leq 0.01$, *** = $p \leq 0.001$, **** = $p \leq 0.0001$.

5.3 The LN-on-a-chip can be used to mount innate immune responses

In vivo, the LN is capable to react to different pathogens through specific pathways to provoke activation, molecular changes and immune clearance. Having shown activation after 'sterile inflammation', we then attempted to use the device to simulate a response to bacterial pathogens using the to the bacteria-derived inflammatory molecule Lipopolysaccharide (LPS), a Gram-negative bacterial cell wall component. This type of stimulation differs from previous PMA/Ionomycin because involves the engagement of specific immune receptors. LPS is usually recognized by Toll-like receptor 4 (TLR4) and induces TLR-mediated activation pathways that lead to Interferon gamma (IFNγ) production with subsequent induction of an inflammation state. TLR receptors and specifically TLR4 are expressed by a variety of immune cells including dendritic cells, $CD4^+$, $CD8^+$ and $B220^+$ that, once engaged with LPS, secrete pro-inflammatory molecules that affect each other, all contributing to the creation of a quick reaction leading to an inflammation state. As a first validation of our model, it was essential to test whether our LN-on-a-chip *in vitro* would be activated and trigger a TLR-mediated response. As before, stimulation was achieved through either static incubation or active perfusion of the device. The hydrogel was incubated with LPS for 12h and PMA/Ionomycin for 4h. As before, CD69 was measured through flow cytometry as a marker of activation. and appeared overexpressed in (Figure 5.3). LPS stimulation was enough to induce activation pathways in $CD4^+$, $CD8^+$ and $B220^+$ leukocytes. Again, stimulation by perfusion was sufficient to activate immune cells to the same level as static conditions, showing transit out of the channel and into the cell laden gels. However, CD69 expression with LPS was less dramatic we compared to PMA/Ionomycin stimulation. This may reflect the need to signal to innate cells contained within the gel which then signal to T cells, and thus a response of similar magnitude may take longer. T cells phenotypes were also analyzed with CD62L/CD44 in response to LPS but no clear shifts in populations were here observed.

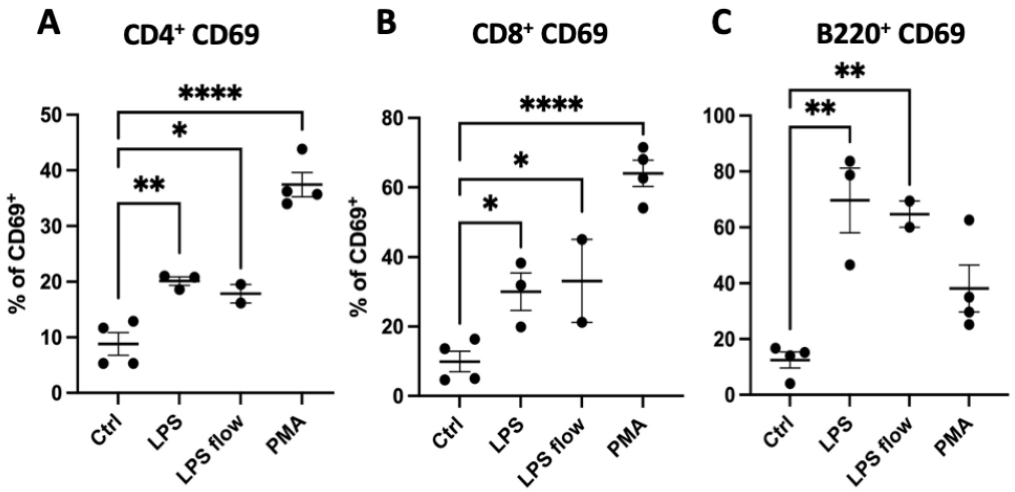

Figure 5.3 The LN device mounts an innate immune response to LPS. Flow cytometry quantification of the expression of CD69 in $CD4^+$**(A)**, $CD8^+$ **(B)** and $B220^+$ **(C).** Samples were either treated with LPS, statically and with flow, PMA, or normal cell culture medium. Each dot represents independent experiment (at least n=2). One-way ANOVA and Tukey's multiple comparisons tests were conducted. ns = not significant ($p > 0.05$), * = $p \leq 0.05$, ** = $p \leq 0.01$, *** = $p \leq 0.001$, **** = $p \leq 0.0001$.

5.4 The LN-on-a-chip is capable of mounting antigen-specific responses

After having determined that a reaction to external stimuli was observable and molecularly discernible, the LN-on-a-chip was then tested for its capacity to model the induction of an immune reaction against a specific antigen. For this purpose, we exploited the Ovalbumin model antigen system and genetically modified OT-I murine model, in which the variable region of the $CD8^+$ TCR is engineered to specifically recognise the OVA peptide SIINFEKL. The devices were fabricated following the same method described previously but the splenocytes included in the hydrogel were isolated from WT and OT-I mice and mixed in a 1:1 ratio to recreate the T cell heterogeneity seen in lymph nodes and determine if we were able to selectively activate one of the two populations by flowing an antigen, namely the OVA peptide solution. In this experiment the WT splenocytes represented an internal negative control that should not respond to OVA. To confirm that these cells were functional, we also included PMA which should activate all cells non-specifically (Figure 5.4A). To assist in differentiation between the two populations, the non-antigen-specific population was isolated from green CAG.egfp spleens so that they could be readily detected by flow cytometry. In these experiments, the device was incubated with SIINFEKL, PMA/Ionomycin or normal medium

both in static and flow conditions after which expression of activation and phenotypical markers were investigated.

With regard to the T cell phenotype, flow cytometry revealed that exposure to PMA/Ionomycin induced a significant decrease in the percentage of naïve $CD8^+$ T cells globally. This happened for both control and OT-I populations either in static or flow conditions. In contrast, SIINFEKL induced a significant decrease in the percentage of naïve $CD8^+$ T cells specifically in the OT-I population. This was not seen in WT cells (Figure 5.4B). PMA/Ionomycin treatment resulted in an increase in the $CD8^+$ EM percentage in both populations. SIINFEKL did not induce a significant change in OT-I $CD8^+$ T cells, but interestingly the addition of flow showed a trending increase in EM (Figure 5.4C). Interestingly, SIINFEKL treatment instead caused a dramatic increase in the CM portion of $CD8^+$ T cells specifically in OT-I. PMA/Ionomycin had no effect on either WT or OT-I. This is probably due to the fact that differentiation into CM T cells requires the engagement of the TCR, which exclusively happens with OT-I cells (Figure 5.4D).

Additionally, CD69 expression was measured. Consistent with the loss of naïve T cells in Figure 5.4B, PMA/Ionomycin supported a significant global increase in both WT and OT-I populations. Conversely, SIINFEKL only induced CD69 overexpression in OT-I T cells (Figure 5.4E). These data show that perfusion of antigen through the device has the capacity to induce an antigen specific response amongst a mixed population of immune cells.

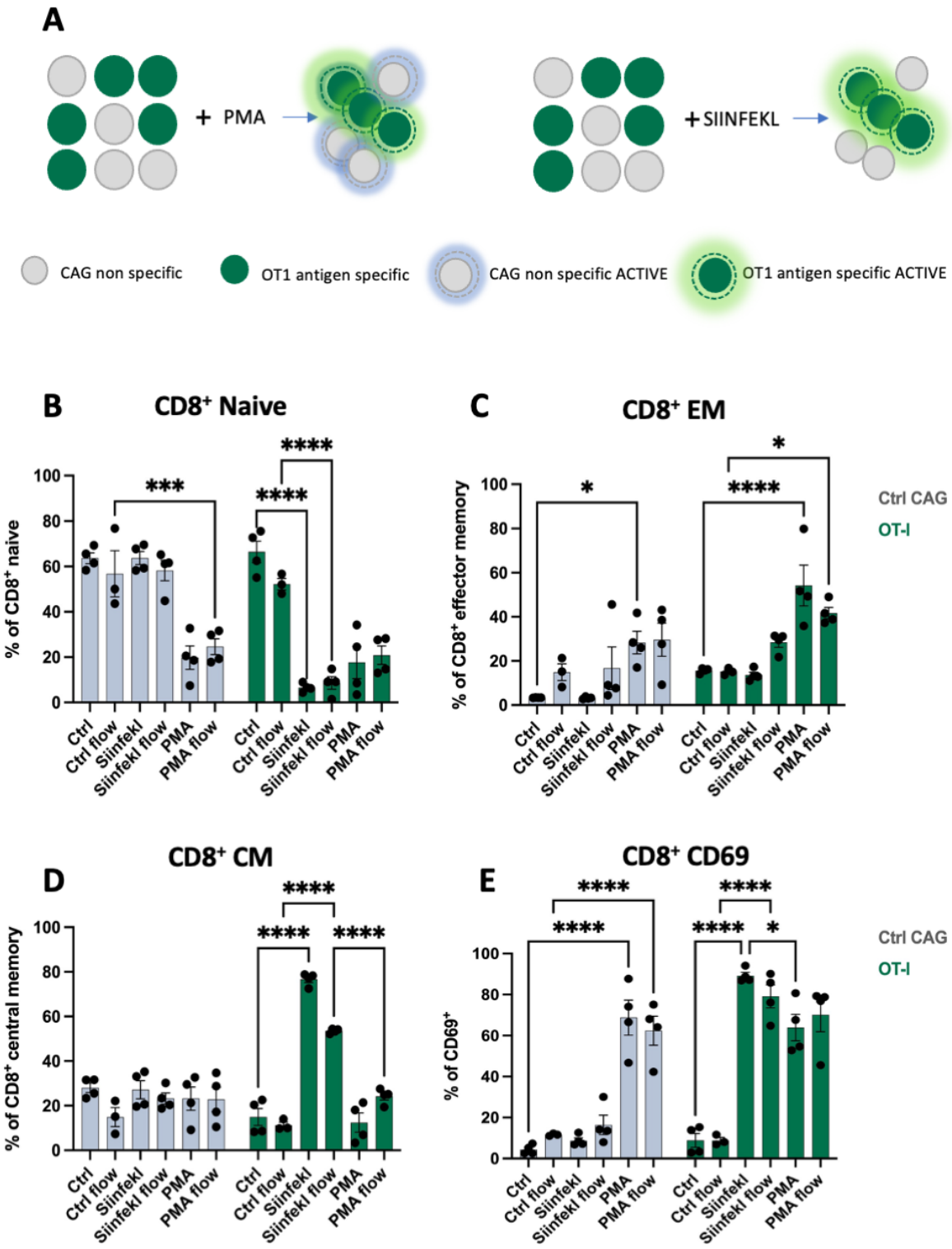

Figure 5.4 The LN device mounts an antigen specific reaction. A) Schematic drawing of the experimental setup. Flow cytometry quantification in OT-I (in green) and WT (CAG, in grey) $CD8^+$ T cells showing percentages of Naïve **(B)**, EM **(C)**, CM **(D)** and $CD69^+$ **(E)**. Devices were treated with ctrl medium, SIINFEKL and PMA, both in static and flow conditions. Each dot represents independent experiment (at least n=3). Two-way ANOVA and Tukey's multiple comparisons tests were conducted. ns = not significant ($p > 0.05$), * = $p \leq 0.05$, ** = $p \leq 0.01$, *** = $p \leq 0.001$, **** = $p \leq 0.0001$.

5.4.1 Antigen stimulation induces cytokine responses

Detection of surface marker changes provides insight into phenotype changes occurring in an immune reaction, but a large component of these complex molecular mechanisms is defined by the humoral immune response. This type of immunity relies on a myriad of secretory macromolecules such as antibodies, cytokines, complement and other antimicrobial peptides, released by immune cells and stroma that finely regulate cells crosstalk and trigger molecular pathways. To examine if changes in this arm of the immune system changed with stimulation, a cytokine array was performed to try and capture cytokine changes in response to different treatments.

The same composition of hydrogel with a 1:1 ratio WT to OT-I splenocytes was used and treated with either normal media, SIINFEKL or PMA/Ionomycin. Medium was then collected and analyzed with a cytokine array, which probes for 111 different molecules (Figure 5.5A&B). This test revealed the presence of a great deal of molecules in the culture medium when stimulated but also in the control condition. Out of 111 cytokines probed, some were not detected, and others were present at comparable levels across conditions. Soluble factors such as VEGF and WISP1 were highest in basal control conditions and were downregulated following stimulation. The potent T cell and monocyte chemoattractant CX3CL1, or fractalkine, was downregulated specifically upon PMA treatment. SIINFEKL stimulation induced a dramatic and specific increase in CXCL9 and CXCL10 compared to control and PMA (Figure 5.5C). Both CXCL9 and CXCL10 are found within lymph nodes and these cytokines bind to CXCR3, regulating immune cell migration, differentiation, and activation there. These are both stroma-derived chemokines and it is likely that here they are secreted by FRCs in response to inflammation cues from activated T cells, such as IFN-γ which has been identified like the key inducer of these molecules. Interestingly, IFN-γ was only detected in the cytokine array at very low levels probably because, being one of the earliest activation molecules secreted, it could have been quickly cleared. MIP-1 was also found upregulated with SIINFEKL. These data indicate that in addition to antigen specific activation, antigen stimulation also drives distinct changes to soluble cues within the lymph node.

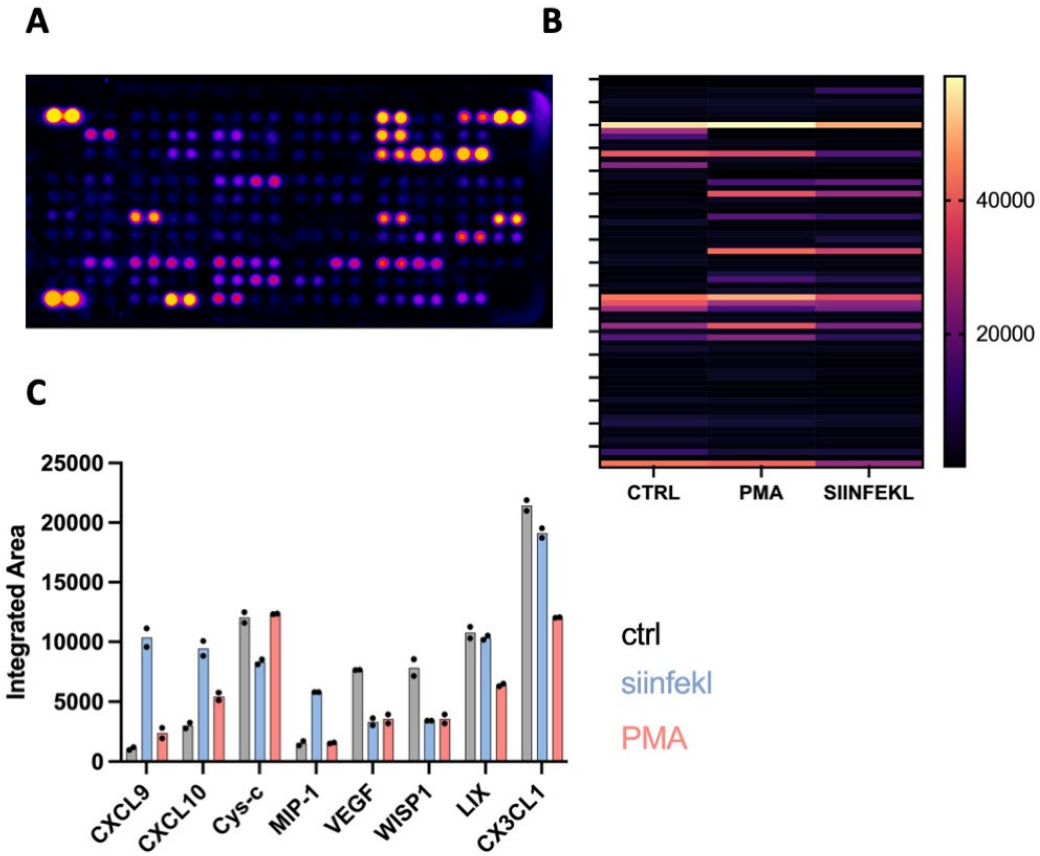

Figure 5.5 Cytokine array A) Cytokine array developed film. Each couple of dots represents a different cytokine detected in the medium. **B)** Heatmap of the cytokine array quantification obtained with ImageJ Macro 'Protein Array Analyser'. **C)** Graph with quantification of selected cytokines of interest showing integrated area of fluorescence. The test was performed on media following incubation with SIINFEKL (in blue), PMA (in red) or control medium (in grey). Each dot represents technical repeats (n=2).

5.7 TDLN modelling

We showed that the device has the ability to respond to different types of immune stimuli, but the lymph node plays a central role in the pathogenesis of numerous different pathologies, including cancer. Anti-tumour immune responses are initiated in the lymph node, but immunity fails, and lymph nodes are often the first site of metastasis. We therefore sought to determine if the device could model changes in the LN seen in cancer. The Shields lab previously showed that tumour-derived signals draining to lymph nodes induce significant remodelling and reprogramming of lymph node stromal cells [119,124]. The stromal compartment has a pivotal role in influencing the microenvironment and controls lymphocytes activity via protein and cytokine secretion profiles. In TDLNs, changes to FRCs function led to dysregulation of the microarchitectural homeostasis within the LN, fibrosis, and aberrant immune localization.

Using these findings as a benchmark to determine the suitability of this device for modelling the tumour draining lymph node, we therefore focused on changes to FRCs within the device following tumour treatment.

5.7.1 Flow cytometry does not capture TCM-induced protein expression changes

To mimic tumour-derived signals draining to the lymph node, tumour conditioned media (TCM) from cultured B16 melanoma cells was collected. The cell-laden device was then incubated in the presence of TCM to see whether it would trigger a reaction comparable with molecular changes occurring *in vivo*. The collected TCM was mixed 1:1 with full RPMI medium and the device was incubated with it for 72h. Medium was replaced daily for a total incubation period of 72h before cells were harvested characterised. Unlike the dramatic changes observed with inflammatory stimuli, incubation with TCM over the period treated was not sufficient to induce significant changes to CD69 expression in $CD4^+$ or $CD8^+$ T cells (Figure 5.6A&B). In addition, TCM treatment here did not trigger any shift in T cells phenotype when CD62L/CD44 were measured (Figure 5.6C-E). B cells markers were also measured such as CD86, IgM, IgD and MHCII but no changes were observed, suggesting that either the TCM was not enough to trigger visible reactions, or the incubation time was not long enough to appreciate a molecular response.

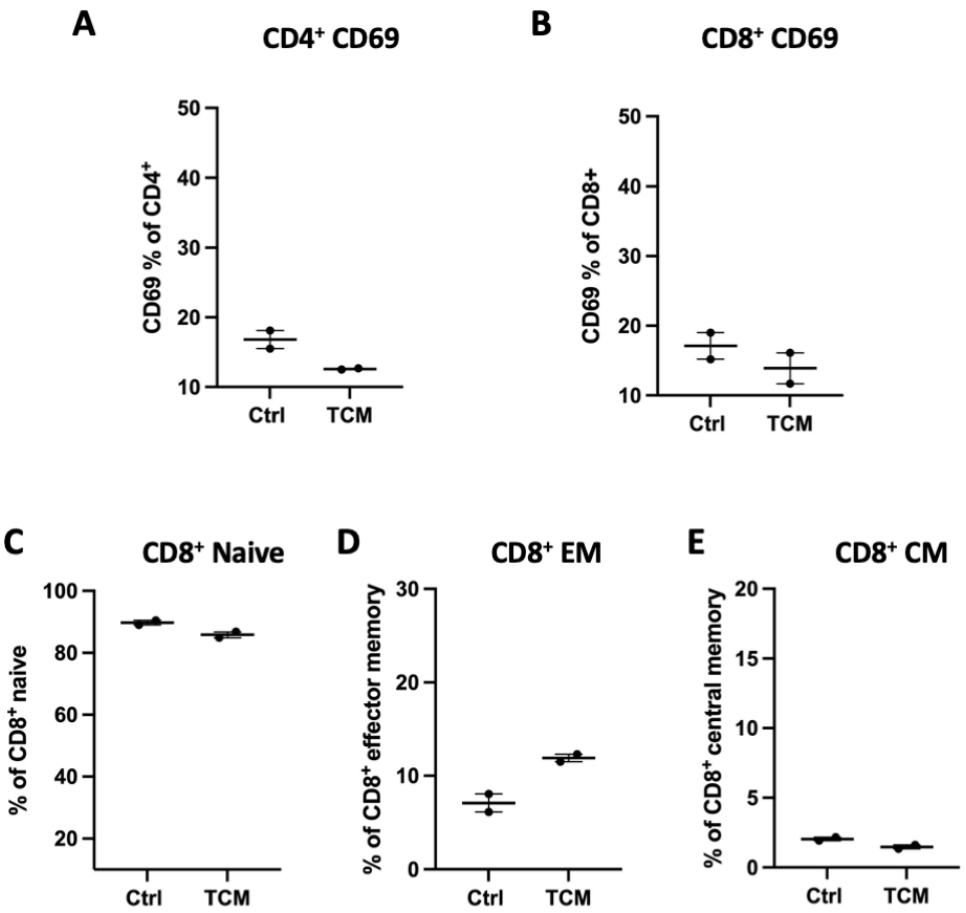

Figure 5.6 Tumour conditioning cannot be captured by flow cytometry Flow cytometry quantification. CD69 measurement following 72h TCM treatment in $CD4^+$ **(A)** and $CD8^+$T cells **(B)**. Each dot represents independent experiments (n=2). $CD8^+$T cells did not undergo phenotypical shifts after TCM treatment. Shown are naïve **(C)**, EM **(D)** and CM **(E)** populations.

5.7.2 TCM triggers gene expression changes observed in *in vivo* TDLNs

The lack of phenotypic molecular changes in immune cells as determined by flow cytometry could be a consequence of the time point; as stromal cells receiving cues need to adapt before signalling to immune cells, it is therefore plausible that to see significant changes at a protein level in immune cells, a longer incubation is required. Therefore, to overcome this issue we increased the incubation time, and started looking at RNA expression levels within the stromal FRCs included within the device. We examined whether TCM treatment of the device was able to induce alterations in RNA expression of key molecules as occurred in the stroma of TDLNs *in vivo* [119]. In particular, FRCs in TDLNs downregulate immune guidance cues *Il-7* and *Ccl-21,* and display activation traits such as upregulation of *Pdpn, Thy1* and *Col1a1*. The hydrogel was incubated then with TCM for 4 days with daily change of medium, after which it was

digested to obtain a mixed single cells solution. Cell sorting isolated three main populations: TRCs, T cells and B cells as shown in figure 5.7A and RNA was then extracted. After extraction qPCR showed that in this case, 4 days of incubation of the device with TCM was enough to induce a significant downregulation in the relative expression of *Il-7* as previously described *in vivo* in a B16 melanoma model (Figure 5.7B&C). In contrast, the other genes analysed which encoding structural molecules *Pdpn* and *Col1a1* did not show the expected overexpression. It is possible that longer incubation times would be sufficient to exhibit similar reprogramming. It is also possible that TCM harvested from a 2D monolayer culture alone may not sufficiently recapitulate the complex mixture of factors released from the tumour microenvironment *in vivo*, and therefore cannot recreate all of the changes in the device.

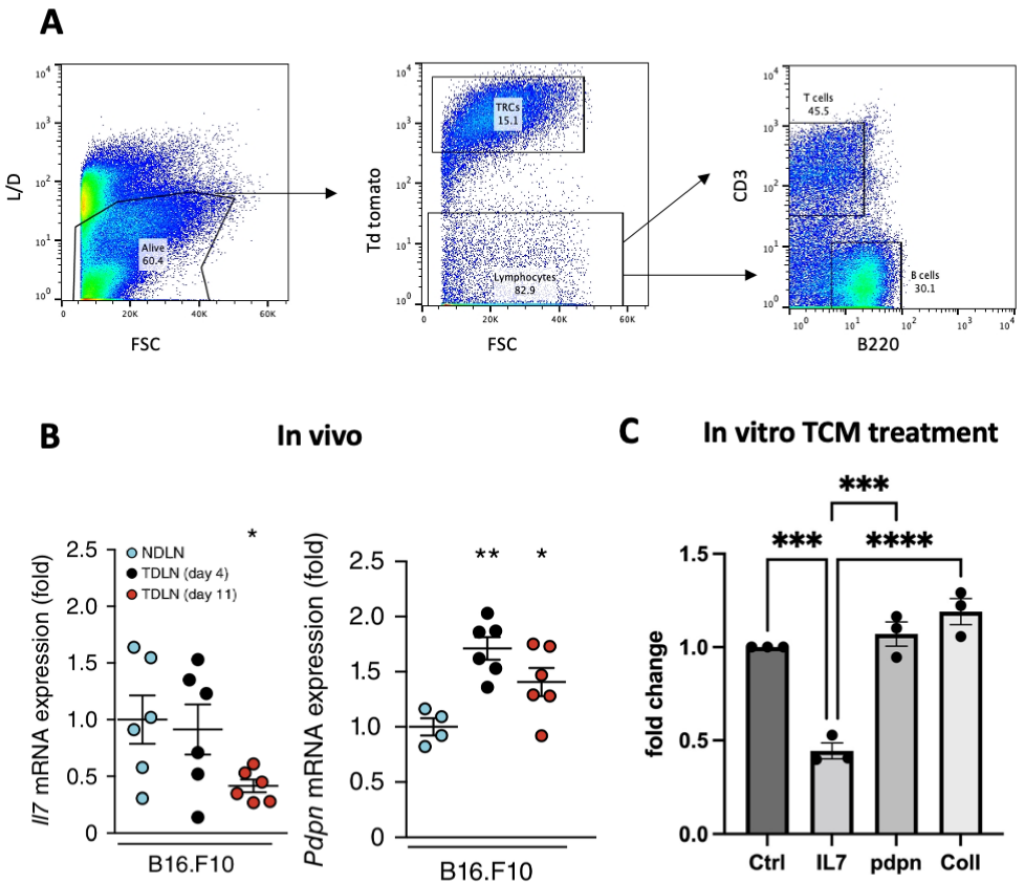

Figure 5.7 TCM causes changes in the gene expression of FRCs. A) Gating strategy used for cell sorting of the LN device after TCM treatment. Td tomato^{+} cells were separated by Td tomato^{-} portion in which CD3 and B220 were used to pull out T and B cells. **(B)** *In vivo* quantitative RT-PCR analysis of *Il-7 and Pdpn*, showed as fold change; reproduced from [119]. Each dot (n=6) representing an independent experiment. **(C)** Quantitative RT-PCR analysis of *Il-7, Pdpn and Col1a1*, showed as fold change. Each dot (n=3) representing an independent experiment. One-way ANOVA and Tukey's multiple comparisons tests were conducted. ns = not significant ($p > 0.05$), * = $p \leq 0.05$, ** = $p \leq 0.01$, *** = $p \leq 0.001$, **** = $p \leq 0.0001$.

5.8 3D bioprinted tumouroids as a source of conditioned medium to prime the LN-on-a-chip

Tumours contain a diverse collection of cells including cancer cells, fibroblasts and immune cells, which together release factors that are drained to LNs and may drive the remodelling and functional adaptations observed there. In light of this and the observation that B16 TCM alone could not recapitulate all changes seen *in vivo*, the final part of this work was focused on the creation of a 3D tumour model with higher level of complexity in terms of cell types, mechanical constraints and soluble composition than a 2D monolayer culture with which to better simulate the tumour upstream of a lymph node. This would provide an upstream stimulus for our model that more closely represents a tumour *in vivo*.

Here, we generated a 3D tumour model, comprising multiple cell types, and its tumour microenvironment (TME). To achieve this, we 3D bioprinted a core-shell tumouroid, which included a core of pancreatic cancer cells, surrounded by a shell of pancreatic CAFs. By allowing reproducible long-term culture, this technique gave tumouroids that have the potential to mimic the upstream tumour, *in vitro,* and be connected to the LN-on-a-chip providing a direct and continuous source of stimulation. Here, as a preliminary step, factors secreted by the tumouroid culture were collected and used to stimulate the engineered LN.
First, the technique for core-shell bioprinting was optimized and then the phenotype of the obtained structures characterized. Moreover, exploring the various applications of this model, the tumouroids were used to mimic a tumour microenvironment (TME), by co-culturing immune cells with the tumouroids in the presence of anti-CTLA4, an immune checkpoint inhibitor (ICI) used in clinic.

5.8.1 CAFs in bioprinted tumouroids reflect features of the *in vivo* tumour microenvironment

After optimization of print reproducibility in shape and size, by tuning cell concentration of the hydrogel and alginate removal procedure, we examined the obtained core-shell structures after alginate removal by confocal imaging and flow cytometry to investigate their phenotype and function as well as successful core-shell formation. Figure 5.10A shows that the generated tumouroids contained both CAFs and tumour cells, and a clear core-shell structure was present with CAFs forming a defined capsule, while also infiltrating throughout the mass core (Figure 5.10A), which resembles the pattern of CAF distribution seen *in vivo (*Figure 5.10B; Leonor

Rodrigues*)*. Deposition of ECM components such as Collagen I, Osteopontin and Perlecan could be detected within the tumouroids, indicative of CAF functionality (Figure 5.10C).

In Shields lab it was found that CAFs are not a distinct population but rather homogeneous and dynamic[253]. For instance, CAFs from early tumours show different expression profiles compared to late tumours and specifically, it was observed CD34 expression in early tumours CAFs (S1) and predominant αSMA expression in late tumours (S3)[254]. Conversely, fibroblasts that grow on 2D plastic lose phenotypic and functional heterogeneity and are dominated by αSMA-expressing fibroblasts probably due to culture support stiffness or lack of cues from a microenvironment. Here then, we investigated whether tumouroids could more accurately recapitulate *in vivo* conditions and regain a certain degree of heterogeneity. CD34 and αSMA expression was measured by flow cytometry from 2D co-culture, 3D bioprinted tumouroids, and those harvested from day 11 tumours grown *in vivo*. As expected, *in vivo* a mix of $CD34^+$ and αSMA^+ expressing CAFs was observed; however, CAFs predominantly expressed αSMA with $CD34^+$ populations barely detectable when cultured in 2D. Interestingly, tumouroids exhibited a mix of $CD34^+$ and SMA^+ CAF, with the re-emergence of $CD34^+$ populations more reminiscent of *in situ* tumours (Figure 5.10D&E). Thus, these data show a successful core-shell tumouroid formation and the re-emergence of phenotypical traits that were lost *in vitro* making this platform favourable to study events and interactions occurring within a tumour.

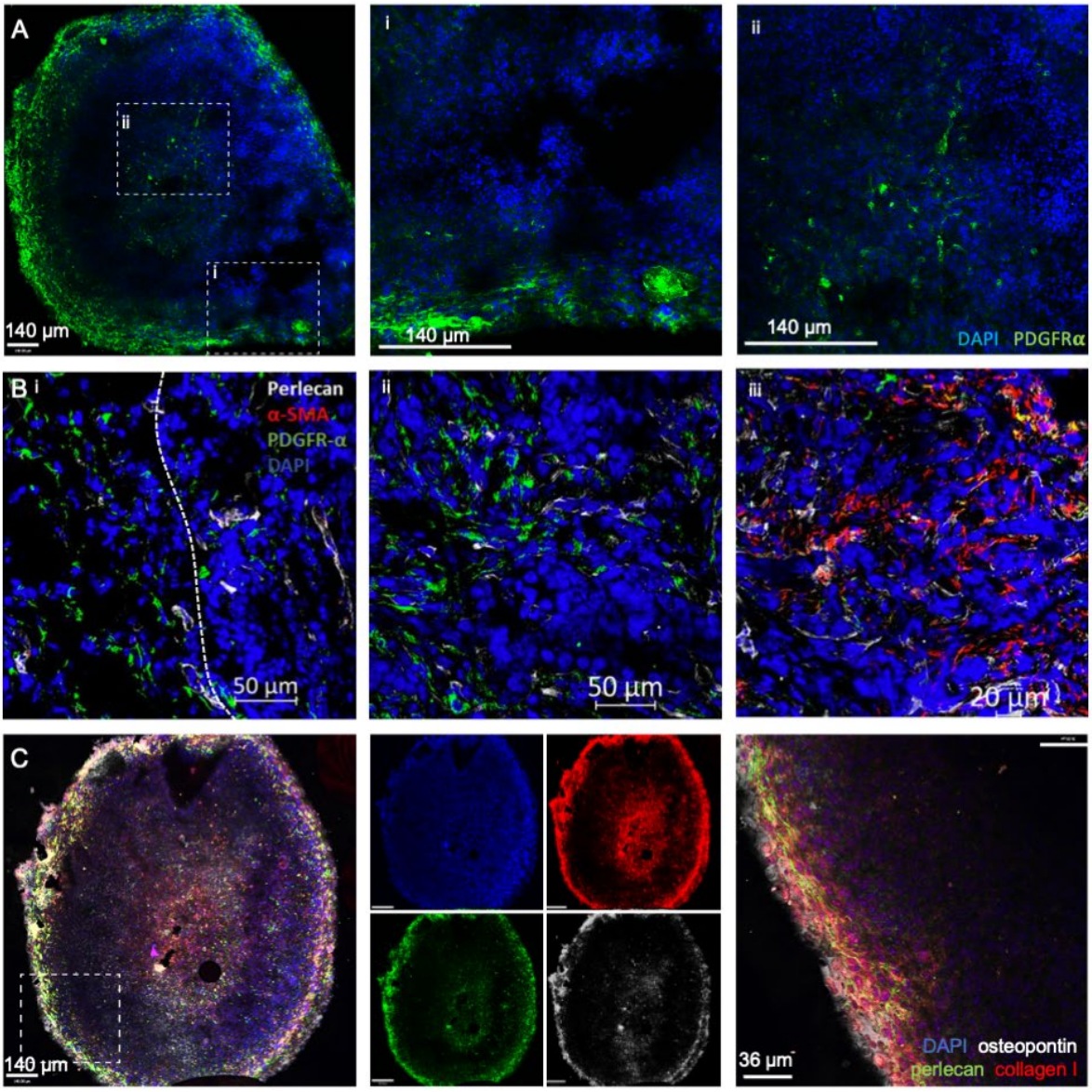
A
ii
i
140 µm
i
140 µm
ii
140 µm
DAPI PDGFRα
B i
Perlecan
α-SMA
PDGFR-α
DAPI
50 µm
ii
50 µm
iii
20 µm
C
140 µm
36 µm
DAPI osteopontin
perlecan collagen I

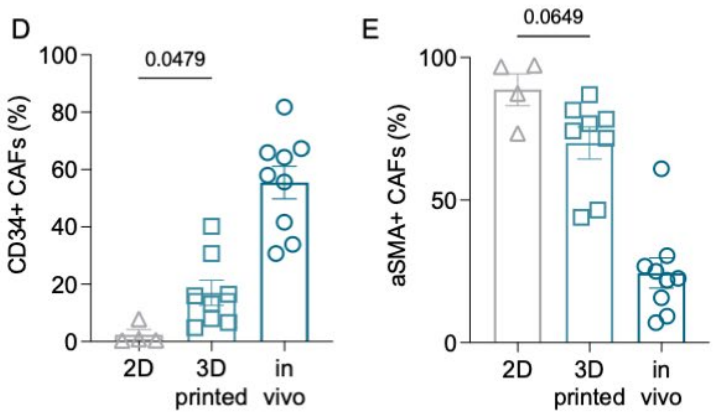
D
0.0479
CD34+ CAFs (%)
100
80
60
40
20
0
2D
3D printed
in vivo
E
0.0649
aSMA+ CAFs (%)
100
50
0
2D
3D printed
in vivo

Figure 5.10 Tumouroid CAFs show *in vivo*-like characteristics. A) Representative confocal image tumouroid sections showing a CAF capsule and CAF network deep within the tumouroid core. CAFs (PDGFRα, green); nuclei (DAPI, blue). Inset i: higher power image of the CAF shell. Inset ii: higher power magnification of CAF-core network. **B)** representative confocal images of CAF networks detected in day 11 mM1 pancreatic tumours *in vivo.* Shown are i) PDGFRa CAFs (green) at the tumour edge (denoted by dotted line), ii) PDGFRa CAFs rich zones within the tumour centre, and iii) aSMA-rich (red) areas within the tumour. Distribution of the ECM molecule perlecan (white) is also depicted. **C)** Representative confocal image depicting *de novo* extracellular matrix deposition within the tumouroid. Merged and individual channels for Perlecan (green), Osteopontin (white), Collagen I (red) and nuclei (blue) are shown. Inset shows a higher power field of ECM at the tumouroid periphery. **D) E)** Flow cytometric quantification of the proportion of $CD34^+$ or αSMA^+CAFs from 2D and 3D cultures, and *in vivo* settings. Scale bars, 140 µm **(A)**, 50 µm **(B**i, ii**)**, 20 µm **(B**iii**)**, 140 µm **(C)** 36 µm (**C** inset).

5.8.2 Inclusion of immune cells in simulated extracellular matrices

In vivo the pancreatic tumour mass gets quickly infiltrated by immune cells which have an important role in disease outcome and response to therapies. The presence of immune cells in the mass also enables a specific crosstalk between tumour and immune cells which leads to secretion of specific signals that downstream might affect the response in the TDLN. Therefore, to further mimic the *in vivo* situation, a mixed population of splenocytes from CAG.egfp mice for easy tracking, was dispersed in a collagen gel, into which the tumouroid was embedded. This meant that the tumouroid was surrounded by immune cells which could infiltrate the mass. These gels were live imaged for 48h and revealed that immune cells were rapidly recruited to the tumouroid from the surrounding ECM (Figure 5.11A). Subsequently, tumouroids were picked from the gel and processed to perform flow cytometry which revealed the diversity of immune cell populations associated with the tumouroid structures (Figure 5.11B). Infiltrating T cells, NK, $CD11b^+$ cells and B cells were detected, with T cells representing one of the most dominant populations identified. The pattern of infiltration of *in vitro* tumouroids was not dissimilar to those measured at different time points of pancreatic tumours *in vivo* (Figure 5.11C, data from Leonor Rodrigues). Conversely, *in vivo*, most infiltrating immune cells are $CD11b^+$ cells, while in this *in vitr*o system "other" cells dominated, which is for the majority composed of B cells. This is probably due to the initial composition of immune cells isolated by spleens which are formed for the most by B and T cells. Importantly, when the tumouroids were sectioned and imaged by confocal imaging CD11b-expressing myeloid populations were observed deep within the tumouroid (Figure 5.11D, white coloured cells). Finally, viability of

the tumouroids was analyzed following the addition of immune cells. While tumouroids alone in culture maintained high viability, we observed a drastic decrease in the percentage of live cells when cultured with immune cells. To demonstrate that cells in the tumouroid died because of a specific action by the immune cells and no other confounding factors (i.e. nutrient depravation) here we show that immune cells in the co-culture maintained high viability (Figure 5.11E).

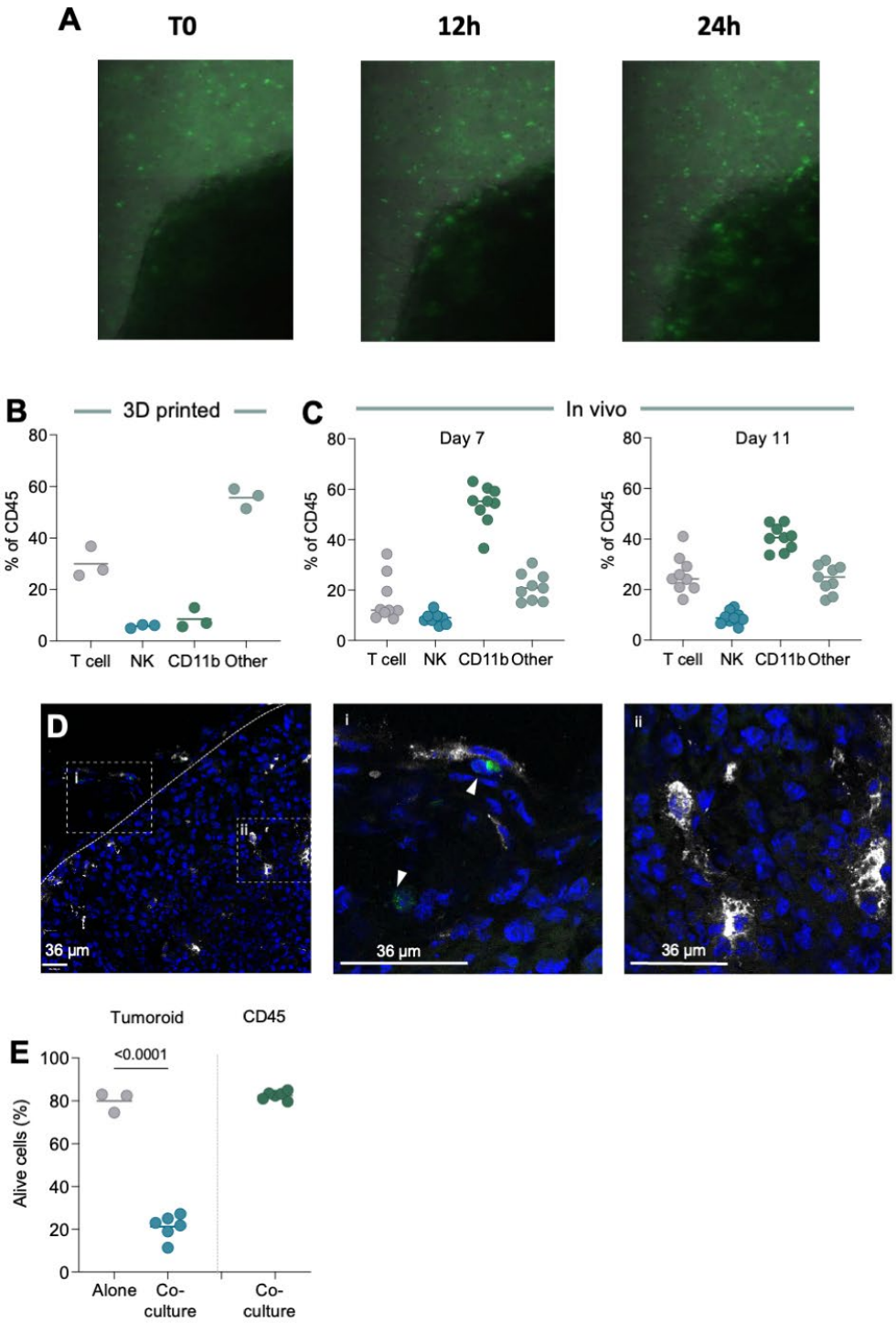

Figure 5.11 Immune cells infiltrate tumouroids as *in vivo*. A) Time lapse images from video analysis of immune cells incubation with the tumouoroid taken at T0, 12h and 24h. **B)** Flow cytometric quantification of tumouroid-infiltrating immune cells (T cells, NK cells, cd11b$^+$ and others; shown as percentage of CD45$^+$ cells). **C)** Flow cytometric quantification of tumour-infiltrating immune cells (T cells, NK cells, cd11b$^+$ and others) detected in mM1 pancreatic tumours *in vivo* at day 7 and day 11. **D)** Representative Confocal images of tumouroid sections after 48h incubation with splenocytes showing B220$^+$ B cells (green) and cd11b$^+$ myeloid cells (white). Inset i, higher power image of leukocytes at the tumouroid periphery; arrowheads denote B cells. Inset ii; higher power view of leukocytes deeper within the core. Scale bars, 36 µm. **E)** Flow cytometry quantification of tumouroid viability cultured at day 5 of culture with and without immune cell co-culture. Viability of co-cultured immune cells also shown.

5.8.3 3D bioprinted tumouroid-derived factors reflects changes observed with TCM treatment

After having created and characterized the basic tumouroid model, we tested whether this more complex TME set-up would be a better upstream stimulus for the TDLN model than 2D TCM by priming the LN-on-a-chip with factors secreted from the bioprinted structures in the presence of immune cells. The presence of these cells can vary among tumours but represents a key element in the creation of an inflamed TME. Considering the importance of such compartment we bathed the LN device with conditioned medium isolated from the engineered TME (TMECM) i.e. bioprinted tumouroids in presence of immune cells in a 3D collagen gel. Following alginate lyase treatment, each tumouroid was cultured for 24h in 3D collagen gels laden with immune cells from CAG.egfp spleen. Then, 2ml of full tumouroid medium was collected, eventually processed similarly to TCM (methods 2.1.3) and used to incubate the LN devices, mixed in a 1:1 ratio with full media supplemented with IL-7 and IL-4.

The LN devices were treated with TMECM for 4 days, exchanging with fresh medium daily. At the end of the incubation, cells were sorted as described previously and RNA was extracted (Figure 5.13A). The same set of genes as for the TCM treatment were measured. qPCR again revealed, in a similar fashion to TCM treatment a downregulation in the relative quantity of *Il-7*, while other genes analyzed, *Pdpn* and *Col1a1* did not show any significant change (Figure 5.13B). It is likely therefore that an increased incubation time is needed to obtain additional changes in gene expression.

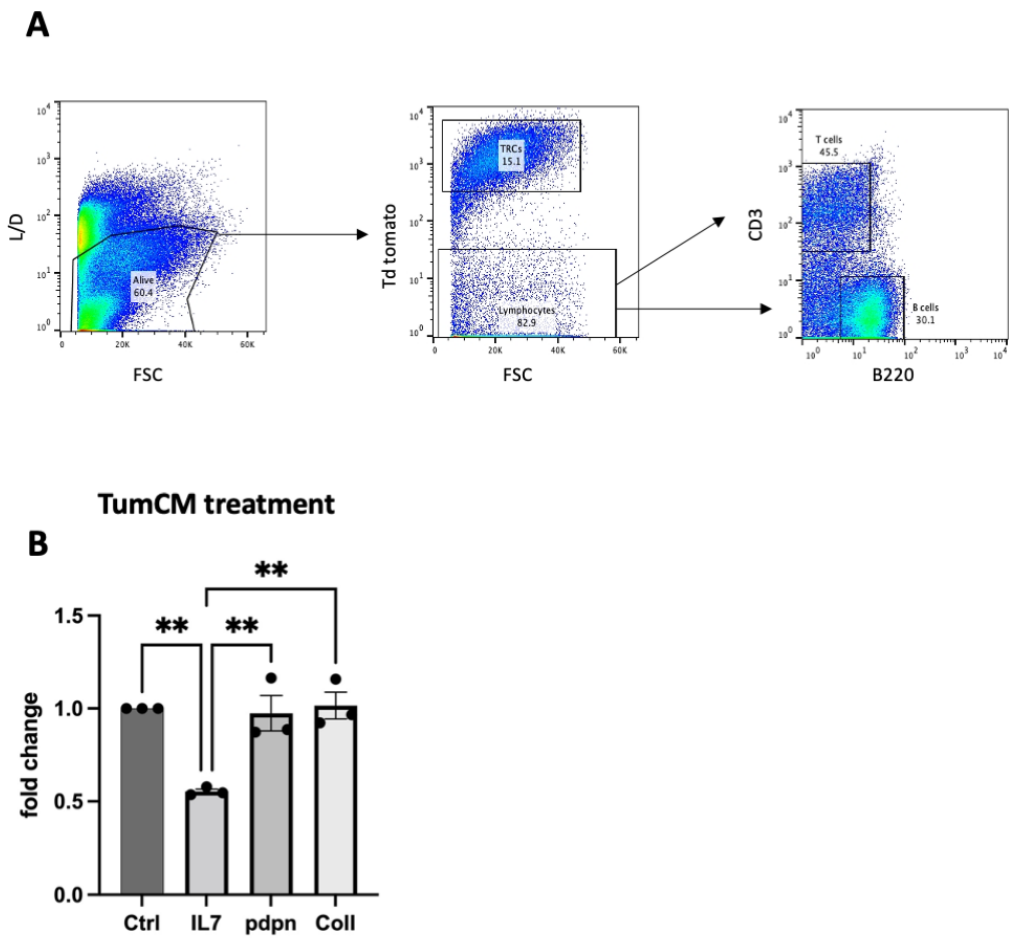

Figure 5.13 Tumouroid-derived factors cause changes in the gene expression of FRCs. TMECM causes changes in the gene expression of FRCs. A) Gating strategy used for cell sorting of the LN device after TCM treatment. Td tomato^{+} cells were separated by Td tomato^{-} portion in which CD3 and B220 were used to pull out T and B cells. **(B)** Quantitative RT-PCR analysis of *Il-7, Pdpn and Col1a1*, showed as fold change. Each dot (n=3) representing an independent experiment. One-way ANOVA and Tukey's multiple comparisons tests were conducted. ns = not significant ($p > 0.05$), * = $p \leq 0.05$, ** = $p \leq 0.01$, *** = $p \leq 0.001$, **** = $p \leq 0.0001$.

5.9 Summary

In this chapter, I have shown the different applications explored in the LN-on-a-chip following the optimization stage. First, we focused on reproducing an inflammation state and successfully induced a general activation and an innate immune response through perfused PMA/Ionomycin and LPS. Then, using the OVA OT-I murine model we successfully induced an antigen-specific response in the device and collected media from different treatment for cytokine analysis. Cells were also live imaged and while appearing motile, in this system they did not show significant changes when movement was quantified. As LNs play critical roles in cancer pathogenesis and

are remodelled *in vivo* when they are downstream of a tumour, we have attempted to apply the LN device in the context of cancer by delivering tumour cells-secreted factors. TCM, a mix of antigens, metabolites and other small molecules secreted by B16s tumour cells, generated a molecular response in a similar fashion to what is observed *in vivo* at a gene expression level when given to the device. In particular, the expression level of *Il-7* appeared in this model downregulated, but not all the other markers changed as expected. This was potentially due to the fact that *in vivo*, tumours are comprised of many cell types, all of which will release factors into their surroundings. Subsequently, we created and characterized a 3D bioprinted model of pancreatic tumour with the aim of priming the LN model with a more representative and complex model. We then recapitulated an engineered TME in the presence of immune cells since the production of immunomodulatory factors by immune cells, such as TGF- β, can modulate expression of proteins like podoplanin[255] and fibroblast activation resulting in collagen deposition. Incubating the LN device with TMECM also induced *Il-7* downregulation, confirming it as one of the early molecules to be altered in the process of a TDLN formation. Although the new model contained multiple cell types in a 3D environment, it did not change the overall effect observed with this set of genes. It is possible that by either expanding the genes set, increasing the incubation time or focusing the attention of the lymphocyte populations, it will be possible to learn more about tumour priming of the LN. Finally, the tumouroids were used to be included in a 3D microenvironment and test the effect of potential drugs like ICIs. I collected medium from tumouroids in the presence of immune cells with and without ICI, which was stored for further testing of the LN device. Due to time restrictions, we could not make use of this ICI medium, but it has been stored and will be used in the near future.

CHAPTER 6

DISCUSSION

The role of LNs in the body is maintaining the homeostasis and facilitate immune reactions as a protection mechanism from pathogens and tumour antigens. Acting as physical bridges, they link cellular elements of innate and adaptative immunity and they allow the development of antigen specific responses. However, in many solid tumours LNs lose their ability to recognize and kill their targets i.e. tumour cells and can serve as initial sites of metastasis. Studies have shown that even before the arrival of tumour cells to the LN, draining factors from the tumour induce dramatic changes to the organ, creating a permissive niche for cancer cells to spread [256]. How this occurs has not been completely clarified yet, but it has been shown that the LN stromal compartment plays a major role in the process [119]. One significant difficulty in understanding such a complex and dynamic phenomenon is the reliance on *in vivo* systems, hence the creation of new *in vitro* models can be of great help to elucidate new insight into the problem. Current 2D *in vitro* systems are not suitable to model high grades of complexity while *in vivo* models, which are biologically better systems, are too complex, expensive and carry ethical issues. A LN-on-chip device could serve as a powerful tool to model different immune related diseases such as infections, autoimmune disorders, arthritis and tumours. Here, I described the development of a new 3D system to model the LN environment and tested its reaction to inflammatory stimuli and tumour cues.

6.1 The PDMS-based device

First, we used a microfluidic device designed by Huang lab [188] and tried to apply it to our research question. It was possible to culture LN isolates and FRCs enclosed in a Collagen I gel in the central compartment and to line the outer channels of the device with a monolayer of endothelial cells. Although the system showed to be very versatile, cheap and optimal for imaging, this platform was developed as a closed device with its top part bound to a glass cover slide. This proved a major limitation for our application, given the desire to perform analyses on recovered cells post perfusion. The success rate of the devices, from manufacturing up to cell seeding, was also lower than hypothesized. This was mainly due to issues regarding the stability and consistency of the Collagen I – IV interface. When successfully achieved, we also noted that the position of the interface varied along with the bases of the pillars that hold the Collagen I gel in place. The resultant irregular shape of the channel, achieved in correspondence to the central compartment, was a potential source of further problems when seeding cells and applying flow to it. Obstacles and sharp corners initiate turbulent flow in channels and in arteries with atherosclerotic plaques [257–259]. This could disrupt the fragile

collagen I/IV interface and change the transport of factors. In order to obtain a more consistent interface, the shape of the pillars was modified from rectangular-shaped to trapezium-shaped with the longer base facing the outer channels, based on other devices that use such structures [189,190,192,260]. This adaptation was designed to assist with efficient Collagen I filling, provide greater anchorage and smaller expanses of interface to boost stability. The new design, although not largely tested, did not seem on its own to give crucial advantages for the device success rate. Another limitation regarded the length of the experiments performable with this model, which is highly dependent on the viability of cells over time in the central compartment. The 3D cultures contained in the central compartment are confined within an enclosed sealed space, and despite the porosity of PDMS which allows a degree of diffusion of nutrients, it was not sufficient for long experiments.

6.2 Sacrificial ink-based device

Having considered the advantages of this microfluidic device but also given all its limitations, we started developing a new microfluidic system, created by 3D printing of sacrificial ink in line with works by Lewis lab that took a similar approach to create vascularized tissues [207–209]. One advantage of these types of devices is the possibility to fabricate them without the need of specific facilities such as clean rooms, making them accessible to more laboratories. This new system allowed the creation of perfusable channels of any desired shape possessing a broad range of width (between 200 and 1000µm) embedded in a gel matrix composed of GelMA. Indeed, this technique has generated complex perfusable shapes such as the cochlea [261] and renal tubules [208]. The main improvement of this system is the relative ease of manufacturing. The fabrication process implied that a cell-laden matrix was poured into a PDMS case where the printing process took place. UV crosslinking of the cell-laden matrix did not seem to impact the overall cell viability within GelMA matrix in static conditions. In fact, FRCs seeded in GelMA showed high viability up to 4 days of culture, but it is likely they can sustain long-term culture. Nevertheless, with this approach I encountered two major limitations; first, despite their high viability FRCs did not obtain a physiological morphology when cultured in the GelMA matrix, making it an unsuitable substrate for our purpose. This is in line with reports in literature that show fibroblasts adhering on top of GelMA surfaces but not able to spread embedded unless its concentration is lowered to <5% [262,263]. At these concentrations, in my experience was never possible to achieve a microfluidic channel by casting and immediately collapsed. Moreover, even when the vessels were successfully printed, the action of linking

them to an external pumping system was often the cause for device disruption and leakage of fluid from the interface between the PDMS case and the hydrogel to the top of the device. I addressed this major issue by pre-treating the glass coverslip and applying some tubing adapters inserted into the PDMS case. While the glass treatment made it more hydrophobic and 'sticky' to hydrogels, the adapters reduced the pressure of fluid at the interface allowing pump-driven flow.

6.3 Hydrogel-based device with a central compartment

Endothelial cells reliably formed monolayers on the GelMA substrate, but despite its versatility and tuneability, GelMA demonstrated poor compatibility with FRCs seeded within. Although they remained alive, they did not show any physiological behaviour such as stretching and matrix remodelling as demonstrated in numerous studies of FRCs grown in 3D collagen I hydrogels [264–266]. In collagen, and devices made with sponge scaffolds [267], FRCs spread to obtain *in vivo*-like morphological features and generate extensive networks. Scanning EM showed that GelMA formed a structure with small pores and short fibers compared to collagen rich gels and this likely impaired the ability of cells to spread. Considering this together with the observation of successful LEC spreading on GelMA and possibility of flow application, I designed a device which contained two channels casted in GelMA and a collagen I central compartment laden with the LN bulk. The need for two materials arose from the fact that collagen I, which also could potentially serve as a good substrate for LECs to adhere, could not sustain casted channels formation if not at high concentrations [268–270]. Other studies have utilized collagen gels to form channels, but the density required (>5mg/ml) would form a too dense fiber structure in which to sustain physiological cell movement as we observed for GelMA. Moreover, the concentration is highly variable among batches and is more difficult to handle at the small volumes required for microfluidics devices due to its increased viscosity. However, its major drawback is represented by the fact that collagen I, easily remodelled by FRCs, quickly shrinks due to a fibres pulling action exerted by these cells and therefore is not suited for long-term cultures. In fact, such cultures are often used in literature to evaluate the contractility activity of fibroblasts by measuring the extent of such contraction [119].

In the current device, LECs adhered to the embedded channels forming a circular intact lumen akin to channels generated other microfluidic systems and showed the ability to respond to biophysical flow forces by altering their morphology. In the presence of flow LECs within the channel were more elongated and aligned with the direction of flow, consistent with previous

studies which showed active cell movement against the direction of flow [271,272]. LN isolates, being primary cell cultures, are more sensitive cells than FRC and quickly died after only 24h of culture. Nonetheless, the addition of IL-7 to the cell culture medium proved to be beneficial to cell survival, especially to $CD3^+$ T cells, and the addition of IL-4 improved B cell viability. In other LN devices to keep primary lymphocytes alive, they undergo strong artificial activation. For instance, B cells are pre-activated B cells with an anti-CD40 antibody [230]. In my system cytokines and FRCs presence was enough to keep T and B cells alive and crucially, it circumvented altering lymphocytes by a pre-seeding activation step. FRCs *in vivo* secrete such survival factors such as IL-7 and IL-4 among a myriad of other cues that sustain lymphocytes [44,45,113]. In this system, they indeed seemed to improve T and B cells viability, compared to control gels where they are absent but alone, they were not able to sustain lymphocytes. It is likely that in the first phases after seeding into the gel, when FRCs start to come out of their round shape, their secretome profile might be altered adapting to the new environment. It is also important to note that, human lymphocytes seem to be more resistant in culture than murine ones and can grow up to 2 weeks with the addition of human cytokines such as IL-2 or IL-15 [273]. Other works have shown increased lymphocytes viability in a 3D bioreactor, without addition of external factors [274]. Although we did not add human cells in this device, this could be the next step to add clinical relevance to the results and prolong experiments duration.

However, the main issue encountered with this model iteration was a lack of factors transport from the GelMA embedded channels into the collagen central compartment. Factors transport is critical to model any organ *in vitro* and the lack of it can cause several issues such as cell survival. In the LN in particular soluble cues are delivered from the SCS into the LN parenchyma therefore this system did not recreate the node. Such unexpected phenomenon was first observed by imaging fluorescent dextran that clearly did not reach the center of the device. Initially, we hypothesized that this issue could be due to an interface effect due to surface tension of the GelMA which takes place during the fabrication process. In order to form the whole GelMA frame around the casted central compartment the hydrogel was poured around a shape and fully crosslinked with UV light, before adding the collagen. We thought then the GelMA molecules preferentially disposing along the edges could create a 'shell' that blocked the factors. Factors transport between multiple adjacent materials has not been investigated fully yet in literature. Thus, because of a lack of references, empirical observations led the proceeding of research. Subsequently, I tried to avoid full UV crosslinking of the GelMA frame but use thermogelation properties of GelMA instead first. In this way I could pour the central collagen, shortly put the device at 37°C to allow material mixing at the interface and finally

UV crosslink the device. Also with this method, I observed the same behaviour, and the perfused factors did not penetrate the collagen gel after 2h. It is possible that this phenomenon was due to different materials porosities which steered factors diffusion into GelMA preferentially. Eventually, this method was abandoned as it did recapitulate the LN setting.

6.4 Single material hydrogel-based device

Since a critical issue of the previous device was due to the presence of a hard interface between two hydrogels, I tested different formulations to find a single material that provided sufficient structural strength to maintain a channel but would also allow for physiological growth and behaviour of cellular components within. Following optimization with different materials and formulations which included PEGDA, chitosan, high concentration collagen, I found that collagen I mixed with GelMA solved the factors transport issue, allowed formation of casted channels and importantly, it did not shrink over time when cultured with FRCs. Moreover, FRCs could stretch and create connections reminiscent of the lymph node network. In this research to find the best hydrogel formulation, I used different techniques to characterize the matrices and rationally progress in the optimization process such as SEM and SHG. A hydrogel formulation containing 5% GelMA and 1mg/ml collagen I resulted in bigger pores and longer and thinner fibrous structures observable by SEM, that reflected the FRCs stretching. Other works as well showed with SEM high porosity at such concentrations[92,263], but there is no characterization of hydrogel with added collagen. The addition of collagen increased FRC stretching probably because of the observable fibrous structures and potentially through cell-ECM signalling pathways that have not been furtherly investigated. Increasing the GelMA concentration above 5%, although allowed good channel formation and flow application, drastically hindered their stretching. On the other hand, SHG imaging showed that FRCs laden in this matrix were active and remodelled the matrix around them forming conduit-like structures, observed as collagen bundles 'wrapped' around their cellular protrusions, consistent with other studies examining FRC function in vivo [80,264]. These structures could explain the preferential positioning of lymphocytes along the FRCs protrusions in this 3D matrix, and preferential survival, in line with the knowledge that the FRC provide guidance and survival cues [112,113,266]. Its these structures and the Conduits formed that function as 'rails networks' to facilitate and direct cell movement and bridge the SCS to the cortex allowing delivery of antigens deep into the organ [4,43,82]. Current *in vitro* LN models do not take this component in consideration and here, I set out to form conduits and increase the complexity of the hydrogel-

based device through photoablation, which makes use of lasers to carve into the matrix. *In situ* micropatterning of vessels in hydrogels is becoming more widespread because of its high versatility and was used to create vessels that were endothelized and perfused [275,276]. A small limitation is that currently relies on multi-photon lasers and custom setups that are not open to any laboratory, but some efforts are being made to bring this to a wider audience. For instance, 'light-SABR' is a recent project by the Institut Pasteur which aims to build an open-source platform for photoablation which is attachable to in-use fluorescent microscopes. Usually, this technique is also constrained to patterning into stiff hydrogels. In my system however, small channels (ca.10µm in diameter) were carved in collagen/GelMA in user-defined patterns, stemming from the main casted channel and evolving from it. With this, it was possible to mimic lymph percolation, show by positive signalling from fluorescent microbeads when they were perfused through the main channel passing into the conduits-like structures. To my knowledge, this particular approach of evolving a vascular network from a casted channel with defined geometry has not been applied to other model systems. This was done in the presence of extruded B cell follicles positioned next to the main channel. Critically, because of the laser precision and the laser type, with this method it was possible to carve conduits with high levels of control on the 3 axes, without affecting cell viability of morphology in the area surrounding the cut. Other systems mostly use this technique to form hollow channels in acellular hydrogels that are then populated. Here, it was possible to carve directly into cell-laden matrices because the commercially available microdissection unit (ZEISS PALM MicroBeam) used for carving makes use of a UV laser, which is designed to isolate high-purity tissues from live cells.

Finally, *In vivo* LN have a specific microanatomical architecture where B cells reside in follicles separated from the T cell zone [2,3,32]; cells positioning and relation to one another is not defined by chance and reflects the organ function. Loss of function of the LN in disease often manifests in altered architecture. Therefore, to mimic LN architecture *in vitro* I developed approaches to impose cellular compartmentalization, generating separate B cell follicles and T cell zone. Cells positioning in the LN is a critical feature for its function *in vivo*, but it is not accurately represented by current *in vitro* LN models. Obtainment of compartmentalization includes self-assembling exerted by the cells in the *in vitro* tissue or by constraining the different cell types into separated chambers or spaces [222,231]. Self-assembling might require longer times to occur and necessitates external activation, while active cell separation is more immediate and was therefore explored. While current multi-compartment LN systems are

limited due to cell type choice and lack of enough interaction space, I developed a multi-compartment system which includes stromal populations and is completely built in hydrogel. Interestingly, the B cells follicles generated are of spherical shape due to the embedded extrusion maximising the interaction surface between B and T cells. B cells spheroids formation and blobs deposition did not give the desired results but extruding a cooled B cell-laden hydrogel solution from a syringe in a 3D bioprinting fashion, successfully allowed compartmentalization. Most importantly, with this technique a hard interface between B and T cells zone was avoided and cells could interact with each other freely observed through live microscopy. In the future, the method could be readily adapted to automated bioprinting system for increased accuracy and consistency.

6.5 Applications of the LN device

After optimizing both the biological and the structural components to allow application of flow, I applied the model with the aim of studying immune reactions and modelling the LN in cancer, which are critical processes not yet fully understood. First, I used PMA/Ionomycin as a general activation stimulus to which lymphocytes responded by displaying classic activation markers observed by flow cytometry. CD69, an early activation marker was dramatically upregulated both in T and B cells, while phenotypically the proportion of naïve cells decreased shifting mostly towards the EM population. Such strong response to activation obtained by PMA/Ionomycin was used as reference and positive control.

Although this experiment gave us some parameters on how cells can react in the device, PMA/Ionomycin is a general activator that in its mode of action does not engage immune specific receptors on the lymphocytes surface. Therefore, I used LPS, a common bacteria-derived molecule, that binds TLR receptors on the surface of immune cells triggering innate immunity mechanisms. By treating the device with LPS, lymphocytes displayed a similar molecular pattern to the one observed previously with PMA/Ionomycin, but T cells phenotype shifts were less evident. Other studies that examine immune responses to LPS *in vivo* also show strong T cells activation but do not show a population shift from naïve ($CD44^-$) to memory ($CD44^+$) phenotype. It seems that LPS in the LN acts by strongly stimulating APCs and B cells to release pro-inflammatory cytokines that indirectly activate T cells [277].
TLR receptors are expressed by many immune cells such as DCs, macrophages, TLR4-expressing T cells and B cells but are also found on some stromal population such as FRCs,

BECs and LECs. FRCs in particular respond to LPS by upregulating IFN- or TLR4-inducible or regulatory genes such as interferon regulatory factor 7, lymphocyte antigen 6 complex, locus A, and lipocalin 2 (LCN2). TLR4 seems correlated with secretion of chemokines that attract neutrophils (CXCL2 and CXCL5), monocytes (CXCL3), and lymphocytes (CXCL13 and CCL20) [278,279]. It seems likely that an orchestrated response to LPS by several cell types in the 3D system might have brought to a general inflammation state, detected in T cells. In addition, TLR4 which specifically is engaged by LPS is found B cells and therefore they can be directly activated. In addition, molecules like TNF-α and IFN-γ produced by macrophages in response to LPS, can potentiate its action and furtherly activate immune cells creating inflamed microenvironment [280].

One of the most important features of the LNs is their ability to recognize a specific antigen, processed and presented to T cells by APCs, and mount an antigen-specific immune reaction. The interaction between APC and the cognate T cell, leads to its clonal expansion resulting in a higher proportion of antigen-specific T cells. In the LN device, we simulated the mixed LN T cell repertoire by mixing WT and engineered OT-I T cells, which specifically react to SIINFEKL. While PMA activated both populations, observed through CD69 upregulation in $CD8^+$ T cells, only OT-1 cells were activated by the OVA peptide, undergoing a significant population shift. from a mostly naïve state to CM ($CD62L^+CD44^+$). The EM ($CD62L^-CD44^+$) population was not here affected as observed with activation from PMA/Ionomycin. This phenotypical difference may be due to the specific mechanism of action which, in case of SIINFEKL, involves the TCR on $CD8^+$ T cells and does not occur with LPS or PMA/Ionomycin. Recent data suggest that TCR engagement and signalling is essential for cytokine-mediated T cell differentiation and memory generation [281,282]. In addition, during immunization by infection or by vaccine, long-lived CM T cells are developed in order to help triggering a quicker and potent secondary response to a specific antigen e.g. in the case of a vaccine booster dose or a second antigen encounter. Interestingly, medium collected after PMA or SIINFEKL treatment identified a diverse array of secreted molecules and significant changes among conditions. Medium from SIINFEKL stimulation showed drastic increase in CXCL9 and CXCL10, IFN-γ-induced activation cytokines, reported to be produced mostly by myeloid and stromal populations which are present in the device [283]. Stimulated T cells in this system might have released IFN-γ that activated the surrounding populations to secrete the two cytokines but IFN-γ was not detected in the cytokine array performed on the media. A reason

for this could be that being one of the initial secreted inflammatory molecules, it could have been cleared before detection. CXCL9 and CXCL10 have a crucial role in the LN in actively inducing recruitment and expansion of CM $CD8^+$ T cells after an infection [283,284]. It is likely then that their upregulation in the device might be linked to the CM $CD8^+$ T cells expansion. These data taken together, suggest that the LN device offers the possibility of multiple readouts, could be included as a part of vaccine studies, especially whether human lymphocytes will be used. It has been shown that *in vitro* human B cells are able to produce detectable antibodies following immunization after 1-2 weeks [285]. Although I did not test directly for this in the current study, it is likely that also antigen-specific antibodies production could be here measured, in addition to quantification of memory T cells. In the future, it would be of great interest to adapt this model to study human immunology and vaccines responses.

6.6 TDLN modelling

In the last part of this thesis, I applied the LN device in the context of cancer with the aim to model a TDLN *in vitro*. A TDLN is not only defined by an increase in shape but by several other molecular alterations, observed in lymphocytes and stromal cells, that together create an immunosuppressive environment for cancer spreading [119,286–288]. *In vivo*, lymph drains from the tumour to the sentinel LN, exposing all its cellular components to a myriad of antigens and metabolites formed in the TME [126,287]. To obtain a source of tumour-cell derived factors *in vitro* we used TCM from B16 cells that was used for incubating the LN device. Following stimulation, lymphocytes did not alter their surface expression of activation markers (CD69) and their T cells phenotypes (CD62L, CD44). This could be due to the incubation time of 72h which could be extended, or the limited set of markers used. *In vivo* an enrichment in PD-1^+ T cells that overexpress CD69 and CD44 is observed, suggesting increased activation of such population[288]. However, what is the effect on lymphocytes exposed to tumour factors is still unclear, and likely confounded by the interaction of multiple cell types. On one hand, activated tumour-specific T cells should exit the LN towards tumours, but on the other hand, the immunosuppressive environment which emerges within the LN, impairs anti-tumour immunity and support metastasis. Recent reports show that stromal deregulation and an increase in the regulatory T cells (Treg) population occur in TDLNs [120,124,287], and these may contribute to the generation of this suppressive niche and failed anti-tumour immunity. In the future, this model could prove a powerful tool to learn whether the increasing Treg phenotype arises from existing T cell populations exposed to tumour drained factors. Previously, the Shields lab identified a

series of key altered genes in the FRC stromal population that define the altered function of the TDLN [119]. Using this data as a marker of tumour induced stromal changes, I quantified key FRC genes after treatment with TCM. TCM induced *Il-7* downregulation, consistent with changes observed *in vivo*. In contrast, other genes such as *Pdpn, Thy1 and Col1a* did not show significant changes. TCM is a commonly used tool. However, it does not fully represent a tumour as it derives from a 2D monoculture system and does not incorporate any other TME cell type. Therefore, it may lack the complexity of signals delivered from the TME, which are needed to induce stromal changes. To address this, we focused on building a more representative tumour model in close collaboration with Huang lab that could be potentially used as an upstream source of tumour factors in direct connection with the LN model. To create the 3D tumour model, we used 3D bioprinting which allowed us to obtain core-shell structures containing pancreatic tumour cells and CAFs. Although many are the existing tumour 3D models in literature [187,289], not many take in consideration CAFs and immune populations. With this approach we could obtain scaffold-free multi-cellular tumouroids in a high throughput manner. In addition, studying CAFs phenotype in the new system we showed for the first time a resurgence of cell heterogeneity in a similar fashion to *in vivo* tumours, where $CD34^+$ and αSMA^+ CAFs population are found together [129]. Although a small percentage of $CD34^+$ CAFs was found in tumouroids, it is possible that by prolonging the cell culture time their relative proportion might change, but this has not been tested. Subsequently, we included the tumouroids in a 3D hydrogel where immune cells were added to mimic the complex situation observed in *in vivo* TME and tested with anti-CTLA4. To my knowledge, the creation of a 3D environment where both core-shell tumouroids and immune cells could interact and be studied was not described yet and such platform could represent a valid tool to study disease and drug treatments. Although we did not proceed to create a continuous physical two-way fluidic system between the tumouroid and the LN compartment, due to time restrictions, we performed some initial experiments where the LN device was treated with medium collected from the previously described engineered TME (TMECM). Following incubation with this richer medium containing also factors from CAFs and immune cells, induced *Il-7* downregulation. The other markers tested did not show significant changes, but it would be interesting in the future to test whether other changes are observed with a continuous two-way flow system where the two compartments communicate directly, or whether by expanding the set of genes measured, it would be possible to capture new altered pathways not previously observed.

6.7 Conclusion and future directions

Organ-on-chip microfluidic technologies together with 3D bioprinting are at the leading edge of the current *in vitro* research. These 3D models can be used to perform studies on cancer cell dynamic, anti-metastatic drug testing, vaccine development and personalized medicine. Such technologies sit in between 2D traditional systems and animal models, and hopefully they will provide new insights on cancer biology, LN transformation and anti-metastatic treatments.
Here, we showed the creation of a novel LN-on-a-chip model which recapitulates several features of the *in vivo* organ, for 3D immunobiology applications such as drug testing and disease modelling. This hydrogel-based device allowed incorporation of multiple cellular components from both cell lines and *ex vivo* tissues in a finely tuned 3D matrix, for their physiological growth. Biophysical flow is facilitated by a fluidic system composed of two channels casted directly into the matrix, which are connected to an external pumping system. We proved the possibility to initiate a wide range of immune responses given different stimuli, up to antigen-specific responses. Finally, we have begun the process of TDLN modelling *in vitro* and were able to measure molecular changes similarly to what is observed *in vivo*. The device allowed multiple types of readouts and we showed its suitability for flow cytometry analysis of surface markers expression, cell sorting and RNA quantification, confocal and live-cell microscopy.

There are still many improvements and opportunities that can be explored in this system that in the future I would like to address. First, in order to obtain more reproducible devices, the fabrication process of channel formation and B cell follicles deposition could be automated and executed with a 3D bioprinted, such as BioArm. In my experience, when I 3D printed channels with a sacrificial ink I struggled to connect them to an external pumping system and thus I have switched to needle-casting. Future work should focus on finding a solution to this issue to create chips in a fully automated way. The LN device was optimized for optimal live-cell imaging, and we managed to observe movement of cells in the 3D environment e.g. T and B cells interacting at the follicle border. It would be interesting, by prolonging the imaging time, to observe whether general cell motility changes in response to an antigen or an inflamed status and whether it is possible to detect formation of germinal centers within the follicles. In addition, with longer culture time it would be possible that FRCs would line and remodel the photoablated conduits. The LN is a highly dynamic organ and in the *in vivo* 3D environment there is constant recirculation of lymphocytes. In the LN device, I have not focused of

movement of cells in and out of hydrogel, but this could be performed by including live cells into the flow system. Similarly, as the LN represents a preferential route for metastatic cancer, tumour cells could be perfused to investigate extravasation mechanisms, and the device could be then used for drug testing of chemo- or immunotherapy compounds. As the LN undergoes alterations even before cancer cells dissemination, further work should be focused on studying this early event in the device. As we showed how the LN device can be transformed *in vitro,* it will be of interest to study in the device whether the transformation process can be reverted through administration of drugs and can be measured molecularly. Besides, it has been shown *in vivo* repopulation of stroma-laden collagen sponges by murine lymphocytes [47]. It would be interesting to examine whether in the LN device, if the hydrogel is only laden with FRCs and photoablated conduits, lymphocytes perfused through the channel would populate it and self-assemble into B and T cells compartments.

Finally, gaining access to human tissues to replace the murine cellular component, would be desirable. Not only this would allow us to perform longer experiments and obtain more information from each device, but it would also benefit the overall clinical translation potential of the model. For instance, this would open opportunities to analyze antigen-specific antibodies secretion from the B cells, which we could not examine. Moreover, building from this optimized 3D culture and flow system, the switching process could be accomplished promptly.

BIBLIOGRAPHY

1. von Andrian, U. H. & Mempel, T. R. Homing and cellular traffic in lymph nodes. *Nature Reviews Immunology 2003 3:11* **3**, 867–878 (2003).
2. van den Broeck, W., Derore, A. & Simoens, P. Anatomy and nomenclature of murine lymph nodes: Descriptive study and nomenclatory standardization in BALB/cAnNCrl mice. *J Immunol Methods* **312**, 12–19 (2006).
3. Willard-Mack, C. L. Normal structure, function, and histology of lymph nodes. *Toxicol Pathol* **34**, 409–424 (2006).
4. Gretz, J. E., Norbury, C. C., Anderson, A. O., Proudfoot, A. E. I. & Shaw, S. Lymph-borne chemokines and other low molecular weight molecules reach high endothelial venules via specialized conduits while a functional barrier limits access to the lymphocyte microenvironments in lymph node cortex. *J Exp Med* **192**, 1425–1439 (2000).
5. Kaldjian, E. P., Elizabeth Gretz, J., Anderson, A. O., Shi, Y. & Shaw, S. Spatial and molecular organization of lymph node T cell cortex: a labyrinthine cavity bounded by an epithelium-like monolayer of fibroblastic reticular cells anchored to basement membrane-like extracellular matrix. *Int Immunol* **13**, 1243–1253 (2001).
6. Sixt, M. *et al.* The conduit system transports soluble antigens from the afferent lymph to resident dendritic cells in the T cell area of the lymph node. *Immunity* **22**, 19–29 (2005).
7. Heesters, B. A., Myers, R. C. & Carroll, M. C. Follicular dendritic cells: dynamic antigen libraries. *Nature Reviews Immunology 2014 14:7* **14**, 495–504 (2014).
8. Schudel, A., Francis, D. M. & Thomas, S. N. Material design for lymph node drug delivery. *Nature Reviews Materials 2019 4:6* **4**, 415–428 (2019).
9. GOWANS, J. L. The Effect of the Continuous Re-infusion of Lymph and Lymphocytes on the Output of Lymphocytes from the Thoracic Duct of Unanaesthetized Rats. *Br J Exp Pathol* **38**, 67 (1957).
10. Gowans, J. L. The recirculation of lymphocytes from blood to lymph in the rat. *J Physiol* **146**, 54–69 (1959).
11. Takeda, A., Sasaki, N. & Miyasaka, M. The molecular cues regulating immune cell trafficking. *Proceedings of the Japan Academy, Series B* **93**, 183–195 (2017).
12. Schoefl, G. I. & Miles, R. E. THE MIGRATION OF LYMPHOCYTES ACROSS THE VASCULAR ENDOTHELIUM IN LYMPHOID TISSUE : A REEXAMINATION. *J Exp Med* **136**, 568 (1972).
13. Mackay, C. R., Marston, W. L. & Dudler, L. Naive and memory T cells show distinct pathways of lymphocyte recirculation. *Journal of Experimental Medicine* **171**, 801–817 (1990).
14. Hunter, M. C., Teijeira, A. & Halin, C. T cell trafficking through lymphatic vessels. *Front Immunol* **7**, 613 (2016).
15. Martens, R. *et al.* Efficient homing of T cells via afferent lymphatics requires mechanical arrest and integrin-supported chemokine guidance. *Nat Commun* **11**, (2020).
16. Brinkman, C. C. *et al.* Treg engage lymphotoxin beta receptor for afferent lymphatic transendothelial migration. *Nature Communications 2016 7:1* **7**, 1–16 (2016).
17. Piao, W. *et al.* Regulatory T Cells Condition Lymphatic Endothelia for Enhanced Transendothelial Migration. *Cell Rep* **30**, 1052-1062.e5 (2020).
18. Ulvmar, M. H. *et al.* The atypical chemokine receptor CCRL1 shapes functional CCL21 gradients in lymph nodes. *Nature Immunology 2014 15:7* **15**, 623–630 (2014).

19. Mori, S. *et al.* Mice lacking expression of the chemokines CCL21-ser and CCL19 (plt mice) demonstrate delayed but enhanced T cell immune responses. *J Exp Med* **193**, 207–217 (2001).
20. Förster, R. *et al.* CCR7 Coordinates the Primary Immune Response by Establishing Functional Microenvironments in Secondary Lymphoid Organs. *Cell* **99**, 23–33 (1999).
21. Miller, M. J., Wei, S. H., Cahalan, M. D. & Parker, I. Autonomous T cell trafficking examined in vivo with intravital two-photon microscopy. *Proc Natl Acad Sci U S A* **100**, 2604–2609 (2003).
22. Krummel, M. F., Bartumeus, F. & Gérard, A. T cell migration, search strategies and mechanisms. *Nat Rev Immunol* **16**, 193–201 (2016).
23. Kaech, S. M. & Wherry, E. J. Heterogeneity and cell-fate decisions in effector and memory CD8+ T cell differentiation during viral infection. *Immunity* **27**, 393–405 (2007).
24. Kastenmüller, W. *et al.* Peripheral prepositioning and local CXCL9 chemokine-mediated guidance orchestrate rapid memory CD8+ T cell responses in the lymph node. *Immunity* **38**, 502–513 (2013).
25. Takeda, A. *et al.* Fibroblastic reticular cell-derived lysophosphatidic acid regulates confined intranodal T-cell motility. *Elife* **5**, (2016).
26. Legler, D. F. *et al.* B cell-attracting chemokine 1, a human CXC chemokine expressed in lymphoid tissues, selectively attracts B lymphocytes via BLR1/CXCR5. *J Exp Med* **187**, 655–660 (1998).
27. Sinha, R. K., Park, C., Hwang, I. Y., Davis, M. D. & Kehrl, J. H. B Lymphocytes Exit Lymph Nodes through Cortical Lymphatic Sinusoids Near to Lymph Node Follicles by a Mechanism Independent of S1P-Mediated Chemotaxis. *Immunity* **30**, 434 (2009).
28. Grigorova, I. L. *et al.* Cortical sinus probing, S1P1-dependent entry and flow-based capture of egressing T cells. *Nat Immunol* **10**, 58–65 (2009).
29. Schwab, S. R. & Cyster, J. G. Finding a way out: lymphocyte egress from lymphoid organs. *Nature Immunology 2007 8:12* **8**, 1295–1301 (2007).
30. Shiow, L. R. *et al.* CD69 acts downstream of interferon-α/β to inhibit S1P1 and lymphocyte egress from lymphoid organs. *Nature 2006 440:7083* **440**, 540–544 (2006).
31. Park, C. *et al.* Lymph node B lymphocyte trafficking is constrained by anatomy and highly dependent upon chemoattractant desensitization. *Blood* **119**, 978–989 (2012).
32. Girard, J. P., Moussion, C. & Förster, R. HEVs, lymphatics and homeostatic immune cell trafficking in lymph nodes. *Nature Reviews Immunology 2012 12:11* **12**, 762–773 (2012).
33. Krishnamurty, A. T. & Turley, S. J. Lymph node stromal cells: cartographers of the immune system. *Nature Immunology 2020 21:4* **21**, 369–380 (2020).
34. Soudja, S. M. *et al.* Disrupted lymph node and splenic stroma in mice with induced inflammatory melanomas is associated with impaired recruitment of T and dendritic cells. doi:10.1371/journal.pone.0022639ï.
35. Malhotra, D. *et al.* Transcriptional profiling of stroma from inflamed and resting lymph nodes defines immunological hallmarks. *Nat Immunol* **13**, 499–510 (2012).
36. Astarita, J. L. *et al.* The CLEC-2–podoplanin axis controls the contractility of fibroblastic reticular cells and lymph node microarchitecture. *Nature Immunology 2014 16:1* **16**, 75–84 (2014).
37. Rodda, L. B. *et al.* Single-Cell RNA Sequencing of Lymph Node Stromal Cells Reveals Niche-Associated Heterogeneity. *Immunity* **48**, 1014-1028.e6 (2018).

38. Brown, F. D. & Turley, S. J. Fibroblastic Reticular Cells: Organization and Regulation of the T Lymphocyte Life Cycle. *J Immunol* **194**, 1389 (2015).
39. Novkovic, M., Onder, L., Bocharov, G. & Ludewig, B. Topological Structure and Robustness of the Lymph Node Conduit System. *Cell Rep* **30**, 893-904.e6 (2020).
40. Katakai, T., Hara, T., Sugai, M., Gonda, H. & Shimizu, A. Lymph Node Fibroblastic Reticular Cells Construct the Stromal Reticulum via Contact with Lymphocytes. *Journal of Experimental Medicine* **200**, 783–795 (2004).
41. Dubey, L. K. *et al.* Lymphotoxin-Dependent B Cell-FRC Crosstalk Promotes De Novo Follicle Formation and Antibody Production following Intestinal Helminth Infection. *Cell Rep* **15**, 1527–1541 (2016).
42. Roozendaal, R., Mebius, R. E. & Kraal, G. The conduit system of the lymph node. *Int Immunol* **20**, 1483–1487 (2008).
43. Roozendaal, R. *et al.* Conduits Mediate Transport of Low-Molecular-Weight Antigen to Lymph Node Follicles. *Immunity* **30**, 264–276 (2009).
44. Alvarenga, H. G. & Marti, L. Multifunctional roles of reticular fibroblastic cells: More than meets the eye? *J Immunol Res* **2014**, (2014).
45. Link, A. *et al.* Fibroblastic reticular cells in lymph nodes regulate the homeostasis of naive T cells. *Nature Immunology 2007 8:11* **8**, 1255–1265 (2007).
46. Denton, A. E., Roberts, E. W., Linterman, M. A. & Fearon, D. T. Fibroblastic reticular cells of the lymph node are required for retention of resting but not activated CD8+ T cells. *Proc Natl Acad Sci U S A* **111**, 12139–12144 (2014).
47. Kobayashi, Y. & Watanabe, T. Gel-Trapped Lymphorganogenic Chemokines Trigger Artificial Tertiary Lymphoid Organs and Mount Adaptive Immune Responses In Vivo. *Front Immunol* **7**, (2016).
48. Fletcher, A. L. *et al.* Lymph node fibroblastic reticular cells directly present peripheral tissue antigen under steady-state and inflammatory conditions. *J Exp Med* **207**, 689–697 (2010).
49. Yip, L. *et al.* Deaf1 isoforms control the expression of genes encoding peripheral tissue antigens in the pancreatic lymph nodes during type 1 diabetes. *Nat Immunol* **10**, 1026–1033 (2009).
50. Dubrot, J. *et al.* Lymph node stromal cells acquire peptide-MHCII complexes from dendritic cells and induce antigen-specific $CD4^+$ T cell tolerance. *J Exp Med* **211**, 1153–1166 (2014).
51. Yang, C. Y. *et al.* Trapping of naive lymphocytes triggers rapid growth and remodeling of the fibroblast network in reactive murine lymph nodes. *Proc Natl Acad Sci U S A* **111**, E109 (2014).
52. Buettner, M., Pabst, R. & Bode, U. Stromal cell heterogeneity in lymphoid organs. *Trends Immunol* **31**, 80–86 (2010).
53. Förster, R., Braun, A. & Worbs, T. Lymph node homing of T cells and dendritic cells via afferent lymphatics. *Trends Immunol* **33**, 271–280 (2012).
54. Clement, C. C. *et al.* Protein expression profiles of human lymph and plasma mapped by 2D-DIGE and 1D SDS–PAGE coupled with nanoLC–ESI–MS/MS bottom-up proteomics. *J Proteomics* **78**, 172–187 (2013).
55. Clement, C. C. & Santambrogio, L. The lymph self-antigen repertoire. *Front Immunol* **4**, 424 (2013).
56. Broggi, M. A. S. *et al.* Tumor-associated factors are enriched in lymphatic exudate compared to plasma in metastatic melanoma patients. *J Exp Med* **216**, 1091 (2019).
57. Clement, C. C., Rotzschke, O. & Santambrogio, L. The lymph as a pool of self antigens. *Trends Immunol* **32**, 6 (2011).

58. Russo, E. *et al.* Intralymphatic CCL21 Promotes Tissue Egress of Dendritic Cells through Afferent Lymphatic Vessels. *Cell Rep* **14**, 1723–1734 (2016).
59. Iolyeva, M. *et al.* Interleukin-7 is produced by afferent lymphatic vessels and supports lymphatic drainage. *Blood* **122**, 2271–2281 (2013).
60. Ulvmar, M. H. *et al.* The atypical chemokine receptor CCRL1 shapes functional CCL21 gradients in lymph nodes. *Nature Immunology 2014 15:7* **15**, 623–630 (2014).
61. Takeda, A. *et al.* Single-Cell Survey of Human Lymphatics Unveils Marked Endothelial Cell Heterogeneity and Mechanisms of Homing for Neutrophils. *Immunity* **51**, 561-572.e5 (2019).
62. Johnson, L. A. *et al.* Dendritic cells enter lymph vessels by hyaluronan-mediated docking to the endothelial receptor LYVE-1. *Nat Immunol* **18**, 762–770 (2017).
63. Hirosue, S. *et al.* Steady-State Antigen Scavenging, Cross-Presentation, and CD8 + T Cell Priming: A New Role for Lymphatic Endothelial Cells . *The Journal of Immunology* **192**, 5002–5011 (2014).
64. Potin, L. *et al.* Antigen presentation via MHC class II by lymphatic endothelial cells dampens CD4+ T cell response (IRC7P.436). *The Journal of Immunology* **194**, (2015).
65. Tewalt, E. F. *et al.* Lymphatic endothelial cells induce tolerance via PD-L1 and lack of costimulation leading to high-level PD-1 expression on CD8 T cells. *Blood* **120**, 4772–4782 (2012).
66. Kedl, R. M. *et al.* Migratory dendritic cells acquire and present lymphatic endothelial cell-archived antigens during lymph node contraction. *Nature Communications 2017 8:1* **8**, 1–15 (2017).
67. Walsh, S. M. *et al.* Molecular tracking devices quantify antigen distribution and archiving in the murine lymph node. *Elife* **10**, (2021).
68. Tamburini, B. A., Burchill, M. A. & Kedl, R. M. Antigen capture and archiving by lymphatic endothelial cells following vaccination or viral infection. *Nature Communications 2014 5:1* **5**, 1–13 (2014).
69. Fletcher, A. L., Malhotra, D. & Turley, S. J. Lymph node stroma broaden the peripheral tolerance paradigm. *Trends Immunol* **32**, 12–18 (2011).
70. Herzog, B. H. *et al.* Podoplanin maintains high endothelial venule integrity by interacting with platelet CLEC-2. *Nature* **502**, 105–109 (2013).
71. Cohen, J. N. *et al.* Lymph node-resident lymphatic endothelial cells mediate peripheral tolerance via Aire-independent direct antigen presentation. *J Exp Med* **207**, 681–688 (2010).
72. Brulois, K. *et al.* A molecular map of murine lymph node blood vascular endothelium at single cell resolution. *Nature Communications 2020 11:1* **11**, 1–15 (2020).
73. Yue, B. Biology of the Extracellular Matrix: An Overview. *J Glaucoma* **23**, S20 (2014).
74. Hinz, B. The extracellular matrix and transforming growth factor-β1: Tale of a strained relationship. *Matrix Biology* **47**, 54–65 (2015).
75. Durbeej, M. Laminins. *Cell Tissue Res* **339**, 259–268 (2010).
76. Zollinger, A. J. & Smith, M. L. Fibronectin, the extracellular glue. *Matrix Biology* **60–61**, 27–37 (2017).
77. Morgado, F. N., da Silva, A. V. A. & Porrozzi, R. Infectious Diseases and the Lymphoid Extracellular Matrix Remodeling: A Focus on Conduit System. *Cells 2020, Vol. 9, Page 725* **9**, 725 (2020).
78. Sobocinski, G. P. *et al.* Ultrastructural localization of extracellular matrix proteins of the lymph node cortex: Evidence supporting the reticular network as a pathway for lymphocyte migration. *BMC Immunol* **11**, 1–11 (2010).

79. Song, J. *et al.* Extracellular matrix of secondary lymphoid organs impacts on B-cell fate and survival. *Proc Natl Acad Sci U S A* **110**, (2013).
80. Martinez, V. G. *et al.* Fibroblastic Reticular Cells Control Conduit Matrix Deposition during Lymph Node Expansion. *Cell Rep* **29**, 2810-2822.e5 (2019).
81. Sixt, M. *et al.* The Conduit System Transports Soluble Antigens from the Afferent Lymph to Resident Dendritic Cells in the T Cell Area of the Lymph Node. *Immunity* **22**, 19–29 (2005).
82. Reynoso, G. v. *et al.* Lymph node conduits transport virions for rapid T cell activation. *Nature Immunology 2019 20:5* **20**, 602–612 (2019).
83. Thierry, G. R. *et al.* The conduit system exports locally secreted IgM from lymph nodes. *Journal of Experimental Medicine* **215**, 2972–2983 (2018).
84. Novkovic, M., Onder, L., Bocharov, G. & Ludewig, B. Topological Structure and Robustness of the Lymph Node Conduit System. *Cell Rep* **30**, 893-904.e6 (2020).
85. Song, J. *et al.* Extracellular matrix of secondary lymphoid organs impacts on B-cell fate and survival. *Proc Natl Acad Sci U S A* **110**, E2915–E2924 (2013).
86. Brassart-Pasco, S. *et al.* Tumor Microenvironment: Extracellular Matrix Alterations Influence Tumor Progression. *Front Oncol* **10**, 397 (2020).
87. Najafi, M. *et al.* Macrophage polarity in cancer: A review. *J Cell Biochem* **120**, 2756–2765 (2019).
88. Kehlet, S. N. *et al.* Excessive collagen turnover products are released during colorectal cancer progression and elevated in serum from metastatic colorectal cancer patients. *Scientific Reports 2016 6:1* **6**, 1–7 (2016).
89. Annabi, N. *et al.* 25th Anniversary Article: Rational Design and Applications of Hydrogels in Regenerative Medicine. *Advanced Materials* **26**, 85–124 (2014).
90. Pérez, R. A., Won, J. E., Knowles, J. C. & Kim, H. W. Naturally and synthetic smart composite biomaterials for tissue regeneration. *Adv Drug Deliv Rev* **65**, 471–496 (2013).
91. Kyburz, K. A. & Anseth, K. S. Synthetic Mimics of the Extracellular Matrix: How Simple is Complex Enough? *Ann Biomed Eng* **43**, 489 (2015).
92. Yue, K. *et al.* Synthesis, properties, and biomedical applications of gelatin methacryloyl (GelMA) hydrogels. *Biomaterials* **73**, 254–271 (2015).
93. Liu, Y. & Chan-Park, M. B. A biomimetic hydrogel based on methacrylated dextran-graft-lysine and gelatin for 3D smooth muscle cell culture. *Biomaterials* **31**, 1158–1170 (2010).
94. Loessner, D. *et al.* Functionalization, preparation and use of cell-laden gelatin methacryloyl-based hydrogels as modular tissue culture platforms. *Nat Protoc* **11**, 727–746 (2016).
95. Pepelanova, I., Kruppa, K., Scheper, T. & Lavrentieva, A. Gelatin-Methacryloyl (GelMA) Hydrogels with Defined Degree of Functionalization as a Versatile Toolkit for 3D Cell Culture and Extrusion Bioprinting. *Bioengineering (Basel)* **5**, (2018).
96. Uchida, K. & Okazaki, K. Lymphadenopathy. *Autoimmune Pancreatitis* 135–141 (2021) doi:10.1007/978-3-642-55086-7_20.
97. Baptista, A. P. *et al.* Lymph node stromal cells constrain immunity via MHC class II self-antigen presentation. *Elife* **3**, 1–18 (2014).
98. Dubrot, J. *et al.* Lymph node stromal cells acquire peptide-MHCII complexes from dendritic cells and induce antigen-specific $CD4^+$ T cell tolerance. *J Exp Med* **211**, 1153–1166 (2014).
99. Malhotra, D. *et al.* Transcriptional profiling of stroma from inflamed and resting lymph nodes defines immunological hallmarks. *Nat Immunol* **13**, 499–510 (2012).

100. Heesters, B. A., van der Poel, C. E., Das, A. & Carroll, M. C. Antigen Presentation to B Cells. *Trends Immunol* **37**, 844–854 (2016).
101. Bajnok, A., Ivanova, M., Rigó, J. & Toldi, G. The Distribution of Activation Markers and Selectins on Peripheral T Lymphocytes in Preeclampsia. *Mediators Inflamm* **2017**, (2017).
102. Assen, F. P. *et al.* Multitier mechanics control stromal adaptations in the swelling lymph node. *Nature Immunology 2022* 1–10 (2022) doi:10.1038/s41590-022-01257-4.
103. Knop, L. *et al.* IL-7 derived from lymph node fibroblastic reticular cells is dispensable for naive T cell homeostasis but crucial for central memory T cell survival. *Eur J Immunol* **50**, 846–857 (2020).
104. Saxena, V. *et al.* Role of Lymph Node Stroma and Microenvironment in T Cell Tolerance. *Immunol Rev* **292**, 9 (2019).
105. Kumar, V. *et al.* A dendritic cell-stromal axis maintains immune responses in lymph nodes. *Immunity* **42**, 719 (2015).
106. Gregory, J. L. *et al.* Infection Programs Sustained Lymphoid Stromal Cell Responses and Shapes Lymph Node Remodeling upon Secondary Challenge. *Cell Rep* **18**, 406–418 (2017).
107. Alexandre, Y. O. & Mueller, S. N. Stromal cell networks coordinate immune response generation and maintenance. *Immunol Rev* **283**, 77–85 (2018).
108. Callahan, V. *et al.* The pro-inflammatory chemokines cxcl9, cxcl10 and cxcl11 are upregulated following sars-cov-2 infection in an akt-dependent manner. *Viruses* **13**, 1062 (2021).
109. Norose, K., Kikumura, A., Luster, A. D., Hunter, C. A. & Harris, T. H. CXCL10 is required to maintain T-cell populations and to control parasite replication during chronic ocular toxoplasmosis. *Invest Ophthalmol Vis Sci* **52**, 389–398 (2011).
110. St John, A. L. & Abraham, S. N. Salmonella disrupts lymph node architecture by TLR4-mediated suppression of homeostatic chemokines. *Nat Med* **15**, 1259–1265 (2009).
111. Ng, C. T., Nayak, B. P., Schmedt, C. & Oldstone, M. B. A. Immortalized clones of fibroblastic reticular cells activate virus-specific T cells during virus infection. *Proc Natl Acad Sci U S A* **109**, 7823–7828 (2012).
112. Steel, K. E., Anderson, A. O. & Mohamadzadeh, M. Fibroblastic reticular cell infection by hemorrhagic fever viruses. *Immunotherapy* **1**, 187–197 (2009).
113. Fletcher, A. L., Acton, S. E. & Knoblich, K. Lymph node fibroblastic reticular cells in health and disease. *Nature Reviews Immunology 2015 15:6* **15**, 350–361 (2015).
114. Siegert, S. *et al.* Fibroblastic Reticular Cells From Lymph Nodes Attenuate T Cell Expansion by Producing Nitric Oxide. *PLoS One* **6**, e27618 (2011).
115. Bordon, Y. Breaking ranks in the lymph node. *Nature Reviews Immunology 2015 15:3* **15**, 132–132 (2015).
116. SMITH, R. O. & WOOD, W. B. CELLULAR MECHANISMS OF ANTIBACTERIAL DEFENSE IN LYMPH NODES II. THE ORIGIN AND FILTRATION EFFECT OF GRANULOCYTES IN THE NODAL SINUSES DURING ACUTE BACTERIAL LYMPHADENITIS. *Journal of Experimental Medicine* **90**, 567–576 (1949).
117. Siggins, M. K. & Sriskandan, S. Bacterial Lymphatic Metastasis in Infection and Immunity. *Cells 2022, Vol. 11, Page 33* **11**, 33 (2021).
118. Ferris, R. L., Lotze, M. T., Leong, S. P. L., Hoon, D. S. B. & Morton, D. L. Lymphatics, Lymph Nodes and the Immune System: Barriers and Gateways for Cancer Spread. *Clin Exp Metastasis* **29**, 729 (2012).

119. Riedel, A., Shorthouse, D., Haas, L., Hall, B. A. & Shields, J. Tumor-induced stromal reprogramming drives lymph node transformation. *Nat Immunol* **17**, 1118–1127 (2016).
120. Munn, D. H. & Mellor, A. L. The tumor-draining lymph node as an immune-privileged site. *Immunol Rev* **213**, 146–158 (2006).
121. Rohner, N. A. *et al.* Lymph node biophysical remodeling is associated with melanoma lymphatic drainage. *The FASEB Journal* **29**, 4512–4522 (2015).
122. O'Connor, R. A. *et al.* Adjuvant immunotherapy of experimental autoimmune encephalomyelitis: immature myeloid cells expressing CXCL10 and CXCL16 attract CXCR3+CXCR6+ and myelin-specific T cells to the draining lymph nodes rather than the central nervous system. *J Immunol* **188**, 2093–2101 (2012).
123. Jones, D. *et al.* Solid stress impairs lymphocyte infiltration into lymph-node metastases. *Nat Biomed Eng* **5**, 1426–1436 (2021).
124. Riedel, A. *et al.* Tumor-Derived Lactic Acid Modulates Activation and Metabolic Status of Draining Lymph Node Stroma. *Cancer Immunol Res* **10**, 482–497 (2022).
125. Qian, C. N. *et al.* Preparing the 'soil': the primary tumor induces vasculature reorganization in the sentinel lymph node before the arrival of metastatic cancer cells. *Cancer Res* **66**, 10365–10376 (2006).
126. Habenicht, L. M., Albershardt, T. C., Iritani, B. M. & Ruddell, A. Distinct mechanisms of B and T lymphocyte accumulation generate tumor-draining lymph node hypertrophy. *https://doi.org/10.1080/2162402X.2016.1204505* **5**, (2016).
127. Ruddell, A., Croft, A., Kelly-Spratt, K., Furuya, M. & Kemp, C. J. Tumors induce coordinate growth of artery, vein, and lymphatic vessel triads. *BMC Cancer* **14**, 1–11 (2014).
128. Hirakawa, S. *et al.* VEGF-A induces tumor and sentinel lymph node lymphangiogenesis and promotes lymphatic metastasis. *J Exp Med* **201**, 1089–1099 (2005).
129. Davidson, S. *et al.* Single-Cell RNA Sequencing Reveals a Dynamic Stromal Niche That Supports Tumor Growth. *Cell Rep* **31**, (2020).
130. Harrell, M. I., Iritani, B. M. & Ruddell, A. Lymph node mapping in the mouse. *J Immunol Methods* **332**, 170–174 (2008).
131. Kohrt, H. E. *et al.* Profile of immune cells in axillary lymph nodes predicts disease-free survival in breast cancer. *PLoS Med* **2**, 0904–0919 (2005).
132. Suy, R., Thomis, S. & Fourneau, I. The discovery of lymphatic system in the seventeenth century. Part I: the early history. *http://dx.doi.org/10.1080/00015458.2016.1176792* **116**, 260–266 (2016).
133. Eimas, R. The Great Anatomy of Paolo Mascagni. *Books Iowa* **38**, 46–53 (1983).
134. Natale, G., Bocci, G. & Ribatti, D. Scholars and scientists in the history of the lymphatic system. *J Anat* **231**, 417 (2017).
135. de Bree, E., Tsiaoussis, J. & Schoretsanitis, G. The History of Lymphatic Anatomy and the Contribution of Frederik Ruysch. *Hellenic Journal of Surgery 2018 90:6* **90**, 308–314 (2019).
136. Dzhagalov, I. L., Melichar, H. J., Ross, J. O., Herzmark, P. & Robey, E. A. Two-Photon Imaging of the Immune System. *Curr Protoc Cytom* **60**, 12.26.1-12.26.20 (2012).
137. Choe, K. *et al.* Intravital three-photon microscopy allows visualization over the entire depth of mouse lymph nodes. *Nature Immunology 2022 23:2* **23**, 330–340 (2022).
138. Kastenmüller, W., Torabi-Parizi, P., Subramanian, N., Lämmermann, T. & Germain, R. N. A Spatially-Organized Multicellular Innate Immune Response in Lymph Nodes Limits Systemic Pathogen Spread. *Cell* **150**, 1235–1248 (2012).

139. Hor, J. L. & Germain, R. N. Intravital and high-content multiplex imaging of the immune system. *Trends Cell Biol* **32**, 406–420 (2022).
140. Henrickson, S. E. *et al.* Antigen Availability Determines CD8+ T Cell-Dendritic Cell Interaction Kinetics and Memory Fate Decisions. *Immunity* **39**, 496–507 (2013).
141. Mingozzi, F. *et al.* Prolonged contact with dendritic cells turns lymph node-resident NK cells into anti-tumor effectors. *EMBO Mol Med* **8**, 1039–1051 (2016).
142. Bajénoff, M. *et al.* Stromal Cell Networks Regulate Lymphocyte Entry, Migration, and Territoriality in Lymph Nodes. *Immunity* **25**, 989–1001 (2006).
143. Lämmermann, T. *et al.* Neutrophil swarms require LTB4 and integrins at sites of cell death in vivo. *Nature 2013 498:7454* **498**, 371–375 (2013).
144. Peniche, A. G. *et al.* Development of an ex vivo lymph node explant model for identification of novel molecules active against leishmania major. *Antimicrob Agents Chemother* **58**, 78–87 (2014).
145. Barrow-McGee, R. *et al.* Real-time ex vivo perfusion of human lymph nodes invaded by cancer (REPLICANT): a feasibility study. *J Pathol* **250**, 262–274 (2020).
146. Belanger, M. C. *et al.* Acute Lymph Node Slices Are a Functional Model System to Study Immunity Ex Vivo. *ACS Pharmacol Transl Sci* **4**, 128–142 (2021).
147. Shim, S., Belanger, M. C., Harris, A. R., Munson, J. M. & Pompano, R. R. Two-way communication between ex vivo tissues on a microfluidic chip: application to tumor–lymph node interaction. *Lab Chip* **19**, 1013–1026 (2019).
148. Franco, R. & Cedazo-Minguez, A. Successful therapies for Alzheimer's disease: why so many in animal models and none in humans? *Front Pharmacol* **5**, (2014).
149. Golding, H., Khurana, S. & Zaitseva, M. What Is the Predictive Value of Animal Models for Vaccine Efficacy in Humans? *Cold Spring Harb Perspect Biol* **10**, a028902 (2018).
150. Fabre, K. *et al.* Introduction to a manuscript series on the characterization and use of microphysiological systems (MPS) in pharmaceutical safety and ADME applications. *Lab Chip* **20**, 1049–1057 (2020).
151. Harrison, R. G. The outgrowth of the nerve fiber as a mode of protoplasmic movement. *Journal of Experimental Zoology* **9**, 787–846 (1910).
152. Kapałczyńska, M. *et al.* 2D and 3D cell cultures – a comparison of different types of cancer cell cultures. *Arch Med Sci* **14**, 910 (2018).
153. Mahmud, G. *et al.* Directing cell motions on micropatterned ratchets. *Nature Physics 2009 5:8* **5**, 606–612 (2009).
154. Kilian, K. A., Bugarija, B., Lahn, B. T. & Mrksich, M. Geometric cues for directing the differentiation of mesenchymal stem cells. *Proc Natl Acad Sci U S A* **107**, 4872–4877 (2010).
155. Nelson, C. M., VanDuijn, M. M., Inman, J. L., Fletcher, D. A. & Bissell, M. J. Tissue geometry determines sites of mammary branching morphogenesis in organotypic cultures. *Science (1979)* **314**, 298–300 (2006).
156. Birgersdotter, A., Sandberg, R. & Ernberg, I. Gene expression perturbation in vitro--a growing case for three-dimensional (3D) culture systems. *Semin Cancer Biol* **15**, 405–412 (2005).
157. Gilbert, L. A. & Hemann, M. T. DNA damage-mediated induction of a chemoresistant niche. *Cell* **143**, 355 (2010).
158. Paszek, M. J. *et al.* Tensional homeostasis and the malignant phenotype. *Cancer Cell* **8**, 241–254 (2005).
159. Vining, K. H. & Mooney, D. J. Mechanical forces direct stem cell behaviour in development and regeneration. *Nature Reviews Molecular Cell Biology 2017 18:12* **18**, 728–742 (2017).

160. Sun, W. *et al.* Organ-on-a-Chip for Cancer and Immune Organs Modeling. *Adv Healthc Mater* **8**, 1801363 (2019).
161. Hingorani, A. D. *et al.* Improving the odds of drug development success through human genomics: modelling study. *Scientific Reports 2019 9:1* **9**, 1–25 (2019).
162. Nam, K. H., Smith, A. S. T., Lone, S., Kwon, S. & Kim, D. H. Biomimetic 3D Tissue Models for Advanced High-Throughput Drug Screening. *J Lab Autom* **20**, 201–215 (2015).
163. Ben-David, U. *et al.* Patient-derived xenografts undergo mouse-specific tumor evolution. *Nature Genetics 2017 49:11* **49**, 1567–1575 (2017).
164. Pan, C., Kumar, C., Bohl, S., Klingmueller, U. & Mann, M. Comparative Proteomic Phenotyping of Cell Lines and Primary Cells to Assess Preservation of Cell Type-specific Functions. *Mol Cell Proteomics* **8**, 443 (2009).
165. Kim, M. *et al.* Passage-dependent accumulation of somatic mutations in mesenchymal stromal cells during in vitro culture revealed by whole genome sequencing. *Sci Rep* **7**, (2017).
166. Kaczmarczyk, J. A. *et al.* Comparative microsomal proteomics of a model lung cancer cell line NCI-H23 reveals distinct differences between molecular profiles of 3D and 2D cultured cells. *Oncotarget* **12**, 2022–2038 (2021).
167. Kim, Y. E. *et al.* Quantitative Proteomic Analysis of 2D and 3D Cultured Colorectal Cancer Cells: Profiling of Tankyrase Inhibitor XAV939-Induced Proteome. *Sci Rep* **8**, (2018).
168. Shields, J. D. *et al.* Autologous Chemotaxis as a Mechanism of Tumor Cell Homing to Lymphatics via Interstitial Flow and Autocrine CCR7 Signaling. *Cancer Cell* **11**, 526–538 (2007).
169. Thippabhotla, S., Zhong, C. & He, M. 3D cell culture stimulates the secretion of in vivo like extracellular vesicles. *Scientific Reports 2019 9:1* **9**, 1–14 (2019).
170. Baker, A. E. G. *et al.* Chemically and mechanically defined hyaluronan hydrogels emulate the extracellular matrix for unbiased in vivo and in vitro organoid formation and drug testing in cancer. *Materials Today* **56**, 96–113 (2022).
171. G Baker, A. E. *et al.* Benchmarking to the Gold Standard: Hyaluronan-Oxime Hydrogels Recapitulate Xenograft Models with In Vitro Breast Cancer Spheroid Culture. (2019) doi:10.1002/adma.201901166.
172. Ingber, D. E. Human organs-on-chips for disease modelling, drug development and personalized medicine. *Nature Reviews Genetics 2022* 1–25 (2022) doi:10.1038/s41576-022-00466-9.
173. Nikolaev, M. *et al.* Homeostatic mini-intestines through scaffold-guided organoid morphogenesis. *Nature 2020 585:7826* **585**, 574–578 (2020).
174. Aisenbrey, E. A. & Murphy, W. L. Synthetic alternatives to Matrigel. *Nat Rev Mater* **5**, 539 (2020).
175. LeSavage, B. L., Suhar, R. A., Broguiere, N., Lutolf, M. P. & Heilshorn, S. C. Next-generation cancer organoids. *Nature Materials 2021 21:2* **21**, 143–159 (2021).
176. Helm, C. L. E., Zisch, A. & Swartz, M. A. Engineered blood and lymphatic capillaries in 3-D VEGF-fibrin-collagen matrices with interstitial flow. *Biotechnol Bioeng* **96**, 167–176 (2007).
177. Ronaldson-Bouchard, K. *et al.* A multi-organ chip with matured tissue niches linked by vascular flow. *Nature Biomedical Engineering 2022 6:4* **6**, 351–371 (2022).
178. Langer, E. M. *et al.* Modeling Tumor Phenotypes In Vitro with Three-Dimensional Bioprinting. *Cell Rep* **26**, 608-623.e6 (2019).

179. Low, L. A., Mummery, C., Berridge, B. R., Austin, C. P. & Tagle, D. A. Organs-on-chips: into the next decade. *Nature Reviews Drug Discovery 2020 20:5* **20**, 345–361 (2020).
180. Greenlee, J. D. & King, M. R. Engineered fluidic systems to understand lymphatic cancer metastasis. *Biomicrofluidics* vol. 14 011502 Preprint at https://doi.org/10.1063/1.5133970 (2020).
181. Zhou, X. *et al.* 3D Bioprinting a Cell-Laden Bone Matrix for Breast Cancer Metastasis Study. *ACS Appl Mater Interfaces* **8**, 30017–30026 (2016).
182. Xu, Z. *et al.* Design and Construction of a Multi-Organ Microfluidic Chip Mimicking the in vivo Microenvironment of Lung Cancer Metastasis. *ACS Appl Mater Interfaces* **8**, 25840–25847 (2016).
183. Sutherland, R. M., McCredie, J. A. & Inch, W. R. Growth of Multicell Spheroids in Tissue Culture as a Model of Nodular Carcinomas. *JNCI: Journal of the National Cancer Institute* **46**, 113–120 (1971).
184. Strelez, C. *et al.* Human colorectal cancer-on-chip model to study the microenvironmental influence on early metastatic spread. *iScience* **24**, 102509 (2021).
185. Augustine, R. *et al.* 3D Bioprinted cancer models: Revolutionizing personalized cancer therapy. *Transl Oncol* **14**, 101015 (2021).
186. Bertulli, C. *et al.* Image-Assisted Microvessel-on-a-Chip Platform for Studying Cancer Cell Transendothelial Migration Dynamics. *Scientific Reports 2018 8:1* **8**, 1–14 (2018).
187. Chen, M. B. *et al.* On-chip human microvasculature assay for visualization and quantification of tumor cell extravasation dynamics. *Nature Protocols 2017 12:5* **12**, 865–880 (2017).
188. Jeon, J. S., Zervantonakis, I. K., Chung, S., Kamm, R. D. & Charest, J. L. In Vitro Model of Tumor Cell Extravasation. *PLoS One* **8**, e56910 (2013).
189. Yun, S. H. *et al.* Characterization and resolution of evaporation-mediated osmolality shifts that constrain microfluidic cell culture in poly(dimethylsiloxane) devices. *Anal Chem* **79**, 1126–1134 (2007).
190. Jeon, J. S. *et al.* Human 3D vascularized organotypic microfluidic assays to study breast cancer cell extravasation. *Proc Natl Acad Sci U S A* **112**, 214–219 (2015).
191. Greenlee, J. D. & King, M. R. Engineered fluidic systems to understand lymphatic cancer metastasis. *Biomicrofluidics* vol. 14 011502 Preprint at https://doi.org/10.1063/1.5133970 (2020).
192. Ran, S., Volk, L., Hall, K. & Flister, M. J. Lymphangiogenesis and lymphatic metastasis in breast cancer. *Pathophysiology* vol. 17 229–251 Preprint at https://doi.org/10.1016/j.pathophys.2009.11.003 (2010).
193. Chung, M., Ahn, J., Son, K., Kim, S. & Jeon, N. L. Biomimetic Model of Tumor Microenvironment on Microfluidic Platform. *Adv Healthc Mater* **6**, 1700196 (2017).
194. Wang, X., Sun, Q. & Pei, J. Microfluidic-based 3D engineered microvascular networks and their applications in vascularized microtumor models. *Micromachines* vol. 9 Preprint at https://doi.org/10.3390/mi9100493 (2018).
195. Gong, M. M. *et al.* Human organotypic lymphatic vessel model elucidates microenvironment-dependent signaling and barrier function. *Biomaterials* **214**, 119225 (2019).
196. Ayuso, J. M., Gong, M. M., Skala, M. C., Harari, P. M. & Beebe, D. J. Human Tumor-Lymphatic Microfluidic Model Reveals Differential Conditioning of Lymphatic Vessels by Breast Cancer Cells. *Adv Healthc Mater* **9**, 1900925 (2020).
197. Vollert, I. *et al.* In vitro perfusion of engineered heart tissue through endothelialized channels. *Tissue Eng Part A* **20**, 854–863 (2014).

198. Ouyang, L. *et al.* Void-Free 3D Bioprinting for In Situ Endothelialization and Microfluidic Perfusion. *Adv Funct Mater* **30**, 1908349 (2020).
199. Golden, A. P. & Tien, J. Fabrication of microfluidic hydrogels using molded gelatin as a sacrificial element. *Lab Chip* **7**, 720–725 (2007).
200. Hansen, C. J. *et al.* Self-Healing Materials with Interpenetrating Microvascular Networks. *Advanced Materials* **21**, 4143–4147 (2009).
201. Li, Z., Yang, J., Li, K., Zhu, L. & Tang, W. Fabrication of PDMS microfluidic devices with 3D wax jetting. *RSC Adv* **7**, 3313–3320 (2017).
202. Gong, J. *et al.* Complexation-induced resolution enhancement of 3D-printed hydrogel constructs. *Nature Communications 2020 11:1* **11**, 1–14 (2020).
203. Gao, G., Park, J. Y., Kim, B. S., Jang, J. & Cho, D. W. Coaxial Cell Printing of Freestanding, Perfusable, and Functional In Vitro Vascular Models for Recapitulation of Native Vascular Endothelium Pathophysiology. *Adv Healthc Mater* **7**, 1801102 (2018).
204. Miller, J. S. *et al.* Rapid casting of patterned vascular networks for perfusable engineered three-dimensional tissues. *Nature Materials 2012 11:9* **11**, 768–774 (2012).
205. Kolesky, D. B., Homan, K. A., Skylar-Scott, M. A. & Lewis, J. A. Three-dimensional bioprinting of thick vascularized tissues. *Proc Natl Acad Sci U S A* **113**, 3179–3184 (2016).
206. Lin, N. Y. C. *et al.* Renal reabsorption in 3D vascularized proximal tubule models. *Proc Natl Acad Sci U S A* **116**, 5399–5404 (2019).
207. Kolesky, D. B. *et al.* 3D Bioprinting of Vascularized, Heterogeneous Cell-Laden Tissue Constructs. *Advanced Materials* **26**, 3124–3130 (2014).
208. Skylar-Scott, M. A. *et al.* Biomanufacturing of organ-specific tissues with high cellular density and embedded vascular channels. *Sci Adv* **5**, (2019).
209. Segeritz, C. P. & Vallier, L. Cell Culture: Growing Cells as Model Systems In Vitro. *Basic Science Methods for Clinical Researchers* 151–172 (2017) doi:10.1016/B978-0-12-803077-6.00009-6.
210. Hussain, T. & Mulherkar, R. Lymphoblastoid Cell lines: a Continuous in Vitro Source of Cells to Study Carcinogen Sensitivity and DNA Repair. *Int J Mol Cell Med* **1**, 75 (2012).
211. Massberg, S. *et al.* Immunosurveillance by Hematopoietic Progenitor Cells Trafficking through Blood, Lymph, and Peripheral Tissues. *Cell* **131**, 994–1008 (2007).
212. Iriguchi, S. *et al.* A clinically applicable and scalable method to regenerate T-cells from iPSCs for off-the-shelf T-cell immunotherapy. *Nature Communications 2021 12:1* **12**, 1–15 (2021).
213. Nianias, A. & Themeli, M. Induced Pluripotent Stem Cell (iPSC)–Derived Lymphocytes for Adoptive Cell Immunotherapy: Recent Advances and Challenges. *Curr Hematol Malig Rep* **14**, 261 (2019).
214. Brown, M. E. *et al.* Derivation of Induced Pluripotent Stem Cells from Human Peripheral Blood T Lymphocytes. *PLoS One* **5**, e11373 (2010).
215. Lan, T. *et al.* Induced pluripotent stem cells can effectively differentiate into multiple functional lymphocyte lineages in vivo with negligible bias. *Stem Cells Dev* **25**, 462–471 (2016).
216. Moura Rosa, P., Gopalakrishnan, N., Ibrahim, H., Haug, M. & Halaas, Ø. The intercell dynamics of T cells and dendritic cells in a lymph node-on-a-chip flow device. *Lab Chip* **16**, 3728–3740 (2016).
217. Haessler, U., Kalinin, Y., Swartz, M. A. & Wu, M. An agarose-based microfluidic platform with a gradient buffer for 3D chemotaxis studies. *Biomed Microdevices* **11**, 827–835 (2009).

218. Kraus, T. *et al.* Evaluation of a 3D Human Artificial Lymph Node as Test Model for the Assessment of Immunogenicity of Protein Aggregates. *J Pharm Sci* **108**, 2358–2366 (2019).
219. Radke, L. *et al.* In Vitro Evaluation of Glycoengineered RSV-F in the Human Artificial Lymph Node Reactor. *Bioengineering 2017, Vol. 4, Page 70* **4**, 70 (2017).
220. Hallfors, N. *et al.* Multi-Compartment Lymph-Node-on-a-Chip Enables Measurement of Immune Cell Motility in Response to Drugs. *Bioengineering 2021, Vol. 8, Page 19* **8**, 19 (2021).
221. Shanti, A. *et al.* Multi-Compartment 3D-Cultured Organ-on-a-Chip: Towards a Biomimetic Lymph Node for Drug Development. *Pharmaceutics 2020, Vol. 12, Page 464* **12**, 464 (2020).
222. Jannat, R. A., Robbins, G. P., Ricart, B. G., Dembo, M. & Hammer, D. A. Neutrophil adhesion and chemotaxis depend on substrate mechanics. *Journal of Physics: Condensed Matter* **22**, 194117 (2010).
223. Ricart, B. G., John, B., Lee, D., Hunter, C. A. & Hammer, D. A. Dendritic Cells Distinguish Individual Chemokine Signals through CCR7 and CXCR4. *The Journal of Immunology* **186**, 53–61 (2011).
224. Sonmez, U. M. *et al.* Chemotactic Responses of Jurkat Cells in Microfluidic Flow-Free Gradient Chambers. *Micromachines 2020, Vol. 11, Page 384* **11**, 384 (2020).
225. Lin, F. & Butcher, E. C. T cell chemotaxis in a simple microfluidic device. *Lab Chip* **6**, 1462–1469 (2006).
226. Birmingham, K. G. *et al.* Lymph Node Subcapsular Sinus Microenvironment-On-A-Chip Modeling Shear Flow Relevant to Lymphatic Metastasis and Immune Cell Homing. *iScience* **23**, (2020).
227. Dura, B. *et al.* Profiling lymphocyte interactions at the single-cell level by microfluidic cell pairing. *Nature Communications 2015 6:1* **6**, 1–13 (2015).
228. Moura Rosa, P., Gopalakrishnan, N., Ibrahim, H., Haug, M. & Halaas, Ø. The intercell dynamics of T cells and dendritic cells in a lymph node-on-a-chip flow device. *Lab Chip* **16**, 3728–3740 (2016).
229. Goyal, G. *et al.* Lymphoid follicle formation and human vaccination responses recapitulated in an organ-on-a-chip. *bioRxiv* 806505 (2021) doi:10.1101/806505.
230. Shanti, A., Hallfors, N., Petroianu, G. A., Planelles, L. & Stefanini, C. Lymph Nodes-On-Chip: Promising Immune Platforms for Pharmacological and Toxicological Applications. *Front Pharmacol* **12**, 2132 (2021).
231. Shanti, A., Hallfors, N., Petroianu, G. A., Planelles, L. & Stefanini, C. Lymph Nodes-On-Chip: Promising Immune Platforms for Pharmacological and Toxicological Applications. *Front Pharmacol* **12**, 2132 (2021).
232. Fletcher, A. L. *et al.* Lymph node fibroblastic reticular cells directly present peripheral tissue antigen under steady-state and inflammatory conditions. *Journal of Experimental Medicine* **207**, 689–697 (2010).
233. Hirosue, S. *et al.* Steady-State Antigen Scavenging, Cross-Presentation, and CD8 + T Cell Priming: A New Role for Lymphatic Endothelial Cells . *The Journal of Immunology* **192**, 5002–5011 (2014).
234. Tomei, A. A., Siegert, S., Britschgi, M. R., Luther, S. A. & Swartz, M. A. Fluid Flow Regulates Stromal Cell Organization and CCL21 Expression in a Tissue-Engineered Lymph Node Microenvironment. *The Journal of Immunology* **183**, 4273–4283 (2009).
235. Munir, H. *et al.* Stromal-driven and Amyloid β-dependent induction of neutrophil extracellular traps modulates tumor growth. *Nature Communications 2021 12:1* **12**, 1–16 (2021).

236. Ingber, D. E. Human organs-on-chips for disease modelling, drug development and personalized medicine. *Nature Reviews Genetics 2022* 1–25 (2022) doi:10.1038/s41576-022-00466-9.
237. Low, L. A., Mummery, C., Berridge, B. R., Austin, C. P. & Tagle, D. A. Organs-on-chips: into the next decade. *Nature Reviews Drug Discovery 2020 20:5* **20**, 345–361 (2020).
238. Bertulli, C. *et al.* Image-Assisted Microvessel-on-a-Chip Platform for Studying Cancer Cell Transendothelial Migration Dynamics. *Sci Rep* **8**, 12480 (2018).
239. Gerigk, M. *et al.* On-chip perivascular niche supporting stemness of patient-derived glioma cells in a serum-free, flowable culture. *Lab Chip* **21**, 2343–2358 (2021).
240. Akther, F., Little, P., Li, Z., Nguyen, N. T. & Ta, H. T. Hydrogels as artificial matrices for cell seeding in microfluidic devices. *RSC Adv* **10**, 43682–43703 (2020).
241. Nie, J. *et al.* Hydrogels: The Next Generation Body Materials for Microfluidic Chips? *Small* **16**, 2003797 (2020).
242. Munir, H., Mazzaglia, C. & Shields, J. D. Stromal regulation of tumor-associated lymphatics. *Adv Drug Deliv Rev* **161–162**, 75–89 (2020).
243. Bekisz, S., Baudin, L., Buntinx, F., Noël, A. & Geris, L. In Vitro, In Vivo, and In Silico Models of Lymphangiogenesis in Solid Malignancies. *Cancers (Basel)* **14**, 1525 (2022).
244. Martinez, V. G. *et al.* Fibroblastic Reticular Cells Control Conduit Matrix Deposition during Lymph Node Expansion. *Cell Rep* **29**, 2810-2822.e5 (2019).
245. Ebrahimi Dastgurdi, M., Ejeian, F., Nematollahi, M., Motaghi, A. & Nasr-Esfahani, M. H. Comparison of two digestion strategies on characteristics and differentiation potential of human dental pulp stem cells. *Arch Oral Biol* **93**, 74–79 (2018).
246. Ford, A. L., Foulcher, E., Goodsall, A. L. & Sedgwick, J. D. Tissue digestion with dispase substantially reduces lymphocyte and macrophage cell-surface antigen expression. *J Immunol Methods* **194**, 71–75 (1996).
247. Autengruber, A., Gereke, M., Hansen, G., Hennig, C. & Bruder, D. Impact of enzymatic tissue disintegration on the level of surface molecule expression and immune cell function. *Eur J Microbiol Immunol (Bp)* **2**, 112 (2012).
248. Majowicz, A. *et al.* Murine CD4+CD25- cells activated in vitro with PMA/ionomycin and anti-CD3 acquire regulatory function and ameliorate experimental colitis in vivo. *BMC Gastroenterol* **12**, 1–9 (2012).
249. Ai, W., Li, H., Song, N., Li, L. & Chen, H. Optimal Method to Stimulate Cytokine Production and Its Use in Immunotoxicity Assessment. *Int J Environ Res Public Health* **10**, 3834 (2013).
250. Ai, W., Li, H., Song, N., Li, L. & Chen, H. Optimal Method to Stimulate Cytokine Production and Its Use in Immunotoxicity Assessment. *Int J Environ Res Public Health* **10**, 3834 (2013).
251. Elyada, E. *et al.* Cross-species single-cell analysis of pancreatic ductal adenocarcinoma reveals antigen-presenting cancer-associated fibroblasts. *Cancer Discov* **9**, 1102–1123 (2019).
252. Davidson, S. *et al.* Single-Cell RNA Sequencing Reveals a Dynamic Stromal Niche That Supports Tumor Growth. *Cell Rep* **31**, (2020).
253. Suzuki, H. *et al.* Induction of podoplanin by transforming growth factor-β in human fibrosarcoma. *FEBS Lett* **582**, 341–345 (2008).
254. Ji, R. C. Lymph Nodes and Cancer Metastasis: New Perspectives on the Role of Intranodal Lymphatic Sinuses. *Int J Mol Sci* **18**, (2017).
255. Wang, G. R., Yang, F. & Zhao, W. There can be turbulence in microfluidics at low Reynolds number. *Lab Chip* **14**, 1452–1458 (2014).

256. el Khoury, G. K., Pettersen, B., Andersson, H. I. & Barri, M. Asymmetries in an obstructed turbulent channel flow. *Physics of Fluids* **22**, 095103 (2010).
257. Ha, H. *et al.* Age-related vascular changes affect turbulence in aortic blood flow. *Front Physiol* **9**, 36 (2018).
258. Polacheck, W. J., Charest, J. L. & Kamm, R. D. Interstitial flow influences direction of tumor cell migration through competing mechanisms. *Proc Natl Acad Sci U S A* (2011) doi:10.1073/pnas.1103581108.
259. Lei, I. M. *et al.* 3D printed biomimetic cochleae and machine learning co-modelling provides clinical informatics for cochlear implant patients. *Nature Communications 2021 12:1* **12**, 1–12 (2021).
260. Yin, J., Yan, M., Wang, Y., Fu, J. & Suo, H. 3D Bioprinting of Low-Concentration Cell-Laden Gelatin Methacrylate (GelMA) Bioinks with a Two-Step Cross-linking Strategy. *ACS Appl Mater Interfaces* **10**, 6849–6857 (2018).
261. Nichol, J. W. *et al.* Cell-laden microengineered gelatin methacrylate hydrogels. *Biomaterials* **31**, 5536 (2010).
262. Acton, S. E. *et al.* Dendritic cells control fibroblastic reticular network tension and lymph node expansion. *Nature 2014 514:7523* **514**, 498–502 (2014).
263. Fletcher, A. L. *et al.* Reproducible isolation of lymph node stromal cells reveals site-dependent differences in fibroblastic reticular cells. *Front Immunol* **2**, 35 (2011).
264. Martinez, V. G. *et al.* Fibroblastic Reticular Cells Control Conduit Matrix Deposition during Lymph Node Expansion. *Cell Rep* **29**, 2810-2822.e5 (2019).
265. Gonzalez Badillo, F. *et al.* Tissue-Engineered Stromal Reticula to Study Lymph Node Fibroblastic Reticular Cells in Type I Diabetes. *Cell Mol Bioeng* **13**, 419–434 (2020).
266. Ayuso, J. M., Gong, M. M., Skala, M. C., Harari, P. M. & Beebe, D. J. Human tumor-lymphatic microfluidic model reveals differential conditioning of lymphatic vessels by breast cancer cells. *Adv Healthc Mater* **9**, e1900925 (2020).
267. Virumbrales-Muñoz, M. *et al.* Enabling cell recovery from 3D cell culture microfluidic devices for tumour microenvironment biomarker profiling. *Scientific Reports 2019 9:1* **9**, 1–14 (2019).
268. Lugo-Cintrón, K. M. *et al.* Matrix Density Drives 3D Organotypic Lymphatic Vessel Activation in a Microfluidic Model of the Breast Tumor Microenvironment. *Lab Chip* **20**, 1586 (2020).
269. Ostrowski, M. A. *et al.* Microvascular Endothelial Cells Migrate Upstream and Align Against the Shear Stress Field Created by Impinging Flow. *Biophys J* **106**, 366–374 (2014).
270. Wang, C., Baker, B. M., Chen, C. S. & Schwartz, M. A. Endothelial cell sensing of flow direction. *Arterioscler Thromb Vasc Biol* **33**, 2130–2136 (2013).
271. Lefort, C. T. & Kim, M. Human T Lymphocyte Isolation, Culture and Analysis of Migration In Vitro. *J Vis Exp* (2010) doi:10.3791/2017.
272. Kuzin, I. *et al.* Long-term immunologically competent human peripheral lymphoid tissue cultures in a 3D bioreactor. *Biotechnol Bioeng* **108**, 1430–1440 (2011).
273. Rayner, S. G. *et al.* Multiphoton-Guided Creation of Complex Organ-Specific Microvasculature. *Adv Healthc Mater* **10**, 2100031 (2021).
274. Brandenberg, N., Lutolf, M. P., Brandenberg, N. & Lutolf, M. P. In Situ Patterning of Microfl uidic Networks in 3D Cell-Laden Hydrogels. (2016) doi:10.1002/adma.201601099.
275. Tough, D. F., Sun, S. & Sprent, J. T Cell Stimulation In Vivo by Lipopolysaccharide (LPS). *Journal of Experimental Medicine* **185**, 2089–2094 (1997).
276. Xu, L. *et al.* TLR9 signaling in fibroblastic reticular cells regulates peritoneal immunity. *J Clin Invest* **129**, 3657–3669 (2019).

277. Deng, M., Li, Y., Chen, T., Chen, K. & Billiar, T. R. Roles of Toll-like Receptors in Regulating Fibroblastic Reticular Cells Pathobiology during Sepsis. *The Journal of Immunology* **202**, (2019).
278. Lee, J. Y. & Sullivan, K. E. Gamma Interferon and Lipopolysaccharide Interact at the Level of Transcription To Induce Tumor Necrosis Factor Alpha Expression. *Infect Immun* **69**, 2847 (2001).
279. Huang, W. & August, A. The signaling symphony: T cell receptor tunes cytokine-mediated T cell differentiation. *J Leukoc Biol* **97**, 477–485 (2015).
280. Hwang, J. R., Byeon, Y., Kim, D. & Park, S. G. Recent insights of T cell receptor-mediated signaling pathways for T cell activation and development. *Experimental & Molecular Medicine 2020 52:5* **52**, 750–761 (2020).
281. Kastenmüller, W. *et al.* Peripheral Prepositioning and Local CXCL9 Chemokine-Mediated Guidance Orchestrate Rapid Memory CD8+ T Cell Responses in the Lymph Node. *Immunity* **38**, 502–513 (2013).
282. Sung, J. H. *et al.* Chemokine Guidance of Central Memory T Cells Is Critical for Anti-Viral Recall Responses in Lymph Nodes. *Cell* **150**, 1249 (2012).
283. Volkman, D. J., Lane, H. C. & Fauci, A. S. Antigen-induced in vitro antibody production in humans: A model for B cell activation and immunoregulation. *Proc Natl Acad Sci U S A* **78**, 2528–2531 (1981).
284. van Pul, K. M., Fransen, M. F., van de Ven, R. & de Gruijl, T. D. Immunotherapy Goes Local: The Central Role of Lymph Nodes in Driving Tumor Infiltration and Efficacy. *Front Immunol* **12**, 518 (2021).
285. du Bois, H., Heim, T. A. & Lund, A. W. Tumor-Draining Lymph Nodes: At the Crossroads of Metastasis and Immunity. *Sci Immunol* **6**, eabg3551 (2021).
286. Dammeijer, F. *et al.* The PD-1/PD-L1-Checkpoint Restrains T cell Immunity in Tumor-Draining Lymph Nodes. *Cancer Cell* **38**, 685-700.e8 (2020).
287. Day, C. P., Merlino, G. & van Dyke, T. Preclinical Mouse Cancer Models: A Maze of Opportunities and Challenges. *Cell* **163**, 39–53 (2015).